NASA CR- 144796

REQUIREMENTS AND CONCEPT DESIGN FOR LARGE EARTH SURVEY TELESCOPE FOR SEOS

FINAL REPORT

Itek Corporation
Optical Systems Division
10 Maguire Road
Lexington, Massachusetts 02173

April 1975

Prepared for
GODDARD SPACE FLIGHT CENTER
Greenbelt, Maryland 20771

Itek Optical Systems / RCA Astro Electronics Division

TECHNICAL REPORT STANDARD TITLE PAGE

1. Report No.	2. Government Accession No.	3. Recipient's Catalog No.
75-9510-1		

4. Title and Subtitle	5. Report Date
Requirements and Concept Design for Large Earth Survey Telescope for SEOS	April, 1975
	6. Performing Organization Code
7. Author(s)	8. Performing Organization Report No.
Paul Mailhot and John Bisbee	75-9510-1
9. Performing Organization Name and Address	10. Work Unit No.
Itek Corporation Optical Systems Division 10 Maguire Road Lexington, Massachusetts	11. Contract or Grant No. NAS5-20074
	13. Type of Report and Period Covered Type III Final Report April, 1974-April, 1975
12. Sponsoring Agency Name and Address	14. Sponsoring Agency Code
Goddard Space Flight Center Greenbelt, Maryland 20771	

15. Supplementary Notes

16. Abstract

This report summarizes the efforts of a one year program of Requirements Analysis and Conceptual Design for the Large Earth Survey Telescope (LEST) for the Synchronous Earth Observatory Satellite (SEOS). A 1.4 meter aperture Cassegrain telescope with 0.6^{o} field of view is shown to do an excellent job in satisfying the observational requirements for a wide range of Earth resources and meteorological applications. The telescope provides imagery or thermal mapping in ten spectral bands at one time in a field sharing grouping of linear detector arrays. Pushbroom scanning is accomplished by spacecraft slew.

17. Key Words (Selected by Author(s))	18. Distribution Statement
SEOS, LEST, Earth Resources, Meteorology, Multispectral, Telescope, Geostationary	

19. Security Classif. (of this report)	20. Security Classif. (of this page)	21. No. of Pages	22. Price*
Unclassified	Unclassified		

*For sale by the Clearinghouse for Federal Scientific and Technical Information, Springfield, Virginia 22151.

PREFACE

Itek Optical Systems Division has been engaged in the period April, 1974 to April, 1975, in requirements review and conceptual design studies for the Large Earth Survey Telescope (LEST) for the Synchronous Earth Observatory Satellite (SEOS). This, the final report for the study, summarizes the activities and conclusions, and presents the conceptual design for LEST. RCA Astro-Electronics Division participated in the study as a subcontractor to Itek, contributing principally in the areas of spacecraft attitude control and detector cooling.

The study has verified that the spatial resolution and radiometric sensitivity requirements of the Earth resources and meteorological communities can be met with a large aperture Earth viewing telescope operating from geostationary orbit. When operating in conjunction with upgraded ground data handling systems, near real time assessment of Earth resources and meteorological events may be made.

The conceptual design of a 0.6° field of view Cassegrain telescope is described, and a prediction of achievable performance is given. The design described is based on existing technology or small extrapolations of existing technology, and is not dependent on major technological breakthroughs.

A schedule leading to first SEOS/LEST launch in 1985, and rough order of magnitude costs for the LEST program are given.

Recommendations for continuing studies are made in certain areas of critical technology.

TABLE OF CONTENTS

1. Introduction 1

2. Requirements 4
   2.1 Applications 4
   2.2 Parametric Trades 4
   2.3 LEST Performance Specifications 12

3. Full-up LEST Conceptual Studies 13
   3.1 LEST System 13
   3.2 Optics 25
   3.3 Thermal Design 82
   3.4 Structures 88
   3.5 Spacecraft Attitude Control and Scanning 98
   3.6 Detector Electronics and Calibration 136
   3.7 Detector Cooling 140
   3.8 Mass Properties 148

4. Alternate Systems 152
   4.1 Strip-Down Design 152
   4.2 Minimum System 152

5. Performance Analysis 154
   5.1 Input Data 154
   5.2 Methods of Analysis 157
   5.3 Performance Prediction 161
   5.4 Discussion 163

6. Degradation Considerations 167
   6.1 Reliability 167
   6.2 Energetic Radiation 168
   6.3 Contamination 171

7. State of the Art and Technical Risks 173
   7.1 Optics 173
   7.2 Detectors 173
   7.3 Cooler 174
   7.4 Attitude Control 174

8. Program Plan and Schedule 176
8.1 Additional Conceptual Studies 176
8.2 SEOS System Phase B, Preliminary Design 176
8.3 Critical Technology Development 178
8.4 Phase C/D 178

9. Rough Order of Magnitude Cost Estimate 181
9.1 Costs Prior to Start of Phase C/D 181
9.2 Phase C/D Through First Launch 182
9.3 Cost for Strip-Down and Minimum Design Systems 189

10. Recommendations for Further Study 191
10.1 Optical Design 191
10.2 Attitude Determination and Control 192
10.3 Detector Array Development 192
10.4 Ground Data Handling 193

Abbreviations and Symbols 195

References 197

Appendix A — Preliminary Performance Specification; Full-Up LEST A-1
Appendix B — Preliminary Performance Specification; Strip-Down LEST . . B-1

LIST OF FIGURES

2.2-1	Conceptual Design Trades	8
3.1-1	SEOS/LEST Inboard Profile	15
3.1-2	Relay/Focal Plane Area	17
3.1-3	Wavefront Error Budget	22
3.2-1	Dichroic Mirror Considerations	29
3.2-2	Howell's Design with 1 cm Thick Beam Splitter	31
3.2-3	Ray Traces of Howell's Design Without Beam Splitter	32
3.2-4	Reflectance & Transmittance of a Thin Gold Mirror	33
3.2-5	Expansion of Fig. 3.2-4	34
3.2-6	Ray Traces of Howell's Design with Beam Splitter	35
3.2-7	Three-Mirror f/5 Telescope	40
3.2-8	f/12 Image Layout for Visible Detector Arrays	41
3.2-9	Ray Trace of 3-Mirror f/5	43
3.2-10	Spot Diagrams for f/5 System	44
3.2-11	MTF of f/5 System	45
3.2-12	Filter Changer Mechanism Allowing any Combination	46
3.2-13	Filter Changer Mechanism Allowing Choice of Four Filters	47
3.2-14	Alternate Changer Mechanism	47
3.2-15	Telescope with Preliminary f/2 Relay Design	50
3.2-16	Ray Trace of f/2 System, 2.2 μm	53
3.2-17	Spot Diagrams of f/2 System, 2.2 μm	54
3.2-18	MTF of f/2 System	56
3.2-19	Ray Trace of f/2 System, 1.63 μm	57
3.2-20	Spot Diagrams of f/2 System, 1.63 and 3.8 μm	58
3.2-21	Ray Trace of f/2 System, 3.8 μm	59
3.2-22	f/1.3 Relay Design	63
3.2-23	Ray Trace of f/1.3 System, 10.8 μm	64
3.2-24	Spot Diagrams of f/1.3 System	65
3.2-25	Ray Trace of f/1.2 System, 11.6 μm	66
3.2-26	Ray Trace of f/1.3 System, 12.3 μm	67
3.2-27	Ray Trace of f/1.3 System, 6.8 μm	68
3.2-28	Ray Trace of f/1.3 System, 3.8 μm	69
3.2-29	Reflectivities of Aluminum and Silver Mirror	72
3.2-30	OCLI Anti-reflection Coatings for Germanium	75
3.2-31	Absorption Coefficient of Germanium	78
3.2-32	Standard Baffle Cones	81
3.2-33	Field Stops for Stray Light	82

3.3-1	Thermal Control Requirements for Telescope	83
3.3-2	LEST Baseline Thermal Control Concept	85
3.3-3	Temperature History of Primary Mirror	86
3.3-4	Temperature History of Metering Shell	87
3.3-5	LEST Thermal Error Budget	89
3.3-6	Total RMS WFE vs. Orbit Time	90
3.4-1	Structural Model	93
3.4-2	Lateral Velocity at Image Plane	95
3.4-3	Primary Mirror Lateral Displacement	96
3.4-4	Secondary Mirror Lateral Displacement	97
3.5-1	Scan Control Considerations	102
3.5-2	Meteorological Monitor Pattern	103
3.5-3	Scan Profile	114
3.5-4	Basic Scan Pattern	120
3.5-5	S/C Rate Control	121
3.5-6	Adaptive Turn Around	123
3.5-7	ACS Control Block Diagram	133
3.6-1	IR Detector Circuit Concept	139
3.7-1	Three-Stage Shallow Cooler for 7° Sun Angle	141
3.7-2	Performance of 3-Stage Cooler Concepts	142
3.7-3	Cooler Cold Plate Temperature vs. Heat Load	143
3.7-4	Schematic of Detector-Relay Lens Assembly	147
3.8-1	System Mass Properties	151
5.1-1	NEE of Silicon CCD	156
5.2-1	MTF Development of Three ERS Bands	158
5.2-2	MTF Development of Four Met Bands	160
5.4-1	EIFOV/NER Tradeoff, Band M5	166
6.2-1	Effect of Proton Radiation on Various Electronic Components	170
6.2-2	Effect of 10 Kev Protons on $MgF_2/A\ell$-Coated Cervit	172
8.0-1	SEOS Program Schedule	177
8.4-1	LEST Hardware and Test Flow	180
9.2-1	Work Breakdown Structure for LEST Phase C/D	183

LIST OF TABLES

1-1	Key Features, LEST Conceptual Design	3
2.1-1	SEOS Earth Resources Applications	5
2.1-2	Spectral Band Requirements for Earth Resources	6
2.1-3	Short List of SEOS Applications	7
2.1-4	Key Meteorological Parameters in Order of Importance	7
2.2-1	Comparison of Wide and Narrow Field Systems	10
2.2-2	Optics Limited EIFOV, Weight vs. Aperture Diameter	10
3.1-1	Design Features, Full-up LEST	19
3.1-2	Summary of Wavefront Error Data	24
3.2-1	Spectral Pass Band, Focal Ratio and Detector Size for Each Spectral Band	26
3.2-2	Glass Dispersion Data: Typical V-Numbers in the Visible	38
3.2-3	Glass Dispersion Data: V-Numbers for IR Material	38
3.2-4	3-Mirror f/5 Design	41
3.2-5	Lens Deck for f/2 Relay; Design of f/2 Relay	51
3.2-6	Lens Deck for f/1.3 Relay	61
3.2-7	Design of f/1.3 Relay	62
3.2-8	f/1.3 Wavefront Errors	70
3.2-9	f/1.3 Wavefront Errors for Thinner Design	70
3.2-10	Optical System Transmittances for f/5 Image	74
3.2-11	Transmittance for Preliminary f/2 Design	77
3.2-12	Transmittance for Hypothetical f/2 Design	77
3.2-13	Transmittance for f/1.3 Relay	80
3.4-1	Normal Modes Description	94
3.5-1	Pointing Error Budget	99
3.5-2	DMSP Star Mapper Characteristics	128
3.6-1	Scan Time Assuming 50% Efficiency	137
3.7-1	Properties of Thermal Finishes	141
3.8-1	LEST Weight Statement	149
3.8-2	SEOS System Weight	150
5.3-1	Performance Predictions for LEST	162
5.4-1	Noise Equivalent Radiance for Essential Spectral Bands	164
6.2-1	Proton Fluence and Shielding	169
9.2-1	Summary of ROM Cost, Phase C/D for Full-Up LEST	182
9.2-2	ROM Cost for Follow-On Full-Up LEST	189

1. INTRODUCTION

This report, issued by Itek Optical Systems Division, presents the results of a one year program of requirements analysis and conceptual design studies for the Large Earth Survey Telescope (LEST) for the Synchronous Earth Observatory Satellite. The study was conducted for NASA, Goddard Space Flight Center (GSFC) under Contract NAS5-20074. RCA Astro-Electronics Division participated as a subcontractor to Itek in the study. Concurrent with the Itek study, which concentrates on the telescope, focal plane and scanning methods, GSFC has been conducting a SEOS system Phase A study in-house.

SEOS is being planned for launch in the mid 1980's as a system for providing multispectral imagery, atmospheric sounding, and data collection for earth resources and meteorological applications. Operating from geostationary orbit, the system could be commanded to view selected areas of the Western hemisphere with particular utilization in the continental United States. Since SEOS would maintain an essentially constant position with respect to the earth, sites of interest may be viewed on command, continuously or repetitively. This capability makes it possible to observe shortlived events and phenomena dependent on sun angle and to make timely observations between clouds as well as performing routine search and monitoring. The size and quality of the telescope will be such that the resolution and sensitivity achieved will provide data that will greatly enhance the capabilities for mesoscale weather prediction and for real time coverage of a large number of earth resources applications.

The objective of the SEOS/LEST study is to determine feasibility and to derive design concepts for the large aperture telescope for SEOS. The activities of the first six months time period of the study, identified as Phase I, were reported in Reference 1 (74-9510-2A). The principal findings of the Phase I activity will be summarized in Section 2 of this report, but the reader should consult the reference for a more detailed understanding of requirements analysis and telescope parametric trades.

The principal activities in Phase II (November 1974 - April 1975) of the study are recorded in this report. In Section 2, after a brief summary of the Phase I efforts, we present the performance specifications for the LEST telescope. The design concept of a full-up (operational mission) telescope is described in Section 3. This description includes design tradeoffs and, where possible, preliminary design details such as optical prescription. Potential cost reduction simplifications possible for a demonstration (strip down) mission are discussed in Section 4. Performance analysis and comparison with requirements is given in Section 5. In Section 6, possible degradation in performance

caused by reliability considerations, or due to long exposure to the space environment are discussed. The relationship of the conceptual design to the state of the art, and possible technical risks are discussed in Section 7. Sections 8 and 9 present program schedule and ROM cost estimates. In Section 10, areas of critical technology warranting continued conceptual study are identified.

Technical Summary

The requirements review and conceptual design studies accomplished in this study program underscore the usefulness and feasibility of an earth viewing, geostationary satellite for earth resources and meteorological applications. LEST performance requirements in terms of resolution, sensitivity, coverage rates, etc. differ with spectral band, application and operating mode. The specifications (Appendices A and B) detail these requirements. As a useful simplification for generally classifying the system, one could consider the following generalized requirements. (The conceptual design, however, is based on the detailed requirements.)

Resolution (EIFOV)

Visible Bands	100 meters
Thermal IR Bands	1000 meters

Sensitivity (NER)

Earth Resources	1-7 $\mu w/cm^2$ ster
Meteorological	.03-3 $\mu w/cm^2$ ster

Coverage Rate

Earth Resources	$20 \times 20^3 km^2/sec$
Meteorological Monitor	$22.5 \times 10^3 km^2/sec$

The key features of the recommended conceptual design are shown in Table 1-1.

TABLE 1-1

Key Features, LEST Conceptual Design (Full-up)

OPTICS	
Aperture	1.4 meter
Basic Telescope	Cassegrain
Field of View	0.6° (375 km)
Focal Planes	
Visible	f/5
Near IR	f/2
Thermal IR	f/1.3
Spectral Bands	
Visible	13 (4 at one time)
Near IR	3
Thermal IR	5 (3 at one time)
Detector Arrays	
Silicon	4
PbS	2
InSb (cooled)	1
HgCdTe (cooled)	3
Scanning	
Technique	Pushbroom
Mechanization	Spacecraft Scan. using CMG's

2. REQUIREMENTS

2.1 APPLICATIONS

In Phase I of this program, reports describing a wide range of potential meteorological and Earth Resources applications for SEOS were reviewed for the purpose of arriving at a set of requirements for a Large Earth Survey Telescope (LEST). The performance specifications in Section 2.3 represent a best compromise among the many applications as derived in our Phase I study. The referenced application reports are:

(Ref. 2) "Earth Resources Applications of the Synchronous Earth Observatory Satellite (SEOS)", ERIM 103500-1-F, December 1973, Environmental Research Institute of Michigan (ERIM).

(Ref. 3) "Meteorological Uses of the Synchronous Earth Observatory Satellite", 31 July 1973, University of Wisconsin (GSFC Contract NAS5-21798).

During the period of the Itek study, the applications and requirements were updated, reviewed, and condensed through the efforts of GSFC, ERIM, data users, and the LEST study contractors. The resolution and sensitivity requirements for each application were reviewed for feasibility from a practical size spacecraft operating at geostationary orbit (35.9×10^3 km = 22,000 miles). The twenty highest priority, and achievable, earth resources applications and their required spectral bands are listed in Tables 2.1-1 and 2.1-2. Meteorological applications for SEOS/LEST are listed in Table 2.1-3, and the key parameters used in serving these applications are shown in Table 2.1-4. For meteorology; nine spectral bands required for visible imagery and IR mapping, and two modes of IR sounding for vertical temperature profile measurement were identified. The LEST design described in Section 3 of this report incorporates the detectors and filters to provide the visible imagery and IR mapping, and provides an image to the IR sounder.

2.2 PARAMETRIC TRADES

In evolving a design concept during Phase I of this study, a large number of parameters and mechanization techniques had to be considered and tradeoffs conducted. Figure 2.2-1 depicts the principal inputs and outputs of the design trades. In this section, we will summarize the parameter design considerations from Phase I which have led to the design concept which has been further developed and evaluated in Phase II.

Table 2.1-1 — SEOS Earth Resources Applications (Listed in Order of Priority)

Application	Related Applications
1. Detecting and monitoring of water-suspended solid pollutants	Water
2. Estuarine dynamics and pollution dispersal	Water
3. Monitoring extent, distribution, and change of snow cover	Miscellaneous
4. Monitoring volcanic regions	Geology
5. Detecting and monitoring development and movement of colored water masses (plankton)	Water
6. Detecting and monitoring fish location and movement	Water
7. Ocean dynamics	Water
8. Detection and assessment of disease and insect damage to forest species	Vegetation
9. Forest inventory and valuation of multiple-use management	Vegetation
10. Evaluation of range forage resources and grazing pressure assessment	Vegetation
11. Management of irrigation	Vegetation
12. Detecting and monitoring oil pollution	Water
13. Diurnal and seasonal variation for lithologic survey	Geology
14. Monitoring and analysis of lake dynamics	Water
15. Wildfire monitoring	Miscellaneous
16. Flood prediction, survey, and damage assessment	Vegetation
17. Monitoring water erosion and deposition	Vegetation
18. Diurnal and seasonal variations for thematic mapping	Geology
19. Monitoring and prevention of aeolian soil erosion	Vegetation
20. Detection and assessment of disease and insect damage to cultivated crops	Vegetation

Table 2.1-2 — Spectral Band Requirements for Earth Resources

Spectral Band, Micrometers	Application																			
	1	2	3	4	5	6	7	8	9	10	11	12	13	14	15	16	17	18	19	20
E1 0.42 – 0.46		√				√							***	√			√	**		
E3 0.47 – 0.52	*	*		**		*	*					√	**	√			√	**		
E4 0.53 – 0.57	√	√				√	√	***	*		***	√	*	√	*	√	*	*		**
E5 0.56 – 0.60	√	√		*	*	*	√					√	√	*				√		
E6 0.60 – 0.65	√	√			√	√	√						√	√				√		
E7 0.65 – 0.69	√	√		√	√	√	√	√	√	√		√	*	√	*	√	*	√	*	√
E8 0.70 – 0.73	√	*	√		√	*	√				√		**	*				**		
E9 0.78 – 0.82								*	*	√			**		*			√	*	√
E11 0.89 – 0.95													√			√	*	√		
E13 2.05 – 2.35			*				*	**	**	*	*		√			√	√	√	***	*
E16 10.3 – 11.3		√	**	√		√	√				**	*	√	√	√	**	**	√	***	**
E17 11.3 – 12.0		√	**	√		√	√				**	*	√	√	√	**	**	√	***	**
E18 12.0 – 12.9		√	**	√		√	√				**	*	√	√	√	**	**	√	***	**

Legend: √ = required
* = second priority
** = third priority
*** = fourth priority

TABLE 2.1-3

Short List of SEOS Applications

Severe thunderstorms, hail, tornadoes
Hurricanes
Flash floods
Frost hazards
Clear air turbulence
Snow pack, spring floods
Sandstorms
Rainfall detection
Atmospheric resources management
Fog prediction
Terminal forecasting
Atmospheric waste disposal and reclamation
Snow, sleet, rain delineation
Lake and sea breezes

TABLE 2.1-4

Key Meteorological Parameters in Order of Importance

1. Boundary layer motion field
2. Vertical stability
3. Temperature lapse rate and surface temperature
4. Regions of strong convective activity
5. Middle and upper troposphere motion
6. Pressure field in boundary layer
7. Moisture field
8. Convergence and divergence
9. Wind shear, jet stream

Fig. 2.2-1 Conceptual Design Trades

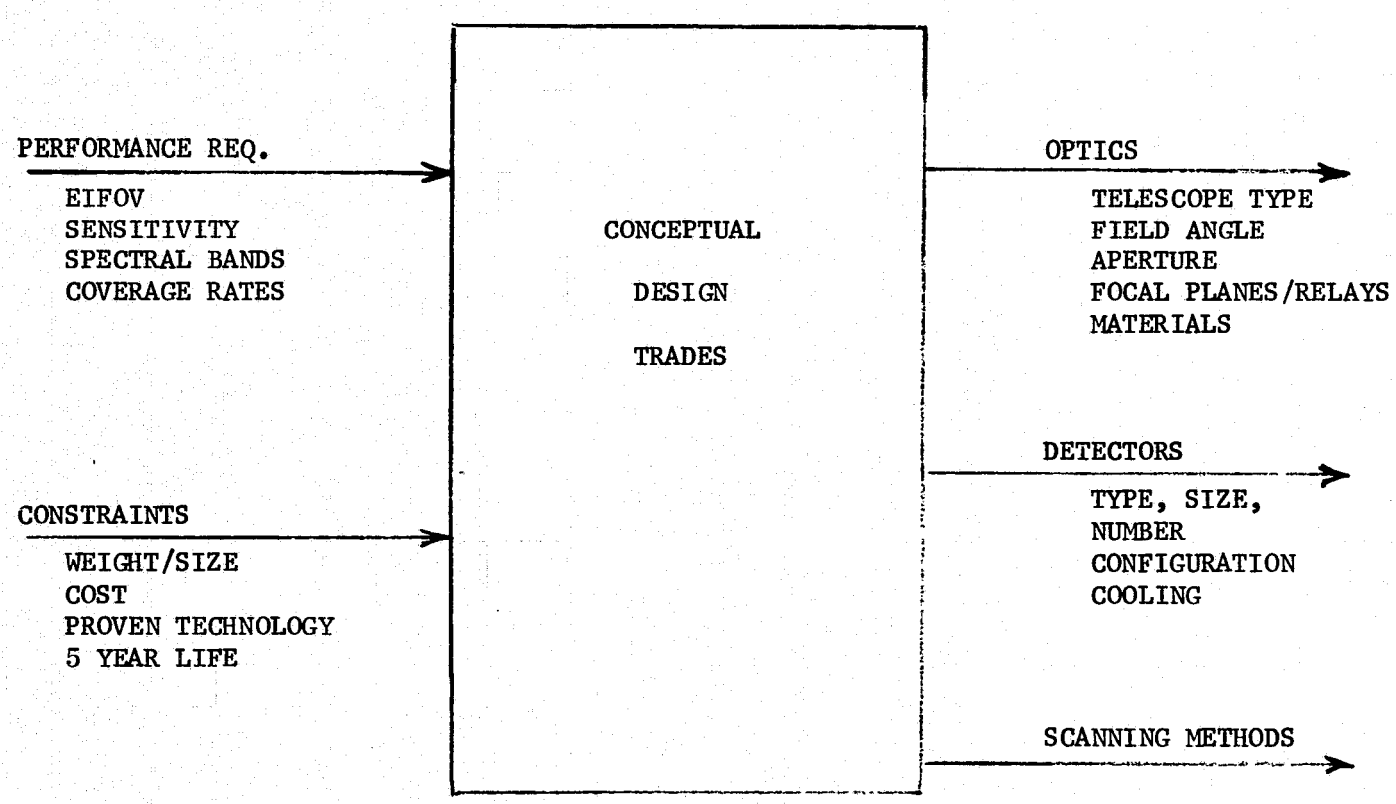

2.2.1 Optics

Selection of an optical system for LEST is not treated as an isolated design choice, but must be an output of a larger consideration of target coverage rate, system complexity, scanning techniques, and numbers of detectors. After considerable thought about the problem, it became apparent that swath width or optical field of view was a useful basis upon which to compare systems. Table 2.2-1 compares, in a qualitative way, some of the attributes of narrow and wide field systems.

The wide field system offers the advantages of lower scan rates and better sensitivity (through the use of more detectors). However, optical complexity, overall length, and weight override these advantages. In Phase I, we compared systems with fields of view of 0.6°, 1.6°, and 4.7°. The 0.6° field requirement was achievable with a two-mirror Cassegrain telescope which is compact and safely within the weight budget. In order to obtain a 1.6 degree field, a three mirror Schmidt Cassegrain design would be required. This configuration would only marginally be within the weight budget even resorting to an expensive and risky beryllium structure. The 4.7 degree reflective Schmidt design was clearly beyond the weight budget, and in addition, had very severe light baffling problems.

The 1.4 meter aperture selected in Phase I is taken as the largest diameter possible within the weight budget. The performance requirement dictating large aperture diameter is spatial resolution in the IR bands. Table 2.2-2 shows how EIFOV due to optics alone, and telescope weight, vary with aperture diameter. This data is for performance at 12 micron wavelength for a system with thirty percent obscuration and perfect optical wavefront.

Selection of relative aperture, or f/number, for each spectral band was made based on parametric performance analysis. For each application and band, optimum (or minimum feasible) detector size, f/number, and integration time were found, consistent with the required EIFOV, radiometric sensitivity and coverage rate. The recommended design, which incorporates focal planes of f/5, f/2, and f/1.3, represents a best compromise toward meeting the entire applications/spectral band matrix. In Section 5 of this report, the performance prediction for each application is tabulated.

2.2.2 Scanning

Areas of interest for viewing from SEOS range from as small as 50 x 50 km to as large as the entire continental USA and its coastal waters. Specific coverage rates are given in the specifications, Appendices A and B. One of the important tradeoffs and conceptual design decisions was selection of a method of scanning. In the planned geostationary orbit, there is nominally no relative translation of the spacecraft with respect to the earth. Therefore, in order to cover an area, controlled pointing of the field-of-view is necessary. There are two fundamental classes of scanning and many implementations of each.

Focal plane scanning is sometimes used in systems with a wide field of view. By use of an electromechanical drive, mirrors or corner cube prisms are rotated in image space to cycle portions of the field to a group of detectors having a field of view less than the optical field of view. Small target areas could be covered with just this one scanning action. However, larger areas would require a second scanning action such that the scanned swath would cover new territory on each cycle. Focal plane scanners tend to be quite bulky and are located in

TABLE 2.2-1

Comparison of Wide and Narrow Field Systems

	Narrow Field	Wide Field	Remarks
Scan Rate to Cover an Area	Higher	Lower	Full Field of Detectors assumed
Number of Detectors	Lower	Higher	Full Field of Detectors assumed
Length of Telescope	Shorter	Longer	
Weight	Lower	Higher	
Scanning Possibilities	Object Space	Object Space Image Space	Full Field of Detectors Reduced Complement of Detectors
Good Optical Resolution Over Field	Routine	Difficult	
Radiometric Sensitivity	See Remarks	See Remarks	Related to number of detectors - which can be higher with wide field.

TABLE 2.2-2

Optics Limited EIFOV, Weight vs. Aperture Diameter

D, meters	E_0 at Nadir, meters	E_0 at 40° N, meters	Telescope* Weight kilograms
1.2	610	920	1,270
1.4	520	790	1,440**
1.6	450	680	1,660

* Cassegrain design.

**Maximum Allowable Weight based on 44% of Titan III geostationary capability.

an area that is already crowded with relay optics, detector arrays and filter changers. Therefore, the second scanning action would most likely be accomplished in object space.

Object space scanning is performed by controlling the line of sight of the telescope. This may be accomplished by means of a rotating or oscillating mirror in front of the telescope or by attitude control of the entire spacecraft. When the field of view of the detector array is smaller than the area to be covered, a series of object space scans would be required. This would be done with a two-axis, gimballed mirror, two-axis spacecraft attitude control, or combinations of spacecraft attitude control and mirror scan. Also, as mentioned above, combinations of image plane and object space scanning are possible.

Object space scanning by means of spacecraft attitude control was selected in our Phase I work as best for the SEOS/LEST mission. Linear detector arrays would sweep the area in pushbroom fashion and coverage of large areas would be accomplished in a series of E-W and W-E scans. Some of the principal considerations leading to this selection are:

- Focal plane scanning is more adaptable to wide field angle optical systems, and it was established that weight, size, and cost of detectors favored a narrow field (0.6°).
- Focal plane scanning would have added an electromechanical device to the system with adverse reliability implications.
- Object space scanning mirrors add weight, and usually result in optical performance degradation. Electromechanical scanners would bring up reliability questions.
- Use of spacecraft attitude control system for scanning adds little or no complexity. These systems are necessary for target selection in any event, and must be precise in order to avoid drift of the line of sight. Torques required for scan reversals and swath indexing were found to be reasonable.

2.2.3 Detectors

Preliminary selection of sizes and number of detectors was made in Phase I as part of the parametric performance analysis. For some spectral bands detector size is the predominant resolution determining factor. For these bands, the smallest detector size available near term (15 μm for Silicon, 30 μm for IR detectors) was specified. For two bands, larger detectors are indicated as compatible with required EIFOV and sensitivity requirements.

Visible band detectors will be silicon devices with suitable filters for limiting the spectral band. Because of the large number of detectors required, only self-sequencing devices such as CCD's and silicon arrays can be considered for these bands.

Two of the near IR bands are in the range suitable for PbS operating at room temperature. The third NIR band (M5, 3.5-4.1 microns) is best provided with cooled InSb detectors. (Note: Phase II developments indicate that locating the detector array for M5 at the f/1.3 focal plane offers design advantages.)

For the three thermal IR arrays, HgCdTe is the logical choice for detector material. Continued advances in the field of applying charge coupling technology

to HgCdTe arrays is essential for a practical multi-element system. The HgCdTe arrays would be cooled to 110°K by a passive radiative device.

2.3 LEST PERFORMANCE SPECIFICATIONS

Performance specifications for the Large Earth Survey Telescope for SEOS are reproduced in appendices of this report. Three different mission levels have been defined for SEOS and these are reflected in the three sets of LEST performance specifications.

The LEST for the Full-up mission SEOS is the ultimate operational system which shall perform as defined in its specification, Appendix A.

The LEST for the Strip-down mission SEOS is a possible first mission system. It would include the same choices of spectral bands and would have the same aperture and optical field. It would perform to the same resolution and sensitivity specifications as the Full-up system but its area coverage rate would be decreased. This relaxation of requirements would make possible some cost saving measures such as reduced detector fields and data rates. The strip-down system should answer all feasibility questions about the full-up system, and therefore should differ only in areas that would be capable of growth to become a full-up system with no redesign.

The minimum system is one that would meet the performance requirements of the strip-down configuration, but would not be capable of growth to full-up.

The specifications are preliminary. It will be noted that many areas are still TBD (to-be-determined). As the design progresses into later phases and interfaces are established, the TBD areas will be resolved.

2.3.1 Preliminary Performance Specification, LEST for Full-up Mission SEOS

See Appendix A.

2.3.2 Preliminary Performance Specification, LEST for Strip-down Mission SEOS

See Appendix B.

2.3.3 Preliminary Performance Specification for LEST for Minimum Mission SEOS

Same as for Strip-down mission LEST, except that both the swath and the optical field is 125 km minimum at nadir (ref. Para. 3.2.1.3 of the specification).

3. FULL-UP LEST CONCEPTUAL DESIGN

In this section we describe the conceptual LEST design for the Full-up SEOS mission. Most of what is presented here is also applicable to the strip-down and minimum designs. An overview of the LEST design and overall error budgets are given in Section 3.1. Sections 3.2 through 3.8 present tradeoffs and design concepts for the major subsystems.

The ways in which LESTS for the reduced missions differ from the Full-up are discussed in Section 4.0.

3.1 LEST SYSTEM

3.1.1 System Description

Figures 3.1-1 and 3.1-2 show an inboard profile of LEST in the SEOS spacecraft and a conceptual LEST relay/focal area. These figures give an overview of the principal features of the LEST preliminary design. A discussion of the individual subsystems including tradeoffs in the design selection is presented starting in Section 3.2. A listing of key features of the design is given in Table 3.1-1.

The Cassegrain optical system appears in a structural form which is almost symmetrical fore and aft with respect to the primary mirror. The secondary mirror is positioned forward of the primary on a graphite epoxy support truss which attaches to the primary mirror support structure. Similarly, the relay/focal plane structure attached at the primary support structure extends aft to position the tertiary mirror, field division assembly and IR relay lenses. The thermal IR focal plane is located near the spacecraft structure for convenient attachment to the radiative cooler. On the pitch axis of the spacecraft, the cooler will be either north or south facing, as selected by a twice a year spacecraft maneuver. The telescope optical/focal plane assembly mounts to the spacecraft outer structure at three mounting fixtures at the primary support structure. The fixtures allow for radial growth of the outer structure without transmitting strains into the optical system.

A combination of passive and active means is employed for maintaining optimum telescope focus and alignment. The mirrors are to be made of ultra low expansion (ULE) material in an egg crate construction. The secondary mirror support truss and relay/focal plane structure are graphite epoxy for strength, light weight, and low thermal expansion. The spacecraft structure and multilayer insulation on the inner surface of the structure passively

damp the thermal excursions of the telescope structure. Active heating holds the primary and secondary mirrors at a 30°C operating temperature. Optical alignment sensors and a focus sensor are included in the conceptual design to detect performance loss due to thermal/structural effects. Signals from these sensors would be used to command actuators on the secondary mirror mount to adjust for performance improvement. Developmental work on sensors and actuators of this type has been accomplished at Itek.

The principal optical components of the telescope and relay system can be seen in Figure 3.1-2. The field division assembly shown just aft of the primary support structure directs images to paths for the three primary focal planes and has provisions for directing portions of the field to the IR sounder and to the frame camera. Spectral filters, their changer mechanisms, and a capping shutter are also located at the field division assembly. The elements of the f/2 and f/1.3 relay lenses are shown packaged in tubular lens cells directed radially toward the passive cooler. The tertiary mirror which is part of the relay system to the f/5 focal plane is supported at the aft end of the graphite epoxy structure in a location that is thermally more benign than that of the secondary mirror.

The celestial sensor assemblies and inertial reference unit are mounted at the primary support structure to minimize boresight errors between the optical axis and the attitude control.

The spacecraft structure surrounding the telescope assembly functions as a thermal and illumination shield, carries telescope launch loads to the booster interface, and is the mounting base for electronics assemblies, attitude control components, solar paddles, and other SEOS instruments.

3.1.2 System Wavefront Error Budget

Throughout this report we will be analyzing optical performance, or image quality, in terms of wavefront error, WFE. This applies to optical design, fabrication and assembly errors, thermal misalignments of optical components and subassemblies, and structural deformations (including vibration, gravity release, and long term creep). In this section we will generate a wavefront error budget, and estimate the probable system WFE at each spectral band.

Because WFE is expressed in waves, it is necessary to correct each item for wavelength. In the case of the telescope design, for instance, the full-field performance was found to be .053λ rms at 0.7 μm; it would therefore be .106λ rms at 0.35 μm and .026λ rms at 1.4 μm. Similar scaling is done for the manufacturing and dynamic entries to the budget.

The numerical entries in Fig. 3.1-3 are taken from a recent analysis of a similar optical system. In some cases, such as the gravity release, we have had to rely on an educated guess, while in others, such as vibration, we have the benefit of computer modeling and hardware experience. The telescope and f/5 relays, being all reflective, are scaled with wavelength for all bands; the numerical entries are referred to the standard test wavelength of 0.63 μm. The refractive relays, however, must be scaled individually. The f/2 and f/1.3 relays can tolerate relatively large manufacturing and dynamic errors because the wavelengths are long. However, these relays are

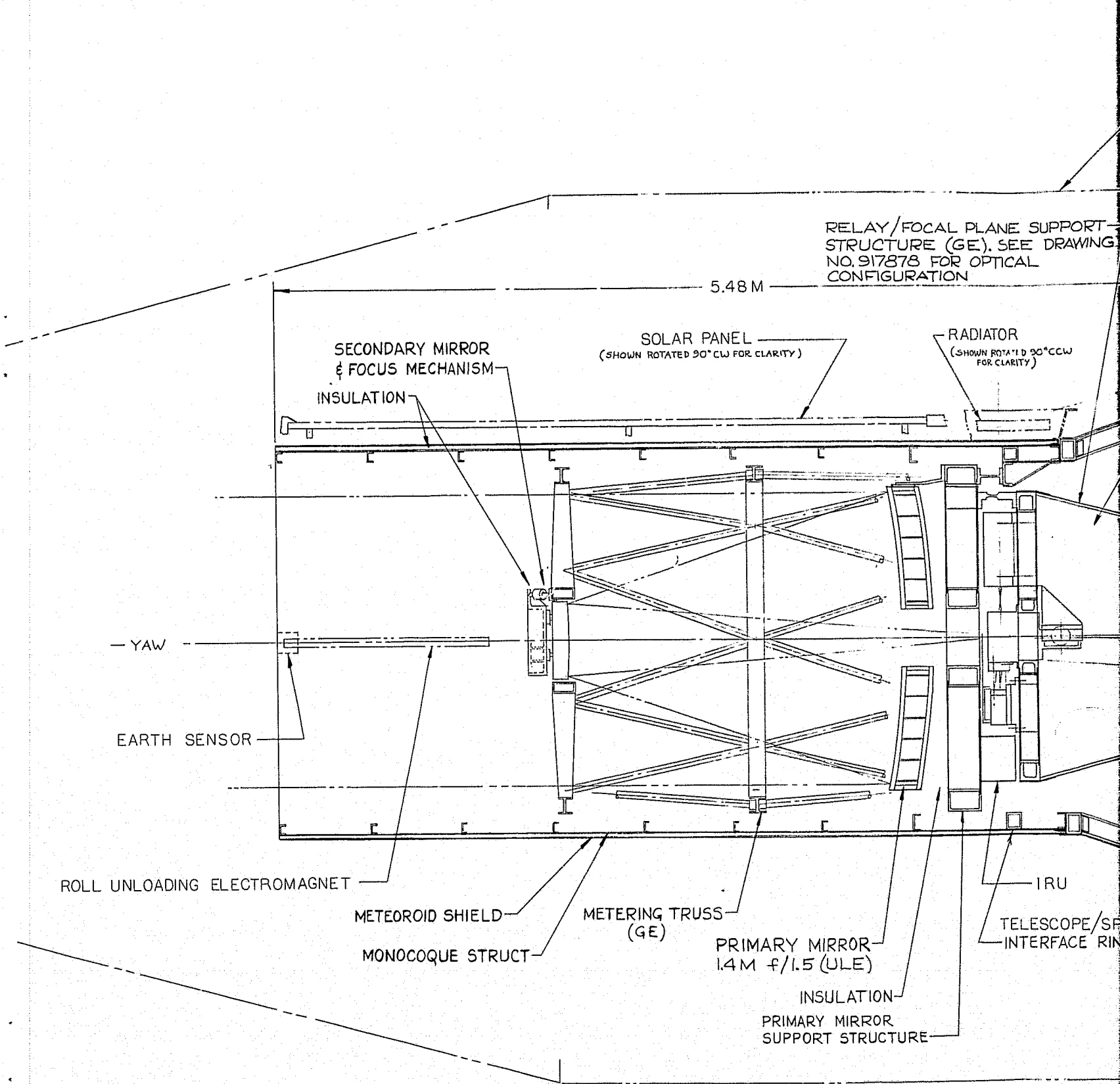

Fig. 3.1-1 — SEOS/LEST in
Cassegrain

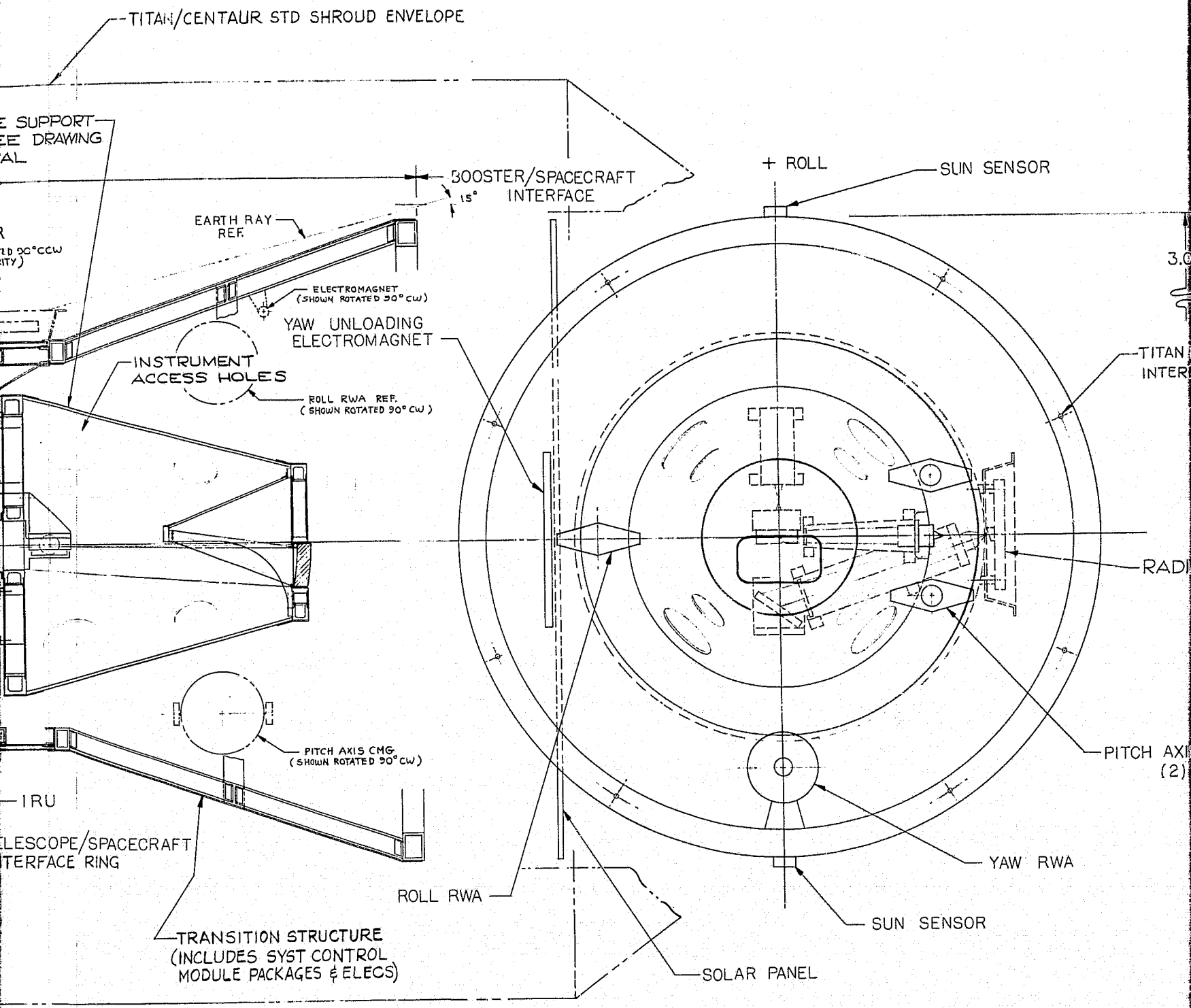

OS/LEST inboard profile, 1.4-meter, 6-degree field corrected

FOLDOUT FRAME 2

D SHROUD ENVELOPE

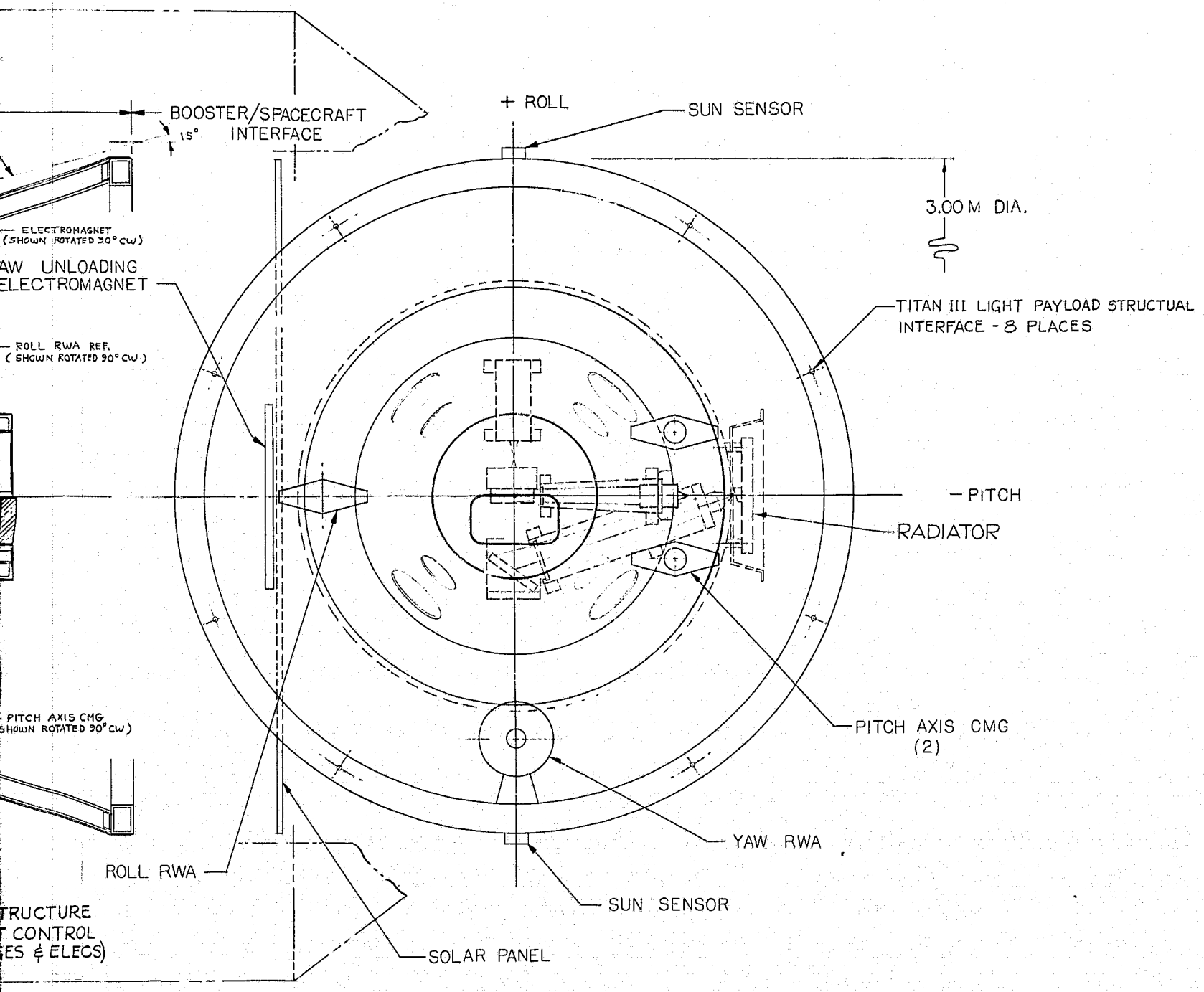

er, 6-degree field corrected

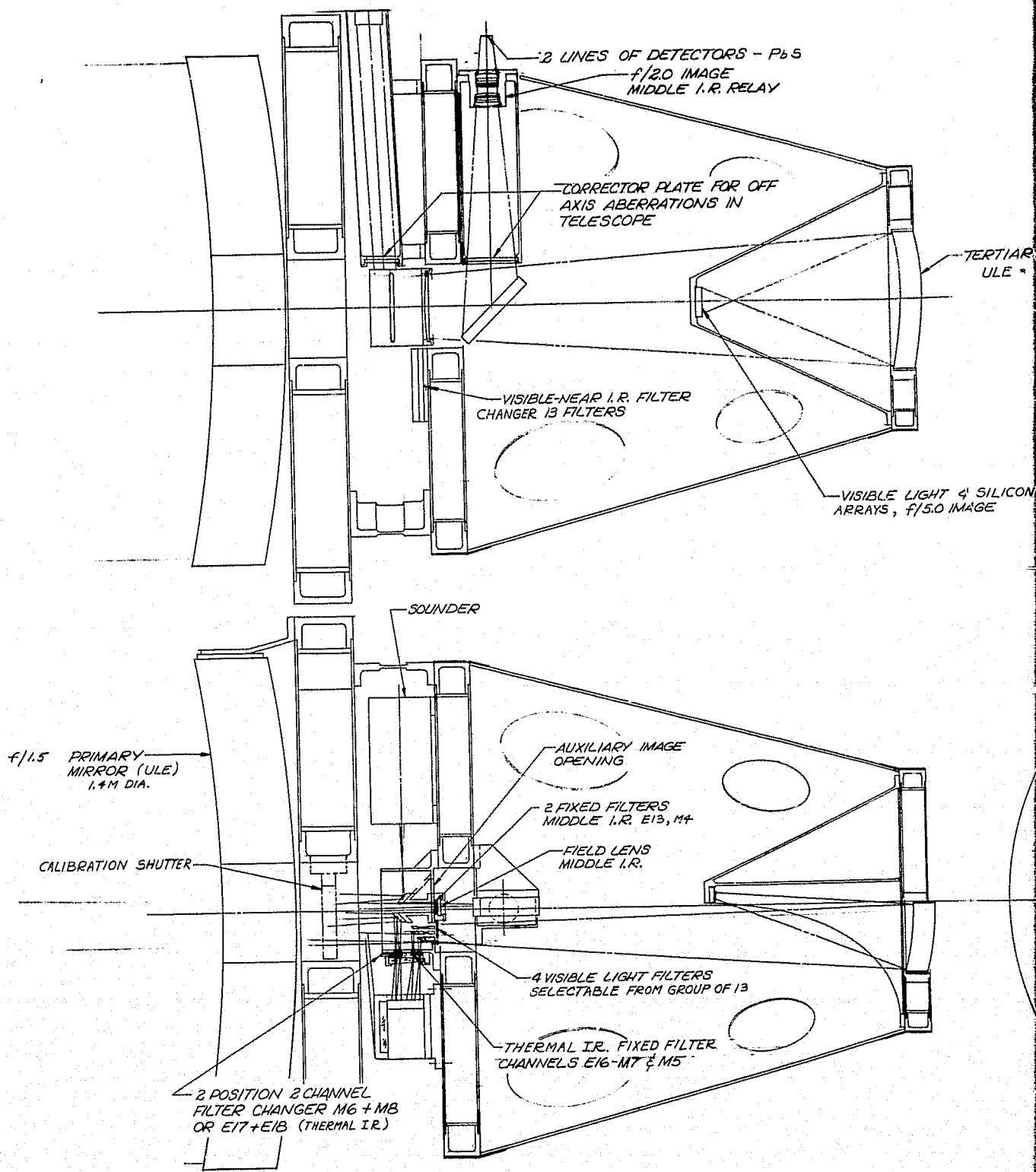

Fig. 3.1-2 — Relay/focal plane area

PRECEDING PAGE BLANK NOT FILMED

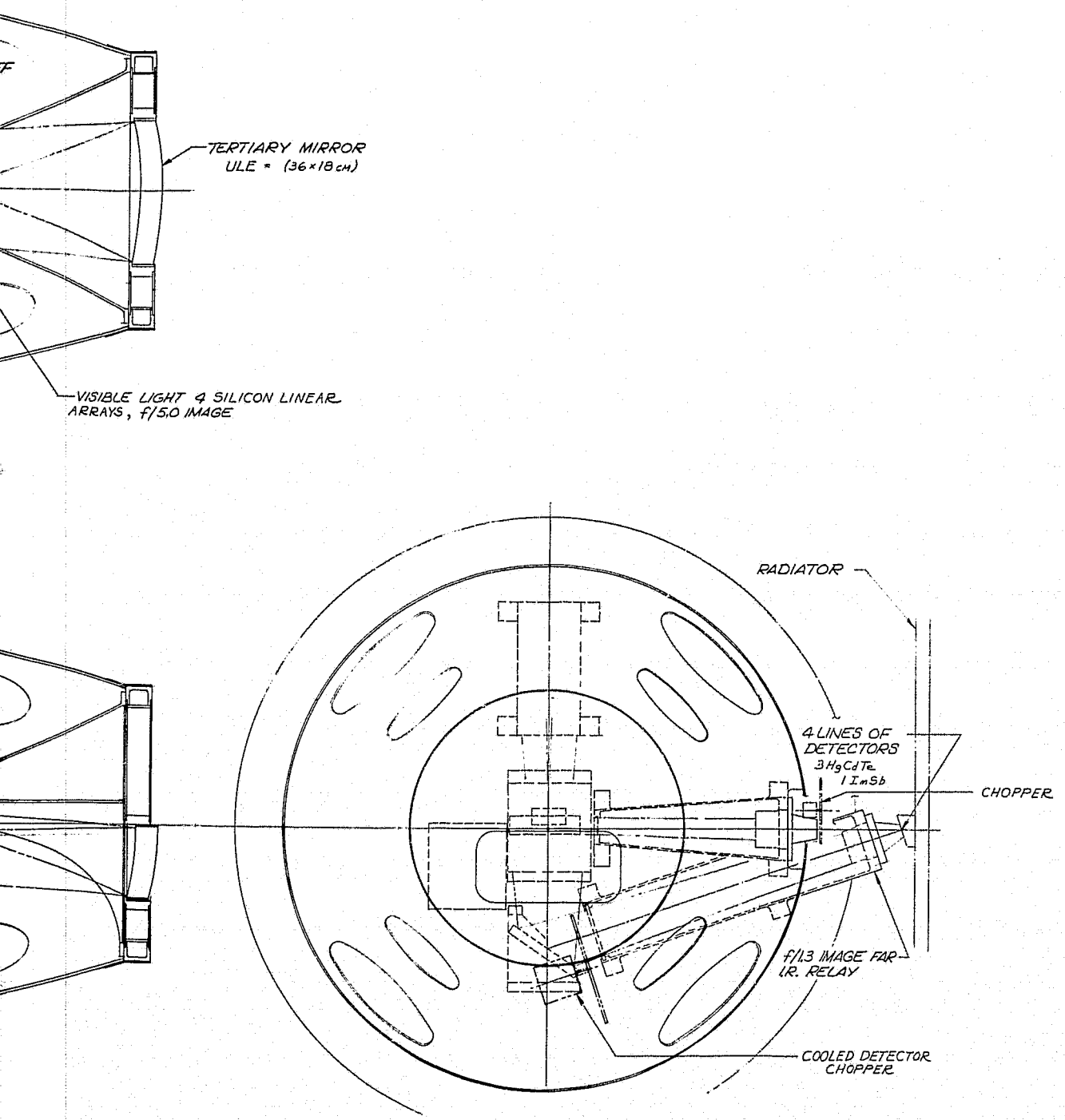

Relay/focal plane area of LEST

FOLDOUT FRAME 17

Table 3.1-1

Design Features Full-up LEST

Telescope	
Optical configuration	Cassegrain
Aperture diameter	1.4 meters
Obscuration (fully baffled)	30%
Wavefront Error* (operational)	0.1λ rms at 0.63 μm
Field of view	0.6°
Speed of Primary Mirror	f/1.5
Telescope f/number	f/12
Mirror Material	ULE
Optical Relays	
Visible bands	f/5
Type	Reflective*
Near IR Bands	f/2
Type	Refractive
Thermal IR Bands	f/1.3
Type	Refractive
Thermal Optical Control	
Low expansion materials	
ULE Mirrors	
Graphite epoxy metering structures	
Insulation	
Superinsulation employed around metering structure	
Active temperature control	
Primary and secondary mirrors actively controlled to 30°C	
Focus and alignment sensors	
Peak performance can be re-established	
Detectors Arrays	
Visible bands	
Type and location	Silicon, linear CCD, f/5 image
Detector size, spacing, number	4 arrays, 4900 element/array, 15x15 μm element size

Table 3.1-1, Design Features Full-up LEST Cont'd

Detectors Arrays Cont'd

Near IR Bands	
Spectral band	E13 (2.05-2.35 μm)
Type and location	PbS, F/2 image
Detector size & spacing, number	1960 elements, 15 μm size
Spectral band	M4 (1.58-1.68 μm)
Type and location	PbS, f/2 image
Detector size & spacing number	104 elements, 280 μm size
Spectral band	M5 (3.5-4.1 μm)
Type and location	InSb cooled to 110°K, f/1.3 image
Detector size & spacing, number	191 element, 100 μm size
Thermal IR Bands	
Type and location	Hybrid HgCdTe/Silicon CCD linear array cooled to 110°K, f/1.3 image
Detector size, spacing, number	3 arrays, 633 element/array, 30 μm size

Filters/Filter Changers

	Bands
f/5 Focal Plane	
3-position	E1, E5, M1
4-position	E3, E6, E9, M2
4-position	E4, E8, E11, M3
2-position	E7, M9,
f/2 Focal Plane	
Fixed filter	E13
Fixed filter	M4
f/1.3 Focal Plane	
Fixed filter	E16/M7
2-position	E17, M6
2-position	E18, M8
Fixed filter	M5

Detector Cooling

Passive conical radiator with detector mounted directly on cold plate.

Altitude Control and Scanning

Pushbroom scanning (east-west) utilizing spacecraft slew.

Attitude control system

Sensors: Celestial sensor assemblies, sun sensors

Control: Pitch - (2) CMG's

Roll, yaw-reaction wheels

Table 3.1-1, Design Features Full-up LEST Cont'd

Telescope Structure

Graphite-epoxy optical structure
Monocoque aluminum outer structure

Physical Dimensions, Weight

LEST: 1,400 Kilograms
Total Spacecraft: 2,375 Kilograms

Power

Solar arrays sized for 1 kw.

*Telescope and f/5 relay operate as 3-mirror system for best image for visible bands

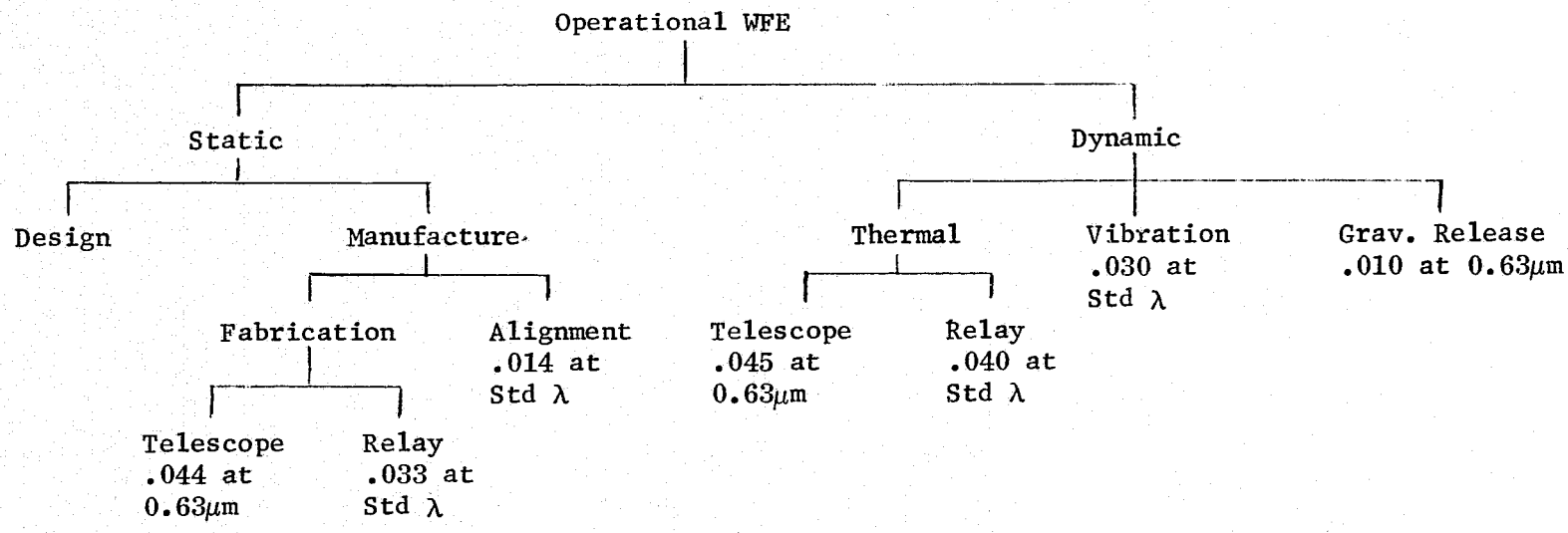

$$(\text{Operational WFE})^2 = (\text{Design WFE})^2 + (.064\,\frac{.63}{\lambda})^2 + (.062\,\frac{\text{Std }\lambda}{\lambda})^2 \qquad F = \begin{cases} f/5 \\ f/2 \\ f/1.3 \end{cases} \qquad \text{Std } \lambda = \begin{cases} 0.63 \\ 1.63\mu m \\ 6.8 \end{cases}$$

Fig. 3.1-3 Wavefront Error Budget

WFE expressed as λ rms at specified wavelength

also more complex, very fast, and are harder to test, so the wavelength advantage is lost. Until the three relays have been toleranced we must be arbitrary in adopting WFE contributions. For convenience we have assumed that each relay is equally sensitive at its standard wavelength to errors of fabrication, thermal misalignment and vibrational displacement.

The operational wavefront error is derived from all the entries in Fig. 3.1-3. The results are given for four field heights (h = 1 at 0°.3 half-field angle) in Table 3.1-2. We will use the h = 0.7 data for system performance calculations in Section 5.3.

It is important to note that in almost all cases the errors of manufacturing and the dynamic errors are significant contributors to the system error budget. As a result it would generally be inaccurate to use the computer-generated design MTF curves for EIFOV prediction. We have therefore used generalized MTF curves to relate the parameter a in Section 5.2 to the wavefront error.

Table 3.1-2 Summary of Wavefront Error Data

Band	λ	Design WFE h = 0	0.4	0.7	1.0	Manufacturing & Dynamic WFE	System WFE h = 0	0.4	0.7	1.0
E 1	.44μm	.056	.081	.084	.084	.127	.139	.151	.152	.152
3	.50	.049	.071	.074	.074	.111	.121	.132	.133	.133
4	.55	.045	.065	.067	.067	.101	.111	.120	.121	.121
5	.58	.042	.062	.064	.064	.096	.105	.114	.115	.115
6	.62	.040	.058	.060	.060	.090	.098	.107	.108	.108
7	.67	.037	.053	.055	.055	.083	.091	.099	.100	.100
8	.72	.034	.050	.052	.052	.077	.084	.092	.093	.093
9	.80	.031	.045	.046	.046	.070	.077	.083	.084	.084
11	.92	.027	.039	.040	.040	.061	.067	.072	.073	.073
13	2.2	.003	.030	.083	.200	.049	.049	.057	.096	.206
16	10.8	.012	.051	.076	.090	.039	.041	.064	.085	.098
17	11.6	.011	.047	.071	.084	.036	.038	.059	.080	.091
18	12.4	.010	.044	.066	.078	.034	.035	.056	.074	.085
M 1	.62	.040	.058	.060	.060	.090	.098	.107	.108	.108
2	.75	.033	.048	.049	.049	.074	.081	.088	.089	.089
3	.76	.032	.047	.049	.049	.073	.080	.087	.088	.088
4	1.63	.100	.130	.180	.380	.066	.120	.146	.192	.386
5	3.8	.193	.239	.314	.282	.110	.222	.263	.333	.303
6	6.8	.025	.081	.125	.132	.062	.067	.102	.140	.146
7	10.8	.012	.051	.076	.090	.039	.041	.064	.085	.098
8	12.3	.010	.044	.066	.078	.034	.035	.056	.074	.085
9	.88	.028	.041	.042	.042	.063	.069	.075	.076	.076

3.2 OPTICS

The LEST optics will consist of the main lightcollecting telescope, plus the relay lenses, mirrors, filters and beamsplitters required to form a series of line images of specified wavelength and spectral bandpass for each linear detector array. In Phase I of this study program, the optical characteristics required for each of these images were defined, and a large number of possible optical systems for obtaining them were identified. In Phase II the number of candidate optical systems has been narrowed down to the one design approach we feel is most promising, and this approach has been examined in some depth, to establish its credibility.

Our goal in selecting a design approach was to simplify the optical system as much as possible, while meeting the performance requirements. The particular configuration shown here is based on a set of constraints and assumptions developed during the Phase I study, but it retains a degree of flexibility which allows adaptation to a wide range of changes in basic performance characteristics. We adhered to this particular set of constraints to narrow the range of topics for study so that we could concentrate on those most critical to establishing its feasibility. We do, in fact, recommend several future changes in these constraints, if detector technology and mission requirements permit.

Briefly, the recommended design approach consists of a Cassegrain telescope forming a relatively slow uncorrected intermediate image, followed by three relay systems forming corrected images on the sensors. All wavelength separation and bandpass filtration is done at the intermediate image, where the larger scale and focal ratio simplify mechanical and optical problems. Wavelength separation is done by dividing the field-of-view into a series of parallel line images, one for each detector array, and inserting a narrow bandpass filter in the relay optical path behind each intermediate line image.

In describing this design we will first discuss the performance characteristics as established in the Phase I study, and show how these led us to select this particular design approach. We will also briefly discuss one alternative configuration which has been suggested elsewhere, and show why we prefer the approach described above. We will then discuss the critical aspects of the selected configuration in detail. We will close with a discussion of recommended changes in the assumed design constraints, and the definition of areas requiring future study.

3.2.1 Optical System Requirements

Two types of observations are to be performed with the SEOS satellite: earth resources and meteorological. In the Phase I study, thirteen spectral bands were identified for earth resources observations, and nine more were identified for meteorological observations. For meteorological observations, all nine bands must be used simultaneously. For earth resources observations, all infrared bands must be used simultaneously, but only selected combinations of the visible light bands need be used for specific observations. Earth resources and meteorological observations will not be made simultaneously. The same detector arrays can be used for both types of observations, if appropriate filter changers are provided to change spectral channels.

Table 3.2-1 lists all 22 spectral bands. It also lists the focal ratio and detector size for each band required to meet performance goals, as

TABLE 3.2-1

Spectral Bandpass, Focal Ratio and Detector Size for each Spectral Band

BAND	BANDPASS	F/NUMBER	DETECTOR SIZE	2.44λ F
E1	0.42-0.46 μm	5	15 μm	5.37 μm
E3	0.47-0.52 μm	5	15 μm	5.98 μm
E4	0.53-0.57 μm	5	15 μm	6.71 μm
E5	0.56-0.60 μm	5	15 μm	7.08 μm
E6	0.60-0.65 μm	5	15 μm	7.63 μm
E7	0.65-0.69 μm	5	15 μm	8.17 μm
E8	0.70-0.73 μm	5	15 μm	8.72 μm
E9	0.78-0.82 μm	5	15 μm	9.76 μm
E11	0.89-0.95 μm	5	15 μm	11.22 μm
E13	2.05-2.35 μm	2	15 μm	10.74 μm
E16	10.3-11.3 μm	1.3	30 μm	36.95 μm
E17	11.3-12.0 μm	1.3	30 μm	36.95 μm
E18	12.0-12.9 μm	1.3	30 μm	39.49 μm
M1	0.55-0.70 μm	5	15 μm	7.63 μm
M2	0.744-0.759 μm	5	15 μm	9.17 μm
M3	0.7617-0.7663 μm	5	15 μm	9.32 μm
M9	0.75-1.00 μm	5	15 μm	10.68 μm
M4	1.58-1.68 μm	2	280 μm	7.95 μm
M5	3.5-4.1 μm	1.3	100 μm	12.05 μm
M6	6.5-7.0 μm	1.3	30 μm	21.41 μm
M7	10.3-11.3 μm	1.3	30 μm	34.26 μm
M8	11.8-12.8 μm	1.3	30 μm	39.02 μm

determined in the Phase I study. The quantity $2.44\lambda F$ is the diameter of the first dark ring in the Airy pattern for a perfect, unobstructed lens, and is included as an indication of how near to diffraction limited the lens design must be.

An examination of the focal ratio (f/number) column indicates that the 22 bands can be divided into three categories by focal ratio, f/5, f/2 and f/1.3. These also represent division by wavelength region into visible and near infrared (f/5), middle infrared (f/2) and far infrared (f/1.3). Silicon detector arrays are used for all f/5 channels, and mercury-cadmium-telluride detector arrays for the far infrared. Bands E13 and M4 use lead sulfide detectors, and M5 uses indium antiomonide detectors.

The focal ratios and detector sizes were selected to optimize performance in the different spectral regions, while maintaining a common detector size and focal ratio over as broad a spectral region as possible. The same focal ratio could not be maintained at all wavelengths; 15 x 15 micrometers represents the minimum achievable detector size in the visible, and therefore a focal ratio less than f/5 will cost unacceptably in ground resolution. In the far infrared, noise associated with the size of the detector element requires that both f/number and detector size be minimized. Similar analysis leads to f/2 for the middle infrared. Thus an absolute minimum of three images of different focal ratio are needed to meet the original performance specifications, according to the analysis of the Phase I study.

Band M5 forms an important anomaly in this analysis. In this case, it was found that the original performance specs could not be met at either f/2 or f/1.3. In fact, a focal ratio of about f/0.5 is indicated, Since this is difficult* or impossible to achieve, it would appear that the performance goals for this band must be revised downward. If so, it might be included in either the f/2 or f/1.3 image. Alternatively, a fourth image of different focal ratio might be added.

The full-up design concept for SEOS developed in the Phase I study has been modified to require 10 instead of 12 detector arrays. The visible/near IR image will contain 4 arrays, plus a filter changer mechanism. The mid-IR f/2 image contains two detector arrays and the thermal IR f/1.3 image contains four detector arrays and filter changers. The telescope has an aperture diameter of 1.4 meters, and the length of the line image to be scanned is 0.6 degrees.

3.2.2 Wavelength Separation Techniques

The function of the SEOS satellite is to scan selected areas of the earth's surface to obtain simultaneous imagery at discrete wavelengths. In ground reconstruction, this imagery is to be recombined in exact registration, to allow spectral analysis of the light from each individual resolution element. It is desirable, ideally, to separate the image into individual resolution elements prior to dividing it spectrally, thus minimizing data reduction problems in ground reconstruction. In practice, this is difficult or impossible to do: SEOS has too many resolution elements and spectral bands for this to be accomplished easily.

---

*We have briefly considered an immersed detector array for M5, but it does not appear to offer a satisfactory solution.

There are two ways in which the image can be divided spectrally which might in principle fulfill this ideal: spectral dispersion with a grating or prism, and spectral division with dichroic beamsplitters. The former was rejected early in the Phase I study as being impractical due to the extremely wide spectral range and the high resolution imagery required. This technique has not been reconsidered. The limitations of spectral division using dichroic mirrors can best be understood by examining Fig. 3.2-1.

Fig. 3.2-1a shows the spectral bandpass regions in the visible and near infrared (all the f/5 images). Fig. 3.2-1b is a typical reflectivity curve for a visible light multilayer dielectric dichroic mirror. In both, the spectrum is plotted in wavenumbers (frequency) rather than wavelength, since the reflectivity curve for the multilayer mirror scales linearly with frequency. Thus the lower curve can be moved bodily left or right and still match the scale of the upper part of the figure.

The important point to note is that the transition region from 90 percent reflecting to 90 percent transmitting is roughly 1400 cm^{-1} wide. This is far too wide to divide the various bands, even if we ignore those that overlap, without substantial transmission losses. The same arguements apply to the far infrared bands, although dichroics designed for that wavelength region may have different characteristics. Therefore, even if dichroic mirrors are used to allow simultaneous viewing of the same resolution element in several different wavelengths, simultaneous viewing of adjacent spectral bands can be done only if separate resolution elements are used. Examination of Fig. 3.2-1 indicates that a minimum of three such geometrically separated images are required, i.g. three parallel line images normal to the direction of scan.

If it is necessary to divide the image geometrically to perform some of the wavelength separation, it makes sense to use the same technique for all of the wavelength separation. The more complex data reduction this entails must be used in part even with dichroic spectral splitting, and geometric splitting can lead to a simpler optical system. Some form of dichroic splitting could still be used to separate the different focal ratio images if desired, since they are for well separated spectral regions.

We will return to discussing wavelength division in describing our final design configuration.

3.2.3 Forming Three Images of Different Focal Ratio

In the LEST optical design, we are faced with two general problems: taking light collected through a common aperture and directing it to three separate optical subsystems, and designing the subsystems so that they will provide images of adequate resolution over the field-of-view and wavelength range required. The lens design problem is complicated by the fact that the first elements in the design are common to all three optical systems. Thus they can be used freely as design parameters in only one of the three optical subsystems. The extended spectral range involved for each focal ratio further complicates the design problem, if refracting elements are to be used.

The first problem, dividing the light between the three optical subsystems, can be approached in either of two ways. First, the main collecting telescope may be designed to provide an image at one of the three focal ratios, and light for the other two images may be split off with a beamsplitter somewhere ahead of the first image. Second, the main collecting telescope may form an

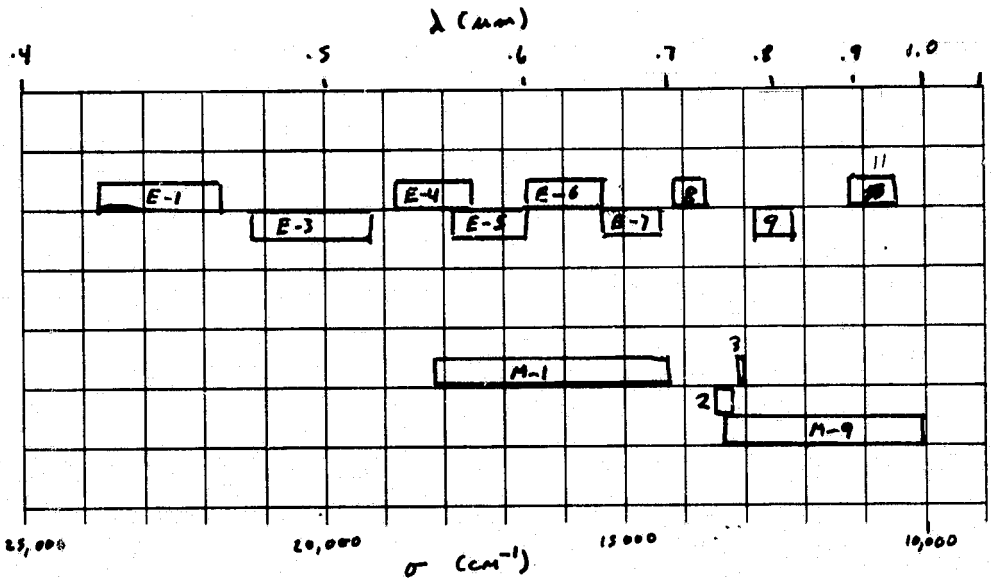

Figure 3.2-1a Division of Visible/Near Infrared Spectrum into E-series and M-series Bandpass Regions

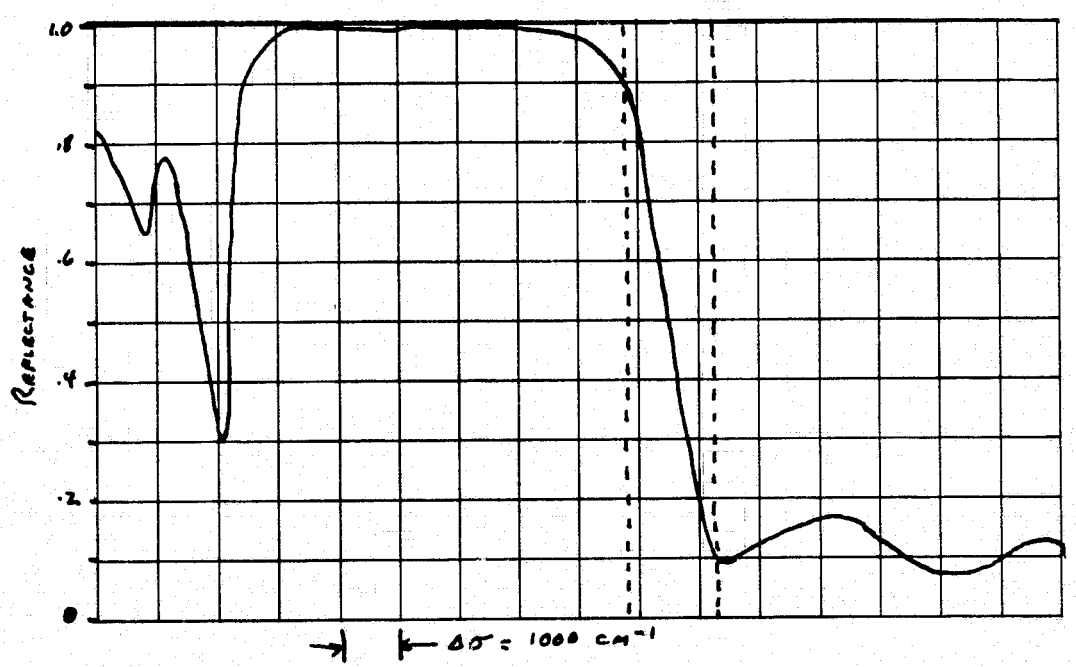

Figure 3.2-1b Typical Reflectivity Curve for Multi-Layer Dichroic Mirror

intermediate image, which is divided gemetrically, with light from each portion being directed to a separate relay lens. An example of the first approach is shown in Fig. 3.2-2, and was designed by Dr. B.J. Howell of NASA/GSFC.

The main optical system in Howell's design is a field-corrected Cassegrain. Four refracting elements have been added to the two mirrors, and provide reasonably good image quality over a field-of-view diameter of 1.2 degrees and a spectral range of 0.49 to 1.01 micrometers (Fig. 3.2-3). (The focal ratio and field-of-view are not those of the current design, but this is of little consequence to the present discussion.) There is evidence that off-axis image quality will deteriorate fairly rapidly at wavelengths less than 0.49 micrometers, but otherwise the image quality is quite good.

The Howell design requires that the infrared radiation be split off ahead of the corrector group, and this presents several problems. First, a multilayer dielectric dichroic mirror of the type indicated in Fig.3.2-1 must be designed to reflect in the shorter wavelength region and transmit longer wavelengths. This would require relocation of the corrector group to the side of the telescope. Further, the region of peak reflectivity is not broad enough to cover the entire f/5 spectral region. Close consideration of Fig. 3.2-1 indicates that three overlapping dichroics would be required to cover the full f/5 spectral region. These could be coated on a single surface, but it is questionable whether the resultant dichroic will transmit well in the infrared.

Another approach to designing the dichroic mirror is to use a thin gold mirror. This reflects well in the infrared and transmits in the visible, Fig. 3.2-4, and is thus compatible with the Howell design. Transmittance is not high over the entire visible and near infrared spectrum, however, and entails some losses for the shortest and longest wavelength f/5 channels, Fig. 3.2-5.

A more serious objection arises from characteristics of the beamsplitter substrate. Two choices are possible; a pellicle mirror and a thick glass plate. Both have deleterious effects on image quality, the former affecting the reflected image and the latter the transmitted image.

The major problem with pellicle mirrors of this size (approximately 30 x 45 cm) is that they are extremely sensitive to vibrations, and can oscillate like a drum head or loudspeaker cone. We have discussed this problem with Mr. Milton J. Schwartz of National Photocolor, one of the principal suppliers of pellicles in this country. While he could give no exact numbers, he stated that the deflection of the mirror surface would be measured in "hundreds of wavelengths", and the fundamental vibration frequency would be less than 30 cps. Even scaling the "Wavelengths" from mid-visible to 12 micrometers, the residual aberrations introduced would be intolerable.

A solid glass substrate also causes problems: inserting a tilted glass plate into a convergent beam of light introduces both monochromatic and chromatic aberrations, the principal one being astigmatism. Fig. 3.2-6 shows the effect of introducing a 1 centimeter thick beamsplitter tilted at 45 degrees into the Howell design, as indicated in Fig. 3.2-2. Fig. 3.2-6 indicates a blur circle diameter of about 200 microns for the 1 centimeter thick plate,

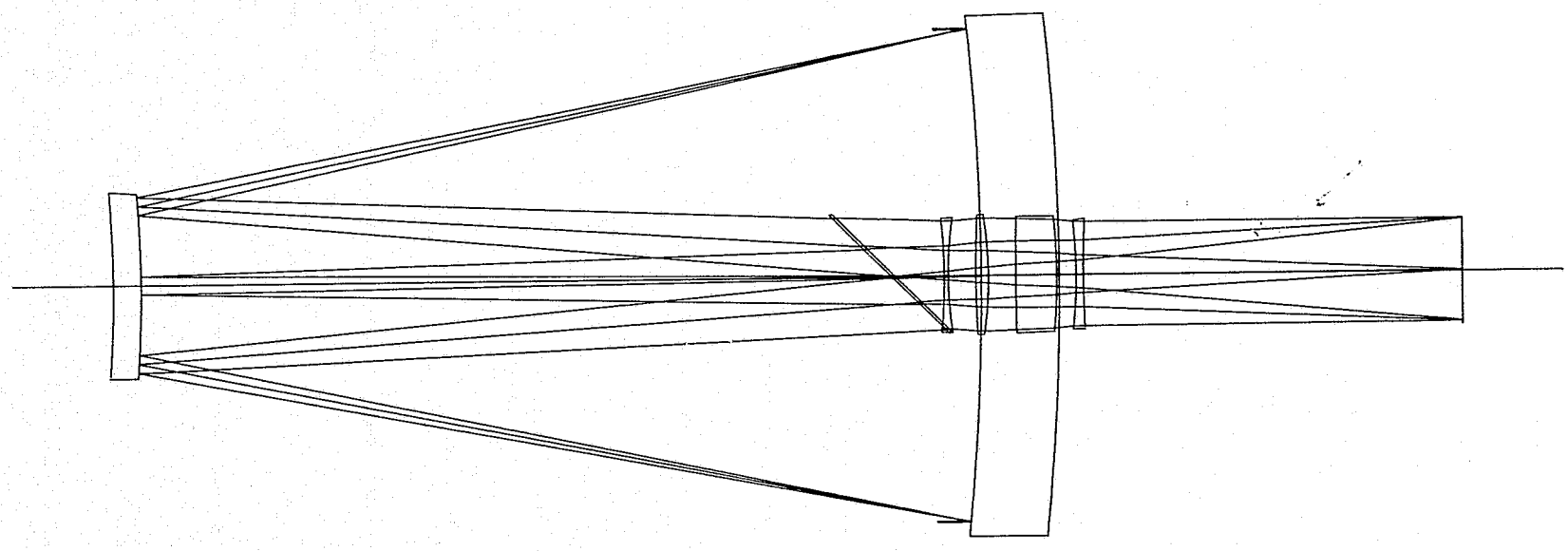

Figure 3.2-2 Howell's Corrected Cassegrain Design, Shown with 1 cm Thick Beamsplitter

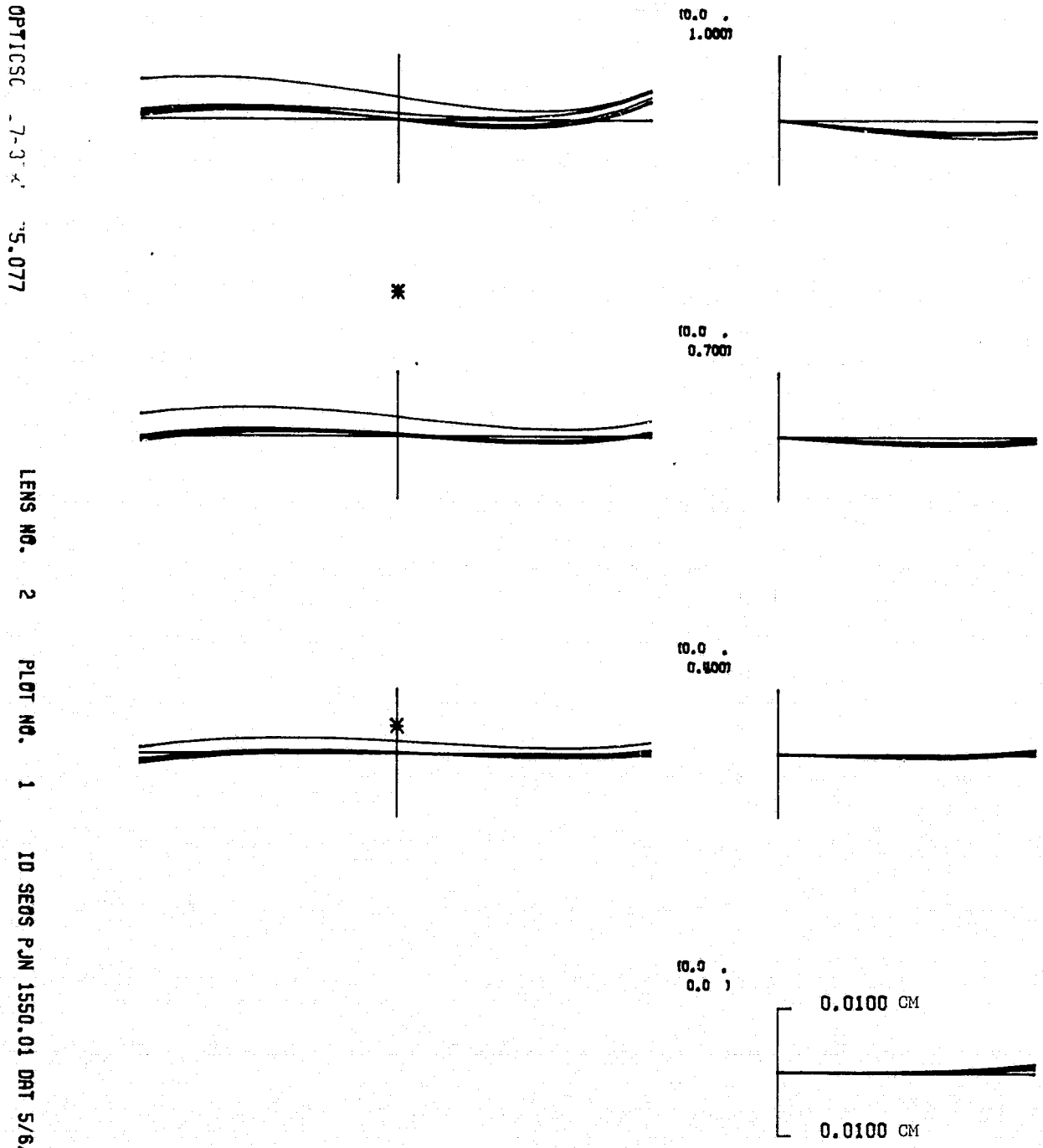

Figure 3.2-3 Ray Trace of Howell's Design Without Beamsplitter, 0.49-1.01μm, 0°6 Half Field

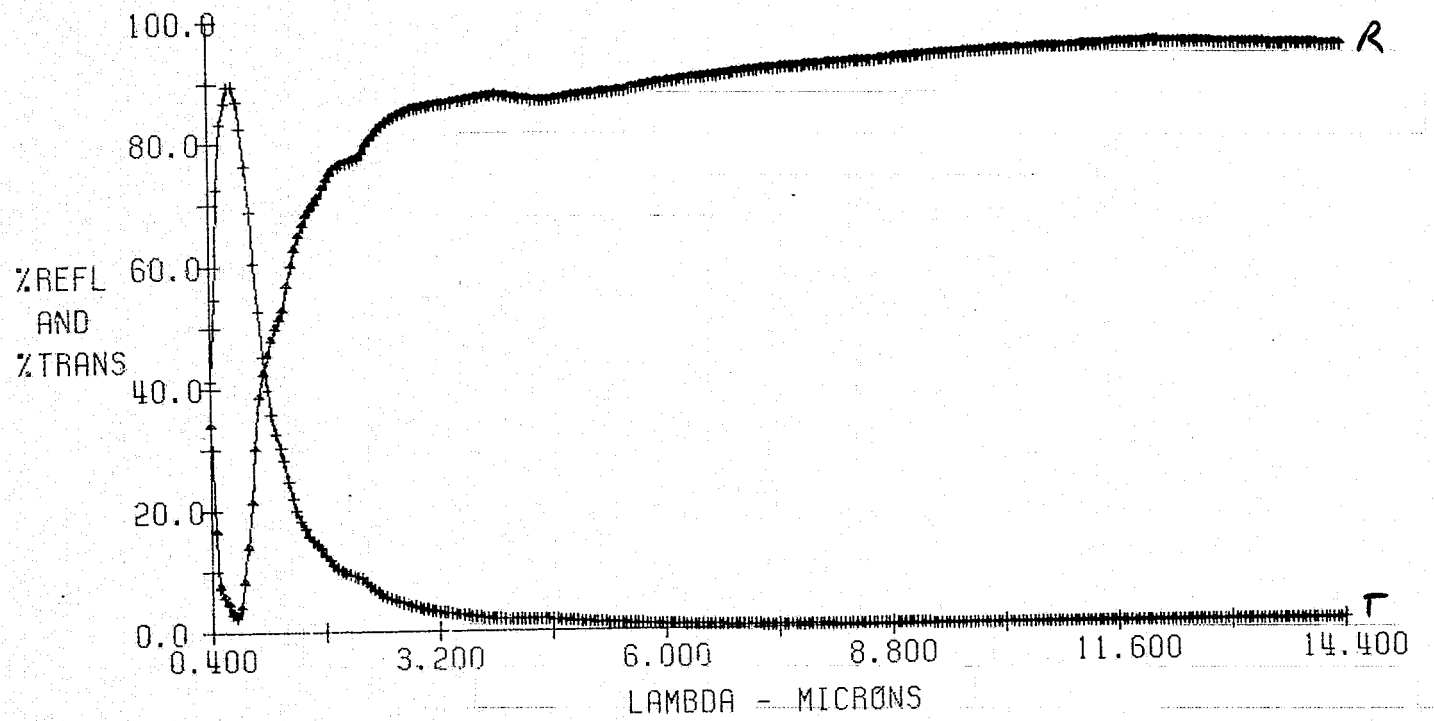

Figure 3.2-4 Reflectance and Transmittance of a Thin Gold Mirror

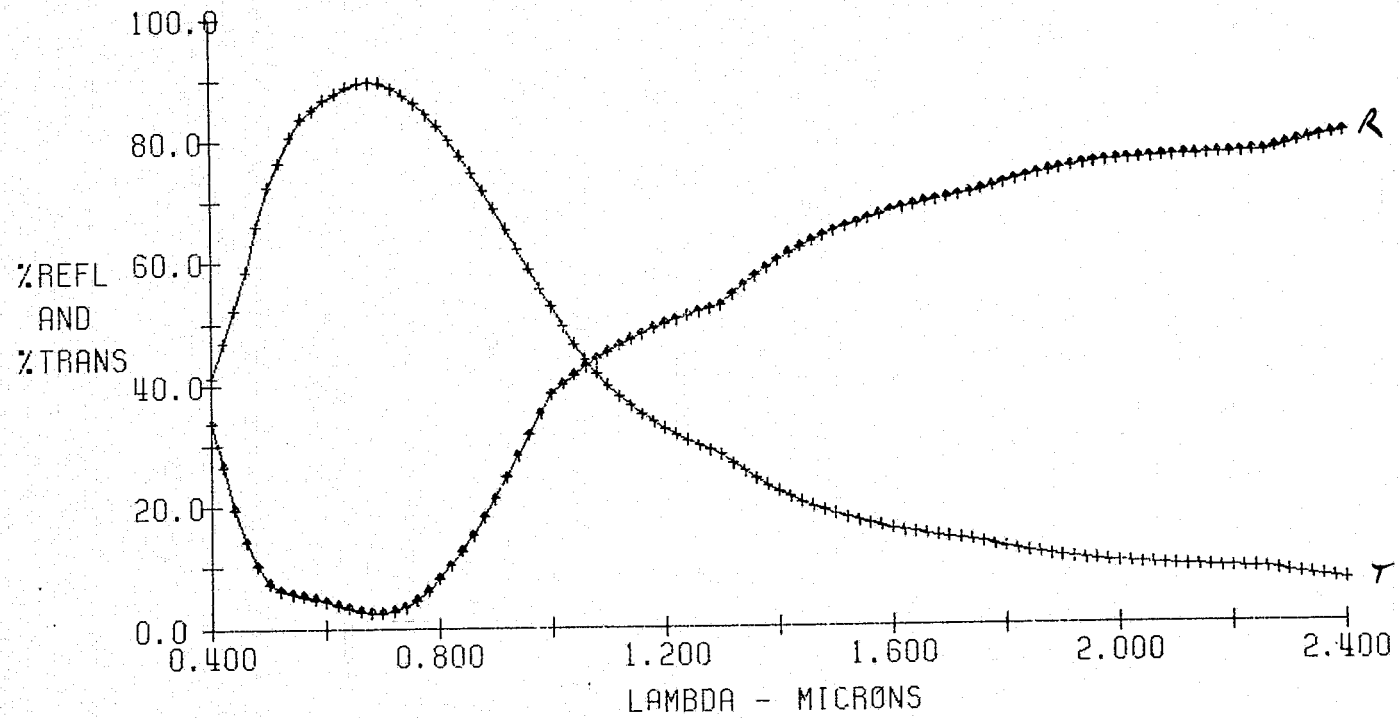

Figure 3.2-5 Expansion of Figure 3.2-4 to show more detail at visible wavelengths.

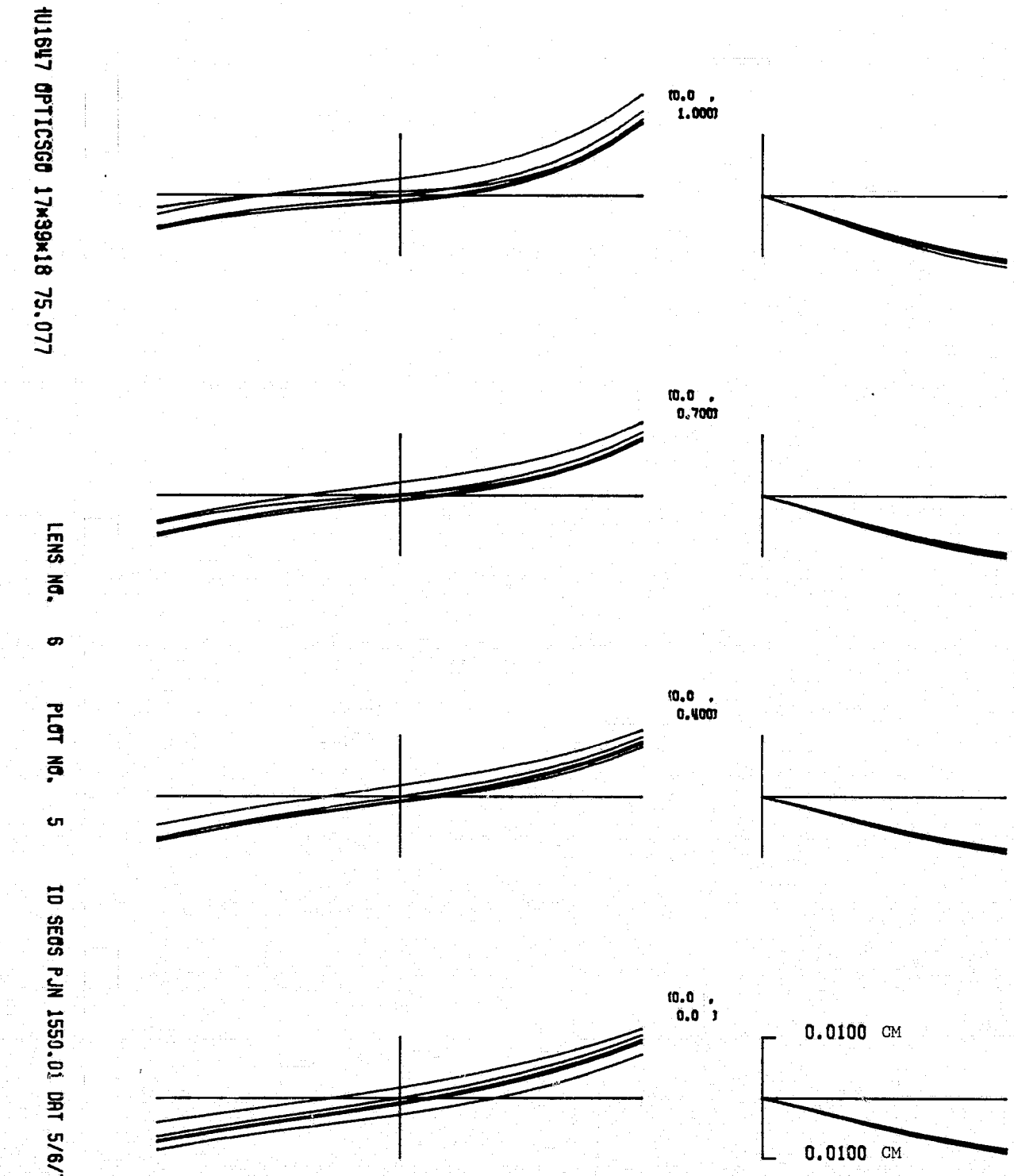

Figure 3.2-6 Ray Trace of Howell's Design
1cm Thick Beamsplitter, 0.49-1.01μm, 0°6 Half Field

and the actual plate thickness would be about 4 centimeters. It should be noted that this astigmatism can be reduced, using cylindrical elements and a wedged beamsplitter substrate. We feel that the sum of all these problems, involving both transmittance and image quality, weigh heavily against this design configuration.

One last comment on this design approach: directing the infrared light out the side of the telescope affects both the structural characteristics of the secondary mirror support structure and the mass distribution of the satellite. This may have adverse affects on its launch configuration.

By comparison, forming an intermediate image and geometrically dividing it into three (or more) sections each of which is directed to a separate relay with mirrors, appears more favorable. No dichroic mirrors are needed; spectral selection is done by inserting the narrow bandwidth filter directly in the optical path for the appropriate line image. Each spectral region may be treated independantly of all others, except for the two mirrors in the main telescope.

In the selected version of this design concept, the intermediate image is formed by the two mirrors of the Cassegrain telescope with no additional corrector elements, and it is therefore not well corected. The relays provide field correction for the telescope as well as for their own aberrations. This intermediate image is at a significantly larger focal ratio (f/12) than any of the final images. This has two advantages: (1) The image is of larger scale, so that the individual line images can be well separated; (2) The large focal ratio, coupled with the remote exit pupil of the Cassegrain telescope, means that the angle of incidence of light on this image plane remains within a very few degrees of normal throughout the field-of-view. These two factors combine to make the intermediate image a logical place to locate the narrow band interference filters; the small variation of angle of incidence is ideal for interference filters, and the spaciousness of the image simplifies designing filter holders and changers.

The major problem with this design approach is providing adequate image quality at all wavelengths. This is discussed below.

3.2.4 Lens Design Problems

Given that the complete optical system is to consist of a Cassegrain-type telescope followed by three or more separate relay systems, the lens designer must choose one of two courses: he can correct the two telescope mirrors to give good on-axis imagery at the intermediate focus, or, he can use the aspheric coefficients of the two telescope mirrors as variables in correcting one of the relay designs. If he chooses the former course, all of the relay designs will be basically similar, and will be either all-refracting or catadioptric. The major differences are likely to be in the glass types chosen for the different spectral regions. If he chooses the second approach, the design of one relay will be very much simplified at the expense of providing a badly aberrated input image for the other relay designs. We have chosen to take the second course: a three-mirror system provides the f/5 image, and all-refracting relays form the other images.

The three mirror telescope is very desirable for our purposes in that it is easy to design, can have a flat image, can be corrected over a field of view of more than 0.6 degrees, and is completely free of chromatic aberrations. Its

simplicity also insures high transmittance. Only one three-mirror design can be used, however: designing three-mirror systems for the other focal ratios would require changes in the primary and secondary mirror aspheric coefficients. Thus we must select which focus will use the three-mirror design; the choice depends on whether or not relays for the other focii can be designed in conjunction with the two telescope mirrors.

Chromatic aberrations due to variation of index of refraction with wavelength form the principal limitations on image quality in refracting lenses covering broad spectral ranges. This is also true for catadioptric lenses, if the refracting components contribute significantly to the power of the lens. (Field correctors, such as those in the Howell design, contribute relatively little to the net power of the telescope, and can be corrected over wider spectral ranges.) Each of the three focal ratios required for SEOS is associated with a broad spectral range, if the entire range is to be covered with one relay. A useful estimate of the difficulty of correcting refracting or catadioptric relays for each may be obtained by examining the dispersion characteristics of typical refracting materials suitable for each spectral region.

Dispersion is measured by the V-number, which is calculated by the equation

$$V\# = \frac{N_2 - 1}{N_1 - N_3} ,$$

where N_2 is the index of refraction at the design wavelength, near the center of the bandpass, and N_1 and N_3 are the indices of refraction at the shortest and longest wavelengths, respectively. The standard wavelengths used in quoting V-numbers for visible light glasses are 0.4861 (1), 0.5893 (2), and 0.6563 (3) micrometers. Table 3.2-2 lists V-numbers for two common Schott glasses for both the standard wavelengths and the catalog wavelengths nearest the SEOS limits for the f/5 relay.

For present purposes, the most important point to note is the relative magnitude of the V-numbers. BK-7 and F-2 are typical of the crown (higher V-number) and flint (lower V-number) glasses which might be used to design an achromatized doublet of moderate focal ratio. The lower V-numbers for the extended spectral range, which indicate a greater variation in index of refraction with wavelength can be taken to mean that it is significantly more difficult to achromatize a lens design of the same focal ratio for the wider wavelength range. In fact, it would be necessary to use at least three glass types, including one or more with special dispersion characteristics, to design a well-corrected relay for the desired spectral range for f/5 imagery.

Table 3.2-3 lists V-numbers for four infrared materials for each individual wavelength channel and for possible combinations of channels at f/2 and f/1.3. Note that in most cases the V-numbers are substantially higher than the visible light examples given in Table 3.2-2. This can be taken as indicating that color correction across the infrared spectral range is more readily accomplished across the visible spectral region. Where the V-number is in the range 400-500 or greater, it may be possible to complete a design with only one glass type.

Four possible choices of infrared bands look interesting: 1) 1.58-4.1 + 6.5-12.9: The V-numbers for ZnS and Si are comparable to those for visible light glasses over the standard spectral bandwidth, while Ge in itself looks adequate for the longer wavelengths. 2) 1.58-2.35 + 3.5-4.1 + 6.5-12.9: This

Table 3.2-2

Glass Dispersion Data: Typical V-Numbers in the Visible

	Glass Types	
Wavelength Range (μm)	BK-7	F-2
0.4861-0.6563*	64.2	36.54
0.4358-1.014**	26.7	15.8

NOTES: * The standard wavelengths for visible light V-numbers.
** The wavelengths closest to the f/5 spectral range listed in the Schott catalog.

Table 3.2-3

Glass Dispersion Data: V-Numbers for Infrared Materials

Wavelength Range (μm)	ZnS*	Si	Ge	ZnSe**
a. Individual channels				
1.58-1.68 (M4)	728	351	---	557
2.05-2.35 (E13)	486	294	116	426
3.5-4.1 (M5)	389	758	328	595
6.5-7.0 (M6)	305	4839	2296	688
10.3-12.9	---	---	3574	131
b. F/2 Combinations				
1.58-2.35	141	74.8	---	114
1.58-4.1	66.1	48.7	---	65.3
c. F/1.3 Combinations				
3.5-12.9	---	---	99.5	29.3
6.5-12.9	---	---	471	37.7
3.5-7.0	54.3	416	119	106
d. Index of refraction				
2.05	2.26260	3.45085	4.10250	2.44643

NOTES: * Same as Eastman Kodak Irtran II
** Same as Eastman Kodak Irtran IV

combination of three relays eases the correction problems for the shorter wavelength channels, and makes anti-reflection coatings easier to design. (This will be discussed further below.) 3) 1.58-2.35 + 3.5-7.0 + 10.3-12.9: This might prove to be the easiest combination for which to provide high quality lens designs, using Ge plus Si for the middle wavelength channels and Ge alone for the longest wavelength channels. These combinations are also reasonably compatible with antireflection coatings. 4) 1.58-2.35 + 3.5-12.9: This is the only two-relay alternative to number 1). OCLI does make a special anti-reflection coating for Germanium which can cover this spectral range. The V-number for Ge makes an all-Germanium design look problematical, however, and ZnSe cannot be used with that antireflection coating.

One point should be stressed in interpreting these comments: Good image quality is needed only across each individual channel. Thus when several channels are combined in one relay, the important chromatic aberration to control is chromatic variation of the monochromatic aberrations, rather than secondary color or axial color, since the latter can be eliminated by refocussing the individual detector array. It should also be recalled that channels M5 and M4 need not be well corrected (see Table 3.2-1). This combination of circumstances might make an all-germanium 3.5-12.9 micrometer relay achievable in spite of what the V-number indicates.

The general conclusion to be drawn here is that from the point of view of color correction, an all-refracting design for the visible and near infrared f/5 relay appears to be difficult to achieve, whereas there are several possibilities for designing refracting relays for the infrared. For this reason, we have elected to use a three mirror design for the f/5 bands and all-refracting relays for the infrared bands.

The above discussion is perhaps an oversimplification of the design problem, and does not deal at all with those problems relating to the relatively fast focal ratios of the infrared relays. Nor does it consider the problem of correcting for the field aberrations of the two mirror main telescope within the relay optics. These can be dealt with effectively only in terms of real relay designs. To explore these, we have set up a three mirror-telescope, plus preliminary designs for the f/2.0 and f/1.3 relays.

3.2.5 Three-Mirror F/5 Design

Fig. 3.2-7 is a computer drawing of the three-mirror telescope, showing ray bundles for three image points. The first two mirrors form an f/12 image, which is relayed to the f/5 focus by the third mirror. The powers of the three mirrors were selected to give a zero net petzval sum, so that the corrected field would be flat. (A residual of higher order field aberrations leads to a curved best focus surface.) This balancing of powers led to a very fast primary mirror (f/1.5) and a relatively large focal ratio for the intermediate image. The three mirrors are conic sections. This third order design was found to give high enough image quality for the present application. Use of higher order aspheric coefficients might lead to somewhat higher image quality and a flatter image. Design data for the three mirrors is given in Table 3.2-4.

One problem with this type of three mirror design is that the output image is in the input light beam for the third mirror. In our case, this problem is overcome by placing the four lines of detectors entirely on one side of the optical axis, away from the center of the field of view, Fig. 3.2-8. The incoming

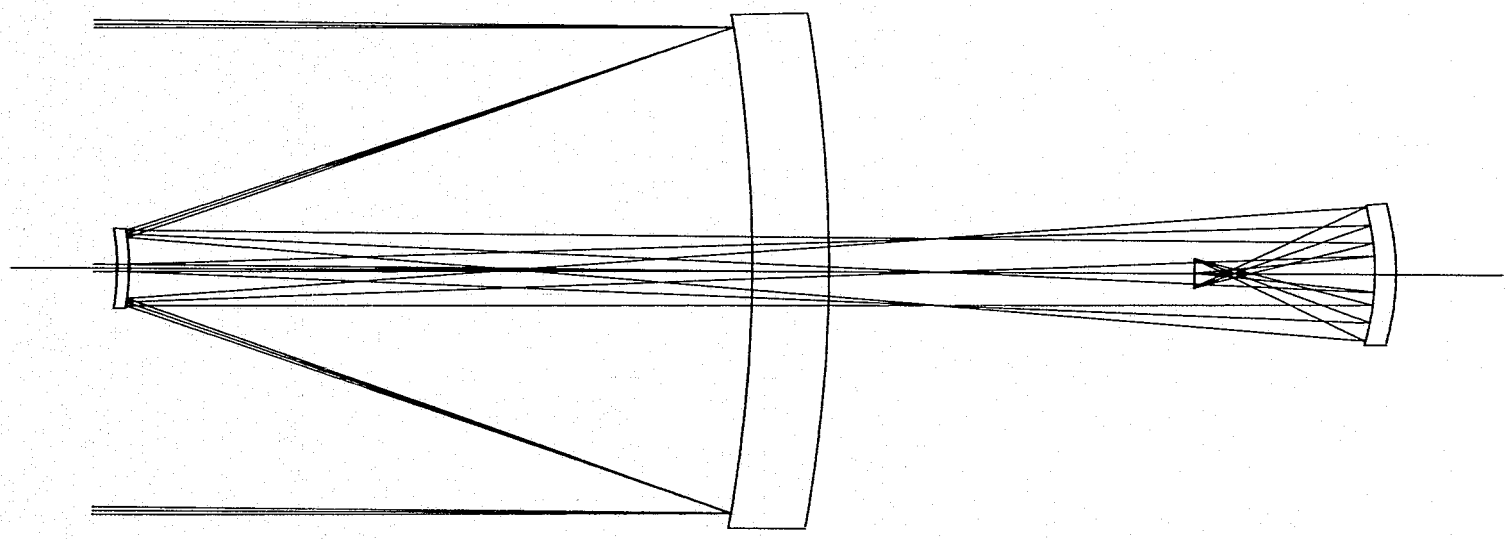

Figure 3.2-7 Three Mirror F/5 Telescope

Table 3.2-4 3 Mirror F/5 Design

LENS NO. 18 LENS OUTPUT DATA

SYSTEM DATA

F-NUMBER =	-5.0000000	ENTRANCE PUPIL DISTANCE =	180.5556000
FOCAL LENGTH =	700.0000000	EXIT PUPIL DISTANCE =	-40.7254634
BACK FOCUS =	-52.2302458	GAUSSIAN IMAGE HEIGHT =	-3.9998000
TOTAL LENGTH =	360.9035000	DP/DV =	0.0
OBJECT HEIGHT =	-0.4000+15	AXIAL BEAM RADIUS =	70.0000000
CHIEF RAY ANGLE =	0.0057140	CHIEF RAY HEIGHT =	-1.0316947
AXIAL RAY ANGLE =	0.0000000		

WAVELENGTHS LOWER 0.7000 MAJOR 0.7000 UPPER 0.7000

SURFACE DATA

SURFACE NUMBER	RADIUS OF CURVATURE	THICKNESS	GLASS TYPE AND/OR N(D)	V(D)	APERTURE DIAMETER
OBJECT	INFINITE	0.7000+17			
1	INFINITE	180.5556	AIR		143.4840
2	-420.0000	-180.5556	-AIR		141.4000
	CONIC CONSTANT =	-0.9545182			
3	-67.3016	235.5556	AIR		21.9562
	CONIC CONSTANT =	-1.1977070			
4	INFINITE	125.3479	AIR		19.8039
5	-73.7366	-52.2302	-AIR		39.2843
	CONIC CONSTANT =	-0.6677627			
IMAGE	-711.0330				

* PAGE

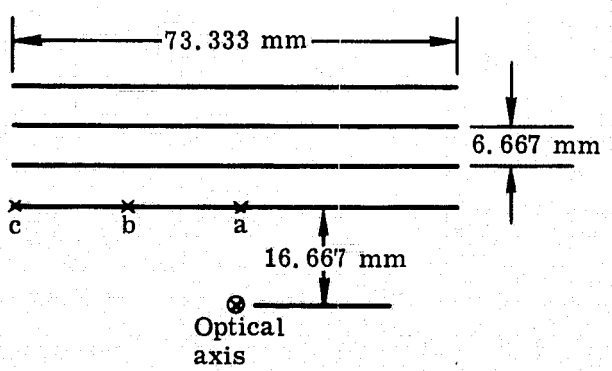

Figure 3.2-8 f/12 Image Layout for Four Visible Detector Arrays, F/5 Image 15 x 15 Micrometer Detectors

light then lies entirely on the opposite side of the optical axis from the output image. There is, in fact, enough clearance to allow placement of a physical stop at the image of the primary mirror between the third mirror and the output image. This could be useful in controlling stray light diffracted by the edge of the primary mirror.

Another characteristic fault of this type of design is a large amount of positive (pincushion) distortion. This may be of no concern in the present application. This should be confirmed analytically in the next phase of the program, however; if distortion is a problem, it will be necessary to add a refracting corrector group to compensate for it. This would change the basic ground rules used in choosing this design approach, and might make another approach preferable.

Image quality of the three-mirror design can be assessed by examining Figs. 3.2-9, 10 and 11. Fig. 3.2-9 is a standard meridional raytrace plot showing ray intercept heights on the image surface as a function of pupil height along the x and y axis of the pupil. Fig. 3.2-10 is a set of spot diagrams for three points along one of the detector arrays in the f/5 image. (The image positions are identified by the points a, b and c in Fig. 3.2-8.) Fig. 3.2-11 plots MTF for these same three image points. The spot diagrams tell the story most clearly: all rays plotted fall well within the boundary of the detector element at 0.7 micrometers, the wavelength at which the rays were traced. Since there are no chromatic aberrations, the same spot diagrams are valid at all wavelengths. The three curves in each MTF plot are for 0°, 45° and 90° orientations of the bars in the resolution target. The differences shown are not of any great significance, and all are reasonably close to the MTF values obtained with a perfect lens having the same central obscuration, as indicated by the crosses.

The general design configuration we have carried over from phase I calls for four detector arrays to cover all thirteen possible f/5 bands. This requires the four rows of detectors shown in Fig. 3.2-8. We plan to place the narrow band filters near the f/12 image, where the line images are 176 millimeters long, and are spaced apart by 16 millimeters. (These are paraxial dimensions: when distortion is accounted for, the actual dimensions may differ by a few millimeters.) With four bands and thirteen filters, some form of filter changing mechanism will be needed. Figs. 3.2-12, 13 and 14 represent three possible approaches to the changer mechanism.

If it is necessary to be able to select any possible combination of four of the thirteen filters, a changer mechanism of the form shown in Fig. 3.2-12 may be necessary. In this example, the thirteen filters are held in a filter carrier when not in use. This filter carrier can be moved vertically to locate a given filter opposite a dovetail slide centered on an image slit. A mechanism similar to a photographic slide changer can then move the filter into place over the slit image.

This type of mechanism is somewhat cumbersome and slow, and leads one to question whether or not it will have sufficient mechanical reliability. Conversely, failure of one of the four detector arrays will not eliminate any specific spectral bands.

In practice, it is not necessary to use all possible combinations of four filters among the thirteen; e.g., the four M-series filters will always be used together, and never in conjunction with any of the E-series filters.

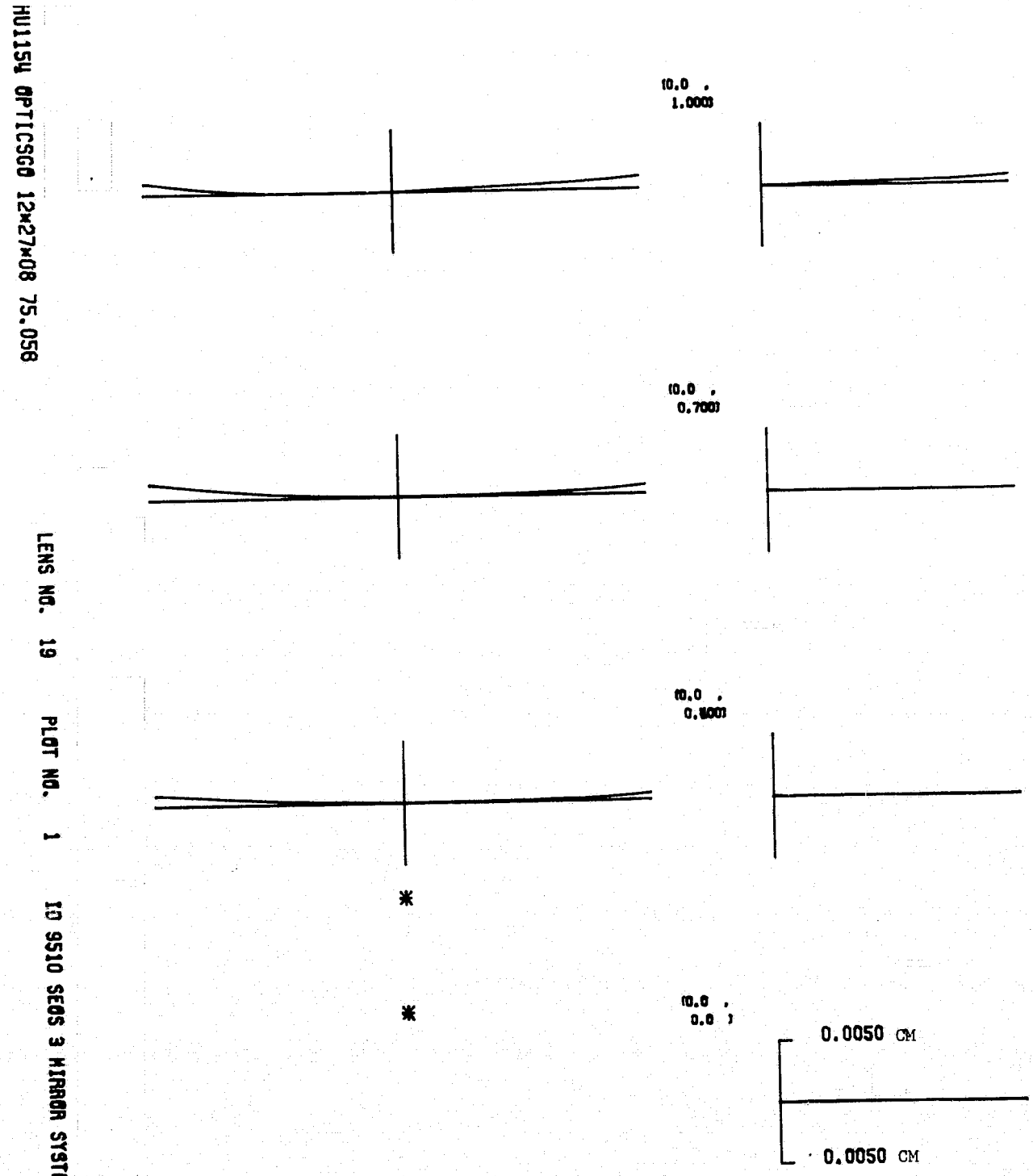

Figure 3.2-9 Ray Trace of 3-Mirror f/5
$\lambda = 0.7\mu m$, 0°38 Half Field

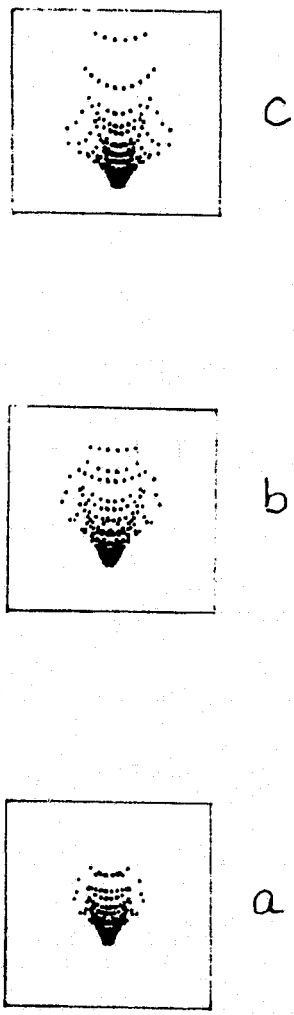

Fig. 3.2-10 Spot Diagrams for f/5 System
at positions a, b, c in Figure 3.2-8

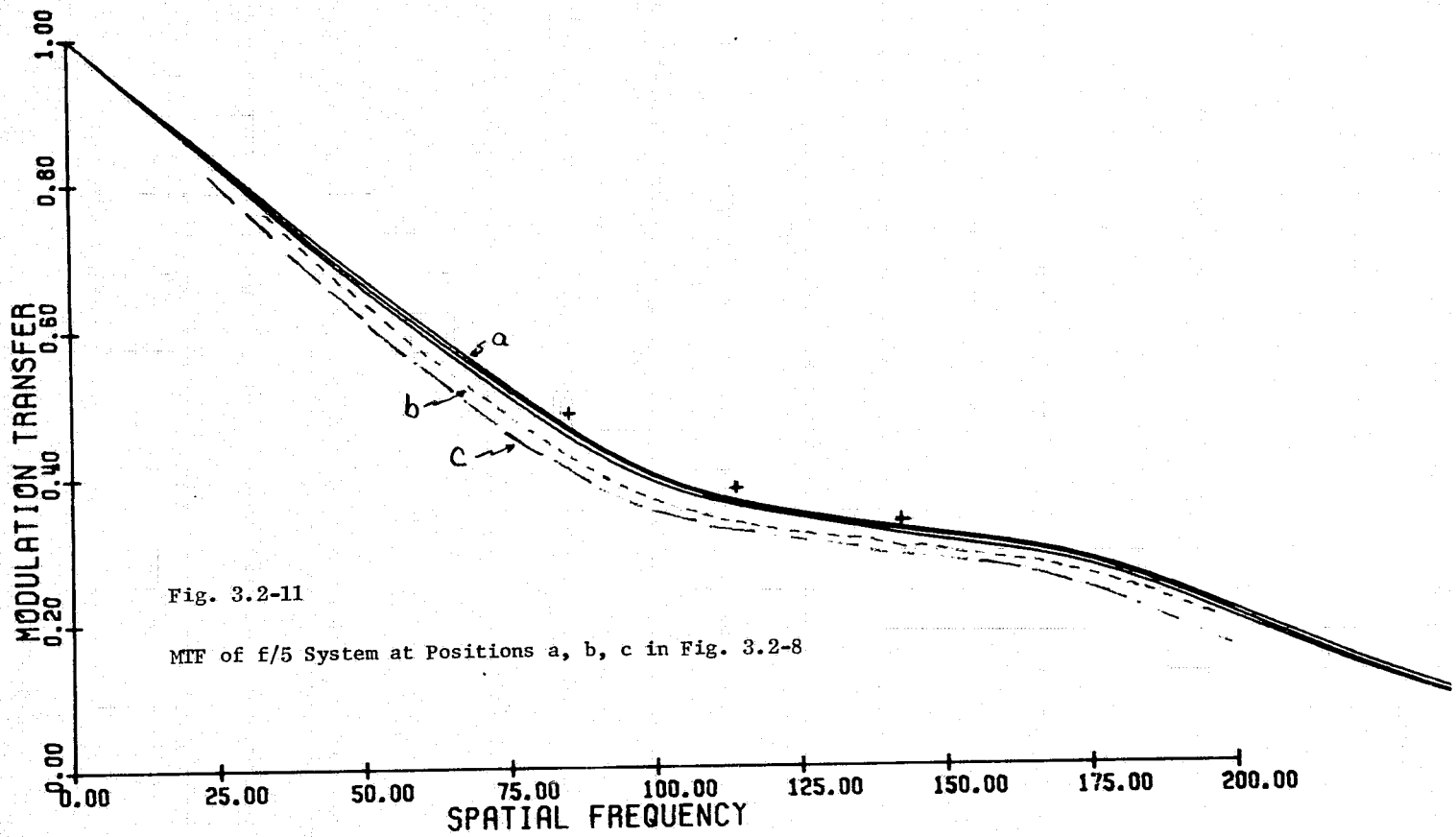

Fig. 3.2-11

MTF of f/5 System at Positions a, b, c in Fig. 3.2-8

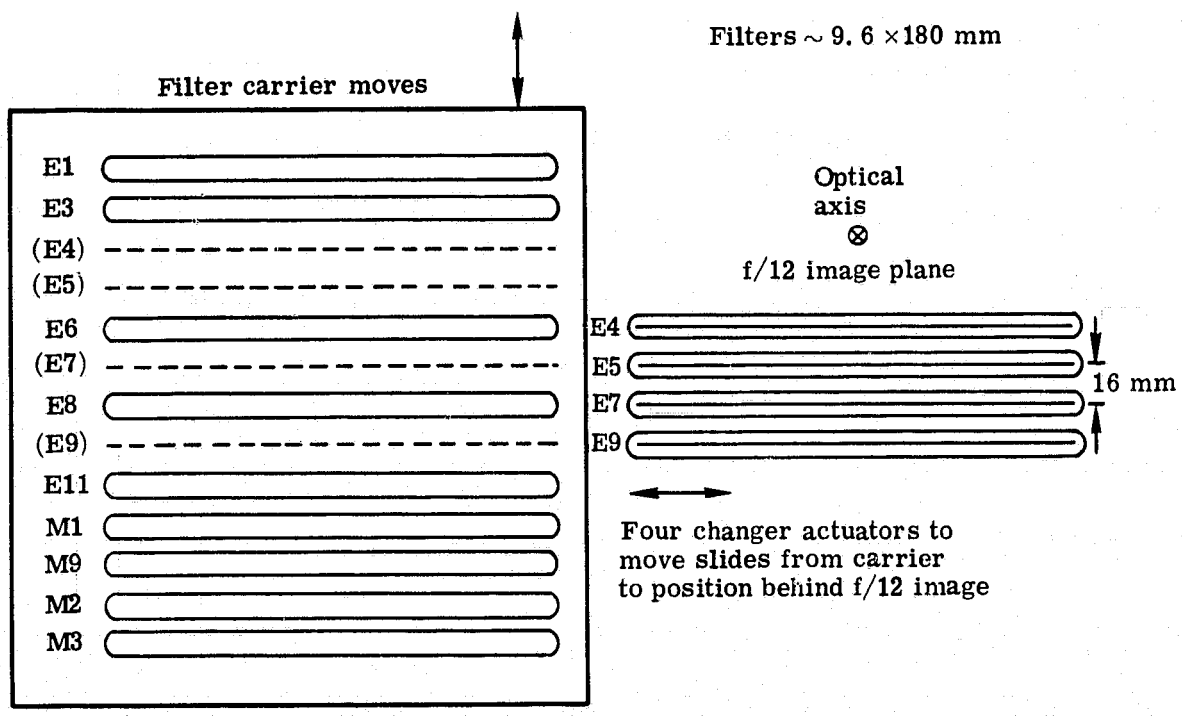

Figure 3.2-12 Filter Changer Mechanism Allowing any Combination of 4 Channels out of 13 F/5.0 Channels to be Used Simultaneously

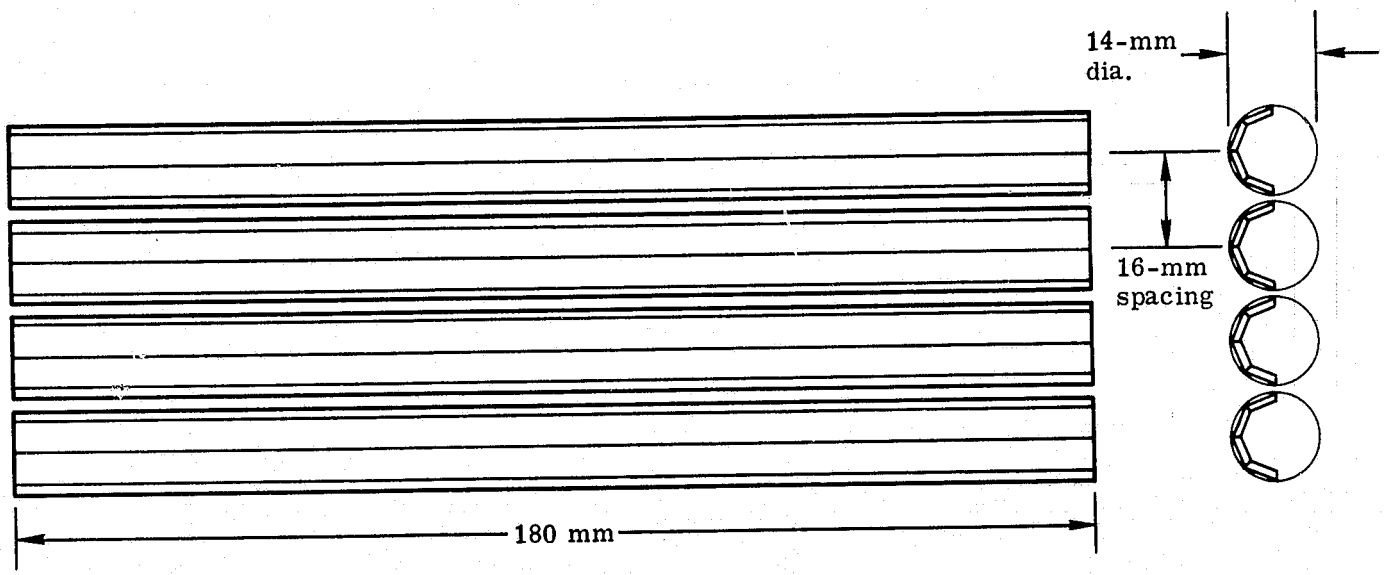

Figure 3.2-13 Filter Changer Mechanism Allowing Choice of One of Four Filters per Channel

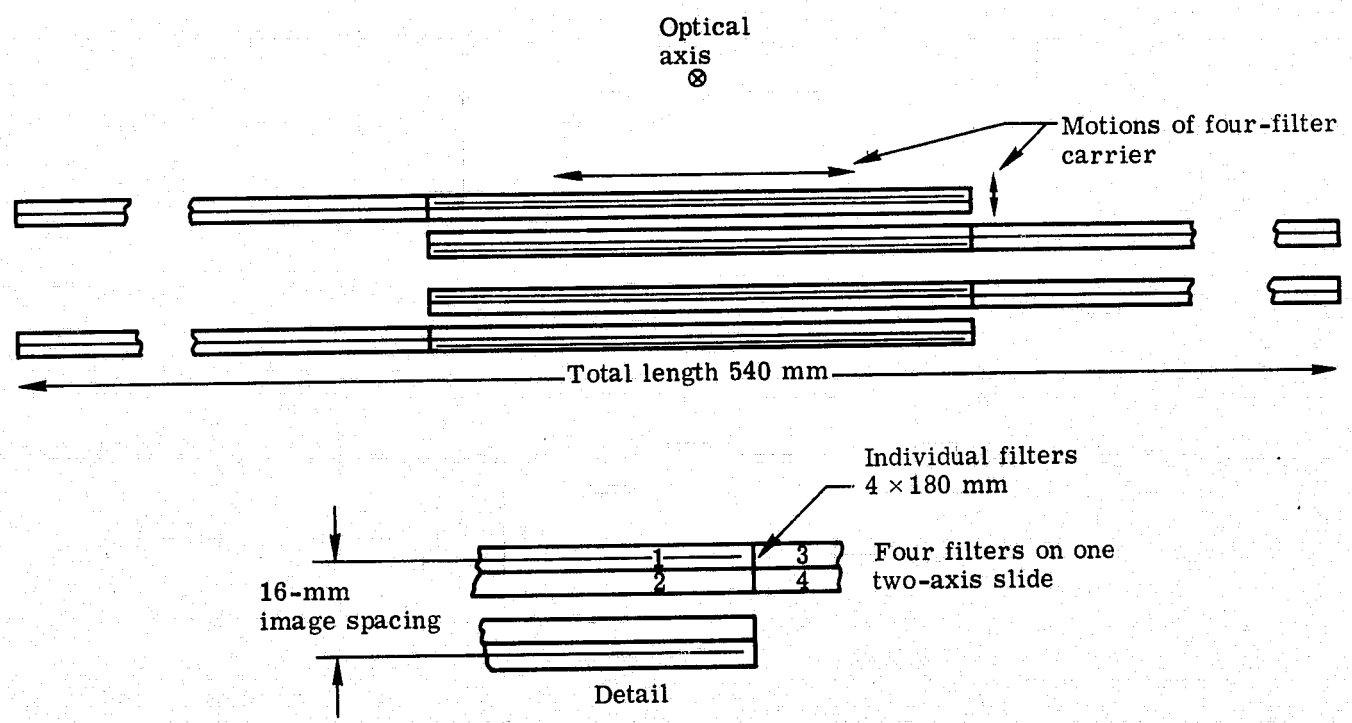

Figure 3.2-14 Alternative Filter Changer Mechanism Allowing Choice of One of Four Filters per Channel

If a changer mechanism can be developed which allows the choice of one of four filters for each image slit, most desired combinations can be made. (Actually, the number of filters required are 4, 4, 3 and 2.) Figs. 3.2-13 and 3.2-14 show two mechanisms for doing this, involving rotating drums of filters or four two-axis slide mechanisms.

All three of these techniques require the construction of long, narrow interference filters. The configuration of Fig. 3.2-12 requires filters which are 180 mm long and 9-10 mm wide. Both of the other examples require filters which are 4 x 180 millimeters. The feasibility of manufacturing these filters must be established eventually; discussions with some manufacturers lead us to be optimistic on this score, but more complete specifications on the desired bandwidth and wavelength tolerances are needed before the manufacturing tolerances can be assessed.

The changer mechanisms of Figs. 3.2-12 and 3.2-14 look rather complex, and the mechanism of Fig. 3.2-13 looks rather delicate and difficult to assemble. Neither of these conditions bodes well for reliability. An alternative approach would be to use 13 detector arrays in parallel lines with a separate filter for each detector array. It would be necessary to space the detector arrays about 1.6 to 2.0 millimeters apart in the f/5 focal plane, to fit them within roughly the same field of view as the four detectors above. This raises questions as to the feasibility and cost of building the detector array. This would, however, eliminate any need for a filter changer mechanism in the f/5 optical system.

3.2.6 F/2 Middle Infrared Relay

The f/12 image formed by the first two mirrors of the three mirror f/5 telescope is very badly aberrated, with wavefront errors reaching 30 wavelengths (at 0.7 micrometers) at the edge of the field. The two major questions in assessing the feasibility of designing the f/2 middle infrared relay are: 1) can the bad aberrations in the input image be controlled in the relay, and 2) can chromatic aberrations be controlled sufficiently to obtain adequate image quality at the E13, M4 bands. It is these two questions we have attempted to answer in our lens design analysis.

We have taken two design approaches, one catadioptric and the other all-refracting, and pursued them far enough to establish whether we can control the aberrations well enough to give confidence that a fully corrected design could ultimately be achieved. The intention was to drop one of these approaches if the other looked particularly promising, and carry the better concept through preliminary design. The all-refracting relay turned out to be most promising, and is discussed in most detail here.

The catadioptric design was an adaptation of the f/5 relay mirror, in which two meniscus elements of silicon (Si) were added to increase its power to give an f/2 image. These two elements were set symmetrically on either side of the stop located between the third mirror and the output image. Correction was attempted by varying the aspheric coefficients of the third mirror and the curvatures of the two elements. One surface of each element was made into a conic. Our goal was to answer two questions: 1) Is the dispersion of silicon low enough to give adequate image quality across the E13 channel, from 2.05 to 2.35 micrometers? 2) Do these two elements plus the aspheric coefficients on the third mirror give adequate control over field aberrations? The answers to both questions were "marginally, no". Primarily because of the color problem, we dropped this approach in favor of the more promising all-refracting design.

In retrospect, we might have had more success with the catadioptric design had we used zinc sulfide (ZnS) instead of silicon. The band by band V-number analysis of Table 3.2-3 (which was performed after this design approach was dropped) shows a significantly slower variation of index across this bandwidth for the zinc sulfide. We now feel that this design approach may also be successful.

The design we have pursued is the all-refracting design shown in Fig. 3.2-15. The reasoning behind this selection goes roughly as follows: An f/12 to f/2 relay is equivalent to an f/1.67 infinite conjugate objective. Such lenses in the visible are typically 6 to 8 element double-Gauss lenses. Therefore we should start with, say, 6 elements. Four of these should be positive lenses of high V-number (crown) glass and two should be negative lenses of low V-number (flint) glass. A field lens is needed near the f/12 image to reimage the stop at the center of the relay. A thin aspheric corrector plate should be placed between the field lens and the relay, where light beams from the various image points are well separated, to give control over the field aberrations in the telescope. This design was set up, and was converging rapidly toward a solution when schedule requirements necessitated our truncating the design effort at this point. Table 3.2-5 gives the design parameters for the final version of this preliminary design.

ZnS (Irtran II) was chosen for the "crown" elements, and was also used for the field lens and corrector plate. Silicon was used for the "flint". Achromatization was done over the wavelength range 2.0 to 2.5 micrometers, where highest image quality is required. Image quality was monitored at 1.58-1.68 micrometers and 3.5-4.1 micrometers*, but no attempt was made to control it at those wavelengths. The initial performance goals were for a 15 x 15 μm image at 2.05 to 2.35 μm, 280 x 280 μm at 1.58 to 1.68 μm, and 230 x 230 μm at 3.5 to 4.5 μm. The results obtained may be judged from Figs. 3.2-16 through 20.

Fig. 3.2-16 shows meridional raytrace data at a series of five wavelengths from 2.05 to 2.35 micrometers. The curves indicate good chromatic correction for all five colors except 2.05 micrometers. This anomaly is an indication that the center of the achromatization range was set at too long a wavelength. A minor modification to the design procedure can correct this defect. The design still shows too large monochromatic aberrations at 0.21° and 0.30° off-axis. We believe that these faults can be corrected through further design effort, probably through modification of the higher order aspheric coefficients on the corrector plate.

Fig. 3.2-17 shows spot diagrams for the on-axis, 0.15° and 0.30° images. A 15 x 15 micrometer square has been included to indicate the detector size. The on-axis image has a very sharp central core surrounded by flare which extends beyond 15 micrometers. This is due to the color at 2.05 micrometers, and can be eliminated by a slight shift in the achromatization range. The image at 0.15 degrees shows a sharp central core with flare which is also due mostly to the 2.05 micrometer color. The image quality is probably acceptable as is, and reachromatization will improve it somewhat. The image at 0.30 degrees is clearly unacceptable, however, and needs further correction. We feel that this can be accomplished.

---

* At the time we were designing the f/2 relay we were maintaining the option of putting the 3.5 to 4.5 μm band at f/2. In the final LEST concept that Band was put at f/1.3.

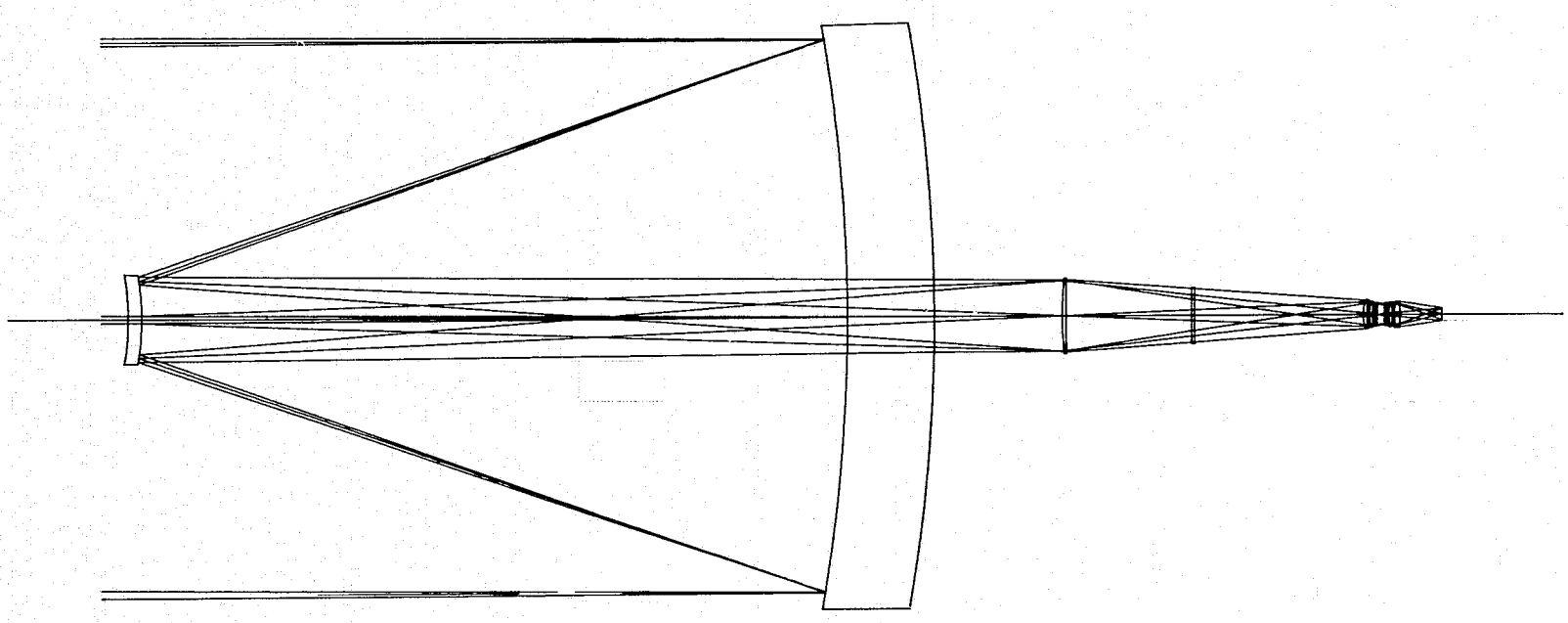

Figure 3.2-15 Telescope with Preliminary F/2.0 Relay Design

Table 3.2-5a Lens Deck for F/2 Relay

```
* CLIC P
ONE52050
ID SEDSGAUS PJN 9510 DAT 2/17/75
LENS NO.   15
ORAT  9 2 1 3 4 5
CS 2 3 2 1 3 2
APS  2
WV 2.0500000D+00 2.2000000D+00 2.3500000D+00 2.1500000D+00 2.2500000D+00
CF  1.0000000D+04 SF  2.5000000D-03
OBJ B   1.0000000D-15   5.3000000D-03   7.0000000D+01  -9.5694468D-01
  0 CV   0.0            AIR
  1 CAI   2.2000000D+01
  1 CV   0.0          TH   1.8055560D+02  AIR
  2 PTH   -1
  2 PIN  -1
  2 RD  -4.2000000D+02
  2 CC -9.5451820-01
  3 YMT   0.0
  3 AIR
  3 RD  -6.7301600D+01
  3 CC -1.1977070+00
  4 N15    2.26260000    2.26122000    2.26001000    2.26166000    2.26080000
  4 TH   1.0000000D+00
  4 RD   7.7935170+01
  5 CV   0.0          TH   3.2000000D+01  AIR
  6 PIN   4
  6 CV   0.0          TH   8.0000000D-01
  6  ASP  0.0          -2.197562D-07 -8.552234D-10  0.0           0.0
  7 CV   0.0          TH   4.2886392D+01  AIR
  8 PIN   4
  8 TH   1.1000000D+00
  8 RD   1.2427146D+01
  9 CV   2.1045598D-02 TH   5.0000000D-01  AIR
 10 PIN   4
 10 TH   9.0000000D-01
 10 RD   2.2952632D+01
 11 TH   5.0000000D-01  AIR
 11 RD  -4.2155980+02
 12 N15    3.45085000    3.44625000    3.44252000    3.44767000    3.44492000
 12 TH   5.0000000D-01
 12 RD  -2.1385480+01
 13 TH   1.0000000D+00  AIR
 13 RD  -2.2732551D+03
 13  ASP  0.0          -1.796616D-06 -1.045676D-06 -4.602350D-09  2.085863D-11
 14 CV   0.0          TH   1.0000000D+00  AIR
 15 PIN  12
 15 CV  -1.2792768D-02 TH   5.0000000D-01
 16 CV   3.6704020D-02 TH   5.0000000D-01  AIR
 17 PIN   4
 17 CV   6.2050371D-03 TH   9.0000000D-01
 18 PIN   0
 18 CV  -5.7623015D-02 TH   5.0000000D-01
 19 PIN   4
 19 CV   1.9139789D-02 TH   1.5000000D+00
 20 YMT   0.0
 20 CV  -5.9892894D-02  AIR
 21 CV  -9.9029125D-02
```

Table 3.2-5b Design of F/2 Relay

LENS NO. 15 LENS OUTPUT DATA

SYSTEM DATA

F-NUMBER =	-2.0280468	ENTRANCE PUPIL DISTANCE =	180.5556000
FOCAL LENGTH =	-283.9265579	EXIT PUPIL DISTANCE =	-4.0312549
BACK FOCUS =	10.6170710	GAUSSIAN IMAGE HEIGHT =	-1.5048108
TOTAL LENGTH =	332.2558631	DP/DV =	0.0
OBJECT HEIGHT =	-0.371D+15	AXIAL BEAM RADIUS =	70.0000000
CHIEF RAY ANGLE =	0.0053000	CHIEF RAY HEIGHT =	-0.9569447
AXIAL RAY ANGLE =	0.0000000		

WAVELENGTHS LOWER 2.0500 MAJOR 2.2000 UPPER 2.3500

SURFACE DATA

SURFACE NUMBER	RADIUS OF CURVATURE	THICKNESS	GLASS TYPE AND/OR N(D)	V(D)	APERTURE DIAMETER
OBJECT	INFINITE	0.700D+17			
1	INFINITE	180.5556	AIR		143.3330
2	-420.0000	-180.5556	-AIR		141.4000
	CONIC CONSTANT = -0.9545182				
3	-57.3016	235.5524	AIR		21.8017
	CONIC CONSTANT = -1.1977070				
4	77.9053	1.0000	IRTRAN II	10.75	18.4448
5	INFINITE	32.0000	AIR		18.4144
6	INFINITE	0.8000	IRTRAN II	10.75	13.6566
	CONIC CONSTANT = 0.0				
	ASPHERIC COEFFICIENTS				
AD= -0.2197562D-06	AE= -0.8552234D-09	AF= 0.0	AG= 0.0		
7	INFINITE	42.8864	AIR		13.6043
8	12.4271	1.1000	IRTRAN II	10.75	7.1888
9	47.5136	0.5000	AIR		6.9085
10	22.9526	0.9000	IRTRAN II	10.75	6.4617
11	-421.5598	0.5000	AIR		6.1422
12	-21.0855	0.5000	SILICON	10.75	5.7366
13	-2273.2551	1.0000	AIR		5.6637
	CONIC CONSTANT = 0.0				
	ASPHERIC COEFFICIENTS				
AD= -0.1796616D-05	AE= -0.1045676D-05	AF= -0.4602350D-08	AG= 0.2085863D-10		
14	INFINITE	1.0000	AIR		5.3061
15	-78.1692	0.5000	SILICON	10.75	5.4471
16	27.2450	0.5000	AIR		5.5103
17	161.1594	0.9000	IRTRAN II	10.75	5.8660
18	-17.3542	0.5000	AIR		6.0812
19	52.2472	1.5000	IRTRAN II	10.75	6.3798
20	-16.6965	10.6171	AIR		6.4703
IMAGE	-10.0980				

* PAGE

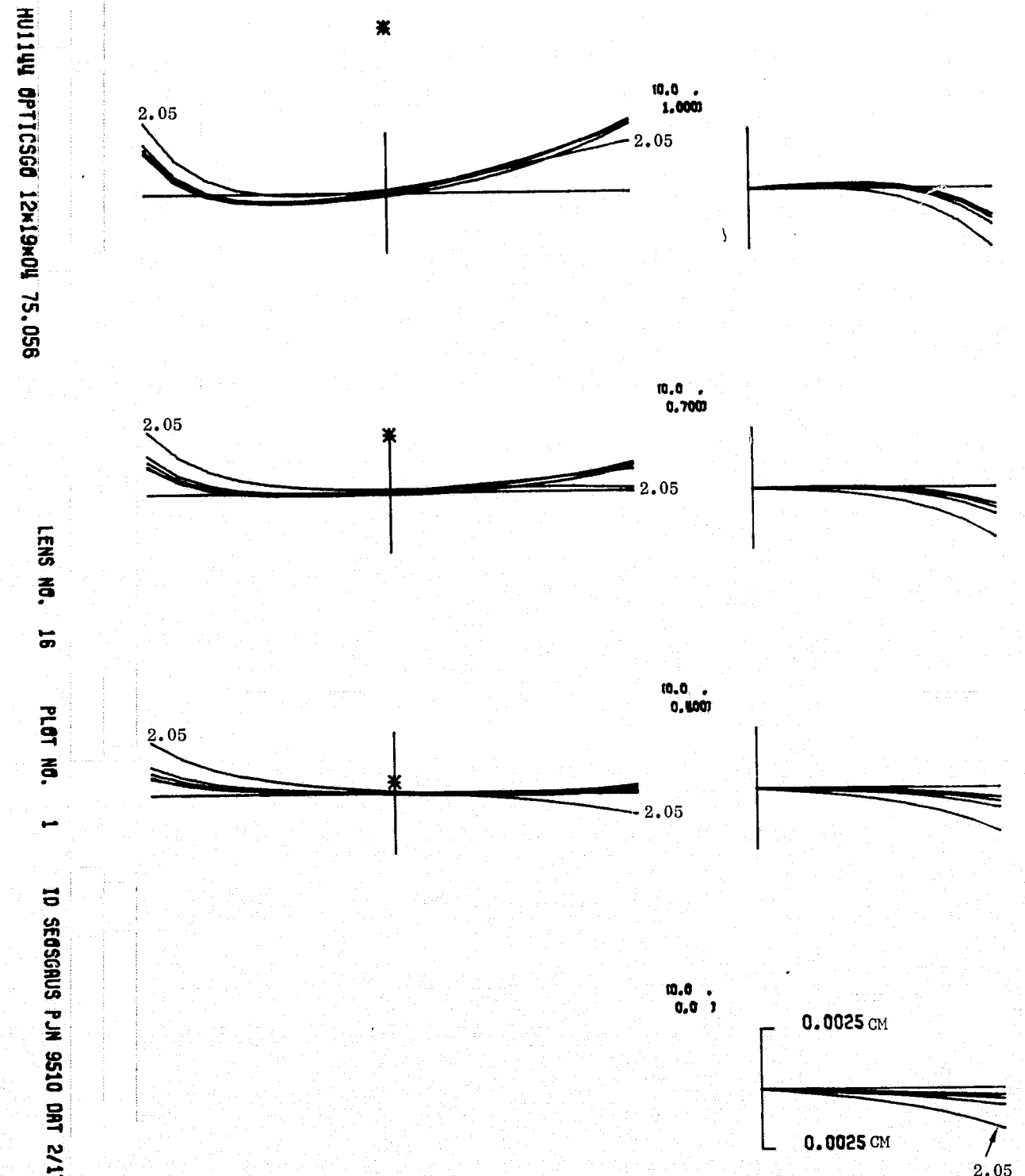

Figure 3.2-16 Ray Trace of f/2 system
2.05 - 2.35μm, 0°3 Half Field

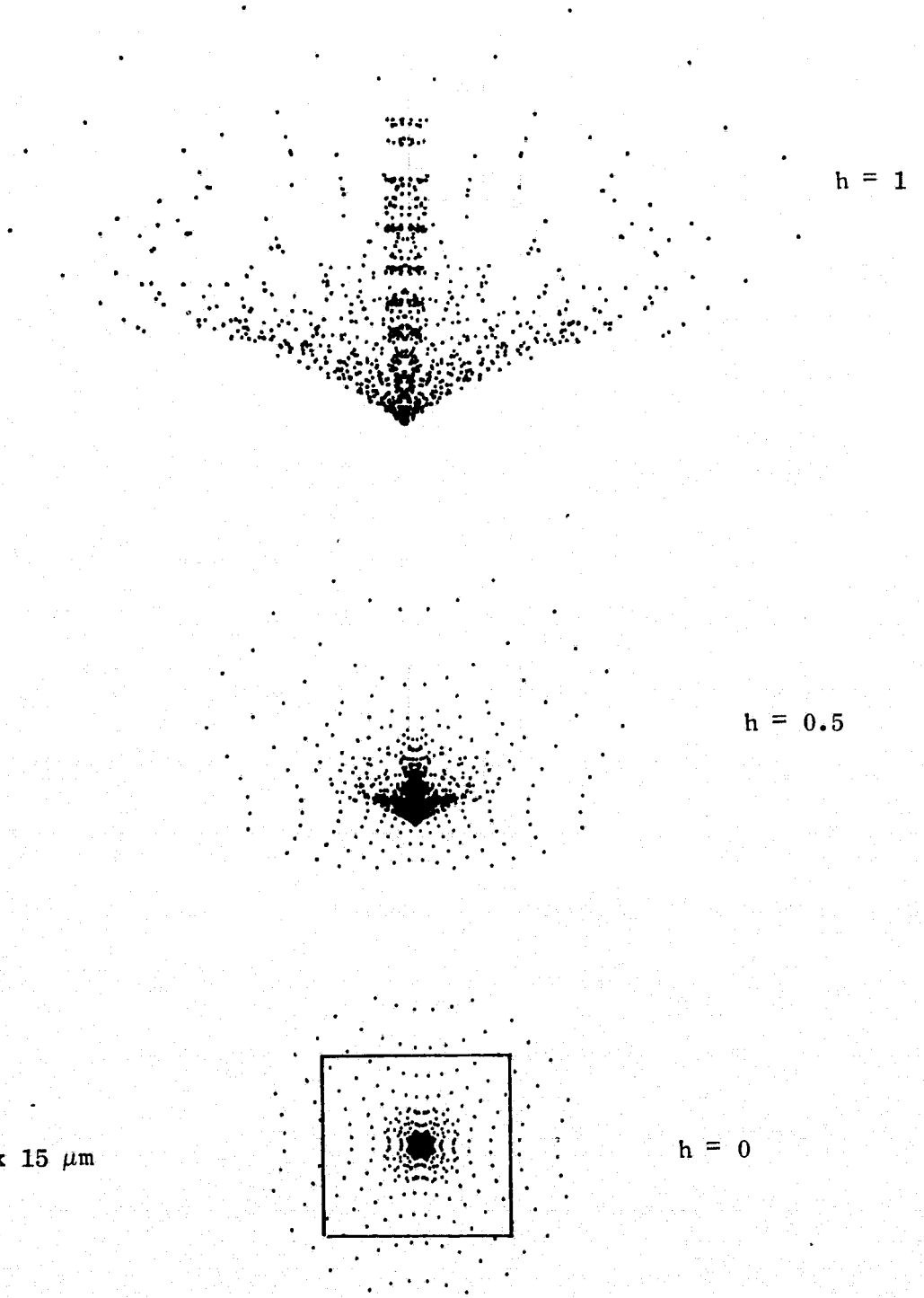

Fig. 3.2-17 Spot Diagrams of f/2 System
2.05 - 2.35μm, 0°3 Half Field

Fig. 3.2-18 shows MTF curves for these same three images. They are monochromatic MTFs, however, for the median wavelength of 2.2 micrometers. Again, only the 0.30 degree image is unacceptable.

Fig. 3.2-19 shows raytrace data at 1.58, 1.63, and 1.68 micrometers. The dominant aberrations are axial color and spherochromatism. The axial color, which gives roughly a 56 micrometer blur circle, is a result of all three wavelengths being well to one side of the achromatization range. Neither aberration is serious, in this case, since the detector size is 280 x 280 micrometers. A spot diagram for the 0.30 degree image is shown in Fig. 3.2-20; the 280 x 280 μm detector is so large that all rays fall well within the detector size.

Fig. 3.2-21 shows raytrace data at 3.5, 3.8 and 4.1 micrometers. In this case, the dominant aberration is axial color, with a blur of close to 200 micrometers on axis. This is four times the axial color at 1.63 micrometers. The reasons for this may be seen by examining the V-numbers for ZnS and Si in Table 3.2-3. It will be seen that the crown and flint roles of the two glasses are reversed at 3.5-4.1 micrometers. Thus the axial color contributions from the positive and negative elements tend to add rather than cancel. (This same effect proved disastrous in an earlier attempt at designing an all-refracting relay based on an existing visible light design.) The resulting spot diagram for the 0.30 degree image is shown in Fig. 3.2-20. While a 100 x 100 μm square is superimposed on the figure, in fact the detector size for an f/2 image should be near 230 x 230 micrometer. Thus, in spite of the extreme color problem, the performance is still probably acceptable.

Our conclusions are that obtaining adequate image quality from an all refracting f/2.0 relay is completely feasible. The present design needs improvement in several important respects. The off-axis image quality needs improvement, clearly. It would also be desirable to improve transmission characteristics by reducing the number of elements. Two possibilities exist: 1) combine the corrector plate and field lens into a single element located where the corrector plate now is; 2) eliminate one or two of the positive elements in the relay. This latter may be very difficult. An earlier attempt to use a triplet design for the relay was a failure. But careful use of aspheric elements may make a simpler design possible.

Transmission problems may also make it desirable to eliminate the 3.5-4.1 micrometer channel from this relay. The 1.58 to 4.1 micrometer wavelength range is too long for most antireflection coatings, and ZnS and Si are high index glasses. More on this appears in section 3.2.8.

3.2.7 F/1.3 Far Infrared Relay Design

In examining possible f/1.3 design configurations, we have considered three possible approaches, an all-reflecting relay, an all-germanium triplet (plus field lens), and an all-germanium five-element (including field lens) design. The first two approaches were dropped when they proved unsatisfactory.

The combination of image size, focal ratio, and the remote exit pupil for the telescope makes it very difficult to achieve an all-reflecting relay design. It is doubtful that a successful approach can be found, even if the f/5.0 visible light design is discarded and the primary and secondary mirror aspheric coefficients are used in the correction procedure. The problem appears to be that angles of incidence on elements in the relay become so steep that higher order

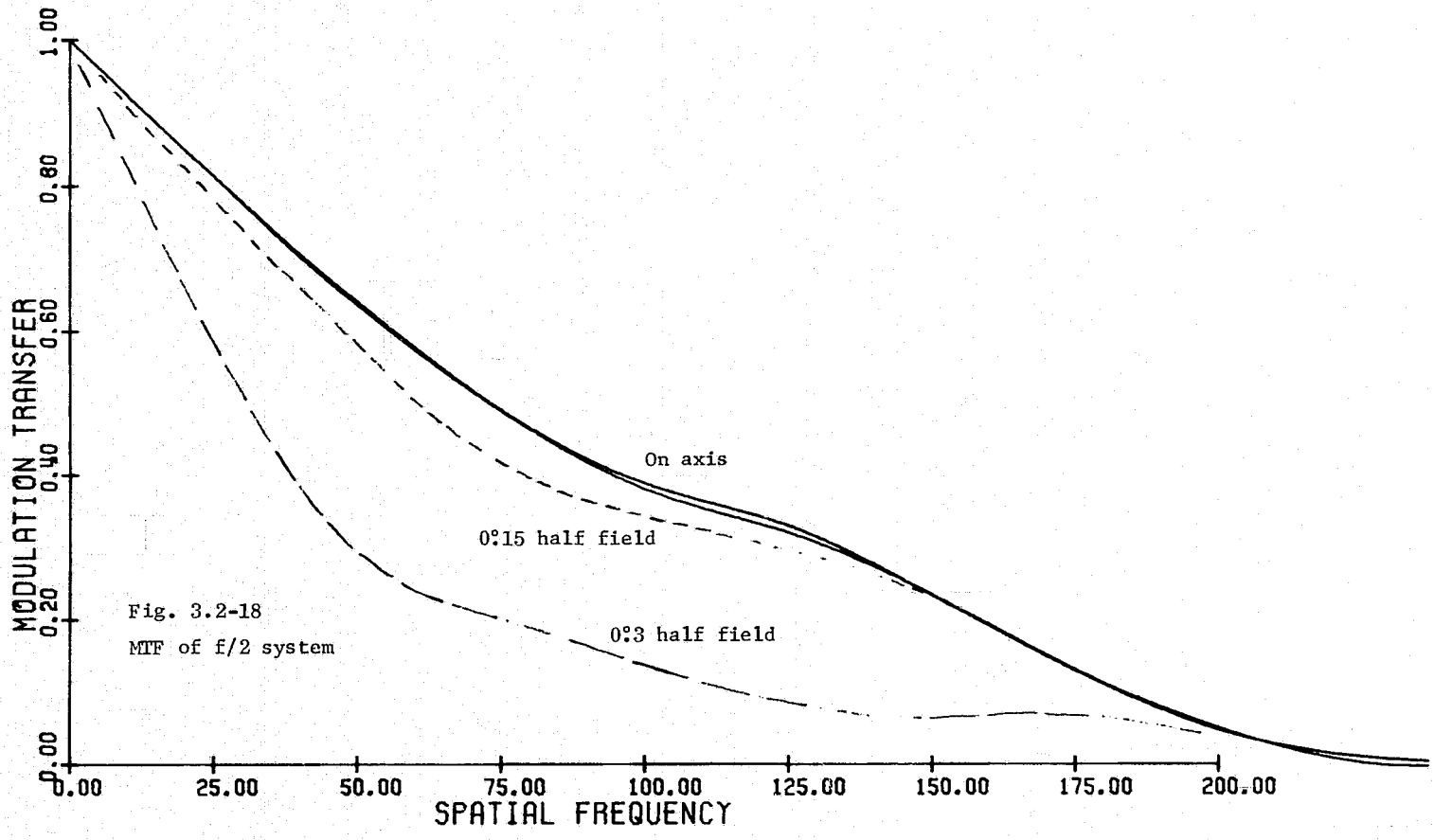

Fig. 3.2-18
MTF of f/2 system

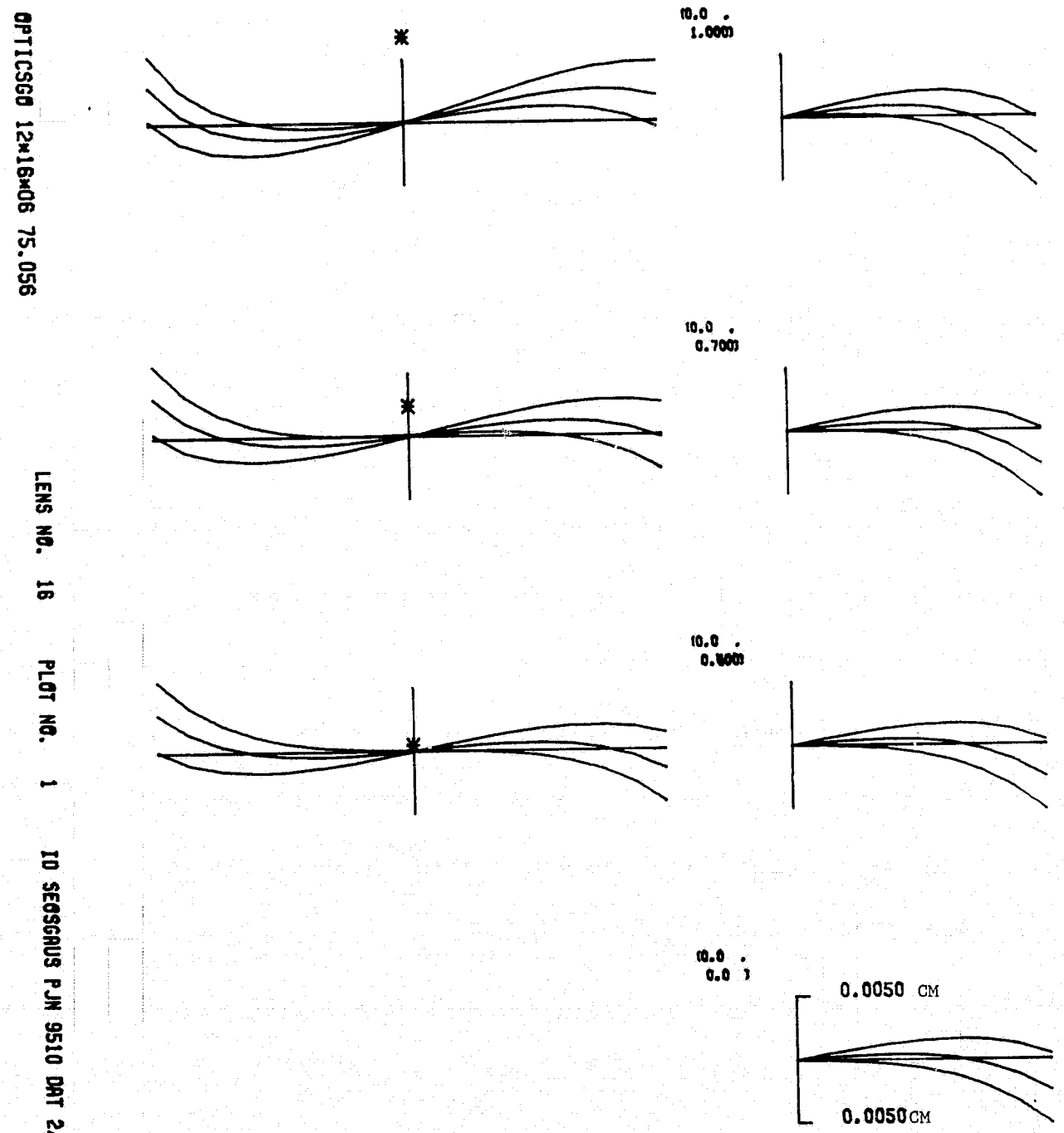

Figure 3.2-19 Ray Trace of F/2 System
1.58-1.68μm, 0°3 Half Field

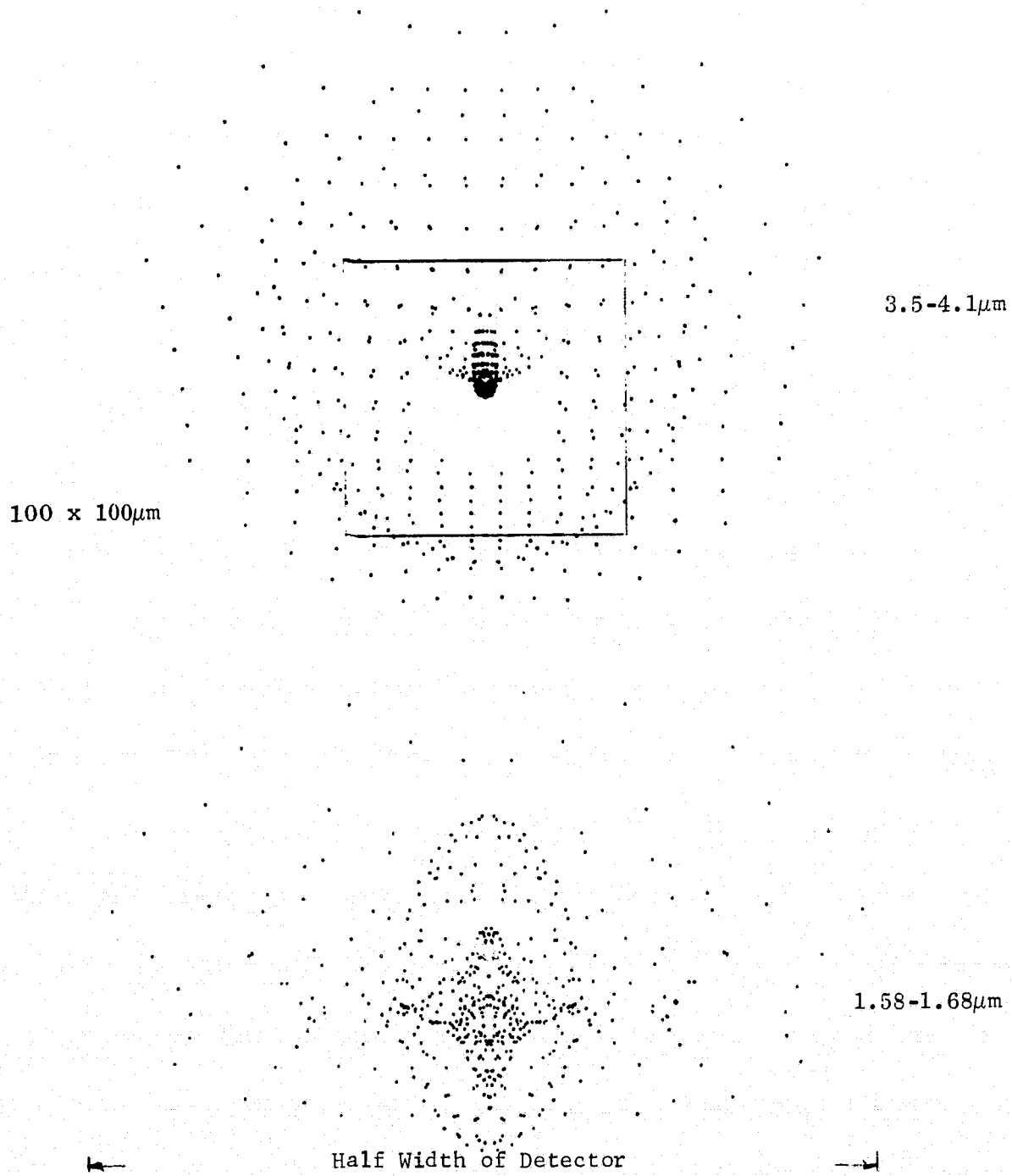

Fig. 3.2-20 Spot Diagram of f/2 system, 0°3 Off Axis

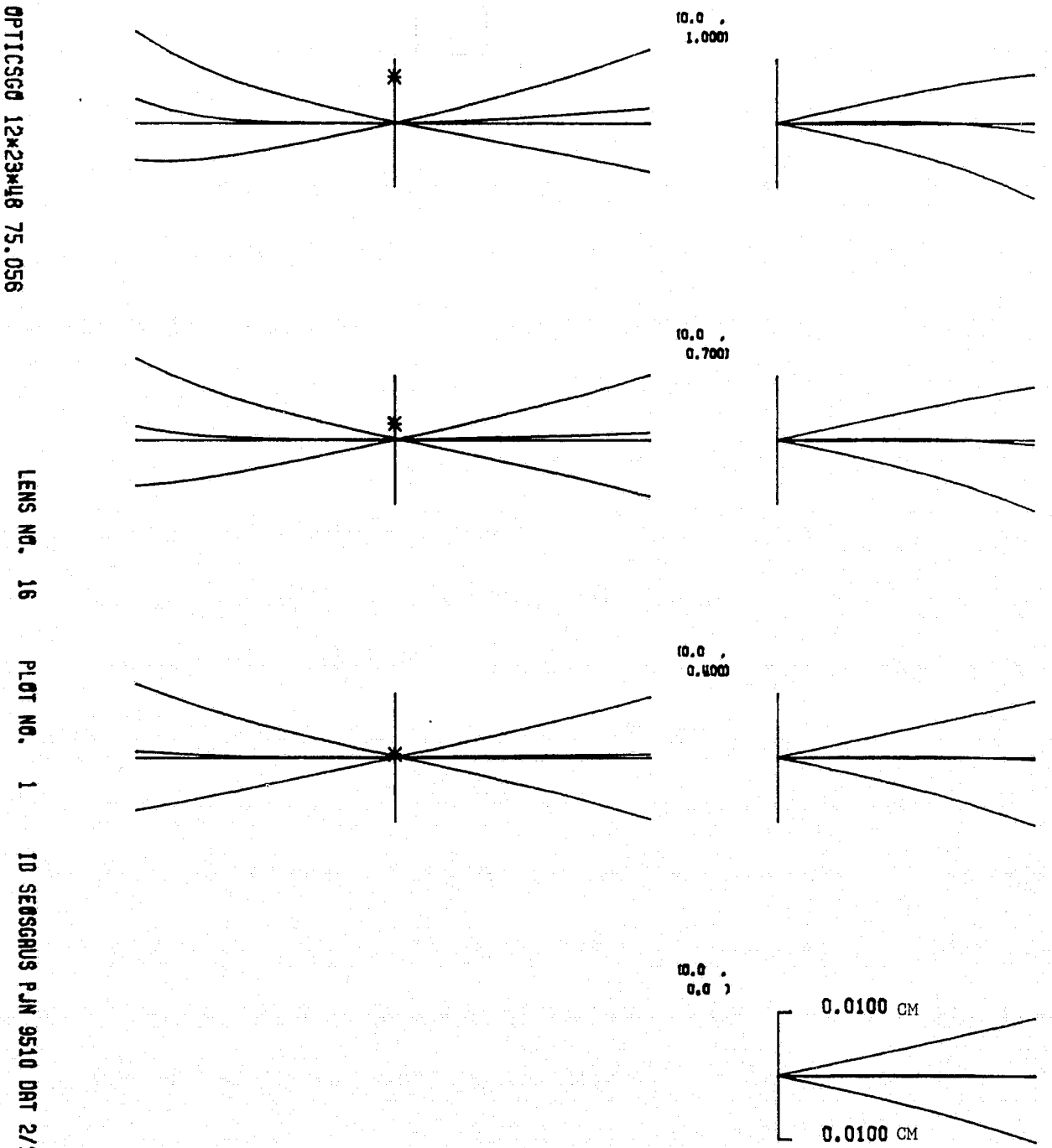

Figure 3.2-21 Ray Trace of f/2 System
3.5-4.1μm, 0°3 Half Field

aberrations get out of control. We have examined variants on the f/5.0 one mirror relay, adding a second mirror. These have proved unsatisfactory. We have not examined catadioptic designs more than superficially. They appear to require as great a thickness of germanium as the all-refracting design, while having much less desirable dimensional configurations.

Our all-refracting, all germanium approaches followed that of the f/2.0 design, with some changes made to reduce the number of elements. First, the field lens and field corrector have been combined into a single element located about where the aspheric field corrector is in the f/2.0 design. Second, the number of elements in the main lens group has been reduced. Our first attempt at a three-element main lens group proved inadequate. Our second choice, a four-element main refracting group (plus the field lens/field corrector) has proven adequate to give the level of image quality we desire.

Tables 3.2-6 and 3.2-7 give the design data for the preliminary f/1.3 relay design. Fig. 3.2-22 shows the complete relay from f/12 image to f/1.3 image. Note in the design data that all refracting elements have spherical surfaces. Also note that the image surface is curved.

Figs. 3.2-23 through 3.2-28 give performance data in the form of transverse aberration plots plus spot diagrams at 0.43° off-axis, 0.30° off-axis and on-axis. Data is given for five spectral bands, 10.3 - 11.3 μm, 11.3 - 12.0 μm, 12.0 - 12.9 μm, 6.5 - 7.1 μm, and 3.5 - 4.1 μm. Table 3.2-8 shows RMS wavefront error for each of these spectral bands as well.

The detector element size is 30 x 30 μm for all spectral bands except the 3.5 - 4.1 μm, which has a 100 x 100 μm detector. In general, most of the rays at each wavelength fall within the detector element size, except for small amounts of flare. The image quality can probably be improved significantly with further design effort. Note, for example, that the transverse aberration plots indicate a residual of spherical aberration. Addition of one or two aspheric surfaces near the image of the stop, say on surfaces 8 and 9 (as numbered in table 3.2-6) would allow this aberration to be reduced significantly, if not eliminated.

Chromatic aberrations are very small at the longest wavelengths. Axial color is more apparent at 6.5 - 7.1 μm, but is still negligible. At 3.5 - 4.1 μm, a considerable amount of axial color is present. It is still tolerable within the larger detector size used at this wavelength, however. Thus this design approach appears completely feasible in terms of image quality, and can cover spectral bands down to 3.5 - 4.1 micrometers. Image quality can be improved somewhat, with further design effort.

Transmittance is a question, still. It is desirable to make the germanium elements as thin as possible to minimize internal absorption of light. The preliminary design uses nominal thicknesses of 1.4 centimeters for the field lens/field corrector, and 0.4 centimeters for each of the other elements, the total thickness being 3.0 cm. Germanium is an extremely stiff material, however, and can be made in thinner elements than normal glass. We therefore briefly looked at the possibility of reducing elements thickness to give a total thickness of 2.4 to 2.5 centimeters. The resultant performance is indicated by the rms wavefront errors of Table 3.2-9. Performance of the nominal design and the thinner element design are quite comparable for on-axis and full-field images at all wavelengths. There is a slight deterioration at intermediate image heights. All of these can be improved with further iterations of the design.

Table 3.2-6 Lens Deck for F/1.3 Relay

```
ID SEOSTRIP PJN 9510 DAT 2/17/75
LENS NO.   39
DRAT 11 2 1 3 4 5
CS 2 3 2 1 3 2
APS  2
WV 1.0300000D+01 1.1600000D+01 1.2900000D+01 1.1000000D+01 1.2200000D+01
CF  1.0000000D+04 SF  2.5000000D-03
OBJ B    1.0000000D-15    7.4200000D-03    7.0000000D+01   -1.3397226D+00
  0 CV    0.0              AIR
  1 CAI    2.2000000D+01
  1 CV    0.0             TH    1.8055560D+02  AIR
  2 PTH   -1
  2 PIN   -1
  2 RD   -4.2000000D+02
  2 CC -9.545182D-01
  3 YMT    0.0
  3 AIR
  3 RD   -6.7301600D+01
  3 CC -1.197707D+00
  4 CV    0.0             TH    2.0000000D+01  AIR
  5 N15     4.00298000     4.00238000     4.00214000     4.00261000     4.00223000
  5 TH    1.4000000D+00
  5 RD    4.8435211D+01
  6 CV    1.3547275D-02 TH    4.9754458D+01  AIR
  7 PIN    5
  7 TH    4.0000000D-01
  7 RD    6.9357952D+00
  8 CV    1.0746237D-01 TH    2.1808743D+00  AIR
  9 PIN    5
  9 CV   -1.3059008D-01 TH    4.0000000D-01
 10 CV   -1.1040992D-01 TH    2.7413179D+00  AIR
 11 PIN    5
 11 CV    1.6264917D-01 TH    4.0000000D-01
 12 CV    8.8139394D-02 TH    4.0603328D-01  AIR
 13 PIN    5
 13 CV   -6.4456899D-02 TH    4.0000000D-01
 14 YMT    0.0
 14 CV   -5.7695325D-02  AIR
 15 CV   -8.8200660D-02
END
```

PRELIMINARY DESIGN
NOT TO BE USED
FOR FABRICATION

Table 3.2-7 Design of F/1.3 Relay

LENS NO. 39 LENS OUTPUT DATA

SYSTEM DATA

F-NUMBER =	-1.3047159	ENTRANCE PUPIL DISTANCE =	180.5556000
FOCAL LENGTH =	-182.6602320	EXIT PUPIL DISTANCE =	-9.9779892
BACK FOCUS =	2.0995127	GAUSSIAN IMAGE HEIGHT =	-1.3553399
TOTAL LENGTH =	315.7345963	DP/DV =	0.0
OBJECT HEIGHT =	-0.519D+15	AXIAL BEAM RADIUS =	70.0000000
CHIEF RAY ANGLE =	0.0074200	CHIEF RAY HEIGHT =	-1.3397226
AXIAL RAY ANGLE =	0.0000000		

WAVELENGTHS LOWER ****** MAJOR ****** UPPER ******

SURFACE DATA

SURFACE NUMBER	RADIUS OF CURVATURE	THICKNESS	GLASS TYPE AND/OR NID	V(D)	APERTURE DIAMETER
OBJECT	INFINITE	0.700D+17			
1	INFINITE	180.5556	AIR		144.1062
2	-420.0000	-180.5556	-AIR		141.4876
	CONIC CONSTANT =	-0.9545182			
3	-67.3016	235.5524	AIR		22.5917
	CONIC CONSTANT =	-1.1977070			
4	INFINITE	20.0000	AIR		25.7575
5	48.4352	1.4000	Germanium	0.14	29.7981
6	73.8156	49.7545	AIR		29.5529
7	6.9358	0.4000	Germanium	0.14	4.4024
8	9.3055	2.1809	AIR		4.2219
9	-7.6575	0.4000	Germanium	0.14	3.3835
10	-9.0572	2.7413	AIR		3.5388
11	6.1482	0.4000	Germanium	0.14	4.5575
12	11.3457	0.4060	AIR		4.4605
13	-15.5142	0.4000	Germanium	0.14	4.4310
14	-17.3324	2.0995	AIR		4.4390
IMAGE	-11.3378				

* PAGE

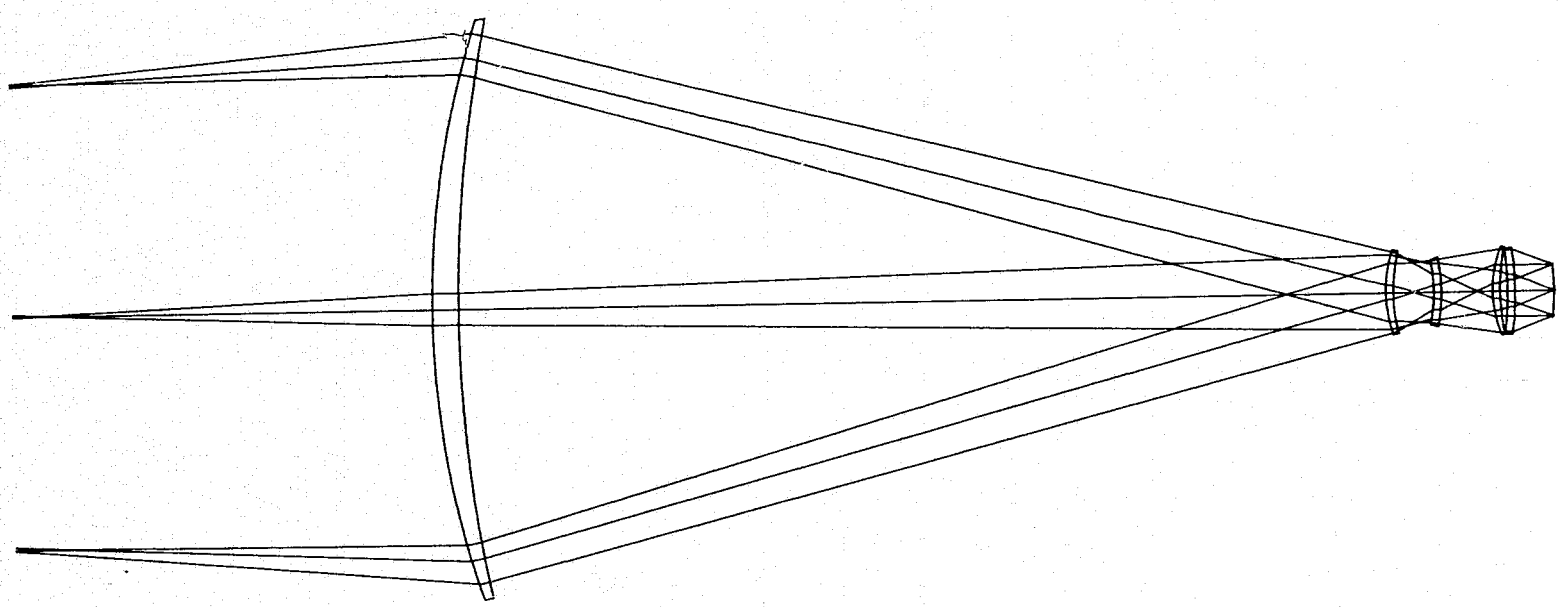

Figure 3.2-22 F/1.3 Relay Design from Intermediate F/12 Image to Output F/1.3 Image. Image size shown is for Diagonal of a 0.6 x 0.6 Degree Field of View

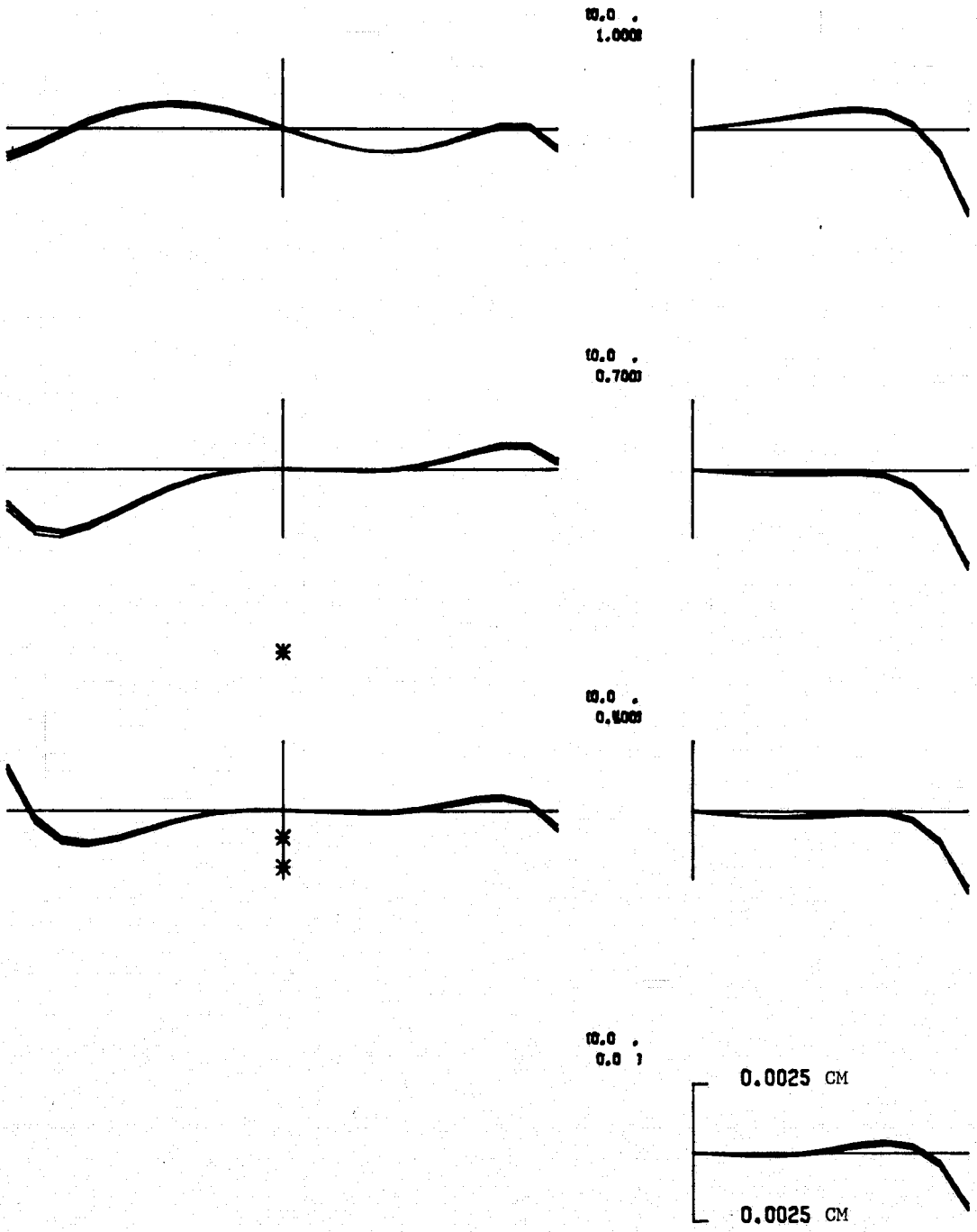

Fig. 3.2-23 Ray Trace of f/1.3 System, 10.3-11.3 μm 0°43 Half Field

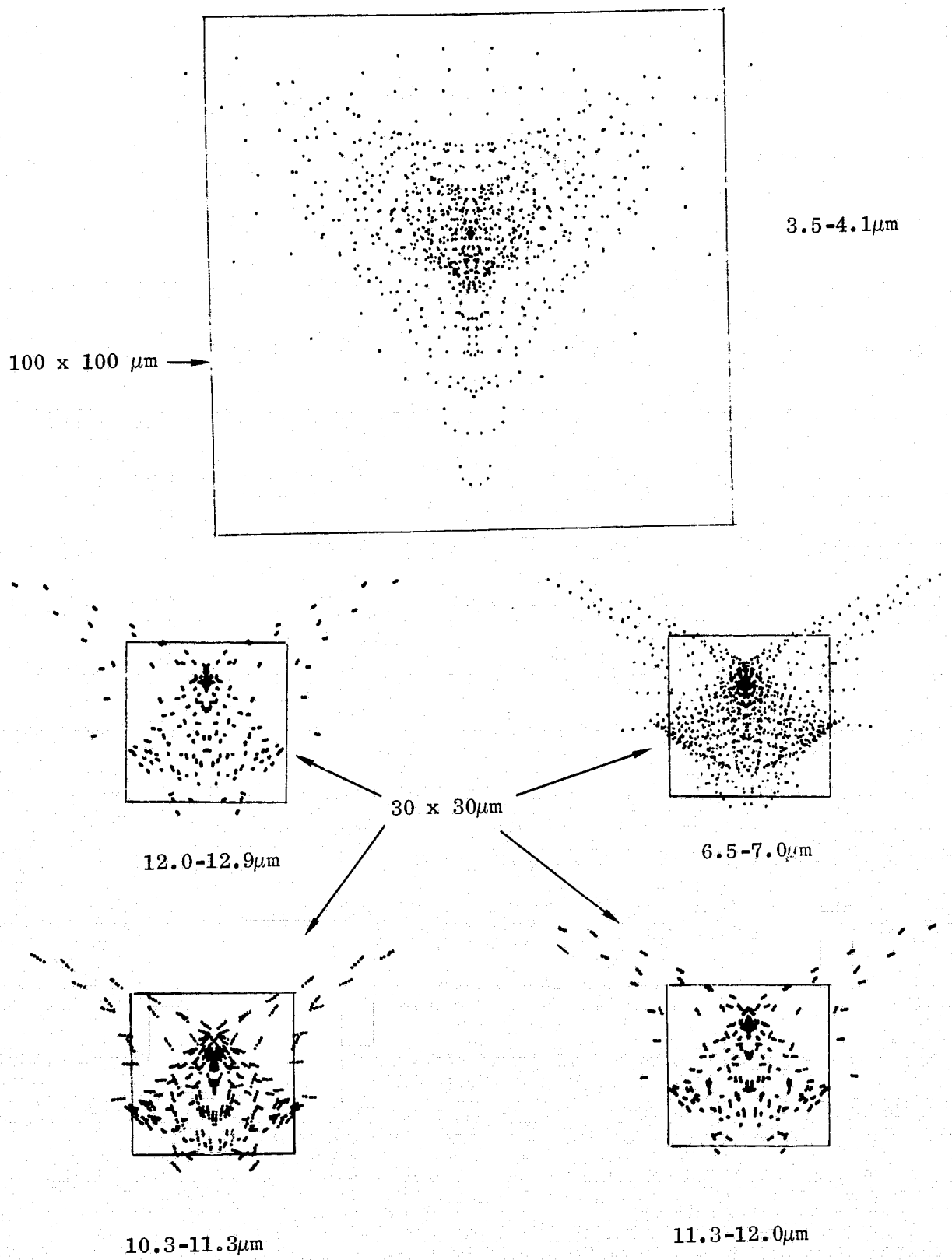

Fig. 3.2-24 Spot Diagrams of f/1.3 System, 0°43 Off Axis

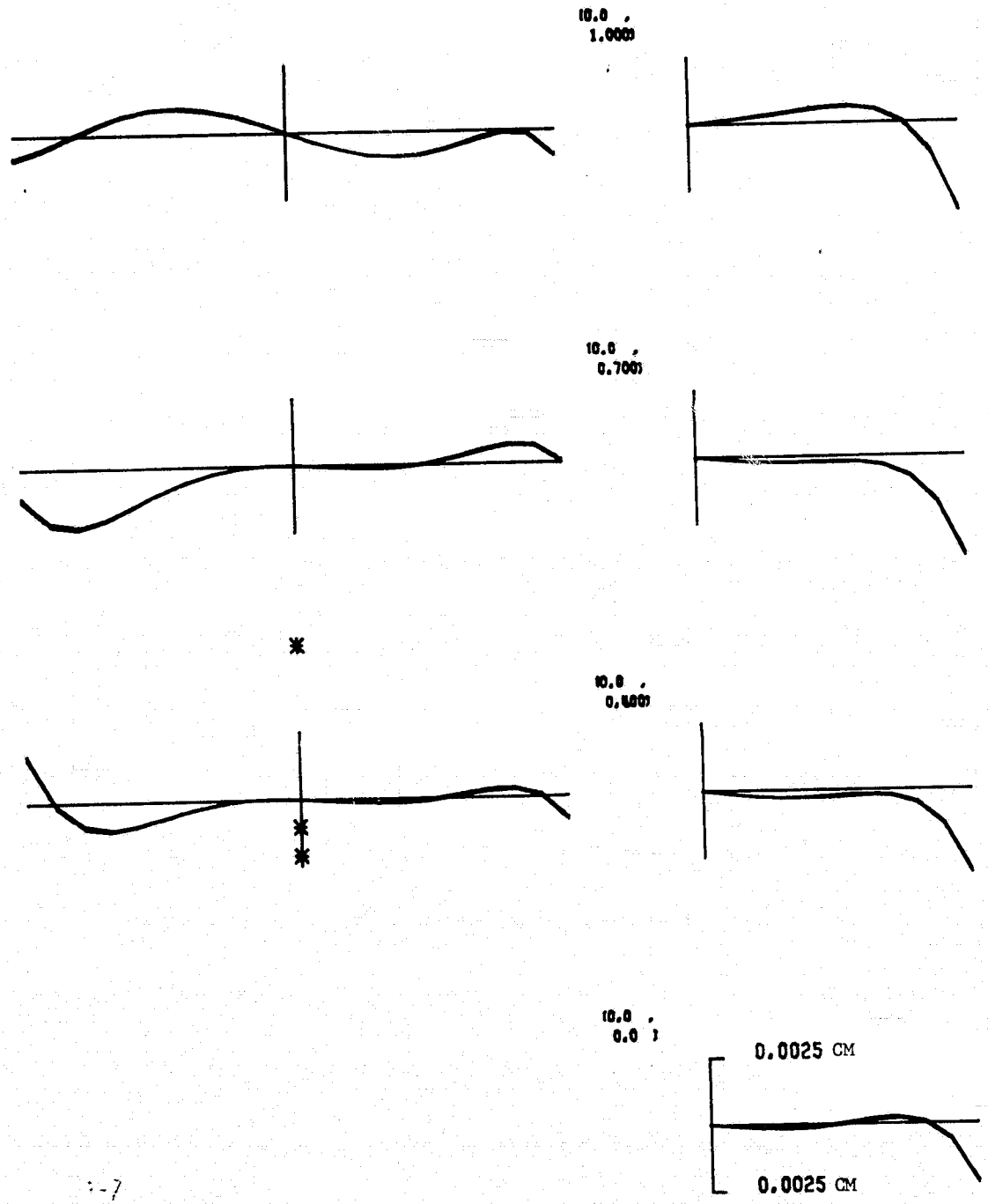

Fig. 3.2-25 Ray Trace of f/1.3 System
11.3-12.0μm, 0°43 Half Field

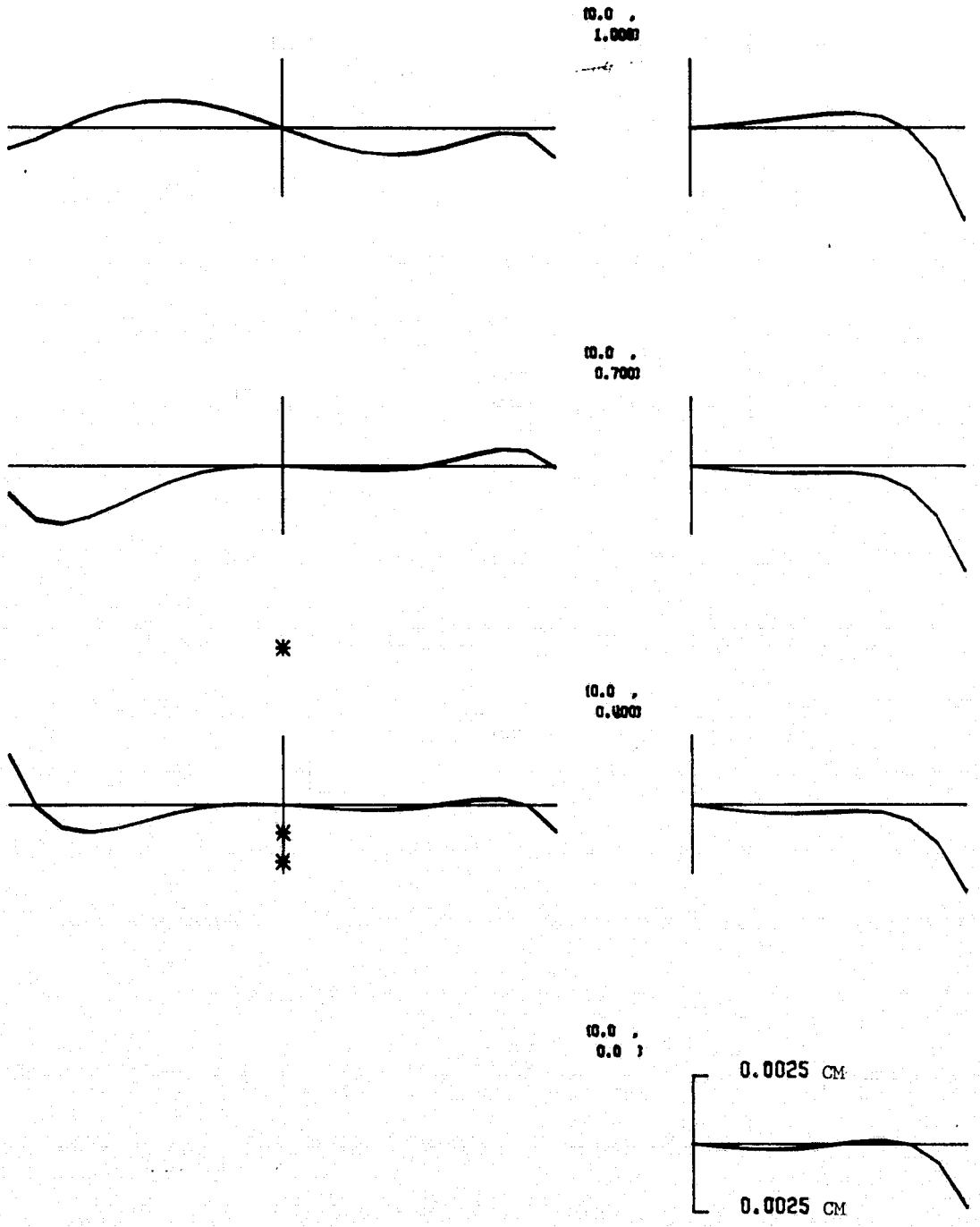

Fig. 3.2-26 Ray Trace of f/1.3 System
12.0-12.6μm, 0.43 Half Field

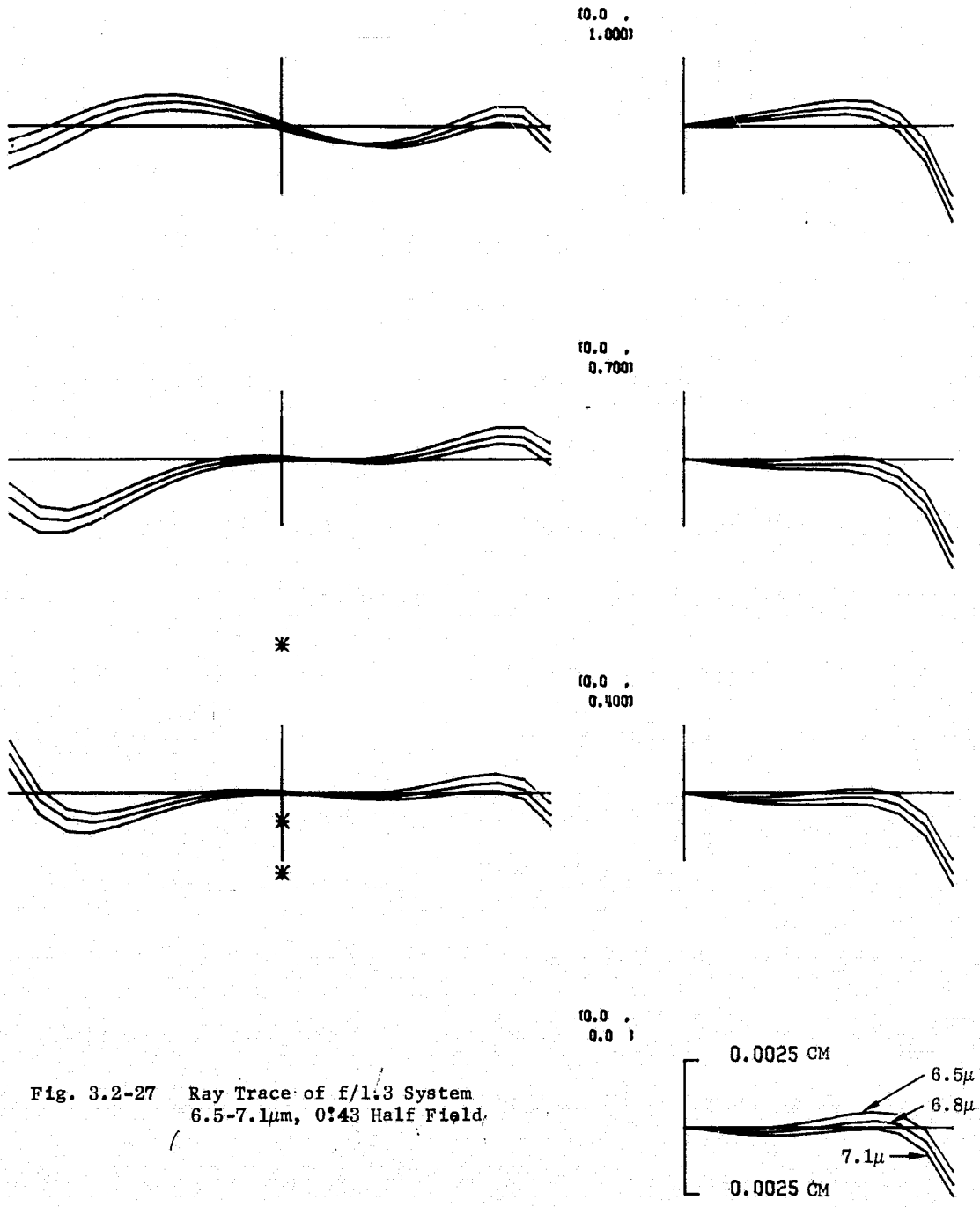

Fig. 3.2-27 Ray Trace of f/1.3 System
6.5-7.1μm, 0.43 Half Field

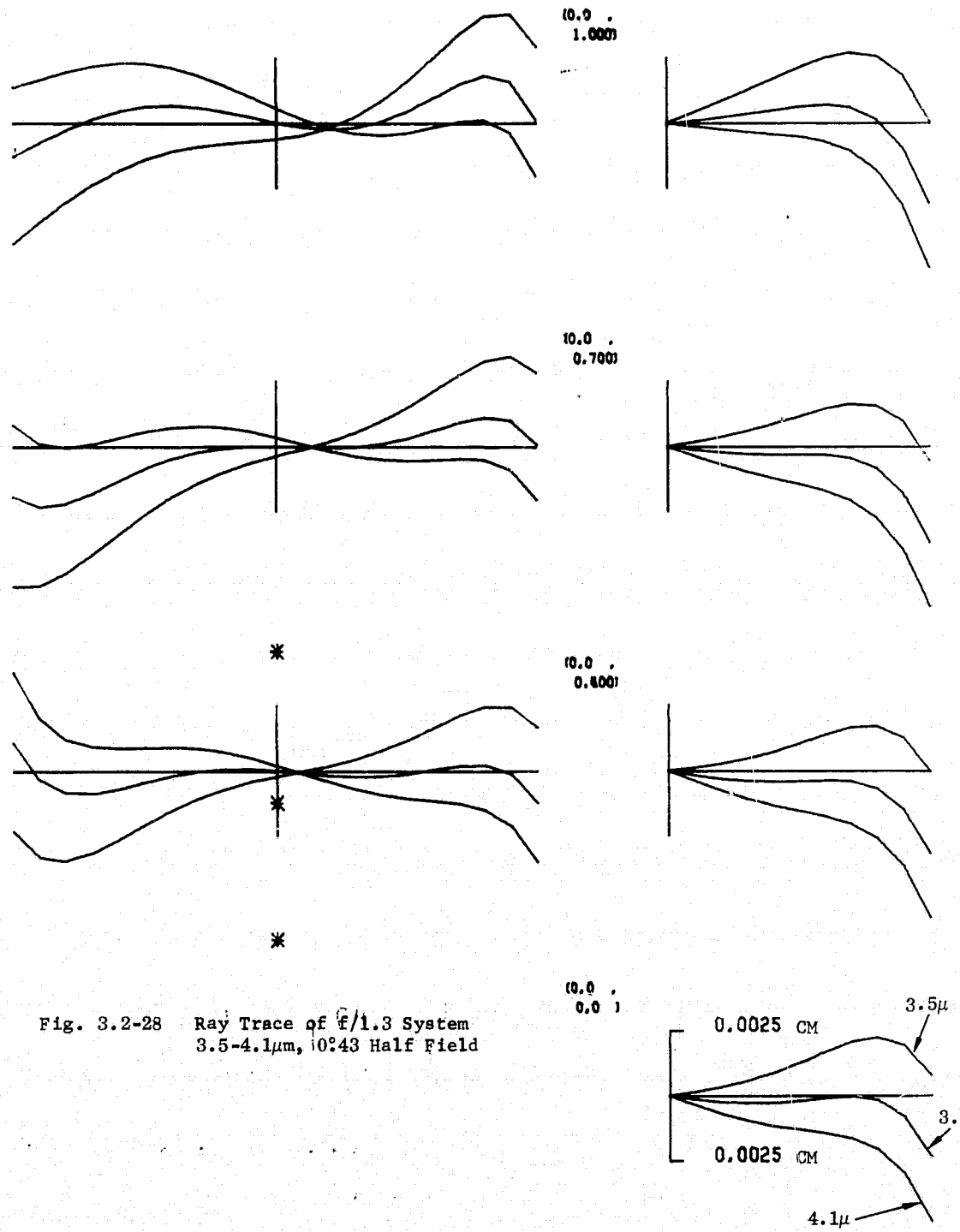

Fig. 3.2-28 Ray Trace of f/1.3 System
3.5-4.1μm, 0°43 Half Field

Table 3.2-8

f/1.3 Wavefront Errors for Preliminary Design in Different Spectral Bands

Band (μm)	Field	Chromatic λ RMS	Band	Field	Chromatic λ RMS
E16, M7	Axis	.012		Axis	.025
10.3-11.3	.17°	.051	M6	.17°	.081
	.30°	.076	6.5-7.1	.30°	.125
	.43°	.090		.43°	.132
E17	Axis	.011		Axis	.193
11.3-12.0	.17°	.047	M5	.17°	.239
	.30°	.071	3.5-4.1	.30°	.314
	.43°	.084		.43°	.282
E18, M8	Axis	.010			
12.0-12.9	.17°	.044			
	.30°	.066			
	.43°	.078			

Band (μm)	Back Focus (cm)
10.3-11.3	2.0967
11.3-12.0	2.0967
12.0-12.9	2.0967
6.5-7.1	2.0890
3.5-4.1	2.0597

Table 3.2-9

f/1.3 Wavefront Errors for Thinner Design

Band	Field	Chromatic λ RMS	Back Focus
10.3-12.9	Axis	.013	1.9531
	.17°	.056	
(10.3, 11.6, 12.9	.30°	.085	
All Eq. Weight)	.43°	.084	
6.5-7.1	Axis	.024	1.9455
	.17°	.096	
	.30°	.147	
	.43°	.129	
3.5-4.1	Axis	.191	1.9171
	.17°	.252	
	.30°	.347	
	.43°	.299	

Total Germ TH. (axial) 2.45 cm

In conclusion, these results indicate that a satisfactory f/1.3 relay design can be made of five elements of germanium, and can cover all far-infrared spectral bands from 3.5 - 4.1 to 12.0 - 12.9 micrometers. The total germanium thickness can be reduced to about 2.4 cm in this design.

3.2.8 Transmission Analysis

The performance analysis of the phase one study assumed an optical system transmittance of 30 percent, including filters and central obstruction. In general, performance calculations indicated that a 30 percent transmittance gives an adequate safety margin for all channels except M5, and that a lower net transmittance can be tolerated on most channels.

The 30 percent figure includes an estimated peak transmittance of 60 percent for the interference filters. The required spectral transmission characteristics for these filters have not been defined in detail at this stage in the SEOS program, other than to give rough bandwidths. The present transmission analysis will therefore continue to assume a 60 percent filter transmittance. The optical system transmittance design goal, exclusive of filters, will therefore be 50 percent.

The central obstruction diameter will be about 44 centimeters, if full baffling is used to keep stray light from striking the f/12 focal surface directly. This gives a central obstruction diameter ratio of 0.314, for an aperture transmittance of 90.1 percent.

There are three other sources of loss in transmittance, the reflectivity of the mirror coatings, the reflections at air-glass boundaries for refracting elements, and bulk absorption within refracting elements. These can be treated separately.

There are three mirrors in the f/5 image train, and these constitute its only optical components. A fourth mirror might be required if the f/5 relay is folded, but it will be ignored here. At least one fold mirror will be required in the f/2 and f/1.3 relays. Thus a minimum of 3 mirrors are required in each optical train.

The primary and secondary mirrors are common to all optical trains, and must therefore reflect well in all wavelengths from 0.42 to 12.9 μm. The choice of coatings for these two mirrors is therefore restricted to two, aluminum with a protective overcoating of SiO_2, or silver with a more complex overcoating. Aluminum is the most common coating, and is rugged, with good aging properties. It has a weak absorption band in the wavelength range 0.8 to 0.9 μm, but the protective overcoating tends to enhance absorption at this wavelength. This absorption band is not present in silver, but silver coatings are not as rugged, and require more complex overcoatings to protect them from corrosion. Such coatings do exist, however, and are practical for smaller mirrors.

In practice, the primary mirror will almost certainly be coated with aluminum, if we are to base our choice on current coating technology. Good protected silver coatings are available on mirrors up to the size of the secondary and tertiary mirrors in the f/5 optical system. Thus our choice is likely to be between three aluminum mirrors and one aluminum plus two silver mirrors. Spectral reflectivity curves for each of these combinations plus single coatings of each material are shown in Fig. 3.2-29. Reflectivities for the aluminum coating are theoretical curves generated by computer. Reflectivities for the aluminum

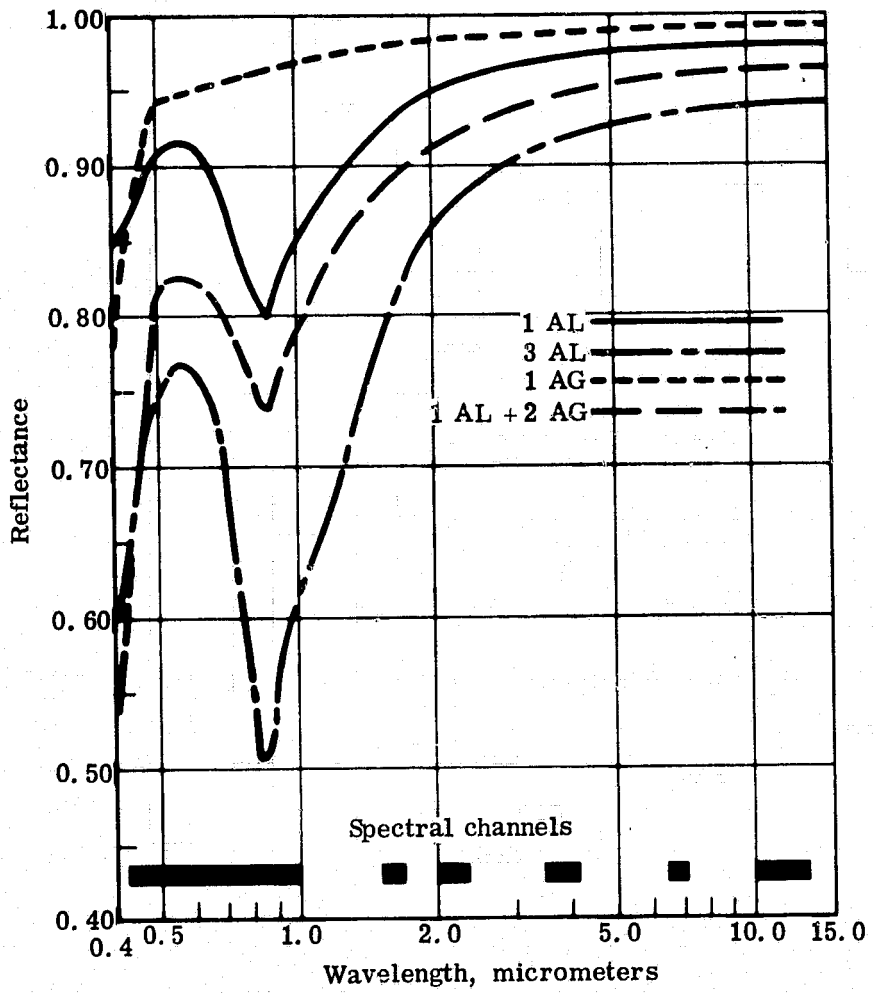

Figure 3.2-29 Reflectivities of Aluminum and Silver Mirrors Singly and in Combination. Aluminum Mirror Overcoated with SiO_x. Silver Mirror Overcoated with Proprietary Protective Coatings.
Aluminum Reflectivities Theoretical.
Silver Reflectivities Measured from Real Sample after 1 Year Aging in Air.

coating are theoretical curves generated by computer. Reflectivities for the protected silver mirror are from measurements on a small sample coating which had been stored in dry air for one year prior to taking the measurements.

The silver reflectivity curve rolls off more rapidly at short wavelengths than the aluminum. The crossover point for the two curves comes in the center of the E1 band, 0.42-0.46 μm. Thus it is questionable which would be superior for the E1 band, three aluminum or one aluminum plus two silver mirror coatings. At longer wavelengths, the latter is clearly superior.

These curves, coupled with the central obscuration factor give the complete transmittances of the f/5 spectral channels. This data has been used to compute channel-by-channel transmittances for the f/5 image. The results are listed in Table 3.2-10. As can be seen, bands M-9 and E11 are marginally below 50% for three aluminum mirrors, but by such an insignificant small value that it is within the range of uncertainties in the measured data. There are no transmission problems with the combination of aluminum and silver mirrors for these channels.

Losses in transmittance due to reflections at air-glass boundaries can be significantly reduced by applying anti-reflection coatings to the surfaces of refracting elements. These coatings may consist of a single quarter-wavelength layer of low index material, or may involve a dielectric stack of two or more layers. In principle, it is possible to approach zero reflectivity over a limited wavelength range with such coatings. Because they depend upon interference, however, it is difficult to suppress surface reflectivities over a spectral range greater than a wavelength ratio of 1.6 to 2.0 X. OCLI does make one special coating for germanium, however, which maintains high reflectivities over a 5:1 range of wavelengths.

We have examined coatings for three materials: zinc sulfide, silicon and germanium. In the first two cases, we have confined our attention to the wavelength region 1.5 to 2.5 μm. With germanium, we have considered the wavelength region 3.0 to 13 μm.

A theoretical calculation for a two-layer anti-reflection coating on zinc sulfide predicts that transmittances for one surface in the 1.58 to 1.68 and 2.05 to 2.35 μm spectral bands range from 0.993 to 0.997. In practice, the actual transmittances will run up to one percentage point lower than this.

Similar calculations for a single-layer anti-reflection coating on silicon predict transmittances range from 0.957 to 1.58 μm to 0.981 at 1.68 μm and from .994 at 2.04 μm to .960 at 2.36 μm. Real values may again be one percent point below this. The calculation curve also illustrates the difficulty of using such coatings for two widely spaced spectral bands. The actual maximum predicted transmittance is 0.995 at 1.90 μm. This could be centered on one of the two bandpasses, but only at the cost of reducing transmittance significantly at the other bandpass. A two-layer coating could also be designed for silicon. It is probably not necessary for the f/2.0 relay, however, since only two silicon elements are included.

Fig. 3.2-30 shows published curves for two OCLI anti-reflection coatings for germanium. In this case, the curves are for a 0.040 inch germanium substrate with a coating on both sides. The lower curve is of most interest to us. Although the high transmittance region extends from 2.0 to about 11 micrometers, it could be redesigned to cover the regions of most interest to us, e.g., 2.5 to 13 micrometers or 3.0 to 16 micrometers. The curve shows three peaks in

Table 3.2-10

Optical System Transmittances
for F/5 Image, Excluding Narrow Bandpass Filters

Channel	Bandpass (μm)	3 Aℓ	Aℓ + 2 Ag
E1	0.42-0.46	.60	.60
E3	0.47-0.52	.67	.72
E4	0.53-0.57	.69	.74
E5	0.56-0.60	.69	.74
E6	0.60-0.65	.67	.74
E7	0.65-0.69	.64	.73
E8	0.70-0.73	.58	.71
E9	0.78-0.82	.51	.68
E11	0.89-0.95	.49	.68
M1	0.55-0.70	.69 – .61	.74 – .72
M2	0.744-0.759	.56	.70
M3	0.7617-0.7663	.55	.69
M9	0.75-1.00	.55 – .46 – .55	.70 – .66 – .72

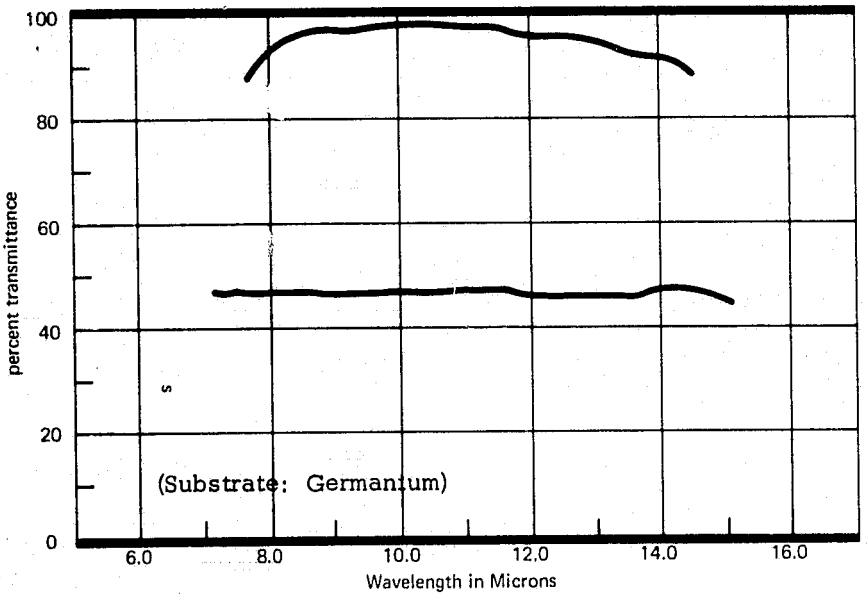

Multilayer Antireflection Coating for the 8μ to 14μ Region

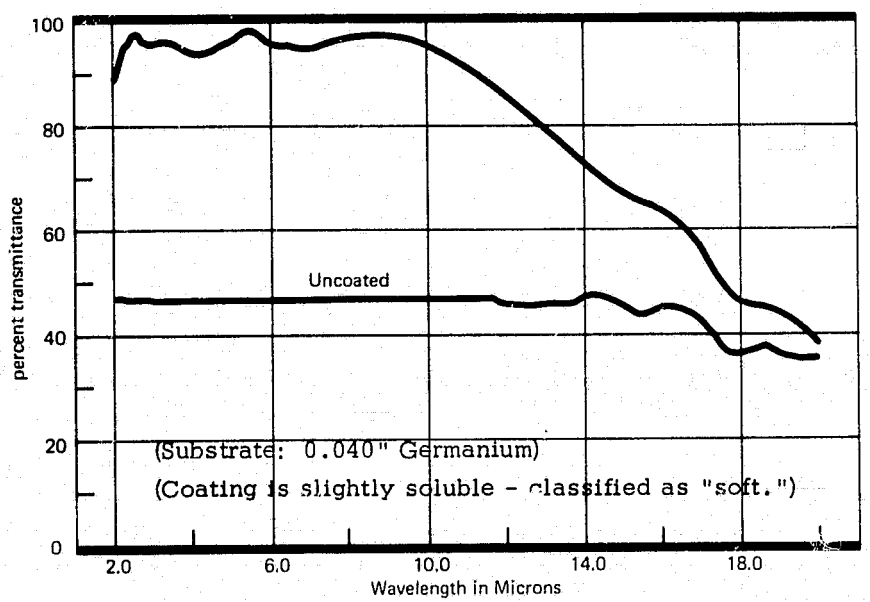

Extremely Wide Band Antireflection Coating

Figure 3.2-30 OCLI Anti-Reflection Coatings for Germanium

transmittance which approach 97 percent. It should be possible to redesign so that at least two of these fall on wavelengths of particular interest, say 6.5 and 11 micrometers. The third band of interest, 3.5 to 4.1 micrometers would then also fall near a peak. It appears, then, that 94-97% is an achievable transmittance per pair of Germanium surfaces.

Reliable bulk transmittance data on infrared materials is hard to obtain. Kodak publishes fairly complete data on the Irtran glasses, but these have such high internal scattering, due to the technique used to manufacture them, that they are useless for our application. We have obtained data on Germanium, which will be discussed below. On zinc sulfide (also known as Irtran 2), and silicon we have had to estimate the absorption coefficient from external transmittance measurements on thin samples.

We have samples of zinc sulfide manufactured by a chemical vapor deposition technique which are about 0.119 inches thick. Measurements on this material indicates an absorption coefficient in the range 0.055 to 0.075 reciprocal centimeters in the 1.58 to 1.68 μm spectral band, and less than 0.015 reciprocal centimeters in the 2.05 to 2.35 μm band. The value of 0.015 represents the limits on accuracy of the measurement process. (These values are more than an order of magnitude less than those given for Irtran II.) Similar measurements for two samples of silicon, 0.042 and 0.254 inches thick, lead to absorption coefficient values of 0.025 to 0.050 reciprocal centimeters of 1.58 to 1.68 μm and 0.015 to 0.025 reciprocal centimeters at 2.05 to 2.35 μm. Note that this range indicates a range of confidence in the data reduction techniques, not a variation with wavelength. It should also be noted that these are specific samples, which may not represent the best which can be obtained.

We have calculated optical system transmittances for the 1.58 - 1.68 and 2.05 - 2.35 μm channels, using the preliminary f/2.0 relay design described in Section 3.2.6. The results are shown in Table 3.2-11. In calculating losses due to surface reflectances and bulk absorption, we have provided a range of values, to represent the error range on our estimated values. The resultant system transmittances fall well within the arbitrary 50 percent goal for the 2.05 - 2.35 μm band, but fall well below that goal for the 1.58 - 1.68 μm band. In that band, however, the 50 percent limit included a safety factor of 2X, so that 25 percent transmittance exclusive of filters might be tolerable. Thus the transmittance of the f/2.0 preliminary design should be tolerable.

There are two possibilities for improving the transmittance. First, use a simpler design. We have shown that a 5-element relay design of germanium is possible for the f/1.3 relay. It may be possible to design a 5-element f/2 relay with three zinc sulfide and two silicon elements. Alternatively, dropping the 3.5 - 4.1 μm channel from this relay opens up the choice of materials again. We might therefore find a combination which have better absorption coefficients than zinc sulfide and silicon.

Table 3.2-12 shows a transmission analysis for a hypothetical five-element, zinc sulfide and silicon design having a configuration similar to that of the f/1.3 relay design. In this case, the 1.58 - 1.68 μm channel will meet the 50 percent transmittance criterion.

Fig. 3.2-31 shows absorption coefficient data for germanium at 300°K. The most significant feature to note here is that germanium has a minor absorption peak at 11.8 μm which can cause serious light losses in the 11.3 - 12.0 μm band. It will be necessary to cool the germanium elements to suppress the emission of

Table 3.2-11

Transmittance for Preliminary F/2
Relay Design (8 Elements) Exclusive of Filters

Band	M4 1.58-1.68μm	E13 2.05-2.35μm
1. Central Obstruction	.901	.901
2. Mirrors (Aℓ-Ag-Ag)	.88	.92
3. 6 Zinc Sulfide Elements		
a. 12 surfaces	.844-.953	.834-.942
b. Bulk Absorption (6.7 cm)	.605-.692	.904-.967
4. 2 - Silicon Elements		
a. 4 surfaces	.849-.885	.885-.922
b. Bulk Absorption (2 cm)	.905-.951	.951-.970
	.311-.440	.526-.675

Table 3.2-12

Transmittance for Hypothetical
Optimized F/2 Design (5 Elements),
Exclusive of Filters

	1.58-1.68μm	2.05-2.35μm
1. Central Obstruction	.901	.901
2. Mirrors (Aℓ-Ag-Ag)	.88	.92
3. 3 - Zinc Sulfide Elements		
a. 6 - Surfaces	.919-.976	.913-.970
b. Bulk Absorption	.848-.886	.918-.989
4. 2 - Silicon Elements		
a. 4 - Surfaces	.849-.885	.885-.922
b. Bulk Absorption (0.8 cm)	.961-.980	.980-.988
	.504-.595	.635-.724

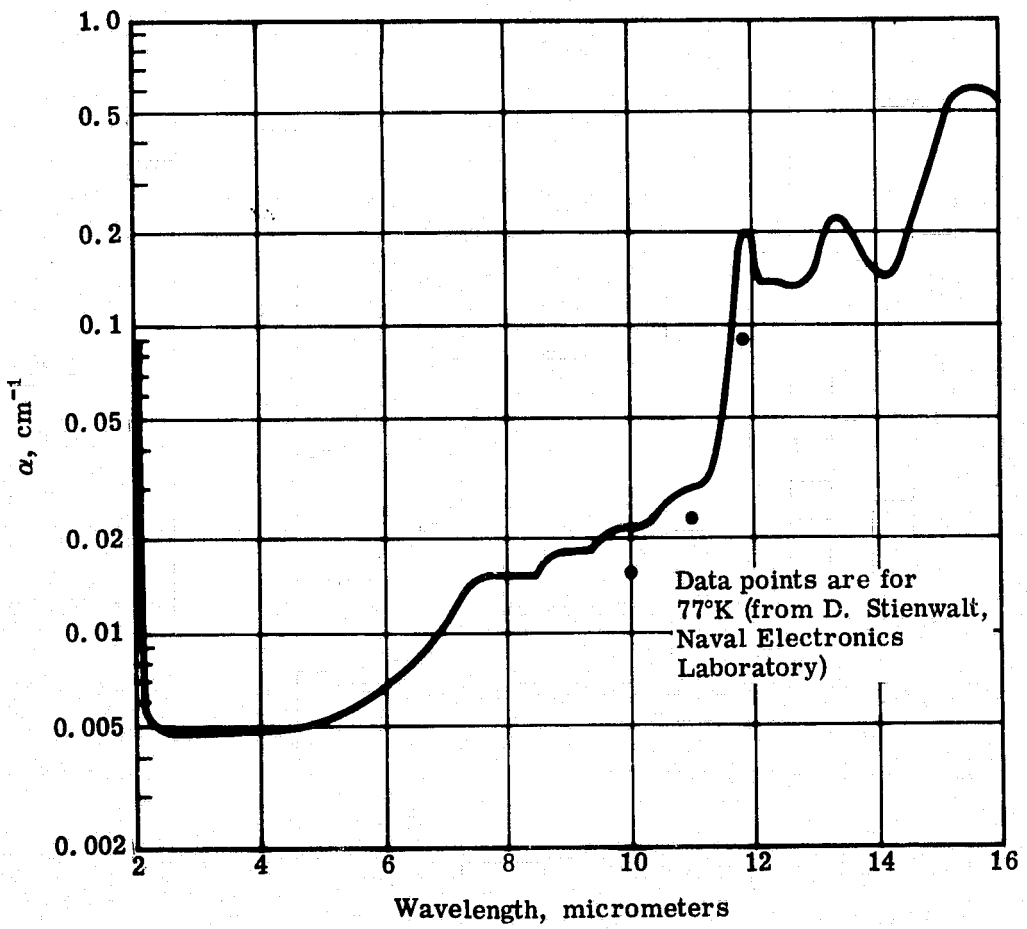

Figure 3.2-31 Absorption Coefficient at 300°K of Optical Grade Germanium

black body radiation due to this factor. This also lowers the absorption coefficient, as indicated by the data points added to the graph from data supplied by Don Stierwalt of the Naval Electronics Laboratory center at San Diego.

In Table 3.2-13, we have used this data to compute the transmittance for the f/1.3 relay in 5 different spectral channels. This assumes 94-97% "transmittances" per pair of surfaces, plus 2.4 centimeters of germanium. These results indicate that the criterion of 50 percent transmittance, exclusive of filters, can be met in all bands, if the germanium is cooled.

Tables 3.2-10 through -13 list ranges of optical transmission, exclusive of spectral filters. Our calculations of performance in Section 5 require that we adopt a total transmission value for each of the twenty-two bands. To do this we have taken the lower end of each transmission range in the tables, and have assumed a 60% filter transmission. The resulting products provide the system transmissions that appear in Table 5.3-1.

3.2.9 Stray Light Control

A complete baffling design for stray light control requires analysis of the amount of stray light which can be tolerated for each channel, and the amount of stray light entering the telescope. Our comments on stray light control will be of a general nature.

Our recommended optical configuration lends itself well to suppression of stray light, because all image sensors are located at the end of relay trains. This, coupled with the fact that the field-of-view consists of separated slit images, allows stops to be used effectively to control stray light. The absence of refracting elements ahead of the intermediate image further reduces the amount of stray light, since they cannot be illuminated directly except by image forming light, and thus cannot scatter stray light.

A conservative approach to baffle design calls for inclusion of baffle cones on the primary and secondary mirrors, as shown in Fig. 3.2-32. These prevent stray light from reaching the intermediate image without first having experienced one or more diffuse reflectances off black-painted surfaces. The cones we have selected lead to a central obstruction of 44 centimeters diameter. A more complete stray light analysis may indicate that smaller baffle cones are acceptable.

The division of the total field-of-view into separate slit images makes it possible to incorporate field stops at the intermediate image, as shown schematically in Fig. 3.2-33. Such stops are very effective at reducing the amount of stray light reaching the output image. The exact nature of these stops depends on the distance by which the slit images are separated, the focal ratio at the intermediate image, and the folding mirror geometries used ahead and or behind the intermediate image.

The only major source of stray light which cannot be controlled by baffling is light scattered by the primary mirror. If the stray light striking the primary is from the earth, normal quality surface finish on the mirror will be enough to reduce scattered light to acceptable levels. If sunlight strikes the mirror directly, for example when viewing the earth's night-side surface, scattering may be a problem. The seriousness of the problem depends on which wavelength channels are being operated, and the fraction of the mirror area which is illuminated by sunlight.

Table 3.2-13 Transmittances for F/1.3 Relay, Excluding Filters

	M5 3.5-4.1μm	M6 6.5-7.0μm	E16, M7 10.3-11.3μm	E17 11.3-12.0μm	E18, M8 12.0-12.9μm
1. Central Obstruction	.901	.901	.901	.901	.901
2. Three Mirrors (Aℓ-Ag-Ag)	.94	.95	.96	.96	.96
3. Germanium Elements					
a. 5 Surface Pairs at 94-97%	.734-.859	.734-.859	.734-.859	.734-.859	.734-.859
b. Bulk Transmittance (2.4 cm)	.989	.977	.933-.946*	.619-.812**	.715-.829**
	.615-.720	.614-.718	.592-.703	.393-.603	.454-.616

* Uncooled (300°K) vs. Cooled (77°K)
** Uncooled vs. Cooled at worst absorption band, 11.8-12.0μm.
Bulk transmittance significantly better 11.0-11.5μm (.88-.93)

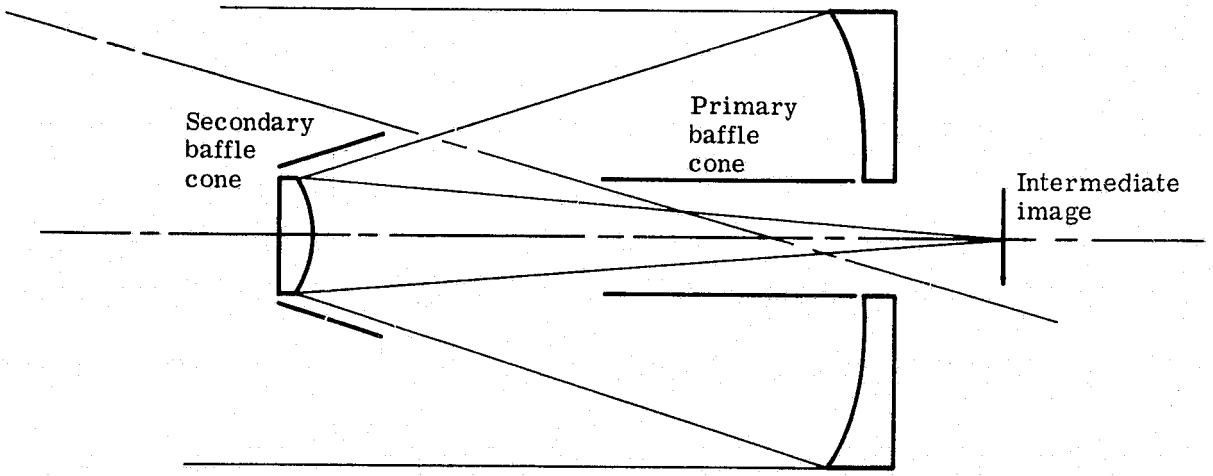

Figure 3.2-32 Standard Baffle Cones to Prevent Stray Light from Reaching Image Directly

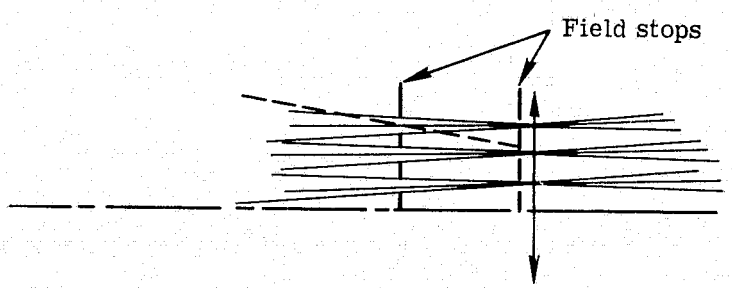

Figure 3.2-33 Field Stops for Slit Images, to Minimize Coupling of Stray Light into Relay Optics

In principal, this scattering may be suppressed by superpolishing the primary. In practice, it will be necessary to do a quantitative analysis of the tolerable stray light levels and the particular operational situation before specifications can be made on how well the primary mirror must be polished.

3.3 THERMAL DESIGN

The Phase 1 Final Report presented a preliminary allocation of thermo-optical errors and associated thermal requirements for the telescope. During Phase 2, error sources were further identified and quantitatively stated, a thermal nodal model of the telescope was developed and run for the case $\beta = 0$, and thermo-optical errors due to both soaks and gradients (including effects of solar flux through the aperture) were calculated over a complete orbit.

Results show that the maximum wavefront error due to thermal effects in the telescope is 0.031λ rms. This error is expected to increase at other times of the year, but is not expected to exceed the total allocation of 0.045λ rms. To this must be added an allowance for thermal effects in the relay systems. This should be fairly small because the relays are housed in an essentially isothermal area behind the primary mirror. We therefore expect to achieve the error budgets outlined in Section 3.1.2.

3.3.1 Thermal Control Requirements

The total operational system wavefront error for LEST is budgeted in Fig. 3.1-3. That portion allocated to thermal effects in the telescope is 0.045λ rms. Three major components contribute to the thermal error of the telescope: metering structure, primary mirror, and secondary mirror. Error sources associated with each component are shown in Fig. 3.3-1 with thermo-optical sensitivities of each contributor.

A uniform soak of the metering structure results in primary-to-secondary despacing, effects of which are wholly restored by refocussing. Tilt and decenter of the secondary relative to the primary mirror are due to diametral gradients across the structure and are only partially correctable by refocussing. Inhomogeneity in expansion coefficient of the metering structure results in primary-secondary misalignment which also is only partially refocussable. That portion which remains after refocussing was estimated to be $0.00034\lambda/°C$ rms wavefront error and is based on $\Delta\alpha = .008 \times 10^{-6}/°C$.

Effects of uniform soak and axial gradients on the primary and secondary mirrors are correctable by refocussing. If, however, axial gradients are not uniform (e.g., lateral variation in axial temperature gradients), varying curvatures are introduced in the element and this effect is not totally refocussable. The residual error in this case depends on both the magnitude and the shape of the varying gradient. Estimates were derived by fitting a best sphere to a composite of calculated local curvatures. The sensitivity to radial gradients shown is an estimate of the residual error after refocussing. Inhomogeneity in expansion coefficient for an optical element produces a figure change when the element is operated at a temperature different from the figuring temperature. Estimates of this effect are based on the work of Friedman[11] and Gasser which involved thermo-optical testing of a 1.8 meter lightweight mirror.

The goal for the thermal design of LEST is to meet the error budget requirements with reasonably long intervals between refocussings. Refocussing intervals do not appear to be a problem but should be investigated in subsequent studies.

FIG. 3.3-1 THERMAL CONTROL REQUIREMENTS FOR TELESCOPE

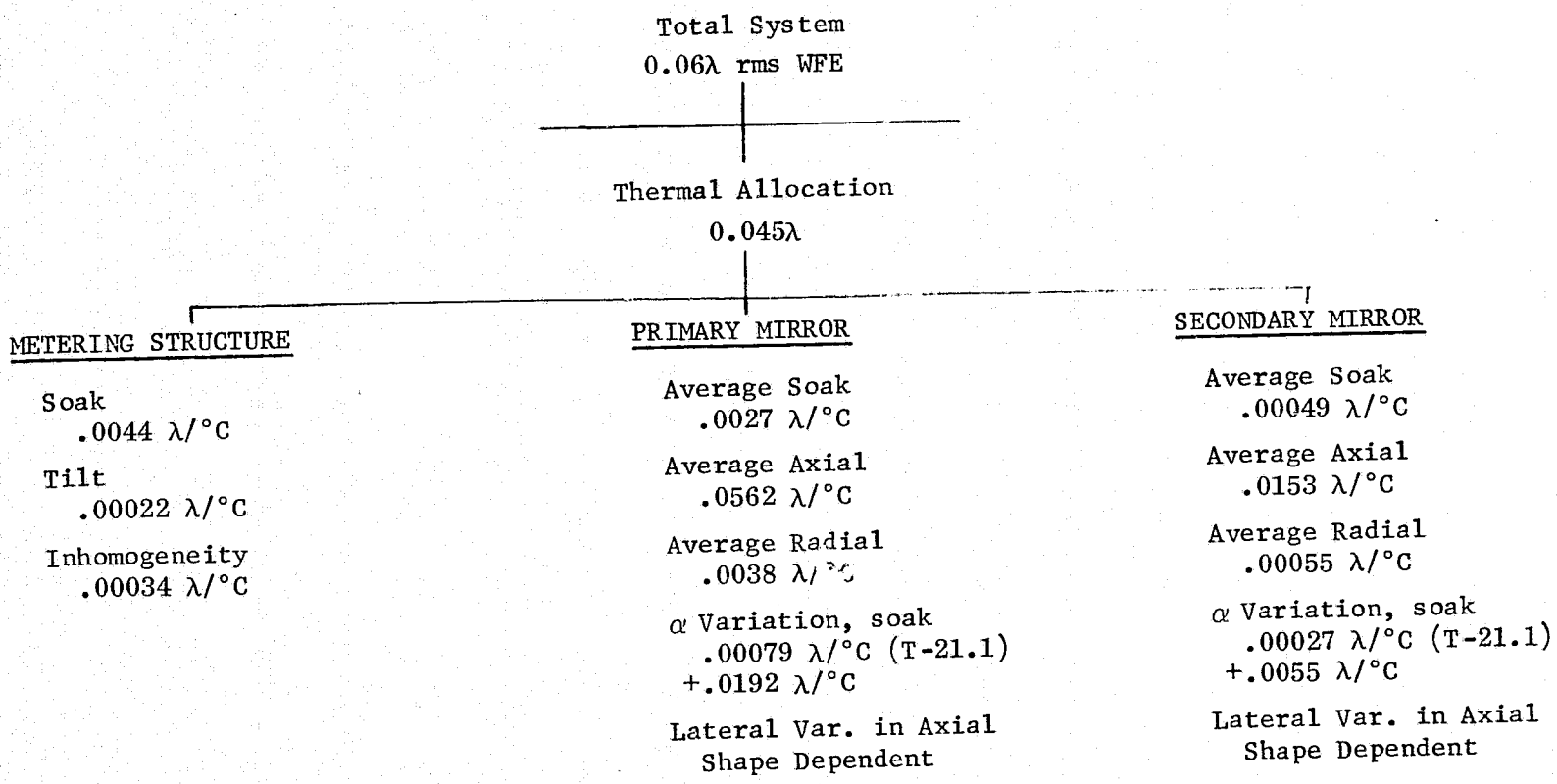

NOTE: Metering structure effective expansion coefficient – $0.1 \times 10^{-6} \frac{m}{m\ °C}$

3.3.2 Baseline Thermal Control Concept

The baseline thermal control concept for LEST includes low expansion material for the primary and secondary mirrors to limit surface distortions caused by thermal gradients. Heaters are used to control the temperature of these elements at 30°C since this is the level which is closest to the mirror figuring temperature and still allows for positive control over most of the 24 hour period. The figure change due to inhomogeneities over the 20 to 30°C range is included in the error budget.

A graphite-epoxy metering shell is used to minimize secondary mirror misalignment due to diametral temperature gradients. Super-insulation is used to limit shell and mirror temperature excursions and gradients. The relatively low α_s/E of .25/.88 was used in the analysis to help maintain positive heater control throughout the year.

Salient features of the thermal control system are shown in Fig. 3.3-2.

3.3.3 Analytical Model and Boundary Conditions

An existing 175-node thermal analytical model was modified for LEST to predict telescope transient temperatures during an orbit. The model simulated operation of the baseline thermal control system and contained 372 conduction connections and 1,955 radiation connections. Internal tube radiation connections were calculated with a view factor program that accounts for the specularity of the primary mirror and also blocking surfaces such as baffles and the secondary mirror. Energy transport within the mirrors includes effects of specular reflections in the core between front and back plates.

Solar fluxes were calculated using an orbital heat rate program and were applied to all external surfaces for the case $\beta = 0$. In addition, incoming solar fluxes through the aperture were apportioned to internal tube surfaces as a function of time in orbit. Thermo-optical degradation of the primary mirror may increase for other β angles which produce longer exposures of this element to solar flux.

3.3.4 LEST Temperature Histories

Typical results from the thermal analytical model are shown in Figs. 3.3-3 and 3.3-4. The first figure shows the temperature response of three axial nodes near the periphery of the primary mirror over one complete orbit. At time zero (true anomoly $\equiv 0°$), the solar vector is behind the vehicle. Active control of the backplate occurs at 8.0 hours. At this time, the axial gradient is about 3.3°C. Solar flux, first incident on the primary at about 10 hours, produces a maximum axial gradient of 4.5°C after exit from the earth's umbra. Although the backplate exceeds 30°C by a few degrees, calculations show that thermo-optical errors stay well within allowable limits.

Temperature histories of four nodes on the graphite-epoxy metering shell are shown in Fig. 3.3-4. These nodes are located circumferentially near the primary mirror and give an indication of the variation of diametral gradient with time. Good radiative coupling limits the maximum gradient at this location to less than 5.5°C. The temperature excursion of the shell, however, is substantial (about 140°C) and is a major contributor to the total thermo-optical error of the telescope. Even so, the total error budget shows that such a large temperature excursion can be tolerated.

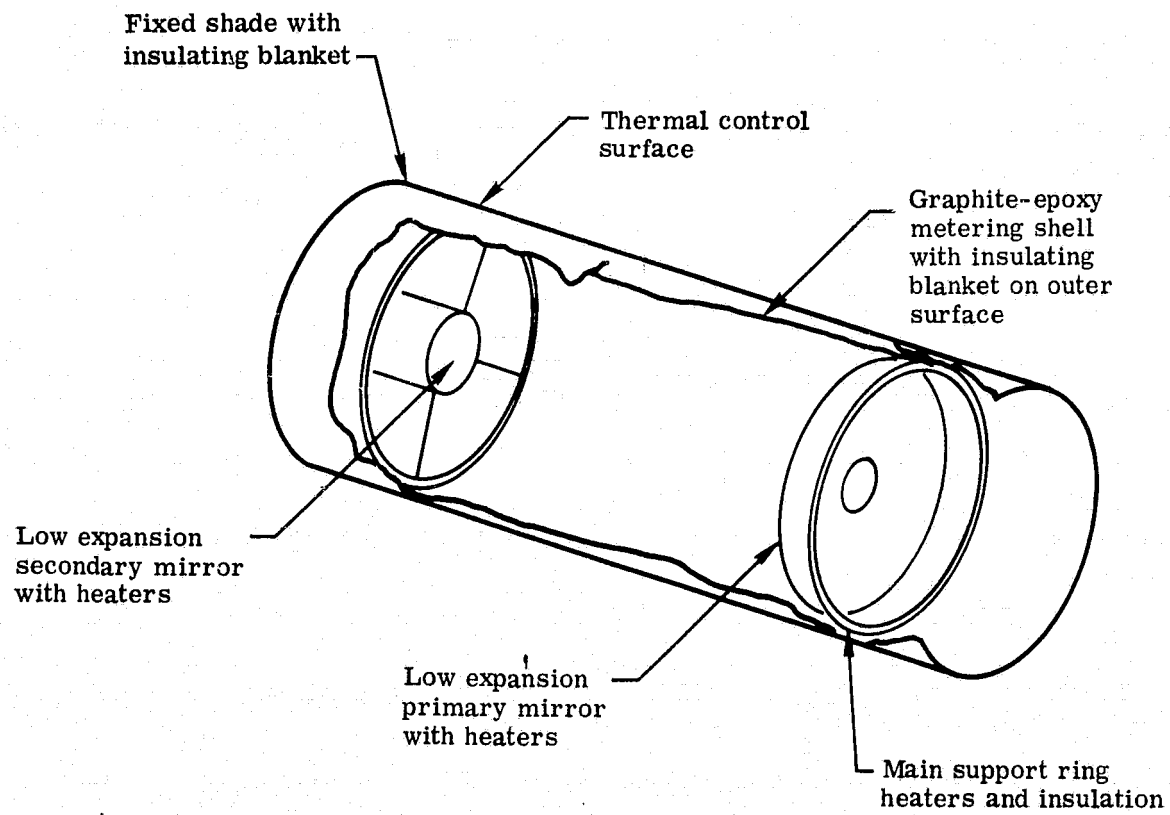

Fig. 3.3-2 LEST Baseline Thermal Control Concept

Fig. 3.3-3 TEMPERATURE HISTORY

OF PRIMARY MIRROR

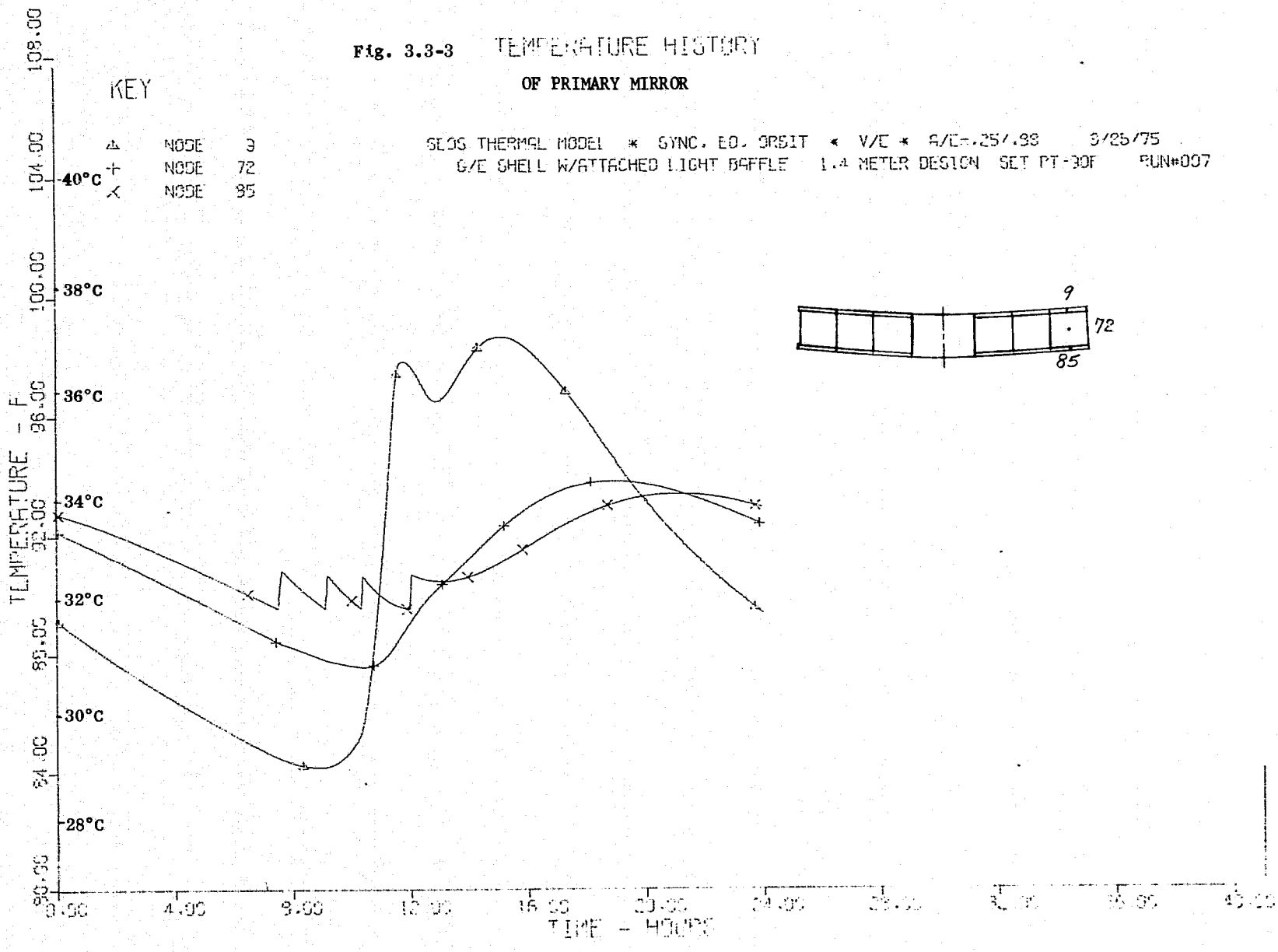

Fig. 3.3-4 TEMPERATURE HISTORY
OF METERING SHELL

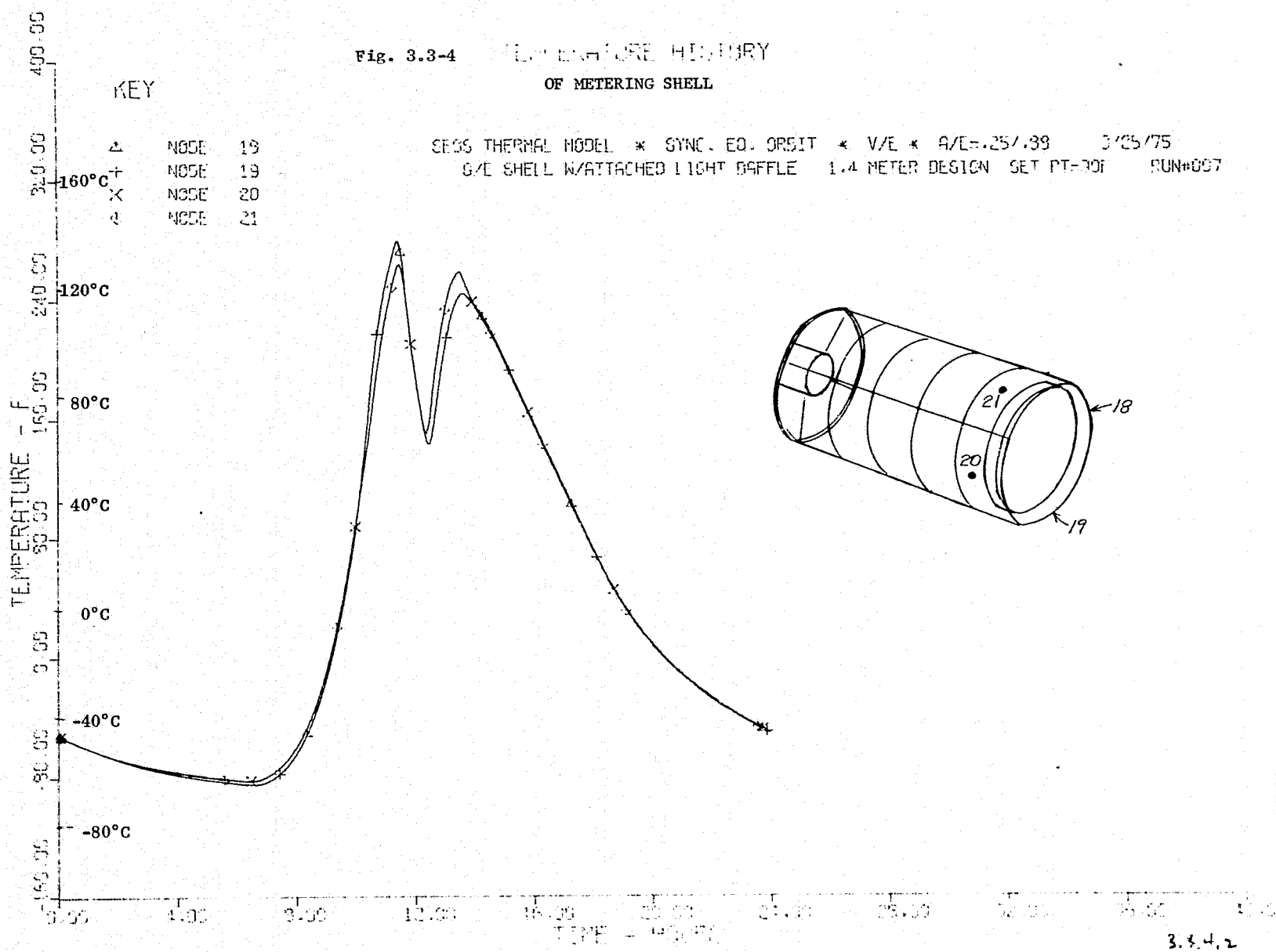

3.3.4.2

However, we are concerned about the effect of such an excursion on the structural materials, and we also question how the hot surfaces might affect the infrared sensors. We can prevent the shell from undergoing a 140°C temperature swing by putting insulation inside, as well as outside, the shell. This solves the materials problem but does not solve the infrared radiation problem, which will require excellent baffle designs.

3.3.5 Thermo-Optical Degradation

Thermo-optical degradations were calculated at various times using the temperature levels and gradients of all components and the sensitivities shown in Fig. 3.3-1. Figure 3.3-5 shows the individual error budget entries at local midnight (true anomoly = 180°). The largest contributors to the total error of 0.029λ rms are the lateral variation in axial gradient of the primary mirror (0.020λ) and effects of inhomogeneity in expansion coefficient of the metering structure (0.019λ). The driving factor for the former is the solar flux absorbed by the primary and for the latter is the temperature excursion noted earlier for the structure. Both are expected to increase, but within the total acceptable limit of 0.045λ rms, at other times of the year.

This information was processed at other times during the orbit. The results, summarized in Fig. 3.3-6, show the maximum wavefront error to be 0.031λ rms.

3.4 STRUCTURES

The LEST telescope structure maintains the critical optical surfaces to within prescribed tolerances, provides protection to the instruments from adverse environmental effects and isolates the on-orbit, operating system from dynamic and thermal perturbations. In addition, the structure must be configured in an efficient, light weight arrangement to accommodate launch vehicle capabilities; it must demonstrate adequate strength to survive launch loadings with no mission degradation; it must be devoid of undesirable dynamic characteristics that would encourage interaction with the pointing or information gathering processes; and it must be constructed of economical and reliable materials with proven manufacturing techniques. These general requirements serve as the basis for the specific structural design criteria and goals.

3.4.1 Structural Design Criteria

The following guidelines were established early in the program and are intended to serve as conservative yet realistic design goals to indicate feasibility of selected structural concepts and design approaches:

1) Thermo-structurally induced mirror strains must not exceed .02λ in which λ = .63 microns.

2) Secondary mirror tip/tilt shall not exceed .05 milliradians during operation.

3) Secondary mirror decenter shall not exceed 100 microns during operation.

4) Dynamically induced wavefront errors must not exceed .030λ.

5) Total line of sight angular velocity must not exceed 28×10^{-6} rad/sec in system lower frequency range during exposure.

LEST
THERMAL ERRORS
RMS WFE AT λ = 633 nm
TRUE ANOMOLY = 180°

0.029 λ

METERING STRUCTURE	PRIMARY MIRROR	SECONDARY MIRROR
Tilt and Decenter .00020 λ	Average Radial .00036 λ	Average Radial .00028 λ
Inhomogeneity .0185 λ	α Variation, Soak .0093 λ	α Variation, Soak .0034 λ
	Lateral Var. in Axial .0197 λ	Lateral Var. in Axial .00018 λ

FIG. 3.3-5 LEST Thermal Error

FIG. 3.3-6 TOTAL RMS WAVEFRONT ERROR
vs. ORBIT TIME
$\rho = 0$

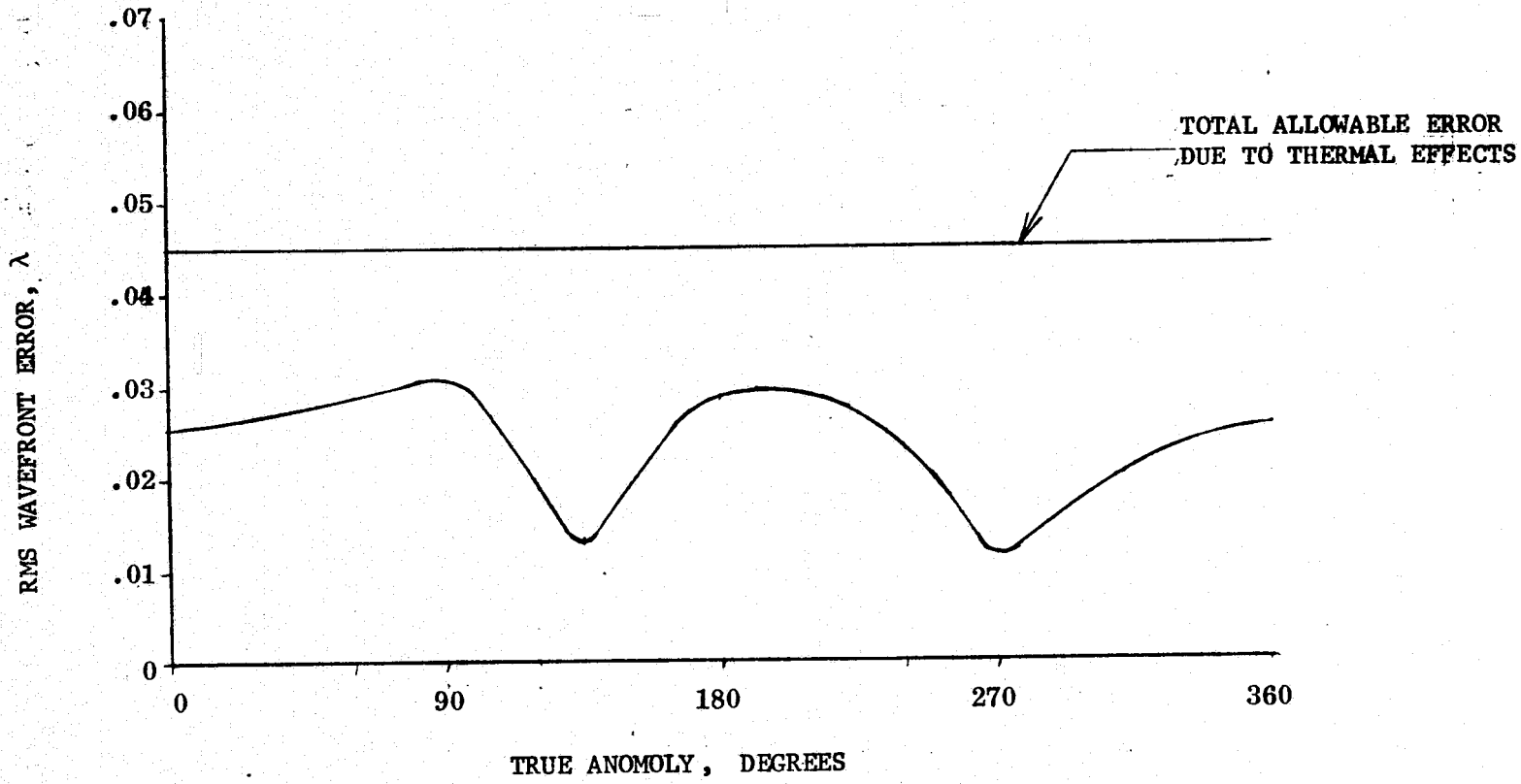

6) Preliminary design load factors which envelope launch vehicles response accelerations shall be:

±12 g	longitudinal
± 6 g	lateral

7) Maximum stresses in optical structures will not be allowed to exceed one half the material's micro-yield stress and maximum stress in optics is not allowed to exceed 1000 psi in tension.

8) As design goals, minimum weight and obscuration are incorporated into the design, and both thermal and structural isolation are maximized.

9) The telescope configuration will be compatible to the Titan/Centaur shroud envelopes and dynamic clearances.

10) Gravity release mirror deformations will not exceed .02λ.

11) Provide protection from errant meteroids for a period of 5 years with a .95 probability.

3.4.2 Configuration

Of significant interest to structural considerations are the mounting arrangements of the reflecting surfaces. As shown in Fig. 3.1-1 the telescope structure consists of a graphite epoxy metering truss to provide support for the secondary mirror and focus mechanism. The truss provides adequate axial and lateral stiffness while allowing minimal weight and obscuration. It is supported at the primary mirror support structure so that both primary and secondary mirrors may behave integrally and be isolated from external sources.

The goal in designing the support structure for this sytem is to provide adequate axial and longitudinal stiffness while successfully isolating the mirror from externally induced loads. The support system consists of an aluminum support bulkhead of honeycomb construction to which the mirror is mounted by 3 flexural supports. The invar flexures are an ideal structural connection in that they provide adequate stiffness in the axial and lateral directions while being compliant in the radial direction. This compliance is desirable in that it can be controlled to induce small mirror strains during temperature soaks. The aluminum honeycomb construction provides attractive stiffness to weight characteristics which are requirements of launch and operational dynamics. The primary mirror is a lightweighted ULE eggrate structure weighing about 25% of an equivalent solid mirror. It is mounted to the main support ring by invar flexures again providing desired compliance in the radial direction and adequate support in the axial and lateral directions.

The instrument support structure designed as a modular unit consists of a conical graphite epoxy shell mounted to an instrument support bulkhead. This bulkhead is also of lightweight honeycomb construction and provides the mounting surface for the various optics. An aft bulkhead provides support for the Tertiary mirror and sensor housing and also provides added stiffness to the composite shell. The instrument structure attaches as a unit to the primary support structure by a set of invar flexures. The telescope structure is housed in an aluminum monoque shell with stiffening rings and is attached to the main support ring by invar flexure. An aluminum meteroid shell provides outer protection for the telescope system for a proposed 5 year mission.

3.4.3 SEOS Dynamics

The dynamic analysis of the Large Earth Survey Telescope was performed to evaluate the effects of pushbroom scanning on image motion and to determine system frequencies and mode shapes. As an aid in the analysis a finite element model of the telescope system was developed for use with the NASTRAN structural analysis program.

As shown in Fig. 3.4-1, the finite element model consisted of 12 nodal points representing the optical elements and telescope structure. Weight and inertia properties were obtained from current mass properties analysis while system stiffness properties were chosen to reflect design goal values. Due to the interest in scan responses and due to structural symmetry, nodal deflections were limited to lateral and axial translations and rotation in a plane parallel to the scan plane. System frequencies and mode shapes were obtained using the normal modes routine of the NASTRAN program and are listed in Table 3.4-1.

Scan Torque Inputs

Based on Phase 1 study tradeoffs, pushbroom scanning evolved as the favored observational approach. Using this technique the required search area is covered by a series of spacecraft sweeps. At the end of each sweep a suitable torque impulse is required to provide proper scan rate reversal. The torque profile for the scanning cycle is described in section 3.5.1.4 of this report. System structural response was obtained for this torque pulse.

Image Motion

The vibration of the individual elements in the system contribute to image motion at the focal plane. The magnitude of the image motion attributed to each element is a function of the optical leverage involved. An expression relating element motion to angular motion of the line of sight for a Cassegrain system was developed from which image motion at the focal plane was obtained.

Transient Response to Scan Reversal Torque

The lateral displacement and velocity responses to the torque profile was obtained for individual optical elements as well as image motion at the focal plane. An allowable angular velocity of the line of sight of 28×10^{-6} rad/sec was determined as the maximum acceptable response based on detailed analyses for similar optical systems. Translated into image motion the acceptable linear velocity at the image plane becomes .018 in/sec. As shown in Fig. 3.4-2, the maximum image motion response remains below this level for a period following the torque removal: slow response attenuation is indicative of the light structural damping present in the system ($\zeta = .005$). The low frequency response of the system reflects the effects of the solar arrays on the system, this affect can also be seen in the response data for the secondary and primary mirrors given in Figures 3.4-3 and 3.4-4.

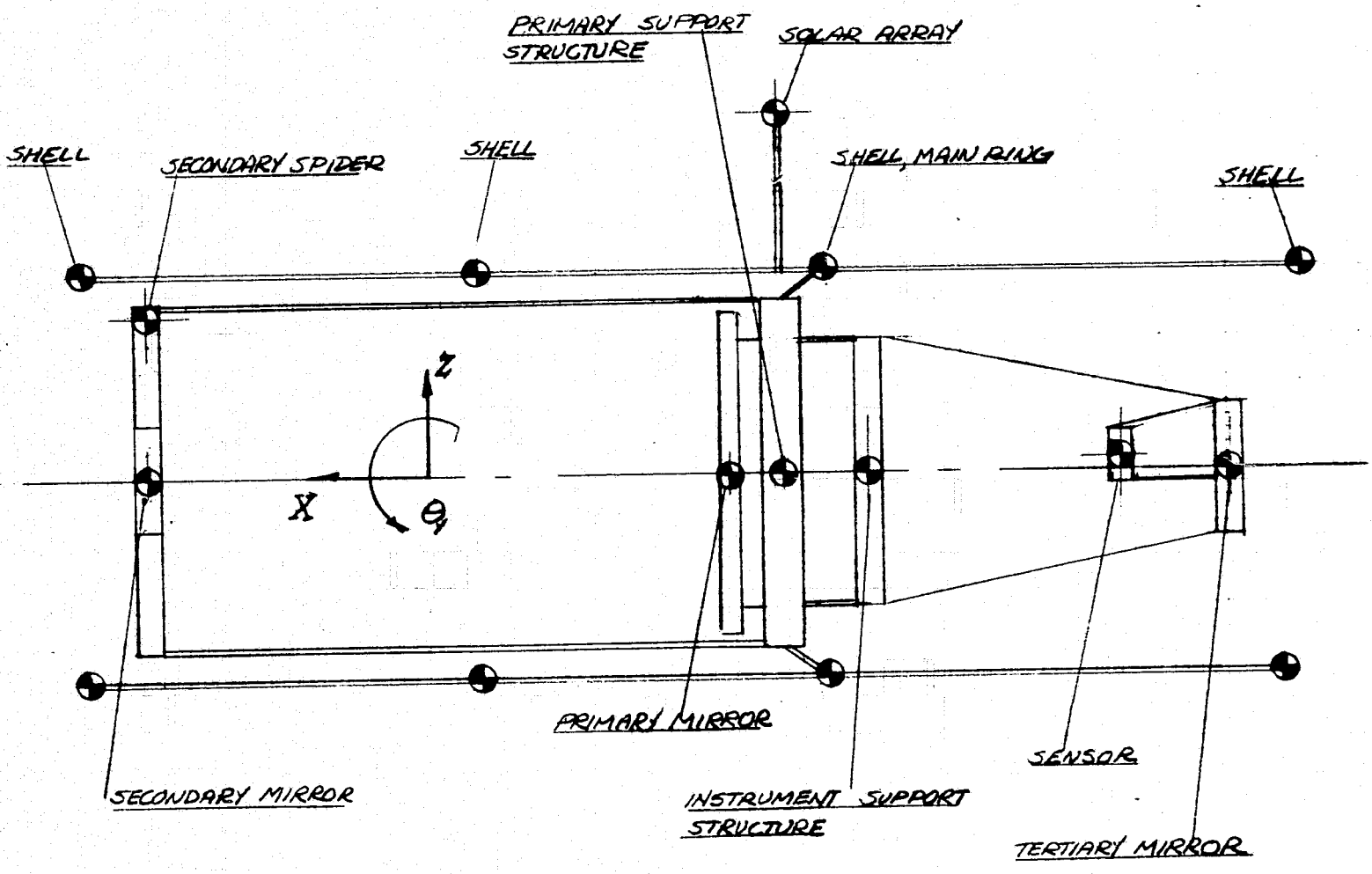

Fig. 3.4-1
Structural Model

Table 3.4-1

NORMAL MODES DESCRIPTION

MODE NO	FREQ (HZ)	DESCRIPTION
1	1.0	COMBINED TORSION & LATERAL BENDING OF SOLAR ARRAYS
2	1.96	LATERAL BENDING OF SOLAR ARRAYS
3	22.65	SECONDARY MIRROR LATERAL BENDING
4	26.30	COMBINED LATERAL BENDING OF METERING TRUSS AND SECONDARY MIRROR
5	29.75	ROTATION OF SECONDARY MIRROR
6	38.6	LATERAL DEFLECTION OF SENSOR COMBINED WITH CANTILL BENDING
7	40.9	LATERAL DEFLECTION OF SENSOR
8	43.9	LATERAL DEFLECTION OF METERING TRUSS
9	55.5	AXIAL DEFLECTION OF PRIMARY MIRROR
10	63.6	COMBINED BENDING OF OUTER SHELL AND PRIMARY MIRROR LATERAL DEFLECTION
11	70.0	COMBINED LATERAL DEFL. OF PRIMARY MIRROR & PRIMARY MIRROR SUPPORT STRUCTURE
12	70.4	AXIAL TRANSLATION OF SECONDARY MIRROR
13	78.3	AXIAL TRANSLATION OF SENSOR
14	79.7	ROTATION OF SENSOR
15	82.1	AXIAL TRANSLATION OF SENSOR
16	84.0	BENDING OF METERING TRUSS
17	132.0	AXIAL TRANSLATION OF METERING TRUSS

Fig. 3.4-2

LATERAL VELOCITY AT IMAGE PLANE

$\zeta = .005$

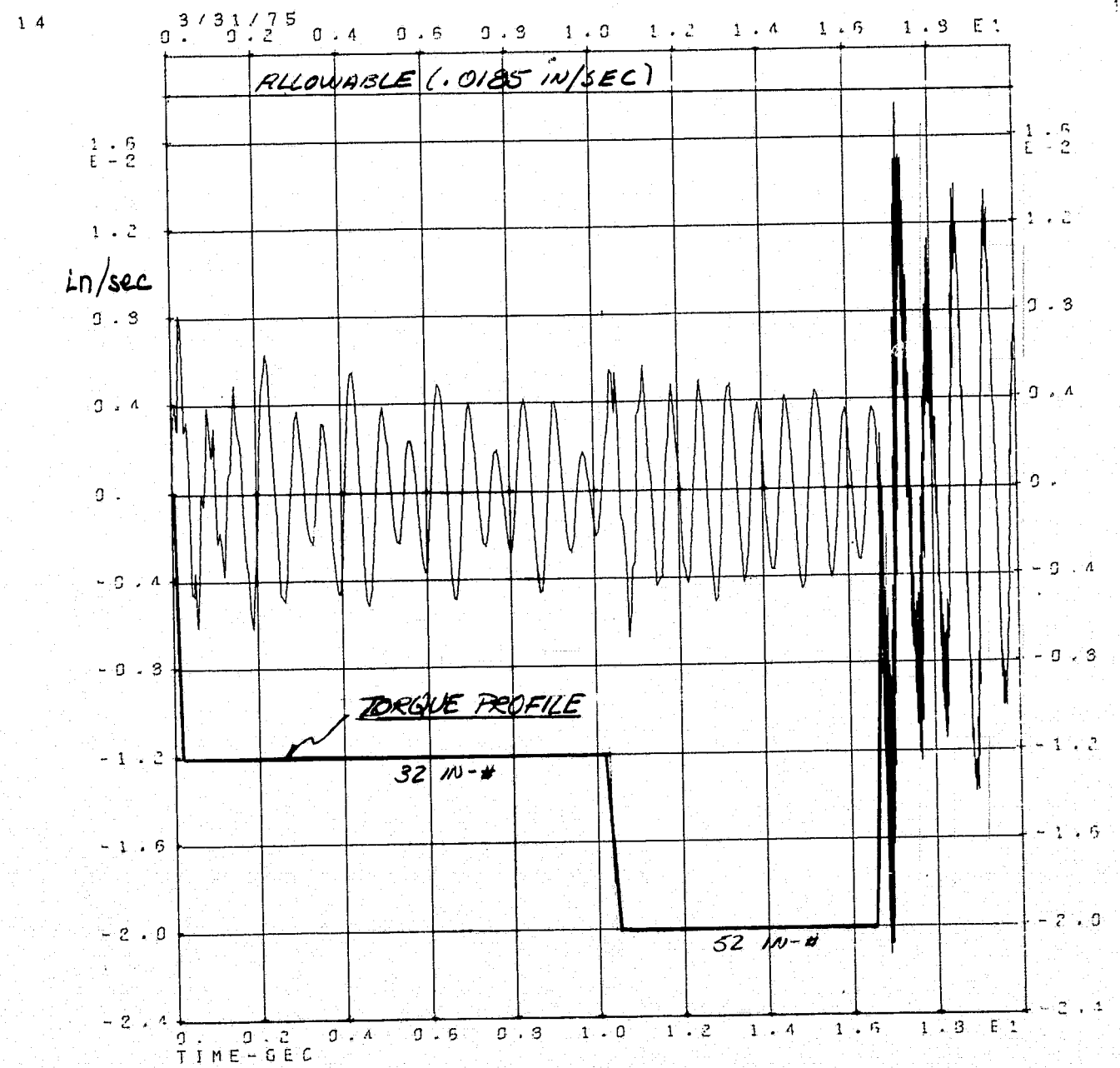

GEOS DYNAMIC ANALYSIS
TRANSIENT RESPONSE TO TORQUE PULSE

Fig. 3.4-3

PRIMARY MIRROR LATERAL DISPLACEMENT

J = .005

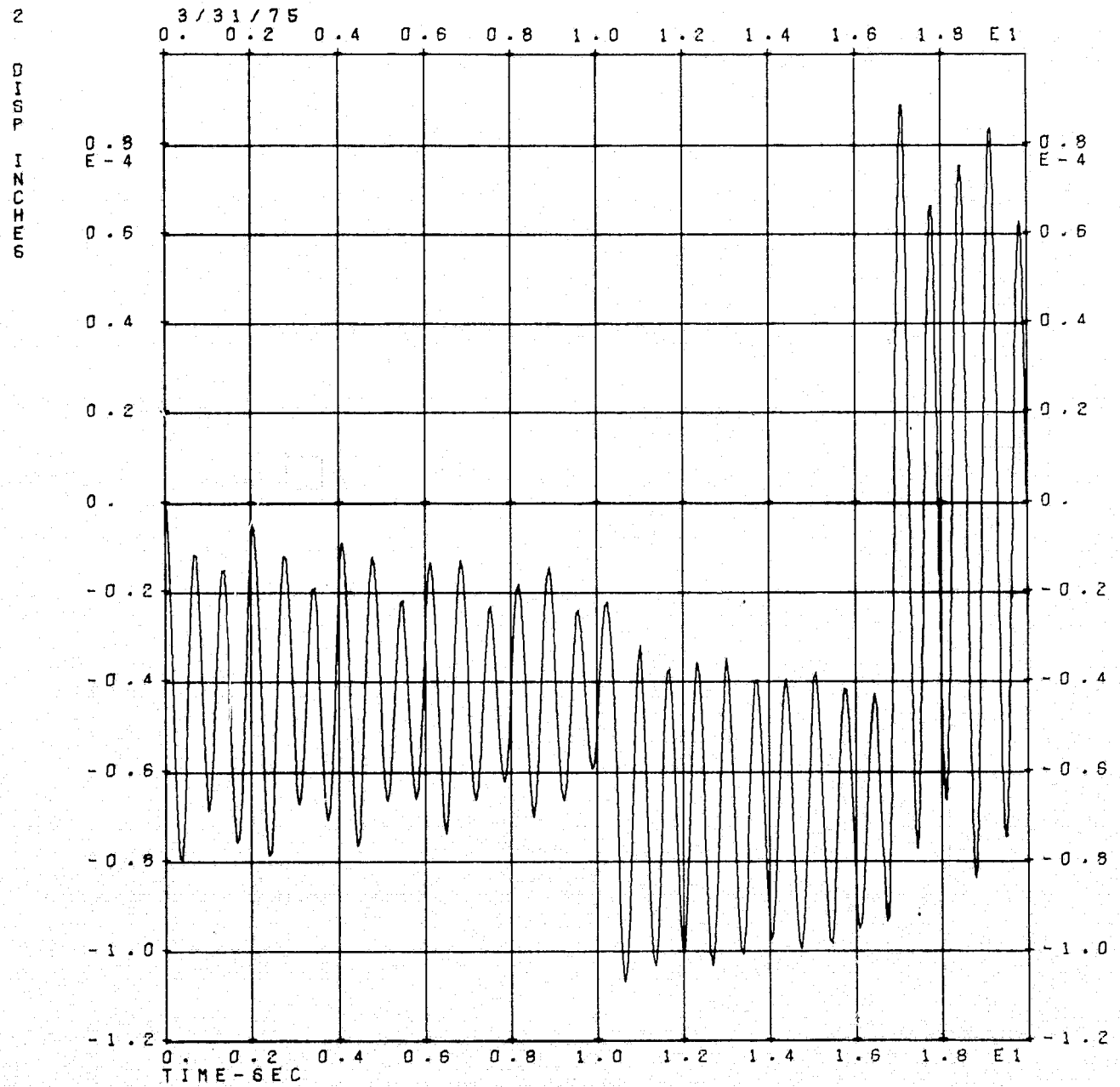

SEOS DYNAMIC ANALYSIS
TRANSIENT RESPONSE TO TORQUE PULSE

Fig. 3.4-4

SECONDARY MIRROR LATERAL DISPLACEMENT

$\zeta = .005$

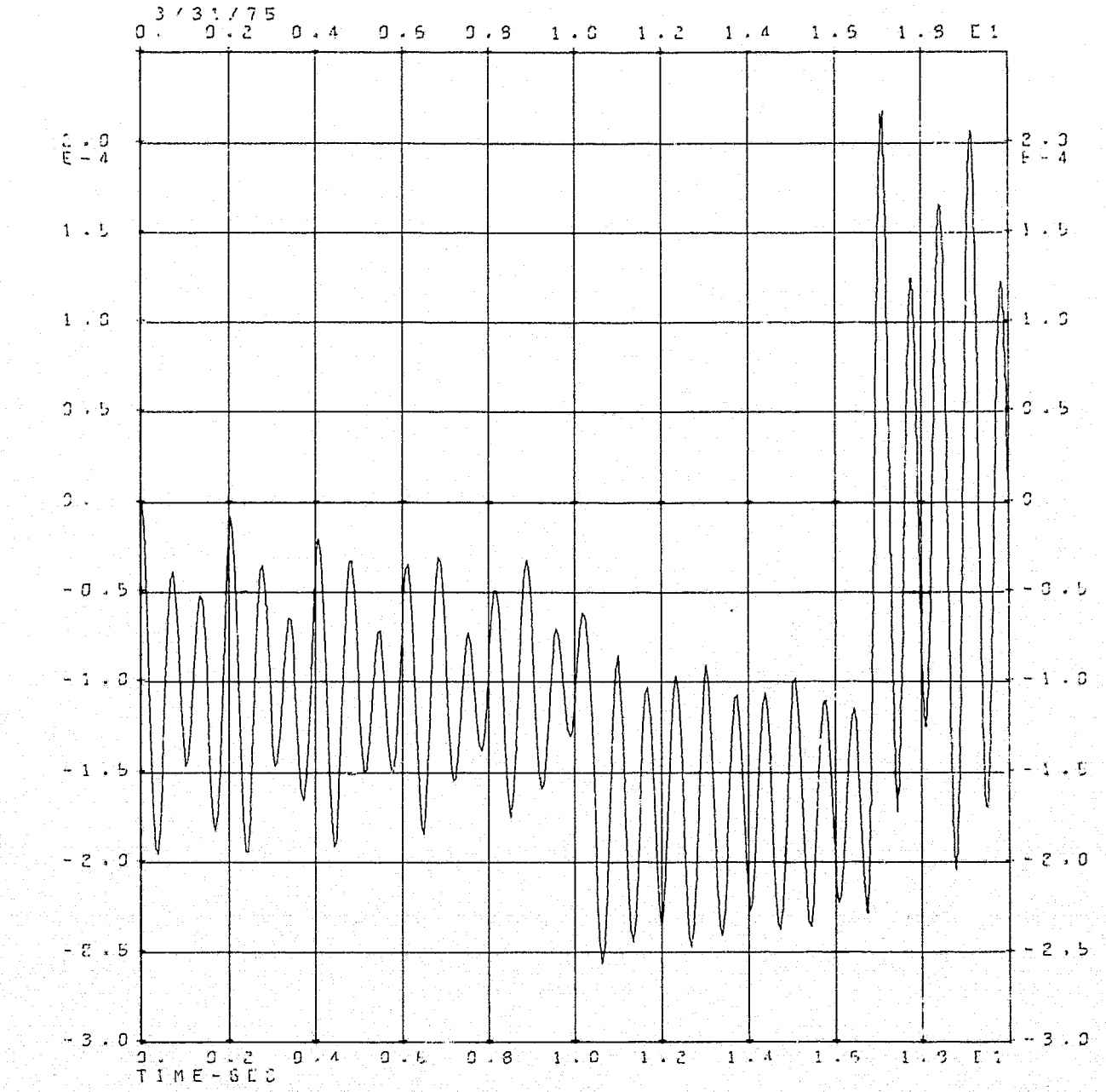

EROS DYNAMIC ANALYSIS
TRANSIENT RESPONSE TO TORQUE PULSE

ORIGINAL PAGE IS
OF POOR QUALITY

3.5 Spacecraft Attitude Control and Scanning

This section investigates the feasibility of precise pointing and precision scanning of the target area via controlling spacecraft attitude, avoiding the difficulties associated with designing the scan into the telescope optical train. The scope of the time-limited study encompasses conceptual approaches and feasibility, not a complete ACS design.

Requirements and constraints are discussed, followed by a brief study of system and hardware aspects. A preliminary ACS configuration is described and comparisons are made to the RCA Defense Meteorological Satellite Program (DMSP) project, which is also an earth pointing stellar-inertial system. Critical areas requiring additional work are discussed in Section 10.

It is concluded that spacecraft scanning is feasible but additional work is recommended in the areas of transient gyro scale factor uncertainty, flexible solar array effects, and detailed attitude determination simulations.

3.5.1 Performance Requirements

This section lists the mission performance requirements in pointing accuracy, stability, and velocity uniformity. An error budget is presented and a typical scanning scenario analyzed.

3.5.1.1 Pointing Accuracy

The pointing accuracy requirement has been given as ± 1 km at the spacecraft subpoint. This is the required static earth location accuracy. Table 3.5-1 shows an error budget divided into attitude determination and attitude control portions.

These errors are for quiescent operation in the primary mode, not while thrusting for stationkeeping or pitch momentum unloading.

The errors are 3σ, combined pitch and roll. The yaw error has not been specified for this study but will be less than the combined pitch-roll error. A static yaw error, unlike a steady yaw

TABLE 3.5-1 POINTING ERROR BUDGET (COMBINED PITCH AND ROLL)

	Sec	Error	
		μrad	Meters
ATTITUDE DETERMINATION			
1. Ephemeris (25 Meter, Each Axis)	.202	.985	35.4
2. Star Sensor (Static)	2	9.69	348
3. Dynamic Error (Kalman Filter Est.)	3	14.5	522
4. Alignment (Star Sensor & RU to Support Ring)	2	9.69	348
5. Alignment, Optical; between image at detector and support ring	4	19.38	696
ATTITUDE CONTROL			
1. External Disturbances (Solar, magnetic, gg, aerodynamic)	.5	4.85	174
2. Internal (Momentum exchange device, noise, gyroscopic coupling torques, magnetic unloading torque	.5	2.42	87
TOTAL 3σ RSS	5.8	28.2	1010

velocity, simply skews the imaged area and will not cause spectral mis-registration.

The dynamic error (Item 3 of Table 3.5-1) is determined by the following sources:

- Gyro low frequency rate errors (orbit or twice orbit)
  - Temperature
  - Supply Voltage
  - Magnetic Field
- Star sensor random measurement error gaussian distribution
- Gyro random drift error
- Star crossing frequency

The value for this error in Table 3.5-1 is an estimate based upon simulation studies on the DMSP program, taking into account higher performance gyros and better star sensor performance. The higher accuracy SEOS application requires detailed attention to items such as gyro magnetic sensitivity which was the largest residual error source in the OAO inertial reference unit (Reference 7).

3.5.1.2 Stability

The pointing stability has been given as:

$\pm$1 sêc in 10 sec.

$\pm$5 sêc in 100 sec.

These requirements apparently derive from image quality based upon a single scan and upon a single frame. The determinents of this performance will be the gyro (drift) and momentum exchange device torque disturbance. These requirements must be considered along with those of Paragraph 3.5.1.4. At this

point, it is sufficient to point out that the Draper Space Gyro (DSG) has a design goal drift of 0.1 sec per day and therefore short term stability will depend upon other time variant error sources.

3.5.1.3 Scan Duty Cycle

Image information is obtained only while scanning. From Reference 1, Tables 4-14 and S4-1 the required scan rates are:

Met	Monitor	2.1	Millirad/sec
Met	Search	10	Millirad/sec
ER	Demonstration Sites	.0463	Millirad/sec
ER	Operational Applications	2.2	Millirad/sec

These scan rates are a constraint in that the star mapper design must be compatible if simultaneous earth and star scanning is done.

3.5.1.4 Scan Velocity Uniformity

In order to maintain registration between the four spectral bands, the scan velocity must be held to within 0.025% as indicated in Figure 3.5-1.

Also, in order to maintain registration in the orthogonal direction, the yaw velocity must be less than 0.025% of the scan (or pitch velocity).

3.5.1.5 Target Scanning Cycle

A sample acquisition and scanning profile is shown in Figure 3.5-2 for the 0.6° FOV LEST system. The three 1500 km square areas must be scanned in five minutes, each requiring three 2.3° E-W or W-E scans. With the objective of maintaining an overall fifty percent scan efficiency, the

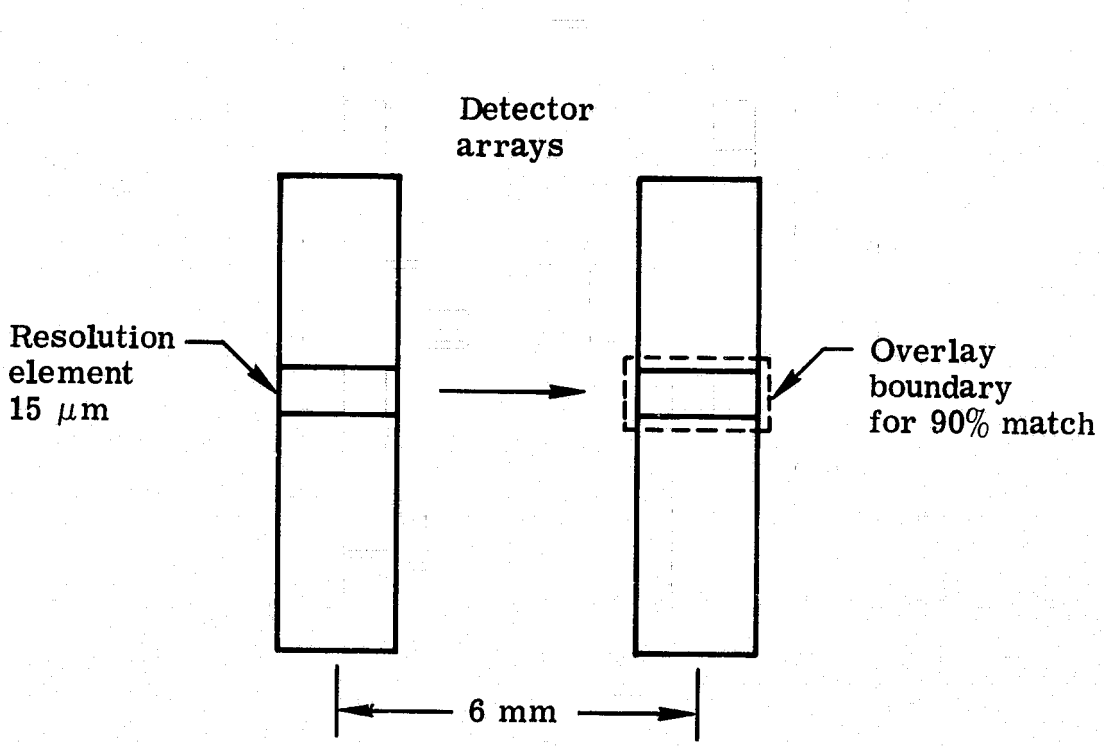

Horizontal mismatch caused by scan velocity variation:

$$\frac{15\ (10\%) \times 10^{-6}}{6 \times 10^{-3}} = 0.025\% \text{ or } 0.008\% \text{ (4 bands)}$$

Similarly, a yaw velocity while scanning will cause a vertical mismatch:

$$\frac{\dot{\psi}}{\dot{\theta}} = 0.025\% \text{ or } 0.008\% \text{ (4 bands)}$$

Yaw rate must be held to less than 0.025% of the scan (or pitch) rate.

Fig. 3.5-1 Scan Control Considerations

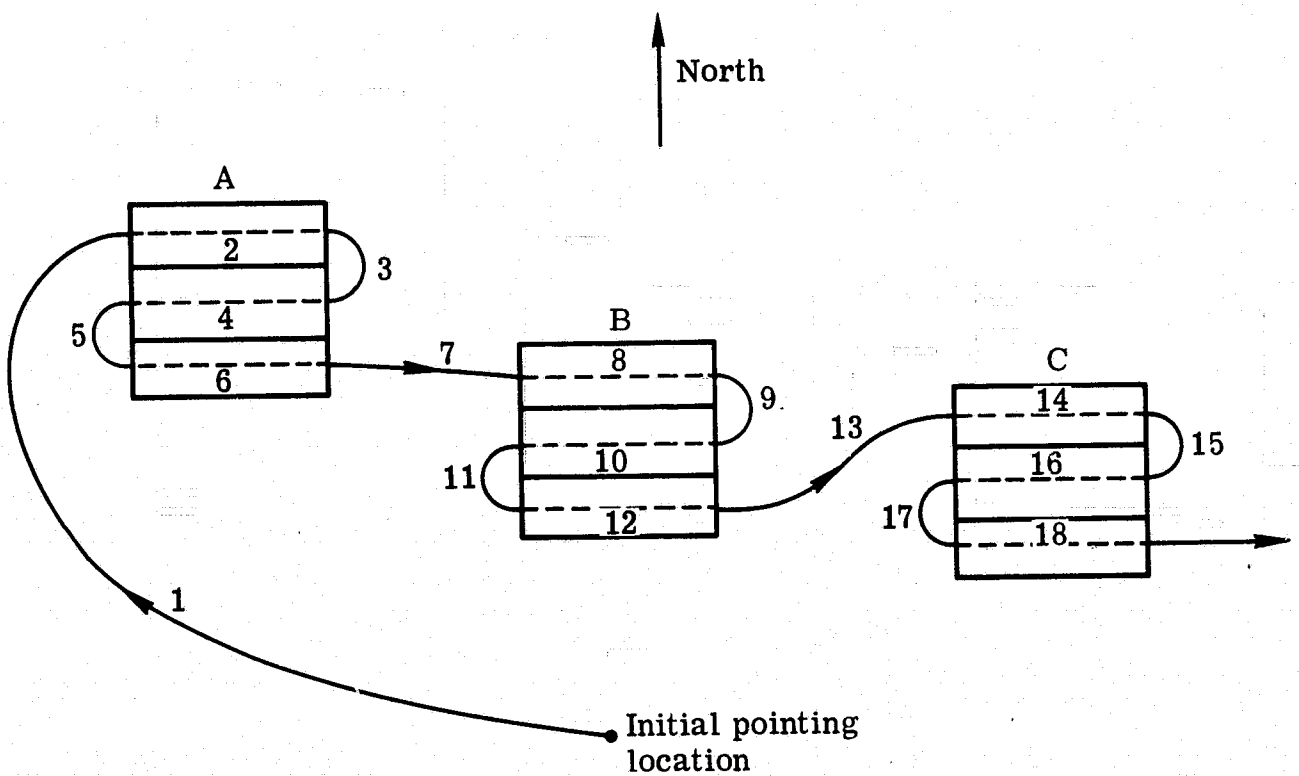

Areas A, B, C each 1,500 by 1,500 kilometers

Fig. 3.5-2 Meteorological Monitor Pattern

linear scan rate is:

$$\Theta = \frac{9 \times 2.3^\circ \times 1000}{150 \times 57.3} = 2.4 \text{ milliradian/sec}$$

If the 150 sec of non-active scan is allocated equally among nine segments, 16.67 sec is available for each scan reversal (including 2 sec settling time). Then, using the equation presented in Section 4.3 of Reference 1:

$$\frac{T_1}{J} = \frac{2\Theta}{t_2 - t_1)\ (t_1 - 3t_2}$$

where:

Θ	$= \frac{2.3}{57.3}$ radians	scan length
T_1	=	second torque pulse
J	= 36,500 in-lb-sec^2	S/C scan inertia
t_2	= 33.33 sec	total scan period
t_1	= 16.67 sec	reversal time (including setting)
t_3	= 2 sec	torque free setting time

$$\frac{T_1}{J} = .45 \text{ milliradian/sec}^2$$

Consider the requirement for slewing from the area of two targets on the West Coast to one target on the East Coast (7.4°). This maneuver can be accomplished in an optimum fashion with an acceleration doublet of 1.66 milliradian/sec^2. For a spacecraft inertia of 36,500 in-lb-sec^2, 5.0 ft-lbs are required.

If necessary, the torque can be reduced by allowing more time for the slew and correspondingly reducing the 16.67 seconds allocated to turnaround.

3.5.2 System Constraints

3.5.2.1 Structural Frequencies and Damping

The successful application of the concept of scanning by the spacecraft itself requires a careful evaluation of the inter-related system parameters which determine performance. Foremost is the structural dynamics of the telescope and resulting optical performance.

In order to achieve a respectable scan efficiency, an abrupt reversal in angular velocity at the end of each scan is required, necessitating a torque profile measured in foot-pounds. The telescope response to these near-impulsive disturbances may cause a transient image blur. The magnitude and duration of this effect is dependent upon the structural properties and the imposed torque profile. Usually, in order to achieve thermal stability and optical performance after the launch environment, the structure is sufficiently stiff (with correspondingly high modal frequencies) such that deflections due to scan torquing are small and quickly damped.

The desirable attributes of the telescope structure are:

- High structural frequencies
- Adequate structural damping
- Low thermal response

Active damping may be added, if required, by utilizing an optical transducer or gyro, suitably located with respect to the modal shape to be damped. Inevitably, structural dynamics limit the three attitude control bandwidths, and therefore scan efficiency and linearity since the time to achieve precise rate control after turnaround is a function of bandwidth.

3.5.2.2 Gyro Drift and Noise

The inertial reference unit (IRU) generates three-axis inertial frame velocity information. The gyros are the heart of the attitude determination and control system. Stringent SEOS performance will be obtained by using gyros which, although not off the shelf today, are currently in production and will be flight tested this year.

Attitude control bandwidth, besides being limited by structural frequencies, may be constrained by gyro noise, the effect of which increases with bandwidth. Two other parameters which measure performance for this application are compensated random drift and torquing scale factor stability. (Other terms which enter the picture at scan reversals are expected to be small). The torquer scale factor stability will determine how long scanning may take place before errors due to this parameter become excessive.

3.5.2.3 Torquer Weight and Power

The momentum exchange device (or torquer) used to control the spacecraft is determined by two considerations. The scan reversal torque and its duty cycle set the power requirement whereas the scan velocity fixes the momentum and therefore weight. The inertia wheel and control moment gyro (CMG) have important differences which affect their selection for a given application. For an inertia wheel the torque requirement reflects directly into power by virtue of the motor I^2R loss. Secondly, maximum torque is constrained by field demagnetization such that each ft-lb of torque requires about one pound of motor weight. More weight may be required to cope with the temperature rise due to the torquing profile. The CMG does not have this disadvantage since output torque is produced by gimbal precession. It controls momentum by changing the direction of a constant magnitude momentum, hence

control is more complex and more CMGs are generally used for a three-axis application than inertia wheels.

The comparison between reaction wheels and CMGs entails more than a weight and power trade-off. For precise pointing applications such as this, the torque disturbance spectrum produced by each may be important. The CMG, due to its constant wheel speed, produces a constant torque-frequency profile whereas the reaction wheel profile changes in frequency as wheel speed varies, thus complicating the mechanical mount filtering design.

3.5.2.4 Ephemeris Accuracy and Update Frequency

Ephemeris data furnishes the link between the stellar-inertial frame and the earth centered frame. Along-track and across-track errors of about 25 meters each are reported in Reference 6 based upon simulation for range, azimuth, elevation, and range-rate data taken during fifteen minutes of every hour.

Altitude errors will cause off-nadir pointing errors. For example, the ground position error is 12% of the altitude error for 6° offset pointing, or 12 meters for a typical 100 meter error.

3.5.2.5 Torque Disturbances

1) Gravity Gradient

The principle moments of inertia of the cylindrical spacecraft are given in Figure 5-5 of Reference 1 and repeated below:

I_x = 1644 Kg M^2 yaw

I_y = 4180 Kg M^2 roll

I_z = 4180 Kg M^2 pitch

When the telescope is directed to nadir, no gg torque exists; however, with the telescope rolled off nadir (N-S), a constant roll gg torque is developed as given by Equation 1:

$$M = \frac{3}{2} W^2 \left(I_z - I_x\right) \sin 2\phi \qquad (1)$$

The peak sinusoidal momentum is:

$$H = \frac{3}{2} W \left(I_z - I_x\right) \sin 2\phi \qquad (2)$$

The steady body torque is cyclic in an inertial frame and results in no momentum accumulation on an orbital basis. This torque and the peak value of the cyclic momentum are, from Equations 1 and 2 (for ϕ = 6 deg):

$$M = 36 \times 10^{-6} \text{ in-lb}$$

$$H = 0.49 \text{ in-lb-sec}$$

The pitch torque due to an E or W offset has the same value but results in a secular momentum accumulation of only 3.1 in-lb-sec/day.

Thus, gg torques and momenta are small and have little impact on control device sizing and momentum dumping frequency.

These results are based upon the basic cylindrical configuration. The geometry is time varient due to the rotating solar array. However, since array inertia is a small fraction of spacecraft inertia, the gg torques will change slightly.

2) Solar Torque

The solar paddle shown in Fig. 3.1-1 is a square-shaped array area of about 9.4 square meters with a moment arm from the center of the area to the centerline of the telescope of

3.44 M. Using a solar pressure value of 9.65×10^{-8} lb/ft^2, the torque is 13.1×10^{-4} in-lb. Assuming continuous or step rotation to maintain sun normalcy, this results in a roll-yaw plane secular momentum accumulation of 113 in-lb-sec/day. This, the largest environmental torque experienced by the spacecraft, results from the unsymmetrical geometry due to the required cooler FOV.

Several steps can be taken to lessen and counteract this disturbance. Panel aspect ratio can be changed to reduce the moment arm. The large array area itself may be efficiently employed to produce a counteracting bias magnetic torque by wrapping turns about the perimeter. An electromagnet, self erecting normal to the panel surface, would have the same effect. In addition roll and yaw electromagnets, via normal desaturation logic, will remove residual momentum.

Utilization of the spacecraft body surface for part of the array, as discussed in Section 3.5.4, would reduce the area of the oriented array and therefore the disturbance.

3) Internal Disturbance Torque Produced by Solar Array

A single square oriented array (1 kw, 148 ft^2, 120 lb) has an inertia of 552 in-lb-sec^2 compared to a spacecraft pitch inertia of 36,500 in-lb-sec^2. Several drive options exist:

1. Continuous motion geared drive.
2. Incrementally "continuous" drive.
3. Incremental drive.
4. Inertially stabilized array.

Each produces a unique torque disturbance profile to the spacecraft pitch axis. The continuous motion geared drive (clock drive) is open loop such that torque disturbances due to gear

teeth, slip rings, bearings, etc. have a direct effect, being attenuated only by spacecraft pitch axis bandwidth and inertia.

The incrementally "continuous" drive (used on RCA Satcom) is a fairly large bandwidth closed loop direct drive with a stepping input. For the inertias given above, a satisfactory stepping rate of 15 $\hat{s}$ec per sec would produce a pitch jitter of less than 0.23 $\hat{s}$ec. This drive has the feedback advantage of attenuating the pitch effects of array drive torque disturbances such as motor cogging torque as well as bearing and slip-ring random and discrete torques.

The incremental drive (Item 3 above) would be advanced 15 degrees at hourly intervals, keeping the sun within $\pm$7.5 deg. between advances. This eliminates the problem of array produced disturbance torque; however, a dedicated time for array advance and attitude settling is needed.

Pitch scan complicates the array drive problem, requiring array drive torque to follow the scan motion for methods 1 and 2 above, analogous to the spacecraft turnaround transient.

The incremental drive could be clamped between the hourly advances, merely adding to the spacecraft inertia.

The last alternative is to keep the array inertially fixed in pitch (using redundant array mounted gyros) thus imposing no array turnaround torque on the spacecraft. Flexible array modes would not be excited. A very low bandwidth control loop would keep the array normal to the sun and counteract gyro drift.

Array modes are another facet of the problem. Two factors determine pitch scan uniformity in the presence of these modes; the array inertia and modal frequencies and damping.

In conclusion, the incremental drive is most conservative, the inertially stabilized drive conceptually attractive, and the geared drive simple. The incrementally "continuous"

drive, used on two RCA programs, needs more study (simulation) to demonstrate compatibility with scanning.

4) Internal Disturbance Torques Produced by Momentum Exchange Devices

The spacecraft contains no tape recorders or other sources of uncompensated momentum. Inertia wheels produce random and discrete torques, the latter varying in frequency with the stored momentum. A significant error can occur at speed reversal due to coulomb friction reversal and cogging torque can increase the effect. The transient error on OAO was 1 sec due to wheel reversal.

The CMG with constant rotor speed, produces constant frequency discrete torques as well as random torques. Gimbal non-linear dynamic characteristics which have been thoroughly studied and reported in the literature in connection with the Large Space Telescope, will not be a problem on the less demanding SEOS.

5) Magnetic Disturbance Torque

Magnetic disturbance torque due to small dipoles in various equipments is slight due to the low value of the earth's field. However, the roll and yaw momentum unloading electromagnets, are in the hundreds of ATM^2 range. The unloading torque will be applied gradually, consistent with the roll and yaw axes bandwidths such that the transient error can be kept negligibly small.

Electromagnets will be located remotely from susceptible gyros and star trackers containing image dissector tubes if the latter are used.

3.5.2.6 Geostationary Orbit

The geostationary orbit represents a constraint in the application of magnetic torquing for momentum dumping due to the small field and impracticality of pitch unloading. The component perpendicular to the pitch axis is only 18% of the total field magnitude and strong coupling exists such that pitch unloading would produce larger effects in roll and yaw. Therefore, the pitch wheel must be sized to accumulate secular momenta consistent with pitch propulsion unloading frequency. It is obvious that the basic spacecraft must be configured to minimize pitch disturbance torques.

3.5.2.7 Scanning Torque Profile

The highest velocity scan mode is that required for the large meteorological search; 4500 km N-S by 9000 km E-W. This is accomplished in eight scans with the 0.6° FOV since the stated area subtends 4.7° by 11.2° from SEOS. For a 50% scan duty cycle, the scan rate is 10.4 mil-rad/sec and the maximum turnaround acceleration is 1.63 mil-rad/sec^2. For a spacecraft inertia of 36,500 in sec^2, the required torque pulse is 5.0 ft-lb.

The torque profile is shown in Figure 3.5-3 for an assumed two second torque free settling time. The turnaround torque profile was developed in Reference 1.

3.5.3 Trade Study Results

Section 3.5.2 discussed the system constraints; the following paragraphs consider system and hardware tradeoffs.

3.5.3.1 Torquer Weight-Power Product Vs. Scan Duty Cycle

The torquer (and momentum storage device) whether reaction wheel or CMG, is chosen to satisfy the momentum and torque requirements. The reaction wheel is considered first.

The fundamental equation for motor power is:

$$P = 1.358\ T\ \left(\dot{\Theta}_W + kT\right) \qquad (1)$$

where,

T = Torque — ft-lb

P = Power — watts

k = Motor Parameter — $\frac{\text{No load speed in rad/sec}}{\text{Stall torque in ft-lb}}$

$\dot{\theta}_w$ = Motor Speed

The scanning momentum is:

$$H = J_s \dot{\theta}_s = 36{,}500 \times .0104 = 380 \text{ in \#s}$$

Substituting for wheel speed

$$\dot{\theta}_w = \frac{\dot{\theta}_s J_s}{J_w}$$

and $$J_w = \frac{W}{g} r^2$$

$$P = 1.358T \left(\frac{H_g}{Wr^2} + kT \right) \qquad (2)$$

If a flywheel weight of 10 lb and radius of gyration of 6 in. is assumed, the power for 5 ft-lb torque, is:

$$P = 1.358 \times 5 \left(\frac{380 \times 386}{10 \times 36} + 5k \right)$$

$$P = 6.79 \ (407 + 5k)$$

Thus, regardless of motor size (and value of k) the power is an exhorbitant 2760 watts. It could be reduced to a reasonable value only by utilizing a large radius of gyration and therefore probably open wheel construction. For example, if r = 14 inches and W = 30 lbs, the power is still rather large (170 watts). Fig.3.5-3 shows the torque, velocity, and power profiles.

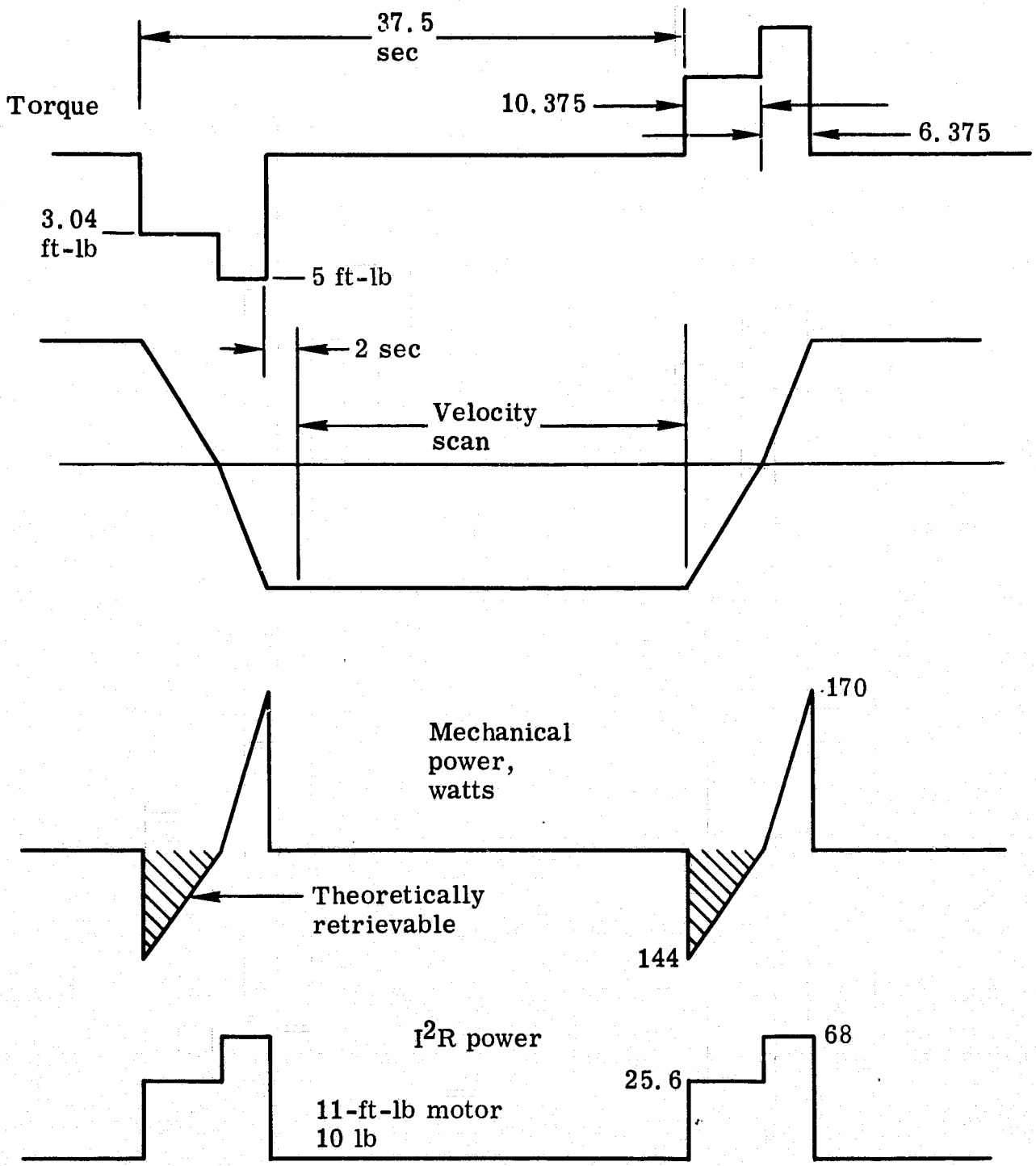

Fig. 3.5-3 Scan Profile

The I^2R loss and motor weight were obtained from an Inland Motor Corp. catalog for brush type motors, but are equally applicable to a brushless motor. The choice of an 11 ft-lb motor weighing 10.3 lb was based upon achieving a reasonable temperature rise of 23°C.

Thus the scan requirements result in a reaction wheel with the following characteristics:

• Brushless Motor Weight	10 lb
• Momentum Wheel Weight	30 lb
• Radius of Gyration	14 in
• Peak Power	238 Watts
• Average Power	53 Watts
• Motor Temperature Rise	23°C

Although the mechanical power could in theory be cyclic instead of dissipative by flowing back and forth between battery and wheel, the added circuit complexity may not be warranted.

The reaction wheel assembly weight would be considerably greater if enclosed. If open, an allowance of 30% of the wheel weight is made for wheel stiffness, bearings, support, etc. Thus a total weight of 50 lbs would be required.

The total average power will not be much greater than the given 53 watts since bearing, hysteresis, and eddy current losses will be small in comparison. Pulsewidth modulation motor control should provide 90% efficiency.

For comparison with the CMG, it is instructive to consider a stress limited reaction wheel since this provides the greatest momentum storage per unit-weight. The stress constraint is represented by the maximum wheel surface speed, V.

Equation 2 then becomes:

$$P = 1.358\ T\left(\frac{V}{r} + kT\right) \qquad (3)$$

Since

$V \simeq 10^4$ in/sec (2:1 safety factor, stainless)

$T = 5$

$r =$ radius of gyration

it is apparent that the mechanical power becomes excessive for a stress limited reaction wheel with a reasonable radius of gyration.

The CMG and reaction wheel can be compared on an energy basis (see Reference 8). The spacecraft energy is:

$$E_B = \frac{1}{2} J_B \dot{\Theta}^2_B \qquad (1)$$

and from the conservation of momentum, the inertia wheel energy is:

$$E_W = \frac{J_B}{J_W} E_B \qquad (2)$$

For the 10.4 millirad/sec Met search,

$J_B = 36{,}500$ in-lb-sec^2 and $\dot{\Theta}_B = .0104$ rad/sec.

$E_B = 1.92$ in-lb

$E_W = 28{,}400$ in-lb

Since power is the time derivative of energy, it is easy to see how exorbitant power demands can arise for scan turnaround.

The CMG, on the other hand, has constant wheel energy and need only furnish the energy stored in the spacecraft body (1.92 in-lb) plus that required to slew the rotor through the precession angle, and losses.

The large inertia ratio does on the other hand, present a simple control strategy. Consider the ideal case of a single axis of a spacecraft in a disturbance-free environment which is inertially at rest with a reaction wheel at zero initial velocity. To slew the spacecraft a given angular displacement, requires moving the reaction wheel the same amount multiplied by the spacecraft to wheel inertia ratio. For the case just considered, this ratio is 14,800. Thus, to move the spacecraft 1 sec requires 4 degrees of reaction wheel displacement.

The foregoing analysis is based upon zero average momentum stored in the RWA. Momentum accumulation due to external pitch axis torques will cause a net momentum that biases the scanning wheel speeds in one direction and increases the mechanical power. The additional power can be realistically determined only after external disturbance torques and a momentum dump profile have been established.

The roll and yaw wheels could be separately sized on the basis of their individual axis requirements. The roll axis inertia is equal to the pitch inertia and slewing is required. Indexing 0.6 deg. at every pitch scan reversal requires less than 1 ft-lb torque. External momentum accumulation also affects sizing.

Roll and yaw reaction wheels may be smaller, use less power, and weigh less.

3.5.3.2 CMG

The control moment gyro (CMG), unlike the reaction wheel, has a fixed rotor speed and thus a constant momentum

magnitude; attitude control is achieved by changing the direction of the momentum vector through precession. The constant speed rotor can be run near its stress limit, thereby achieving maximum momentum storage density. (A hybrid device, the double-gimbaled momentum wheel, is simple but unsatisfactory for this application which requires large pitch scanning torques).

The simplest configuration of true CMG's consist of an orthogonal set of three single gimbal CMG's with attendant high loop interaction. A set of three scissored pairs avoids this and simplifies control at the expense of hardware. Redundancy for reliability must also be considered. Other arrangements which have been analyzed in the technical literature are symmetrically disposed sets of 4, 5, and 6.

It is sufficient for this study to point out the weight and power advantage of CMG's in high torquing applications and cite an example. The Sperry Model 30 DG CMG has the following characteristics:

- Weight 30 lb
- Momentum 30 ft-lb-sec
- Torquer Output
  - Peak 5 ft-lb
  - Continuous 1.25 ft-lb
- Torquer Power
  - Peak 200 Watts
  - Continuous 12.5 Watts
- Wheel Power 6 Watts

This unit is actually a DG reaction-wheel with 20 degrees gimbal motion. However, it is representative for sizing since the momentum is in the ball park (24 ft-lb-sec are required for pitch scan). The induction motor can be replaced with a synchronous motor, one gimbal removed, and gimbal freedom increased.

A scissored pair of these units would require about 30 degrees precession, allowing for 10 ft-lb-sec of secular momentum storage. During the 10 mil-rad/sec linear scan, the gimbal reaction torque would be 5 in-lb, or less than 1 watt of torquer I^2R loss. Insufficient data does not allow a turnaround power profile to be calculated; however, it will be much less than the reaction wheel.

CMG's are preferred for pitch axis scan based upon size-power product. Even with a large radius of gyration, reaction wheel power has been shown to be excessive.

3.5.3.3 Scan Control Method

The basic scan is defined before considering implementation. A roll and/or pitch maneuver will direct the telescope LOS from its previous location to the desired point. Orbital rate (earth's rate) correction is appropriately applied to keep the LOS directed to the desired earth point. A pitch scan is superimposed with roll steps at each turnaround. More complex scans, based upon earth track considerations (i.e., uniform surface velocity), could be devised upon the geometry and implemented with the computer, if necessary.

As shown in Figure 3.5-4 the spacecraft is commanded to point "A" which is west of the target area by an amount which will ensure uniform scan velocity by the time the target boundary is crossed at "B". At the eastern boundary "C", as detected by gyro data, turnaround is programmed. The processed gyro data detects re-entry of the boundary at "D" and this process continues for the remainder of the scan. Roll indexing (0.6°) at turnaround is initiated by the pitch gyro exiting the target area at "C".

The scan block diagram of Figure 3.5-5 was obtained from Reference 4. A pulse train drives the gyro torque generator,

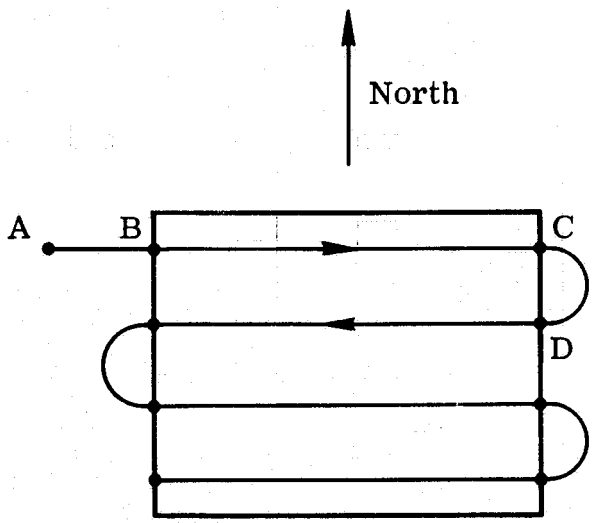

Turnaround torques
from C to D

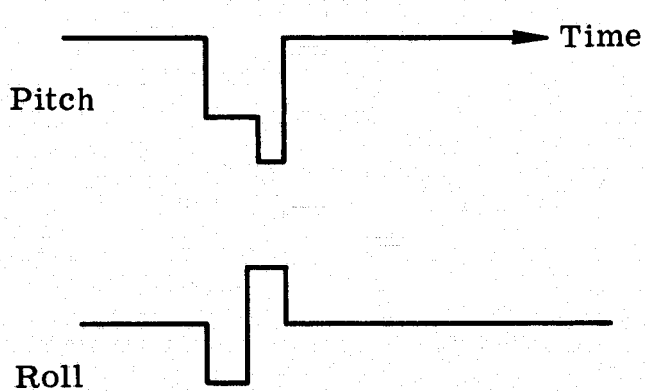

Fig. 3.5-4 Basic Scan Pattern

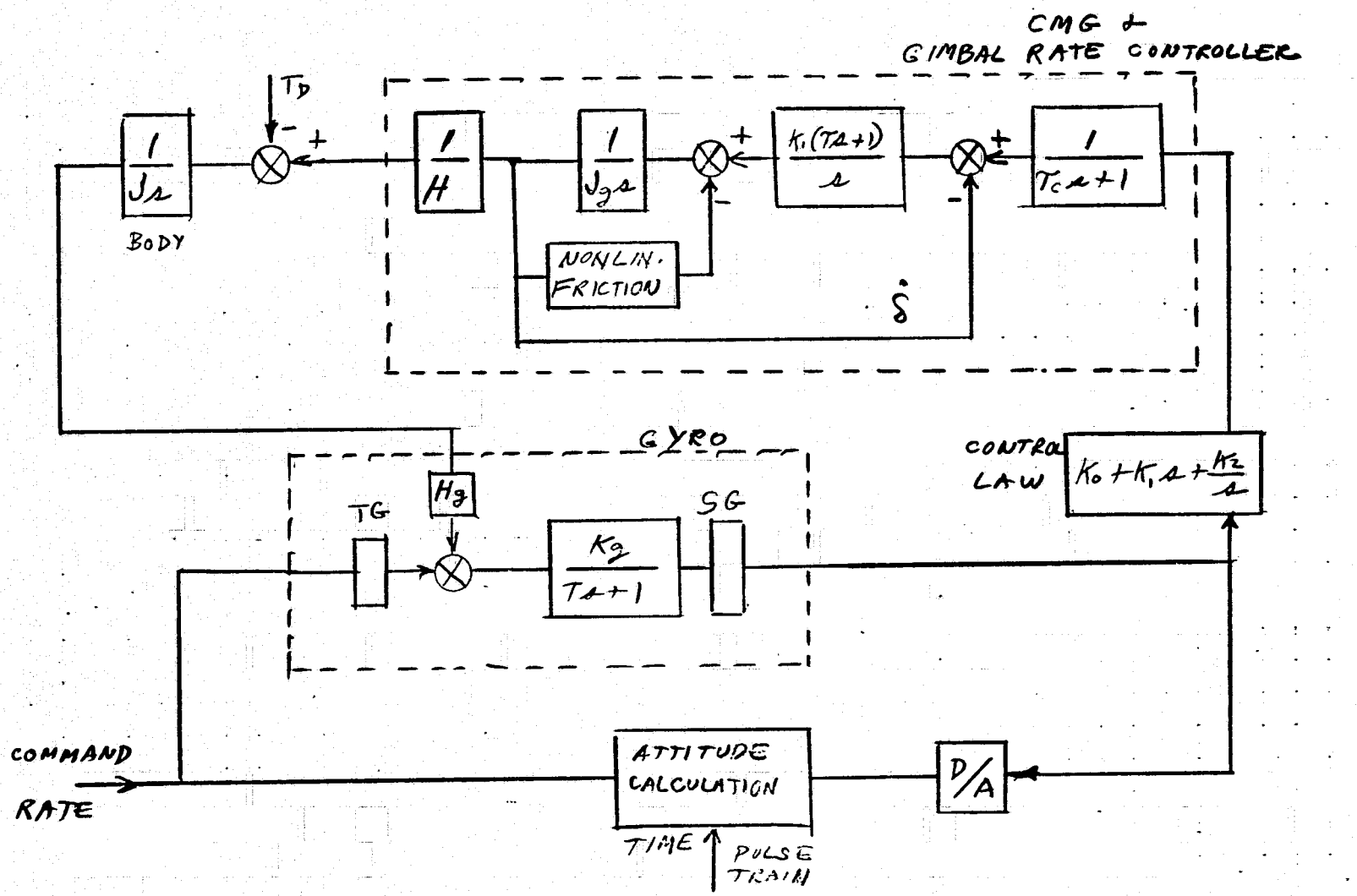

Fig. 3.5-5 S/C Rate Control

with frequency proportional to desired rate. The gyro float precesses, creating an error signal in the gyro signal generator which is converted to a digital signal for attitude calculation and used in analog form to control the CMG's through the control law. The CMG's precess the spacecraft, thereby nulling the gyro float position. Design must ensure that the float stops are not engaged; the signal generator would provide this information.

Simulation described in Reference 4 indicated an error of 0.002 $\hat{sec}$, 0.4 sec after application of a 0.25 μrad/sec range. This was for a CMG gimbal bandwidth of 16 Hz and overall loop bandwidth of 2 Hz.

For the 10 mil-rad/$\hat{sec}$ SEOS scan, the error would be 80 sec, assuming linearity. The time for velocity settling is 2 sec, Figure 3.5-3.

The turnaround settling transient can be greatly reduced by adaptive feed-forward or modelling. This is shown conceptually in Figure 3.5-6. The actuator is adaptively controlled by the computer to produce the desired velocity and displacement at the beginning of each 2 sec. torque free settling time.

Two approaches to implementing the scan have been given. Feasibility has been demonstrated from a CMG weight - power standpoint and it also appears feasible from a control loop standpoint, although simulation is needed to demonstrate that noise and flexible modes do not unduly restrict bandwidth.

3.5.3.4 Gyro Performance While Scanning

The frequency of stellar update of the gyros, for given scan and position performance criteria, depends upon its basic parameters and how it is used as discussed in References 4, 5, and 8.

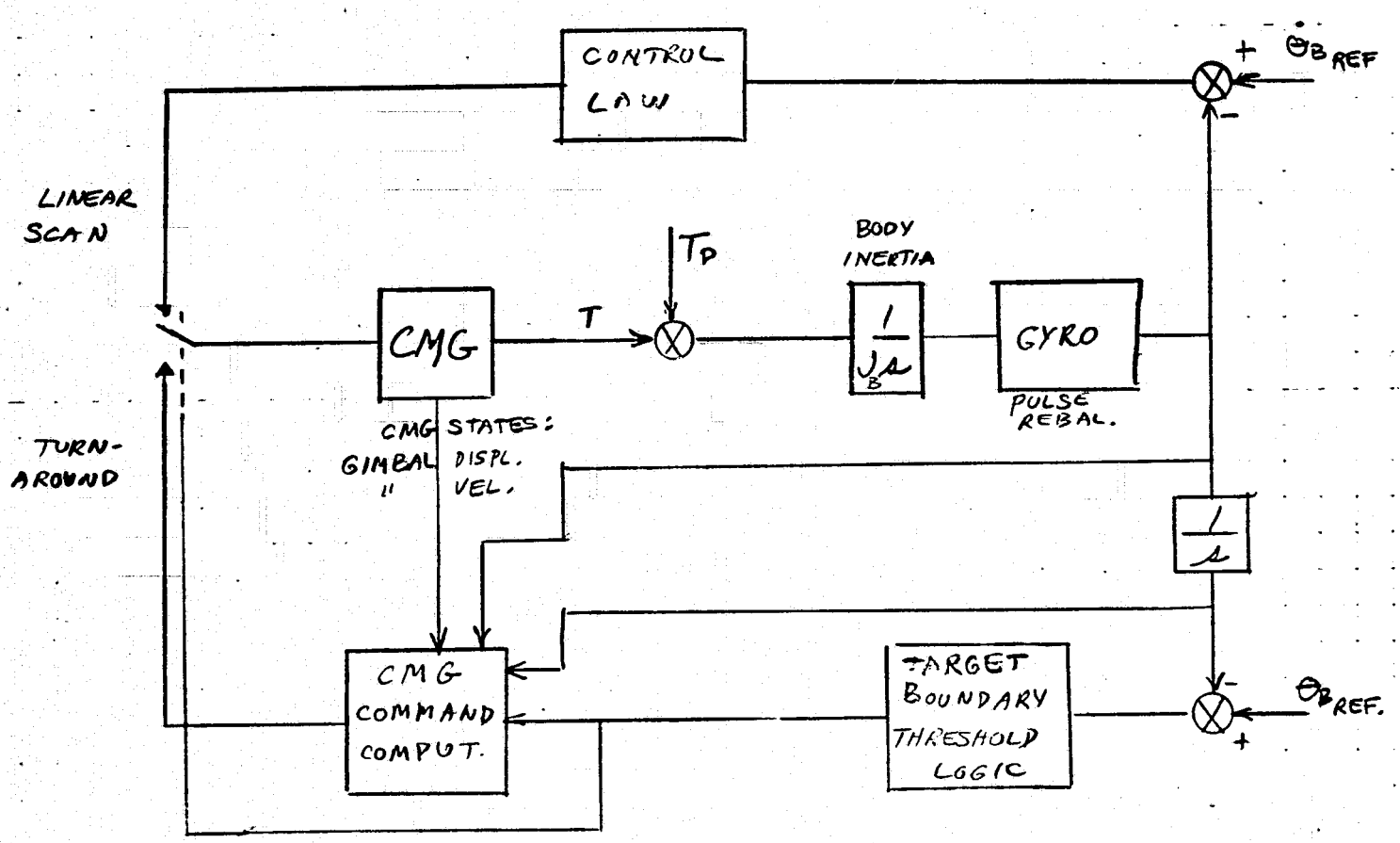

Fig. 3.5-6 Adaptive Turn Around

A totally strapdown system is proposed for SEOS, consistent with its development time frame and current state-of-the-art. Although a gimbaled IRU, studied in Reference 8, reduces torquing scale factor errors, no space proven stable platform with SEOS accuracies exists.

Secondly, the Draper Space Gyro (DSG), developed from the Third Generation Gyro (TTG), offers large improvements in performance which allow a strapdown configuration and infrequent stellar updates. The important design goal parameters from Reference 5 are:

- Scale Factor Stability — < 1 ppm
- Drift Uncertainty — $\simeq 0.1$ sec/day
- Noise Jitter — $\simeq 0.002$ sec (0.1 to 4 Hz Band)

The meteorological search consists of eight alternate direction scans of 11.2 degrees.

The scale factor uncertainty difference for positive and negative pulses can be calibrated. Therefore, the scale factor error for the eight alternate scans would theoretically be zero, since the net pitch scan is zero.

The pitch gyro is precessed at orbital rate and this results in a scale factor error which increases with time (.054 sec per hour), using the 1 ppm value. However, this would be taken out by the Kalman filter as a gyro bias error.

The most critical error source for this application is a transient error due to thermal effects when the spacecraft velocity is changed and the gyro torque input current pulses vary the I^2R loss.

In a 66 hr test at the Charles Stark Draper Labs, a third generation gyro was alternately torqued at 0.4 millirad/sec for 3 minutes and at 7.5 millirad/sec for 1 hour. The resulting scale factor uncertainty was 2.2 ppm, 1σ. This effect needs additional study as applied to typical SEOS profiles.

This cursory look at one error source neglects other effects such as input axis misalignment. Gyro drift uncertainty would cause a negligible error of 0.005 sec in one hour.

Thus, torquer scale factor transient error and input axis alignment will be the major error contributors.

3.5.3.5 Gyro Drift and Stellar Update Frequency

The gyro bias term will be estimated and corrected for (without scanning), for several days after launch.

The remaining drift uncertainty term of 0.1 to 1.0 sec/day is negligible compared to the torquing and misalignment terms. Thus, the required stellar update frequency depends mainly on scan duty cycle and not random drift.

3.5.3.6 Star Sensor Application

Many variations exist for implementing stellar updating of the IRU. A totally strapdown system is assumed achievable based upon the Draper Space Gyro, a computer with Kalman filter, and a suitable star sensor.

The interrelationship between the earth scanning mission and obtaining stellar update information must be considered. The matrix to choose from involves three broad categories:

1) Mission constraints, simultaneous or sequential earth and star scanning.
2) Reference stars; sun, polaris, others.
3) Compatible sensors; sun sensor, star mappers and trackers.

First we will consider the mission constraint. It would be desirable to obtain stellar information while scanning the earth. Mission time would not be diminished by dedicated intervals for stellar updates.

A mapper obtains slit crossings from stars of opportunity, and the electrical filter associated with precisely determining the time of the slit crossing event is optimized for the nominal star field velocity across the slit. Therefore, the choice of a mapper to eliminate the time-to-update constraint imposes a scan velocity constraint.

From Paragraph 3.5.1.3 the met monitor and ERS operational applications have scans at 2.1 and 2.2 milrad/sec, respectively. This is twice the scan rate of the star mapper used on the DMSP program. Vendor consultation indicates that the present mapper could be used with electrical filter circuit changes. Indeed, a mapper could be designed for optimum operation at 10 milrad/sec and filters switched for equal performance at the lower 2.1 and 2.2 milrad/sec rates. The spacecraft will usually be scanning at the lower rates so that design and filter switching for 10 milrad/sec may not be required.

The 2.2 milrad/sec scan rate exceeds the 1.75 milrad/sec maximum rate for a recently developed precise star tracker.

It can be concluded that simultaneous earth and star scanning is restricted to utilizing a mapper.

In considering reference stars (3.5.3.2 above) the sun and polaris provide an ideal combination in that both are available almost continuously and their angular separation is large.

Unfortunately, precise sun sensors (several sec$\hat{}$) are nulling type devices requiring platform movement. The most precise digital sun sensor identified is that developed for OAO with with an accuracy of 1 min$\hat{}$ (inadequate for this application). Therefore reference stars other than the sun will be used.

The stars intercepted by the sensor FOV remain fixed for the 6-month interval between solstices, when the spacecraft is flipped about the yaw axis.

The swath will vary with N-S offset pointing ($\simeq 6°$). Thus, the star catalogue will be constant for 6 months, alternating, with slight changes for orbital precession (see Paragraph 3.5.3.8

As identified earlier, the mapper is compatible with simultaneous earth scanning, whereas the star tracker is not. A state-of-the-art tracker recently developed for the High Energy Astrophysics Observatory (HEAO) has a calibrated design goal accuracy of 1 sêc with a 2° x 2° FOV. It utilizes an image dissector tube with a 98.7% probability of detecting eighth magnitude stars.

Computer calibration of over 100 points in the FOV is required, and temperature control to 2°C.

The DMSP mapper, with a specified 6 sêc (1σ) has yielded 2 sêc (1σ) accuracies in tests. In addition, a mapper developed for SAMSO had a 1 sêc bias and 2 sêc (1σ) random error.

Since the mapper has been the subject of more extensive development, and its accuracy is comparable to the tracker with greater FOV, it is preferred for the SEOS mission. The random error can be reduced, due to multiple crossings of the same star as the earth is scanned. Roll indexing 0.6° must be taken into account.

Two mappers with the projection of their LOS 90° apart in the orbital plane, are used. This improves measurement and estimation of error about the LOS as compared to a single sensor. The FOV's must be directed sufficiently out of the orbital plane to avoid sun interference. The choice of this angle is based upon attitude determination simulations which

take into account star availability, gyro drift, sensor noise, and disturbances. The constraints are FOV, sun shade design, and sun angle.

A silicon star mapper with the following characteristics has been developed and flight qualified on the DMSP program.

TABLE 3.5-2 . DMSP STAR MAPPER CHARACTERISTICS

Parameter	Value
Weight	6.8#
Power	1.5 watt
FOV	10°
Accuracy	6 $\hat{sec}$, 1σ
Star Detect. Mag.	$\simeq$ 3.8 MV
90% Prob. Detection (Si)	Brightest 380 stars

A conceptually attractive attitude sensing scheme utilizes an inertial platform containing gyros and at least three narrow FOV star trackers. A Kalman filter would not be required since star data is available continuously from two known guide stars. At six month intervals when the spacecraft is flipped, two other stars are chosen (hence, three trackers). In fact, with low enough sensor noise, and high bandwidth, the main function of the gyros would be for acquisition. The spacecraft is controlled via the three gimbal readout angles.

Another way to obtain continuous stellar information uses two double gimbaled trackers instead of a platform, trading three gimbals for four. Stellar tracking loops must accommodate spacecraft scanning motion.

However, even with large increases in size to obtain precise bearings and readouts (the weight must also increase to maintain stiffness) the multiple gimbal moving mechanical interfaces pose thermal, and lubrication problems.

RCA, while recognizing the potential of these schemes, chooses to advance the accuracy of the highly developed, flight qualified, mapper-gyro-Kalman filter system rather than risk a major development program.

3.5.3.7 Computer Usage

Computer memory and arithmetic capacity is best estimated by comparison with the DMSP computer.

NUMBER OF 16 BIT MEMORY WORDS

Command and Control	4722
Attitude Determination & Control	6083
Primary Attitude	5074
Total	15,879

Redundant computers are used. Usage is 211 millisecond of the 500 ms cycle time; 291 ms when a star update occurs.

The SEOS computer will require less star catalogue and possibly lower cycle time. However, heavy reliance on the computer will be made to achieve the desired pointing accuracy. The DMSP Kalman filter has 6 states, estimating the three Euler attitude angles and gyro bias terms. This may be increased for SEOS. Other possible applications, in addition to the DMSP usage, would be heavy reliance on modelling in the following areas:

- Gyro thermal transient scale factor change.
- Precise scan turnaround via CMG control.
- Daily thermal modelling (i.e., telescope structure).

- Gyro magnetic correction terms.
- Environmental torques (see Reference 8)
- On orbit calibration and mis-alignment determination.

It is estimated that approximately 20,000 to 24,000 words of memory would be needed.

3.5.3.8. Propulsion Usage

Propulsion is required for the following:

1. N-S Stationkeeping
2. E-W Stationkeeping
3. Pitch Momentum Dump

1. N-S stationkeeping will require about 152 ft/sec per year velocity change. With a spacecraft weight of 6600 lb., the yearly impulse is 31,200 lb-sec, which requires 142 lb of hydrazine (I_{sp} = 220). The yearly drift without correction would be 1 deg/year. At the end of one year, the spacecraft subpoint would describe a daily figure 8. This is deterministic, and spacecraft pointing could be controlled to compensate for the effects. Another approach, by proper choice of launch time, would split the drift over the spacecraft lifetime such that at mid-life the drift is zero.

Another approach (for an allowed error of 1 deg. for example), using the biasing scheme, would require 426 lb of propellant for the last three of the five years spacecraft life.

It is recommended to use no N-S stationkeeping and balance the five-year lifetime drift ($\pm$2.5 deg.). The impact on star detection, computer loading, gyro programming, and launch time constraint needs further study.

2. E-W stationkeeping requires a modest 3.6 ft/sec per year or 3.4 lb of hydrazine at 100°W longitude.

3. Pitch unloading will be required for gg and solar pitch torques. The small gg momentum calculated in Paragraph 3.5.2.5, (3.1 in-lb-sec/day) for a constant 6° offset would require less than 1 lb of propellant per year for 80-inch thruster separation.

A comparable solar pressure momentum accumulation will result as the spacecraft sun orientation changes daily, and due to uncertainties in array solar pressure force vector and spacecraft center of mass locations. These effects can be quantitatively determined only by simulation after initial design.

3.5.3.9 Backup Control

Backup control is proposed for the following reasons:

1. Little flight experience with earth oriented stellar-inertial systems at this time.

2. Provides reference frame to more easily capture (star identity and Kalmen filter convergence) in the stellar-inertial primary mode.

3. Provides fall-back in case of temporary outage of primary system. This would allow time for self corrective action or generating ground commanded "workarounds".

This rationale is related to the present time frame; experience gained with stellar-inertial systems by the time SEOS is in the design stage may warrant exclusion of the back-up system.

Consisting of an earth sensor and sun sensor, the backup system would provide control for multiple failures in the primary system. (The primary system would be designed to operate with degraded performance for a single point failure. Momentum exchange devices, gyros, computers and star sensors would be redundant).

In this context, the excellent OAO performance can be cited as proving gyro reliability in space. A precise pointing earth oriented spacecraft has much more complex software and control functions, however.

3.5.4 Preliminary ACS Concept

A first cut ACS is proposed in this section. While it closely follows the DMSP configuration in many respects, significant departures are identified.

A block diagram is shown in Figure 3.5-7. The system consists of the following components:

1.	IRU	Inertial Reference Unit
2.	CSA	Celestial Sensor Assembly
3.	SS	Sun Sensor
4.	ESA	Earth Sensor Assembly
5.	RC	Reaction Control
6.	MU	Magnetic Unloading
7.	PU	Propulsion Unloading
8.	CPU	Central Processing Unit

1. The IRU consists of four (4) near state-of-the-art Draper Space Gyros, modified with PM torquers. The DMSP configuration of an orthogonal triad plus one skewed is retained.

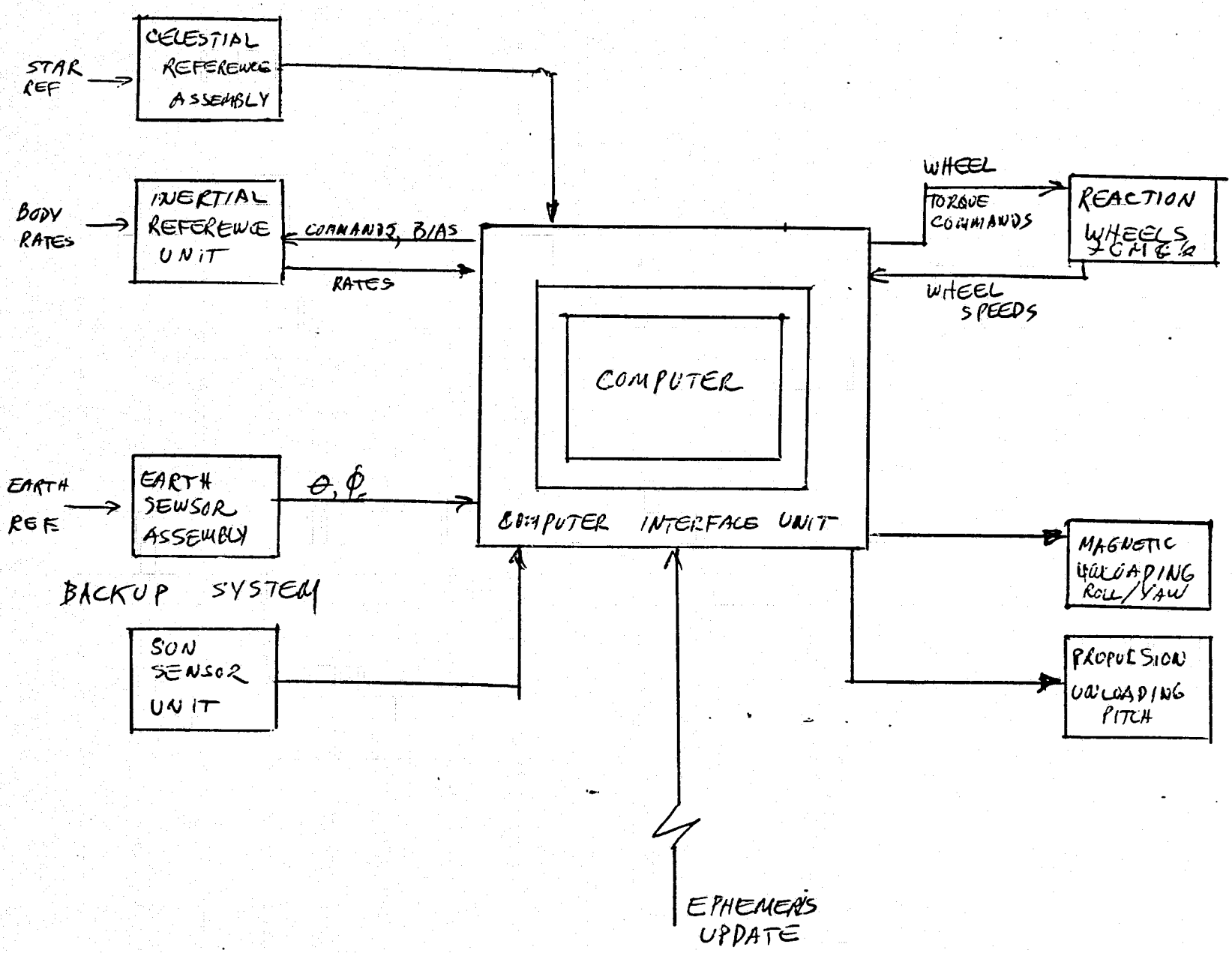

Fig. 3.5-7 ACS Concept Block Diagram

2. The celestial sensor assembly is the silicon DMSP mapper, modified as required to provide greater accuracy. Unlike the DMSP, two will be used, primarily for better Kalman filter estimation in the 14 times slower orbit.

3. The sun sensor is a passive digital device, as used on DMSP. Four are required for backup yaw attitude determination.

4. The flight proven earth sensor, unlike DMSP, will scan the earth in two orthogonal directions. This allows backup pitch and roll attitude measurement while SEOS is offset pointing or earth scanning.

5. The reaction control assembly consists of a scissored pair (mechanically uncoupled) of CMG's for pitch control and reaction wheels for the other two axes. With the CMG precession axis along yaw, the roll RWA could substitute for a failed CMG, but not with fast turnaround. A redundant yaw wheel might be required.

6. Magnetic unloading consists of roll and yaw electromagnets to unload the roll and yaw RWA's. This is done by respective wheel speed thresholds. Electromagnet current is applied gradually consistent with the control loop bandwidth. For a fixed roll-yaw momentum, the RWA's speeds would be daily sinusoidal. If zero speed traversal should pose a problem, magnetic torquing can be used to maintain unidirectional RWA speed.

   In addition, a large bias dipole will be attached to the solar array to counteract the solar pressure torque.

   The magnetic unloading closely follows the RCA Satcom design, also a geostationary orbit spacecraft.

7. Propulsion unloading for pitch will consist of two small hydrazine thrusters, as on RCA Satcom. The required one hour warmup before firing is consistent with the slow pitch momentum accumulation.

8. The central processing unit consists of redundant RCA SCP-234 computers, as an DMSP, but with memory increased to between 20,000 and 24,000 words.

The alignment critical IRU and two CSA's will be mounted on or suitably referenced to the primary mirror support structure. The electromagnet which produces a roll torque is located parallel to the yaw (optical) axis and radially opposite from the IRU. (The CSA is not magnetically susceptible). The electromagnet which produces a yaw torque is located parallel to the roll axis remote from the IRU.

3.6 DETECTOR ELECTRONICS AND CALIBRATION

The focal area will be a complex joining of optics, detectors, coolers, and electronics. We have treated the optical relays in Section 3.2, and we will discuss the detectors and their cooling in Sections 5.1 and 3.7. In the present section we want first to establish the requirement for radiation chopping for the infrared detectors, and then to present a block diagram of the conceptual electronics circuitry made necessary by the chopper. We conclude with a brief discussion of radiometric calibration.

3.6.1 DC Stability and Low Frequency Noise Considerations

Table 3.6-1 shows the application groups for SEOS and lists the line time of one sweep for the near and long-wave infrared bands. The line time determines the low frequency cutoff when considering the effects of 1/f noise and drift on the NER and radiometric accuracy performance of LEST.

The worst case line time (or time of sweep) is 107 seconds for the 100 minute earth resource survey of a 16.8° diameter portion of the earth's disc. Assuming the use of a shutter that clamps and restores the dc level at the beginning of each scan, the detector array and following electronics would have to be dc stable to a value equal to or less than the NER for a particular band for 107 seconds. This very difficult requirement would be reduced proportionately for smaller areas of interest within the total 16.8° coverage but would soon be bounded by the next most severe requirement of 18.75 seconds for the meteorological applications.

Chopping vs. Non-Chopping

Chopping (either an optical modulator or an electronic chopper) can be used in radiometers to minimize the effects of both 1/f noise and drift in the detector or electronics. Electronic chopping is inherent in the use of CCD commutated arrays where all detectors are sampled at least once per pixel providing an output that is a pulse amplitude modulated signal. This means that the electronics which interface with the CCD output do not handle dc signals and their requirements are considerably relaxed.

However, 1/f noise or drift in the detector element itself is unaffected by the CCD sampling process and the only way to reduce the errors associated with these noise sources is to chop the incoming radiation by interrupting the photon stream before the detector element. This 1/f noise is a particular problem in infrared detectors, primarily below 100 Hz.

The chopping frequency is chosen to be at least twice the highest video frequency and comfortably above the 1/f noise corner. This translates the video to a higher frequency that has the form of an amplitude modulated carrier. Later the carrier is demodulated with a synchronous detector to recover the baseband video signal and only the noise between the chopping frequency and one sideband.

The penalty for chopping is equivalent to multiplying the original peak signal by a factor of $\sqrt{2}/\pi$ or 0.45. This factor is the RMS of the fundamental frequency of the chopping square wave. Since the detector noise is not modulated by the chopper the end result of chopping is to reduce the signal-to-noise ratio to 45% of its original value. However, in the presence of 1/f noise, chopping may result in an overall improvement in SNR or at least improved radiometric accuracy for low frequency scene elements.

Table 3.6-1

Scan Time Assuming 50% Efficiency

	No. of Sweeps	Scan Rate mr/Sec.	Time For Frame Min.	Scan Time Sec.
Meteorological-Monitor Only	8	2.1	5	18.75
Meteorological-Monitor and Search	8	10	5	18.75
Earth Resource(16.8° Disc)	28	2.2	100	107

The layout drawings show radiation choppers for the f/2 and f/1.3 image planes.

3.6.2 Circuitry

The visible band CCD detectors pose no special circuitry problems. The integration time is 1 ms and there are almost 5000 elements per array, giving a 5 MHz video rate, which is not excessive. With a charge transfer efficiency of 0.9999, the number × inefficiency product is Ne = 0.5, which would seriously degrade the system MTF. We will therefore have to break each array into ten or more sections, which in any case would probably be done to get a good yield of high quality elements.

The infrared detector circuitry has to be more complex because of the radiation chopping. If we need a 10 ms exposure, and chop at 500 Hz to get above the 1/f noise, it is not satisfactory merely to integrate on the hybrid HgCdTe/CCD chip for ten cycles; to do so would lose the benefits of chopping. Fig. 3.6-1 shows a concept for how the signal and noise should be treated; it is by no means optimized, but shows how existing technology might be applied to the LEST IR circuitry.

The 500 Hz chopper is open for 1 ms, during which time the HgCdTe output signal-plus-noise is integrated in the diffusion area. After 1 ms the transfer gate opens momentarily to fill the CCD register. The chopper then closes and, while the HgCdTe output noise is being integrated, the register is read out to the A/D converter at a 633 KHz video rate. This process is repeated, so that the converter is alternately processing S + N and N. With a register and differencer we alternately get (S + N) -N and N - (S + N) at 1 ms intervals. The "valid data" switch closes every 2 ms to pass the original 500 Hz signal. A bank of nine 633 element registers and an adder then gives the desired 10 ms of integration.

3.6.3 Radiometric Calibration

Calibration of the thermal channels can be accomplished using a calibrated blackbody shutter which obscures the optical path immediately after the primary mirror. This shutter will be activated during the turnaround time at the end of each scan. It will consist of a flat plate with a contiguous pattern of small holes or cavities machined into its surface. When coated with a high emissivity black paint such as 3M Black Velvet (type 401-C10) this type of blackbody has a measured emissivity above 0.997. Therefore a precise knowledge of temperature will yield a secondary blackbody standard of known radiant energy.

The temperature of the shutter can be measured to better than 0.1°C accuracy using Platinum Resistance Thermometers. The isothermal properties of the shutter can be controlled to better than 0.1°C using a flat heat pipe as the substrate for the blackbody cavity face.

Operationally, the shutter-derived signal would be used in a dc feedback loop as a reference or clamp level for the video in all channels.

Since voltage versus radiance is a linear function for all detector types used in LEST, the radiance from the scene can be accurately measured by comparing the scene voltage to the clamp voltage.

The zero radiance point required for a two point check of the calibration curve can be achieved by viewing space occasionally during the time the gyros are updated. This poses no problem for the temperature control subsystems.

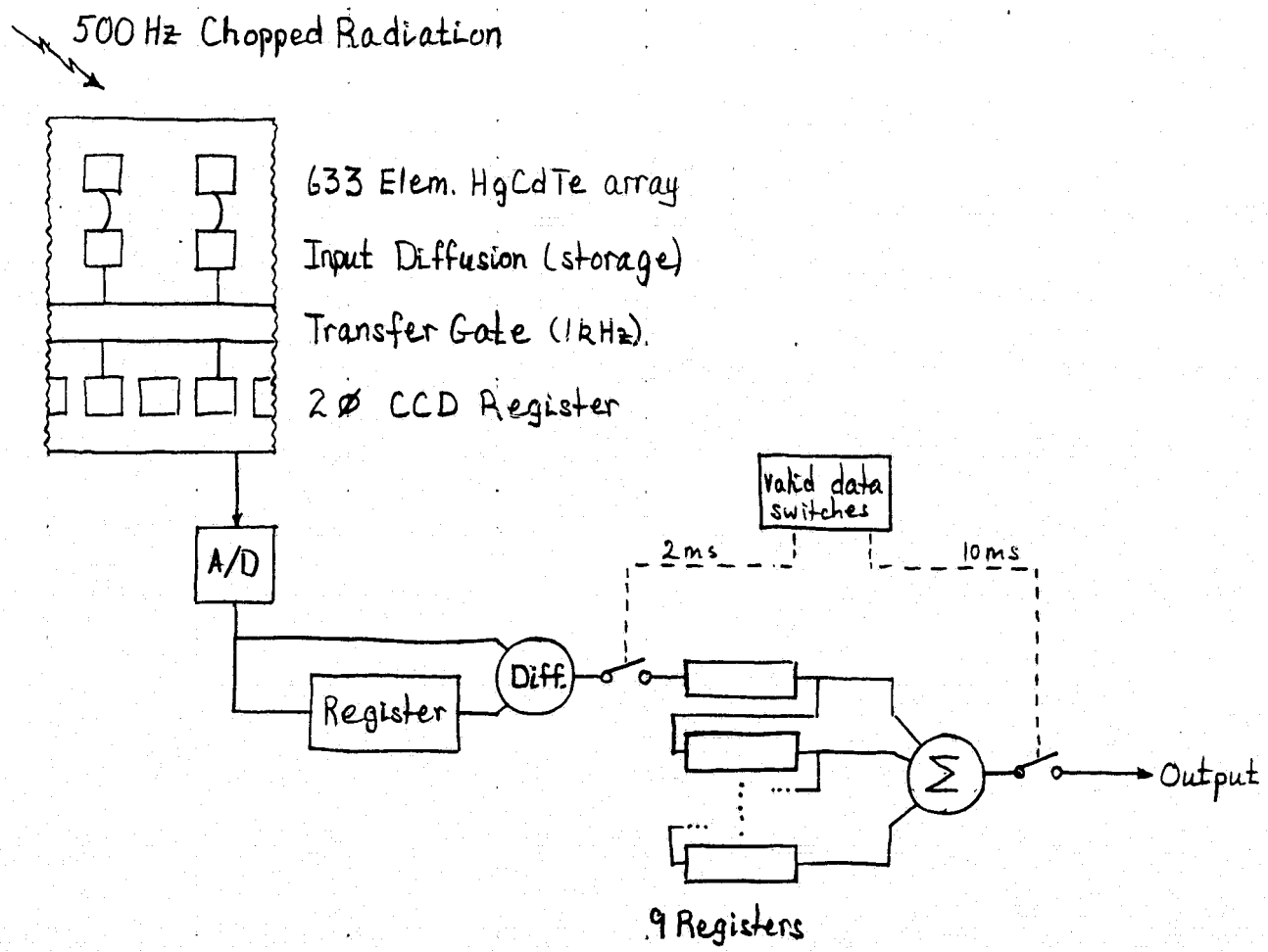

Fig 3.6-1 IR Detector Circuit Concept

Both space and the blackbody shutter can be used as zero references in all bands below 1.68μm.

Bright celestial objects may be used for periodic checks on the spectral reflectivity of the telescope mirrors.

The maximum point of the "visible" band calibration curve can be calibrated in orbit using reduced aperture side looking prisms that reflect the sun to illuminate a small portion of the telescope entrance pupil.

The foregoing techniques are similar to those used successfully for in-orbit calibration of MSS and VISSR.

3.7 DETECTOR COOLING

The design of a passive radiation cooler to achieve the 110°K detector temperature discussed above depends upon the required operating temperature, temperature margin, cooling capacity, orbit altitude, sun and earth positions with respect to the cooler location, and spacecraft appendages within the field-of view of the cooler.

For an earth-oriented three-axis stabilized spacecraft at synchronous altitude, the most important parameters in determing the cooler configuration are the sun position and spacecraft components within the cooler field-of-view. The solar inputs to the cooler are minimized by mounting the cooler in the plane of the ecliptic. The spacecraft thermal input can be minimized by spacecraft design such that no spacecraft elements are within the cooler field-of-view. Our LEST concept uses both of these techniques; the spacecraft is rotated 180° on its axis twice a year, and the solar paddles are opposite the cooler.

For the purposes of this study, three 3-stage cooler configurations were studied. One, Fig. 3.7-1, was for a spacecraft which can be rotated twice a year, is tilted 7° out of the orbit plane, and has no spacecraft elements within the cooler 75.0° half angle conical field of view. This represented the probable LEST case. For comparison we analyzed the same concept except that spacecraft elements were allowed up to a cooler conical field-of-view angle of 63.5°. The third concept was for a spacecraft which is never rotated but is tilted 7° out of the orbit plane, and which can accept spacecraft elements up to a cooler conical field of view half angle of 60.0°. Spacecraft elements outside the stated fields-of-view have negligible effect on the cold plate temperature or cooling capacity.

The performance characteristics of the three cases are shown in Figure 3.7-2, and Figure 3.7-3 shows the selected LEST concept in greater detail. Parasitic heat leaks due to electrical wires and detector fields-of-view are considered to be part of the thermal load and are not included in these charts.

3.7.1 Design Description

The baseline design assumes a spacecraft which is rotated 180° twice a year at the equinox, has no spacecraft elements inside the cooler 75.0° half angle conical field-of-view, and the spacecraft axis is tilted 7° out of the orbit plane.

Figure 3.7-1 is a crossectional view of this design. The other two coolers are quite similar, differing primarily in angles and depths. Twelve inches was chosen as the cold plate diameter for all three passive coolers in order to

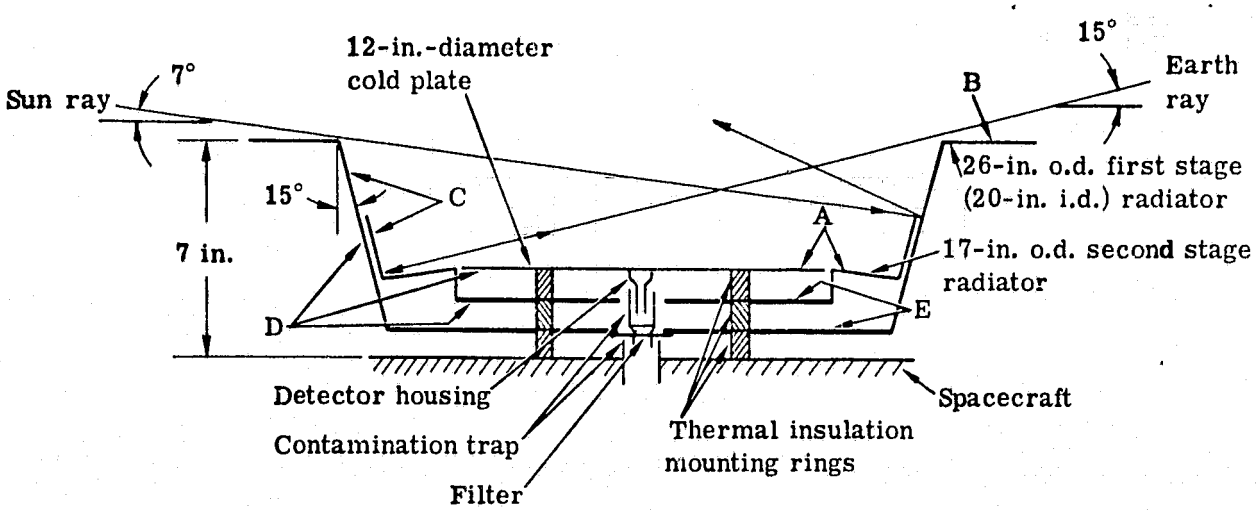

Finishes:
A—White paint
B—Second surface mirrors
C—Denton silver
D—Multilayer insulation
E—Vapor deposited gold

Fig. 3.7-1 — Three-stage shallow cooler for 7-degree sun angle

Table 3.7-1 — Properties of Thermal Finishes

Finish	Solar Absorptivity (α)	Infrared Emissivity (E)
White paint	0.4 (degraded)	0.9 (at ambient temperature) 0.85 (at cyrogenic temperature)
Second surface mirrors	0.10 (degraded)	0.85 (at ambient temperature) 0.8 (at cryogenic temperature)
Denton silver	0.10 (degraded)	0.05 (degraded)
Multilayer insulation	0.05 (effective)	0.05 (effective)
Vapor deposited gold	0.5 (degraded)	0.05 (degraded)

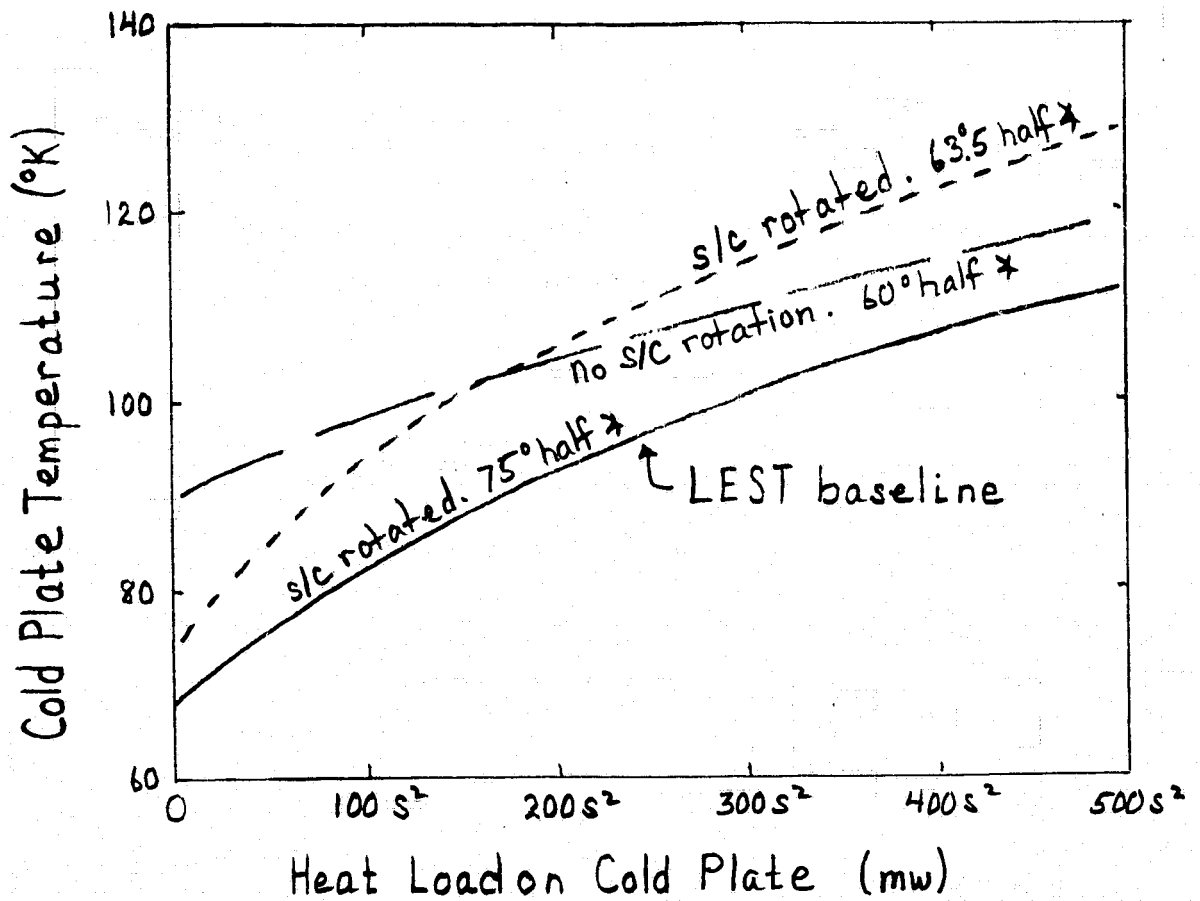

Fig. 3.7-2 Performance of Three 3-Stage Cooler Concepts
S/C at 301°K, S = Cold Plate Diameter (ft)
Heat Load on Middle Stage = S^2 watt

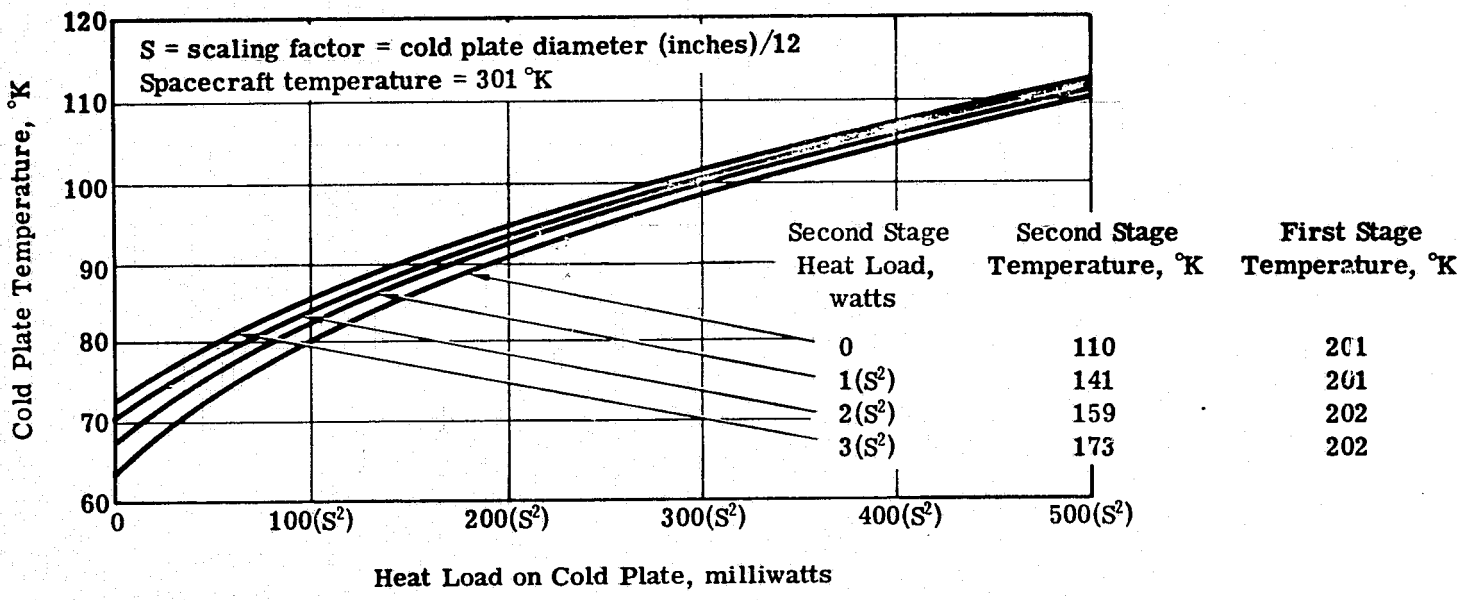

Fig. 3.7-3 — Cold plate temperature versus heat load on cold plate for three-stage shallow cooler for 7-degree sun angle

provide a basis for comparing performance and size. Cooler capacity is a function of the square of the cold plate diameter if all cooler dimensions are scaled up or down linearly. All coolers are three stage in order to obtain maximum cooling capacity and to provide a second and third temperature level for detector operation if desired or required.

All coolers use five basic thermal finishes whose properties (worst case conservative values for analysis purposes) are given in Table 3.7-1.

The first stage (outer) cone is designed to reflect the solar energy out of the cooler with a single reflection, and to prevent any direct solar input into the second stage (inner cone) and third stage (cold plate), or any earth IR and albedo input to the cold plate. The first stage radiator cools the first stage cone in order to minimize the thermal radiation and conduction heat inputs to the second stage and the radiation heat input to the cold plate.

The second stage is designed to reflect the earth IR and earth reflected solar energy out of the cooler with a single reflection and to prevent any earth related energy from reaching the cold plate. The second stage radiator cools the second stage in order to minimize the radiation and conduction heat inputs to the cold plate.

The physical configuration shown is not the only possible configuration. In fact, slight changes, such as moving the first stage radiator inside the first stage cone at the level of the second stage cone aperture, could improve the cooler performance slightly by reducing the radiation coupling between the first stage and cold plate as well as reduce the first stage temperature slightly. Hence, a detailed study of various configurations could result in the optimum shape for maximum cooler performance. Also a trade study of cooler performance versus first and second stage radiator sizes could be made to determine the minimum size cooler which could be used once the detector heat loads, required operating temperatures, and parasitic heat leaks, have been determined.

For all cooler designs the exposed inner cone surfaces (those surfaces which can see each other and/or the cold plate) must be highly polished prior to finishing with gold or silver in order to achieve maximum specularity as well as to achieve minimum values of α and E.

The thermal isolation mounting rings are designed to minimize the conduction coupling between stages and still provide sufficient strength and alignment during the launch environment.

Pre-cooldown thermal control can be achieved by use of a deployable cover, ground commanded or sensor controlled heaters, or a combination of both.

Sensor temperature control can be achieved by use of sensor controlled heaters at each detector array.

3.7.2 Cooler Analysis

All cooler designs were analyzed using a steady state, N-body computer program. Four body thermal nodal models of the coolers were generated with the nodes as follows:

Node 1	Cold Plate
2	Second Stage
3	First Stage
4	Spacecraft

The thermal inputs and couplings were computed for worst case conditions; Fig. 3.7-3 shows the results.

3.7.3 Estimate of Required Cooler Capacity

The heat load to be radiated by the cooler can be determined by calculating the parasitic radiative and conductive fluxes into the cold plate.

The conductive losses per °K are

$$K = \frac{K_S A_S}{L_S} + \frac{K_C A_C}{L_C} \quad N_W$$

where

K_S is the thermal conductivity of the support tube = 0.005 W/in °K

A_S is cross section area of tube = 0.62 in^2 (for 2 in. diameter 0.1 in. thick tube)

L_S Length of Support tube = 10 in.

K_C is the thermal conductivity of constantan wire = 0.5 W/in °K

A_C is the cross sectional area of the wires = 8×10^{-5} in^2

L_C is the length of the wires = 12 in.

N_W is the number of wires = 50

The total conduction loss is (3.1 + 1.7 =) 4.8×10^{-4} watts/°K, and totals 96 mw for a 200°K ΔT.

The radiative loss consisting of the view factor between the cold relay optics and the 300°K end of the relay optics tube is given by:

$$Q_R = \frac{\pi D^2}{4} \times \epsilon \times \sigma \, (T_2^4 - T_1^4)$$

where

D is the diameter of the support tube = 2 in.

ϵ is the effective emissivity = 1

T_1 is the temperature of the detector = 105°K

T_2 is the temperature of the support end = 300°K

σ is Stephen Boltzman constant - 3.66×10^{-11} w/in^2/$°K^4$

Q_R = 0.92 watts

Detector generated I^2R loss is 2000 elements at 10×10^{-6} per element equal to .020 watts.

Summary of thermal inputs to cooler cold plate:

Conduction from supports and detector wires	0.096 watts
Radiation Loss	0.92
Detector I^2R Loss	0.020
Total Parasitic Heat Inputs	1.04

Based on the cooler design of Fig. 3.7-1 and data of Fig. 3.7-3, the cooler cold plate diameter would equal 0.48 meters and the maximum cooler diameter would be 1.05 meters for a parasitic heat load of 1.04 watts and an array temperature of 105°K.

3.7.4 Detector-Optics Interface

The interface or transition between the cooled detector array assembly and the warm optics requires design considerations that should minimize the heat leak to the cooler, reduce problems of optical defocus and misalignment, and also provide effective anti-contamination of cold optics.

The detector, which is in good thermal contact with the cold plate, requires effective thermal isolation from the warm spacecraft. This generally means the detector mount will tend towards small cross section, relatively non-rigid support structures such as thin stretched bands, thin wall tubes, etc. Good design practice would then dictate that the detector and fast optical relay be solidly connected and the transition between cold and warm be done with slower optics.

These principles are used in the detector-relay optics concept in Figure 3.7-4. The basic structural element tying the cold plate, detector assembly relay lens and corrector plate is a polycarbofil tube. The tube is supported near the detector end by stretched thin Kapton bands from a support cone. Although a tolerance analysis is required for verification, this structure should provide the necessary rigidity between the relay and the f/12 bundle from the telescope.

The tube is vented into an anti-contamination trap to prevent contaminant accretion on cold optics. With no exposed cold optics the thermal channels will be free of the signal degradation problems that have plagued many of the current operational radiometers using passive coolers.

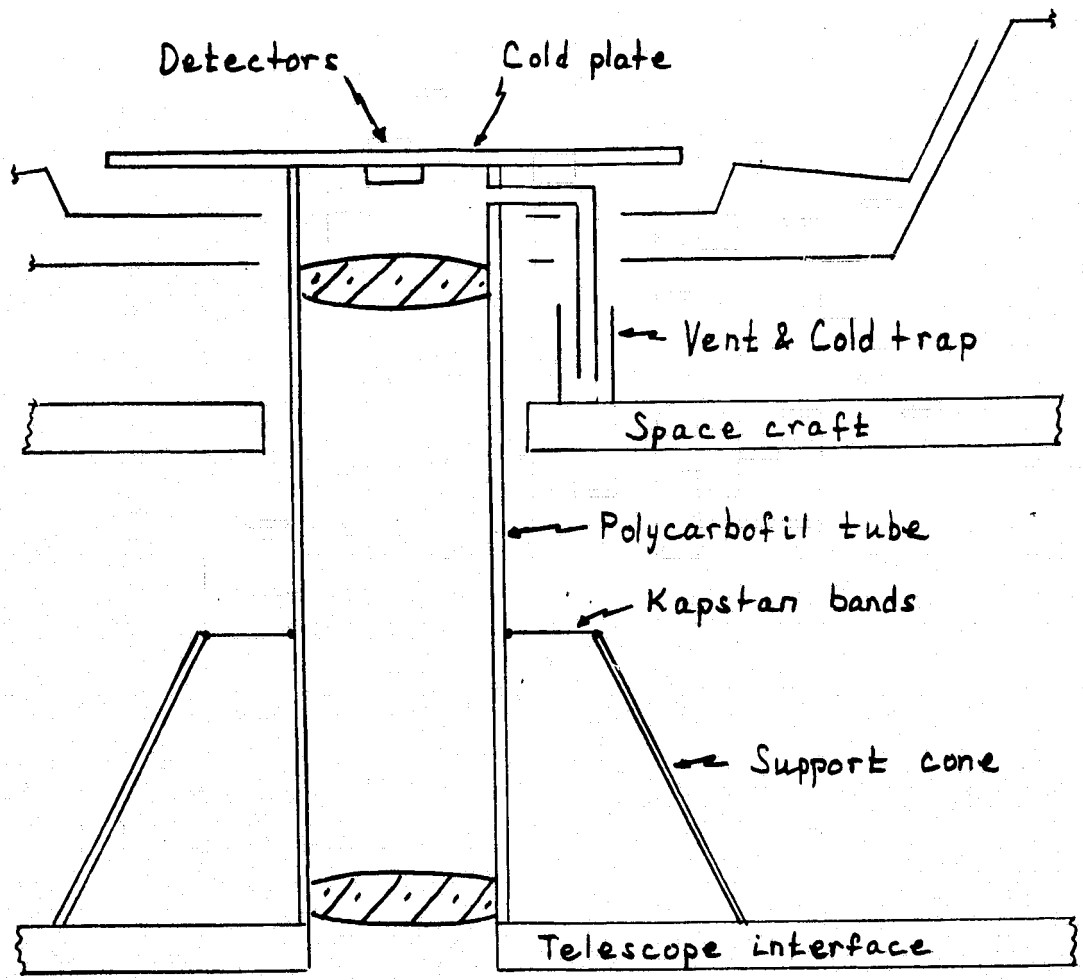

Fig. 3.7-4 Schematic of Detector-Relay Lens Assembly for Detectors Requiring Cooling

3.8 MASS PROPERTIES

A preliminary weight estimate for LEST is presented in Table 3.8-1, and for the total SEOS spacecraft in Table 3.8-2. The material and section thickness is included in Table 3.8-1 for most items. Weight contingencies, consistent with the conceptual nature of the design at this time, are identified in the Tables.

The weight of the primary mirror is based on monolithic (fused egg crate) construction, 56 inch diameter and 6 inch overall thickness. Front and back plates are each one half inch thick, and the core weight is twenty percent of an equivalent solid section.

Weights for the truss structure that supports the secondary mirror, and the conical focal area support structure are for graphite epoxy construction.

The weight of the entire structure surrounding the telescope optical assembly has been included in the LEST weight, Table 3.8-1; i.e., 295 kg for meteoroid shield and 237 kg for the transition structure. The 127.5 kg structure listed in Table 3.8-2 is the structure required for mounting the spacecraft attitude control, communication and power systems within the total structure.

It can be noted that both the LEST weight and the total spacecraft weight (including the assigned contingencies) are less than the specified target weights. The principal areas of reduced weight compared to the Phase 1 results are:

- Greater use of graphite epoxy in place of invar or aluminum.
- Simpler focal plane area; elimination of all but two of the 12 or more relay lenses planned at the end of Phase 1.
- Limitation of station keeping to E-W only.

SEOS mass properties, including center of gravity and moments of inertia, are summarized in Figure 3.8-1.

Table 3.8-1

DATE: OCT 11 1974
REV: ____ ____

LEST DETAIL
WEIGHT STATEMENT

SH____ OF ____
REF. DWG. 917870

1	2	3	4	DESCRIPTION	CODE	t	MTL.	QTY.	WEIGHT Kg W/O CONTIN.			WEIGHT Kg W - CONTINGENCY		
LEST				SYSTEM ASSY							1199.6			1397.8
	STRUCTURAL ASSY				1000					473.6			544.6	
		TRANSITION STRUCTURE			1101	.2	AL	1	237.8			273.5		
		METERING TRUSS ASSY			1102		GE	1	43.1			49.6		
		PRIM MIRROR SUPT ASSY			1103		INV	1	63.3			72.8		
		SECOND MIRROR SPIDER			1104		GE	1	11.3			12.9		
		LIGHT BAFFLES			1105	.06	AL	2	7.5			8.6		
		DETECTOR SUPT STRU			1106	.1	GE	1	61.9			71.2		
		BULKHEAD			1107	.1	AL	1	48.7			56.0		
	OPTICS ASSY				2000	-	-	1		179.6			206.6	
		PRIMARY MIRROR			2001	6	OLE	1	170.5			196.1		
		SECONDARY MIRROR			2002	2	OLE	1	9.1			10.5		
	DETECTOR ASSY				3000	-	-	1		108.2			124.3	
		FOLD ASSY			3001		GE	1	4.6			5.3		
		FOLD ASSY			3002		GE	1	2.5			2.9		
		FOLD ASSY			3003		INV	1	2.9			3.3		
		IR SOUNDER			3004		EZE	1	16.7			19.2		
		EZ RELAY ASSY			3005		AL	1	13.3			15.3		
		F1,3 RELAY			3006		AL	1	13.3			15.3		
		F5 FOCAL PLANE			3007		EZE	1	.2			.2		
		F5 FOCAL PLN STRU			3008		GE	1	28.9			33.2		
		MIRROR			3009		FS	1	14.5			16.7		
		COOLER			3010		-		11.3			12.9		
	PERFORMANCE CONTROL ASSY				4000	-	-	1		29.3			37.0	
		FOCUS SENSOR ASSY			4001	-	ELE	1	3.6			4.7		
		DECENTER ASSY			4002		ELE	1	6.9			8.9		
		TILT ASSY			4003		ELE	1	7.5			9.8		
		SECONDARY			4004		-	1	11.3			13.6		
	THERMAL SYSTEM ASSY				5000	-	-	1		19.7			22.7	
		PRIM MIRROR INS			5001		NRC	1	1.9			2.2		
		SECONDARY MIRROR INS			5002	1	NRC	1	.3			.4		
		PASSIVE			5003	1	NRC	1	17.5			20.1		
	METEROID SHIELD ASSY				6000	.09	AL	1		295.9			340.3	
	ELECTRONICS ASSY				7000	-	-	1		93.3			122.3	
		MESA			7001	-	ELE	1	42.9			49.3		
		EDAP			7002		ELE	1	13.6			17.7		
		DETECTOR BABLE			7003		ELE	1	5.7			8.6		
		CABLE			7004		ELE	1	31.1			46.7		

TABLE 3.8-2

SEOS SYSTEM WEIGHT

		WEIGHTS (kg)	
ACS	71.0		
Power (Including 1 KW Array)	155.2		
TT&C	35.0		
Wide Band Communication	65.0		
Thermal	25.0		
Station Keeping (E-W Only)	68.0		
Harness	45.0		
Adapter and Separation System	135.0		
Structure	127.5		
Spacecraft		726.7	
Spacecraft Contingency		181.7	
Spacecraft Total			908.4
Estimate for Data Platform and Microwave Sounder		65.0	
Total Without Telescope			973.4
Telescope (With Contingency)		1,397.8	
Total SEOS			2,371.2

FIGURE 3.8-1

SYSTEM MASS PROPERTIES

DESCRIPTION	WEIGHT WITHOUT CONTINGENCY	WEIGHT WITH CONTINGENCY	$\bar{X}$	$\bar{Y}$	$\bar{Z}$	YAW I_X	PITCH I_Y	ROLL I_Z
LEST	1199.6	1397.8	2.21	0.02	0.0	867.5	2387.6	2379.7
SPACE CRAFT	791.9	973.4	1.20	-0.18	-0.08	521.1	1383.1	1513.7
SEOS	1991.5	3271.2	1.81	-0.06	0.03	1412.36	4258.7	4399.9

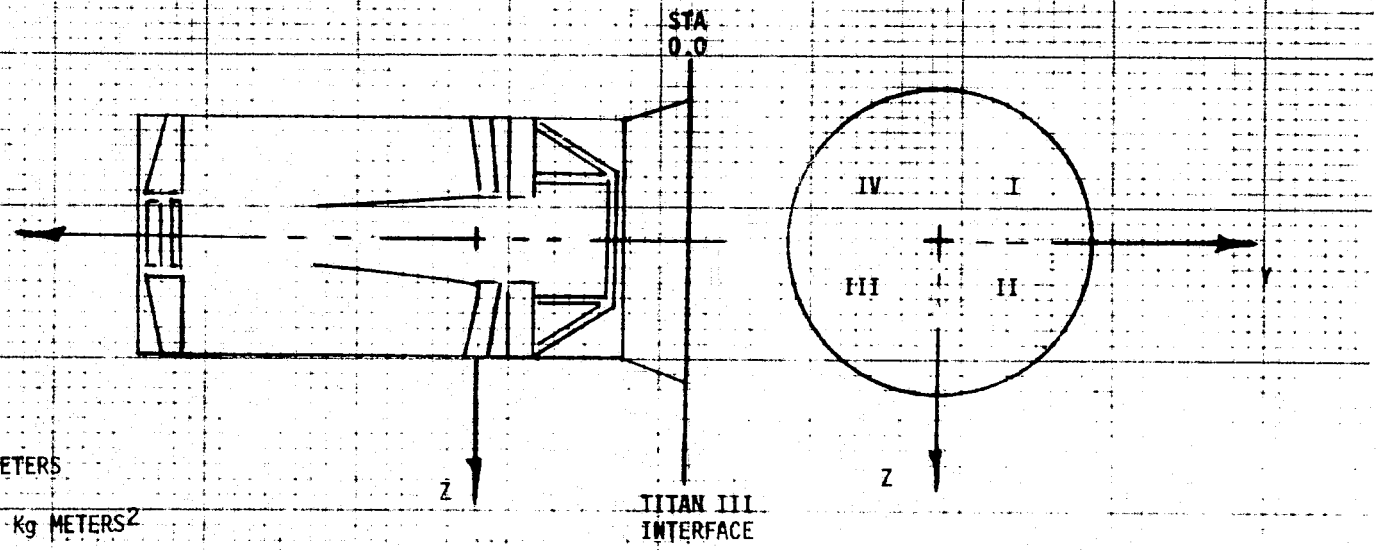

WEIGHT Kg

CENTER OF GRAVITY - METERS

MOMENTS OF INERTIAS - Kg METERS^2

4. ALTERNATE SYSTEMS

The full-up system that has been described in Section 3 meets most, and exceeds many, of the requirements sets imposed by the large number of potential SEOS applications in the full-up mission. In accordance with the statement of work, we have also considered strip-down and minimum design possibilities.

4.1 STRIP-DOWN DESIGN

The objective of a strip-down LEST design would be to prove the SEOS concept in advanced demonstration missions at reduced costs. The requirements of the strip-down system and restrictions on its design are as follows:

Resolution (EIFOV) - same as full-up

Detector field - selectable

Sensitivity (NE$\triangle\rho$, NE$\triangle$T) - same as full-up

Spectral bands - same as full-up

Area coverage rate - lower, as required

Total optical field - same as full-up

Configuration - should be capable of "growing" to full-up

The parameter that is selectable in satisfying the above stated requirements is the number of detectors. In particular, we propose that the field of view of each array be the central 0.2 degree of the 0.6° lateral field of the full-up configuration. Thus, but one third as many detectors, preamps and A/D converters would be required. Also, the total detector data rate would be reduced to one third. This would result in some, but not a dramatic, reduction in total LEST cost.

The time required for scanning a given area would be three times higher for the strip-down system. EIFOV and sensitivity performance would be unchanged, since the same linear scan rate would be employed as for the full-up system.

No significant weight reduction would be offered for the strip-down system since the aperture diameter and basic telescope configuration would be unchanged.

4.2 MINIMUM SYSTEM

The requirement for the minimum system is that it offer the same performance as the strip-down, but that growth capability to full-up is not required. Again, since the same EIFOV and sensitivity requirements must be met, a 1.4

meter aperture diameter telescope would be required. The corrected field for the minimum system would be 0.2° rather than 0.6°; therefore, the design and manufacturing costs for the relay and correcting optics would be reduced. The lateral field of the detector arrays would also be 0.2°. In the field sharing concept shown for the full-up system essentially all of the 0.6° field in the scan direction is utilized to bring images to the ten detector arrays and the IR sounder simultaneously. If the field were reduced to 0.2° for a minimum system design it would not be possible to image at all arrays at once. Therefore, multiple swaths of the same area would be required as some form of focal plane selector is operated between sweeps. An alternate approach to multiband operation with a narrow (0.2°) field would be to use beam splitters for energy sharing. However, this is not attractive because of the loss of sensitivity, and the optical complications of beam splitters which have been discussed earlier.

It is questionable whether the modest cost savings in relay optics would justify the loss of full multiband operation implicit for the minimum system.

5. PERFORMANCE ANALYSIS

Our purpose in this section is to predict the performance of the baseline LEST in terms of EIFOV and NER. We need to do this only once because the frame times and fields of view of the Full-Up, Strip-Down and Minimum LESTs have been adjusted to allow a constant scan rate. While we present this data as the ultimate LEST performance, we appreciate that there may be further improvements possible if another iteration of tradeoff analysis were made.

In Phase 1 of this study we used such parameters as EIFOV, NER and scan rate for inputs to determine LEST hardware data such as aperture, f/number, detector dimensions, number of detector elements, and exposure times. The Asymptote Analysis method used for these tradeoff studies was thoroughly discussed in the Phase 1 Final Report. The ERIM requirements had been given in such a way as to make it natural to hold NER fixed while striving for best EIFOV by trading sensor parameters. The result was a standardized aperture diameter and three compromise f/numbers, but detector dimensions and exposure times were allowed to vary at will.

In Phase 2 we have adopted a few compromise exposure times in order to make the sampling logic as simple as possible. We have also adopted a standard scan rate of 2.2 mr/s to simplify the vehicle control subsystem. This gives the one-tenth worst case earth resources rate discussed in the Phase 1 Final Report Supplement, and also matches the meteorological monitoring requirement.

In the following subsections we will develop the predictions of LEST performance based on these adopted compromise parameters, and will compare the results with the NASA requirements. We start by outlining the method of analysis, and we list the input data. The resulting predictions show that in most cases we will meet the required EIFOV and NER for the various Earth resources applications. We also find that LEST achieves over half of the EIFOV or NER goals for the meteorological applications.

5.1 INPUT DATA

In this section we will specify and give the basis for the various parameter values used to calculate the EIFOV and NER predictions.

5.1.1 Optics

There are two parameters which directly affect MTF and therefore EIFOV; these are obscuration and wavefront error. The amount of obscuration will depend on the field of view and the degree of baffling required to keep stray light out

of the focal area. An advantage of the relayed optics we have proposed for LEST is that there is an intermediate image where a stop can be placed to control stray light. As a result we can reasonably adopt a value of 30% (diameter) for the central obscuration. Without the stop it would be necessary to have much more complex stray light control, especially since some observations must be made at local midnight, when the sun is illuminating the primary mirror.

The wavefront error is wavelength dependent. In an all-reflective system the relation is: $WFE_\lambda = \lambda_0 \ WFE_0/\lambda$, where λ_0 is the design wavelength for WFE specification. The situation is more complex in most refractive systems, where chromatic aberrations can strongly affect performance. Wavefront error budgets were discussed in Section 3.1.2, where we saw that we must consider the contributions from design, static (manufacture, alignment, and test) and dynamic (gravity release, thermal misalignment, vibration). Adopted values are presented in Section 3.1.2 and in the table summarizing performance, Table 5.3-1.

System transmission depends on the amount of obscuration, reflectances of the mirrors, transmission of the lenses, and filter transmissions. All but the filters have been defined, Section 3.2.8. The transmission of the filters will depend on amount of blocking (background rejection), and the steepness of the slopes on either side of the pass band. Until detailed filter specifications have been established, we will use an average filter transmission value of 60%. The resulting system spectral transmission is given in Table 5.3-1.

5.1.2 Detectors

We have chosen four detector types to cover the thirteen ERS bands and nine Met bands in LEST. The thirteen bands between 0.4 and 1.0 μm will be assigned to four silicon CCD arrays of 4900 elements each; this includes bands E1-E11 and M1,2,3,9. While we have assumed room temperature operation, there may ultimately be tradeoffs that would call for moderate cooling. The current state-of-the-art is a noise equivalent signal of NES = 40 electrons, and we have used this for calculating spectral noise equivalent exposure, NEE. However, there are already some indications that CCD development progress will reduce NES to 20 electrons or less. The NEE calculation assumes the relative spectral response of thin silicon and a quantum efficiency at 0.6 μm of 75%. The resulting absolute spectral NEE is given in Fig. 5.1-1. The dimensions of the CCD element is taken to be 15 x 15 μm, but again CCD technology is improving so rapidly that substantially smaller sizes will soon be available. One possible result of this progress may be that we could use faster optics and thus perhaps reduce the number of f/numbers to be provided.

We will use multi-element arrays of PbS for bands E13 and M4. Again we have assumed room temperature operation, but there would be real detectivity gains if the PbS were put on the 150°K sun shield of the cryogenic radiator. We have not done this to date because we can meet the performance requirements without it. The E13 array is made up of 1960 elements each 15 x 15 μm in size; the M4 array consists of 104 elements each 280 x 280 μm. Performance of PbS is expressed in in terms of D*. We took average catalogue values for current single element detectors and have therefore assumed that the yield statistics for multi-element arrays will improve to give similar detectivities over the next few years. This may require some funded development

Band M5, at 3.8 μm, is beyond the spectral reach of PbS, even when cooled. We must therefore assign Band M5 a special material. PbSe would give

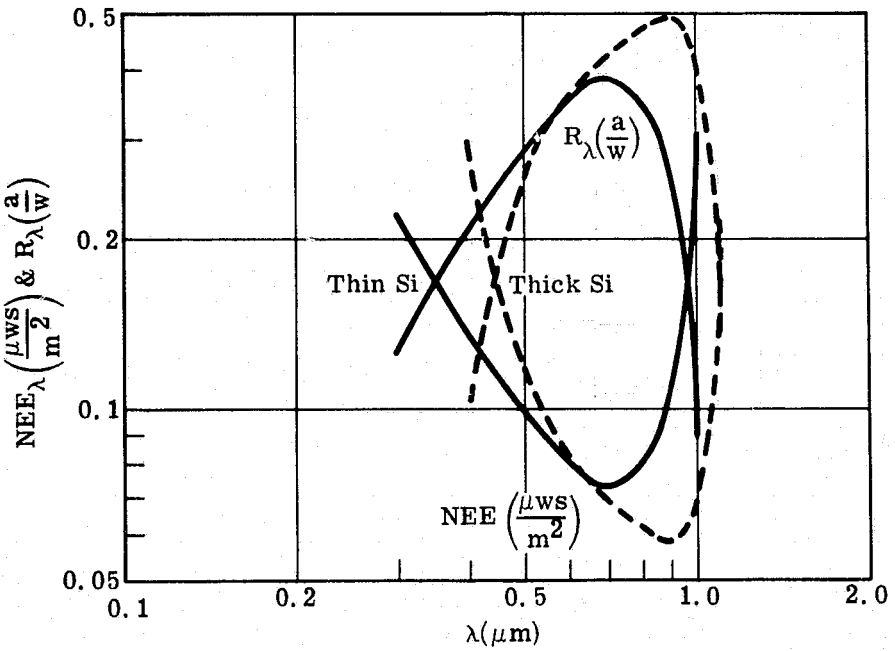

$$NEE\left(\frac{\mu ws}{m^2}\right) = 10^6\left(\frac{\mu w}{w}\right) \times NES(e)/e\left(\frac{e}{as}\right) \times R_\lambda\left(\frac{a}{w}\right) \times A(m^2)$$

$$R_\lambda\left(\frac{a}{w}\right) = q_{0.6}\left(\frac{e}{p}\right) \times Q_{0.6}\left(\frac{p}{ws}\right) \times \frac{R_\lambda}{R_{0.6}} \times \frac{1}{e}\left(\frac{e}{as}\right)$$

$q = 0.75$ (assumed)

$Q_\lambda = 5.0 \times 10^{18}\ \lambda\ (\mu m)$

$R_\lambda/R_{0.6}$ from NASA 335 P319 & EG&G

$e = 6.24 \times 10^{18}$

NES = 40 (assumed)

$A = 15 \times 15\ \mu m = 2.25 \times 10^{-10}\ m^2$

Fig. 5.1-1 NEE of Silicon CCD

the best D*, but experience has shown it is somewhat unstable with time. We have therefore chosen 100 x 100 μm InSb, which must be operated as cold as possible (110°K in our design). We will discuss Band M5 further in Section 5.4, along with other bands that do not meet the NER specifications.

Finally, we have three rows of 30 x 30 μm HgCdTe detectors, 635 elements to the row; these serve Bands E16-18 and M6-8. Band M6, at 6.8 μm, would benefit from a different chemical composition from the others, but in the interest of economy we have used a 10-12 μm peak HgCdTe. The arrays are cooled to 110°K. Like the PbS, the HgCdTe (and InSb) detectivity is taken from current single element performance data.

5.2 METHODS OF ANALYSIS

EIFOV is defined at the 50% system MTF point, irrespective of scene modulation or signal/noise ratio. NER is defined for sufficiently large targets that the MTF may be taken as unity. These two definitions, then, are mutually exclusive because they describe different conditions; the calculated NER cannot be achieved at the calculated EIFOV, and vice versa. One advantage of these definitions, however, is that the two performance parameters may be treated separately, as follows.

5.2.1 EIFOV

The system MTF is the product of the MTFs of the various component parts of LEST, with the assumption that all components have linear responses. We have based our EIFOV analysis on only the first three components: optics, detector, and image smear. These three will ordinarily be the largest contributors to LEST performance curves, but ultimately it will be necessary to examine the rest of the SEOS system. This would include digitization of the signal data processing, and image reconstitution on the ground.

The optics MTF always cuts off at D/λ (lp/μr), but its shape depends on obscuration of the aperture and wavefront error. We have taken computer generated MTF curves for this analysis, and have used the obscuration and wavefront error data presented in Section 5.1 above.

The detector MTF is a sinc-function cutting off at DF/ℓ (lp/μr). This implies a uniformity of response over the sensitive surface which will not usually be found in practice. However, we have no adequate statistical modeling on which to base a refined MTF curve.

The smear MTF is a sinc-function cutting off at $1/\dot{\theta}t$ (lp/μr). Since the detector is sampled every t seconds then the Nyquist limit is at $1/2\ \dot{\theta}t$ (lp/μr). For this reason we will terminate the smear MTF at the Nyquist frequency in the figures which accompany this discussion.

Figure 5.2-1 plots the development of system MTF for three representative ERS bands; E7 is visual, E13 is near IR, and E17 is thermal IR. The detector, optics and smear are represented by dashed lines, and their product is the solid line which is terminated at 50% modulation. The EIFOV at this point is found by dividing 18* by the angular frequency.

$$* \quad \text{EIFOV} = \frac{36 \times 10^6 \ (\text{m})}{\text{cutoff freq.} \ (\frac{\text{lp}}{\mu\text{r}}) \times 2 \ (\frac{\text{lines}}{\text{lp}})} = 18/\frac{\text{lp}}{\mu\text{r}}$$

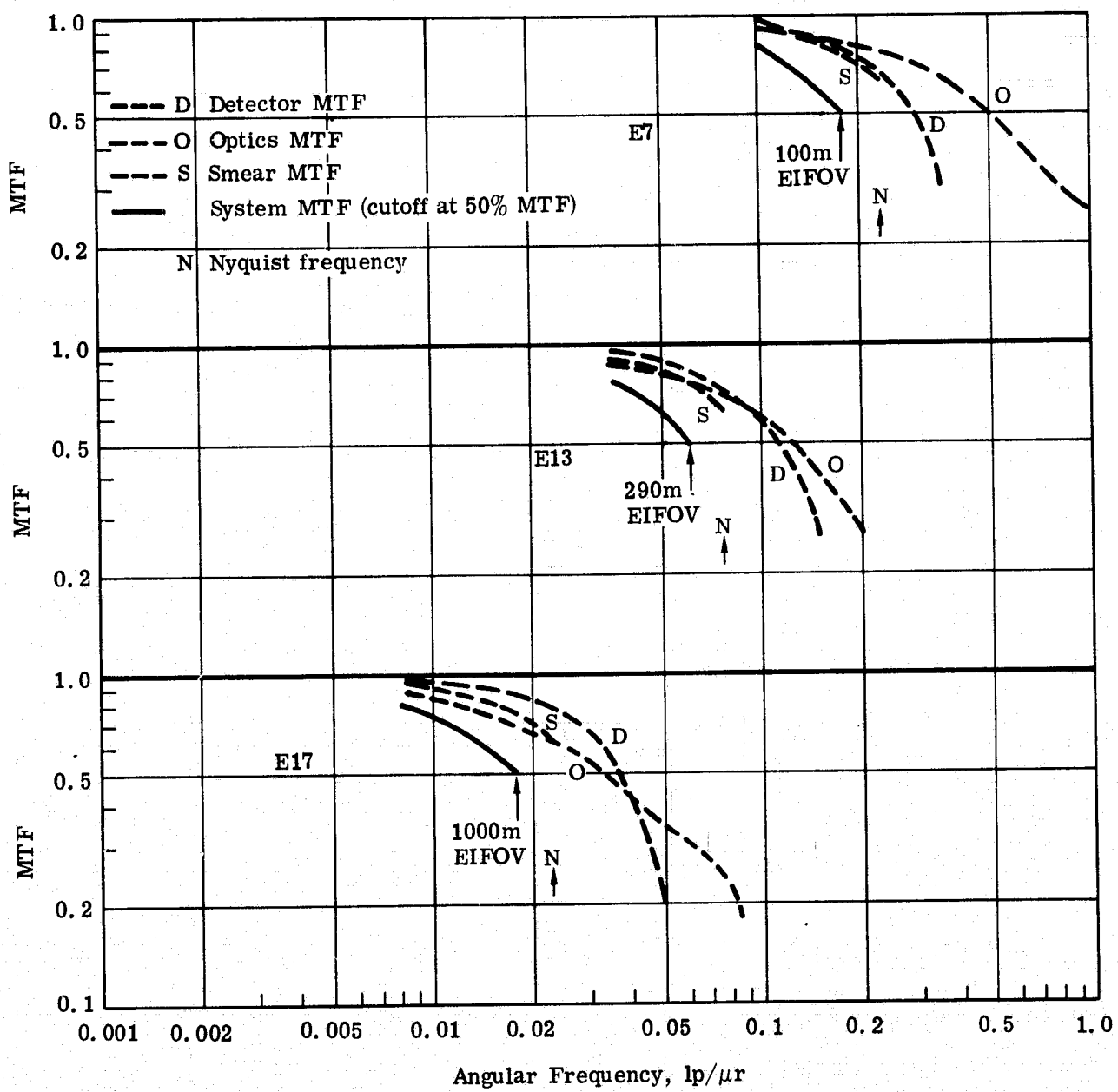

Fig. 5.2-1 MTF Development of Three ERS Bands

We see that no one component MTF predominates over the others. Optics are relatively more important in E17 than in E7, and it may be that the visual wavefront error budget could be relaxed a little and the thermal IR budget could be tightened. It is also worth noting that in all cases we are operating below the Nyquist limit, which should make aliasing prevention somewhat easier to accomplish.

The MTF development for some of the meteorological bands is strikingly different, Fig. 5.2-2. In the case of M2 and M3 we use the 15 μm ERS detectors in order to cut down on the number of arrays, even though the detector MTF is much better than required. In order to achieve the Met NER, however, we are forced to increase the sampling time from 1 ms to 10 ms (M2) and to 30 ms (M3). The result is that it is the smear MTF which determines the system performance in these two bands. We also see in Fig. 5.2-2 that M2 and M3 are Nyquist limited at 64% modulation before they reach the 50% modulation which defines EIFOV. In both M2 and M3 the limit is well within the 3000m EIFOV requirement, so there is no practical problem with this resolution ambiguity

Band M6 in Fig. 5.2-2 presents this same ambiguity, but again the Nyquist limit is well within the 6000m resolution specified for this band. In this case the same detector is used for M6 and E17, and we saw in the previous figure that there is little opportunity for tradeoffs of the detector dimensions.

Band M5 in Fig. 5.2-2 illustrates the difficulties that this band has presented from the beginning. It does not share its detector with any other band, so we can select the detector dimension for this band alone. We can also select the sampling time, t. In the case illustrated we have achieved 2000m EIFOV with a 100 μm detector and 16 ms sample time compared to a specification of 1200m. A smaller detector would move MTF_e to the right, but in order to preserve the NER (which is already out of spec) we would then have to expose longer, and MTF_i would move to the left. We will discuss this tradeoff in greater depth in Section 5.4.

We have been discussing MTF analysis as a method for predicting LEST EIFOV. As was pointed out in the Phase 1 Final Report, it is not necessary to do this analysis graphically. A useful and accurate estimate of EIFOV is obtained if we rss the EIFOV values of the optics, detector, and smear. In the performance predictions tabulated in the next section of this report we list these individual resolution contributors:

$$E_{optics} = 18\ a\lambda/D$$

$$E_{detector} = 18 \times 1.67\ \ell/DF = 30\ \ell/DF$$

$$E_{smear} = 18 \times 1.67\ \dot{\theta}t = 30\ \dot{\theta}t$$

$$E_{Nyquist} = 18 \times 2\ \dot{\theta}t = 36\ \dot{\theta}t$$

$$E_{system} = \left\{ \begin{array}{l} (E^2_{optics} + E^2_{detector} + E^2_{smear})^{1/2} \\ \text{or} \\ E_{Nyquist} \end{array} \right\} \text{ whichever is larger.}$$

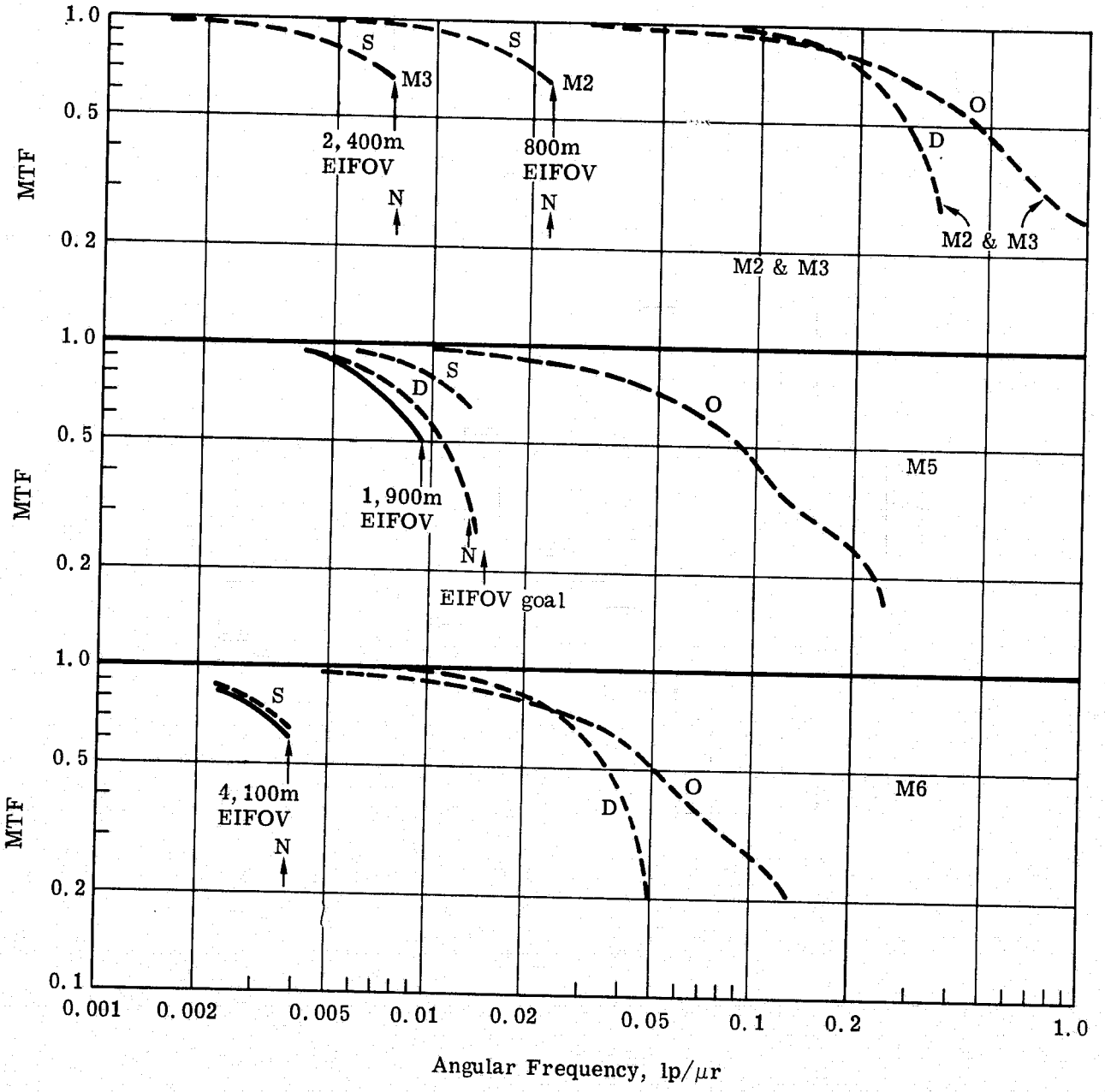

Fig. 5.2-2 MTF Development of Four Met Bands

Comparison of the tabulated system resolutions with the MTF analyses of Figs. 5.2-1, 2 show excellent agreement.

5.2.2 NER

The other performance parameter to be predicted is the NER ($\mu w/cm^2 sr$). For bands E1-11, M1,2,3,9, a Silicon CCD detector is assumed, with a noise equivalent exposure of NEE (see Fig. 5.1-1). Then we have the following relations:

$$NEE = \frac{H\,t}{SNR}\ \left(\frac{\mu ws}{m^2}\right)$$

$$H = \frac{\pi NX}{4F^2}\ \left(\frac{w}{m^2}\right)$$

$$N = \text{NER at SNR} = 1$$

$$t \quad (ms)$$

$$NER = \frac{0.127\ F^2\ NEE}{Xt}$$

The detectors used for the near and thermal ir bands are characterized by D*; with radiation chopping we get:

$$D^* = \frac{SNR\ \sqrt{\Delta f}}{H\sqrt{A}}\ \left(\frac{cm}{w\sqrt{s}}\right)$$

$$\Delta f = \frac{1}{2t}\ \left(\frac{1}{s}\right)$$

$$\sqrt{A} = \ell\ (\mu m)$$

$$\text{Chop factor} = 0.45$$

$$NER = \frac{6.25 \times 10^{11}\ F^2}{\ell X D^* \sqrt{t}}$$

We have used these two NER relationships for the performance predictions below.

5.3 PERFORMANCE PREDICTION

We have established that it is possible to use formulae to get very good estimates of the EIFOV and NER available from LEST; the equations give resolutions which are in excellent agreement with graphical MTF analysis. We have therefore used the formulae to calculate the performance predictions presented in Table 5.3-1.

The first two columns identify the spectral band. The next lists the wavefront error from Section 3.1.2. The factor a is the ratio of the MTF cut off frequency to the frequency at which the MTF is 50%; it was derived from standard curves for 30% obscuration.

Column 5 indicates the f/number at each detector array; with fixed aperture diameter this defines scale. Column 6 gives optical transmission from Section 3.2.8, and Column 7 gives the detector size. With size and scale specified, and a 0.6^o field of view, we then get the number of detector elements required, Column 8. An r indicates that the band is picked up by an array that has already been counted. The noise equivalent exposure for CCD arrays is from Fig. 5.1-1, and the detectivities of the various infrared detectors was derived from manufacturer's data, as discussed in Section 5.1.

Table 5.3-1 - Performance Predictions for LEST

1	2	3	4	5	6	7	8	9	10	11	12	13	14	15	16	17	18
														Predicted		Required	
Band	λ μm	WFE λ RMS	a	f	X	ℓ m	N_e	NEE $\frac{\mu ws}{m^2}$	D* $10^{\frac{10cm}{w\sqrt{s}}}$	t ms	E_o m	E_e m	E_i m	EIFOV m	NER $\frac{\mu w}{cm^2 sr}$	EIFOV m	NER $\frac{\mu w}{cm^2 sr}$
E1	0.44	0.15	5.1	f/5	0.36	15	4900	0.12		1	29	64	66	96	1.1	100	0.9
3	0.50	0.13	4.7	f/5	0.43	15	4900	0.10		1	30	64	66	97	0.74	100	4.8
4	0.55	0.12	4.6	f/5	0.44	15	4900	0.088		1	33	64	66	97	0.64	100	1.4
5	0.58	0.12	4.6	f/5	0.44	15	4900	0.082		1	34	64	66	98	0.59	100	1.6
6	0.62	0.11	4.4	f/5	0.44	15	r	0.078		1	35	64	66	98	0.56	100	1.0
7	0.67	0.10	4.2	f/5	0.44	15	r	0.074		1	36	64	66	99	0.53	100	1.2
8	0.72	0.093	4.1	f/5	0.43	15	r	0.074		1	38	64	66	99	0.55	100	2.1
9	0.80	0.084	4.0	f/5	0.41	15	r	0.080		1	41	64	66	100	0.62	100	3.7
11	0.92	0.073	3.9	f/5	0.41	15	r	0.12		1	46	64	66	100	0.93	100	6.2
13	2.2	0.096	4.2	f/2	0.32	15	1960		10.0	3	119	160	198	280	3.0	300	0.8
16	10.8	0.085	4.0	f/1.3	0.35	30	635		1.0	10	557	500	660	1000	3.2	1000	5.0
17	11.6	0.080	4.0	f/1.3	0.24	30	635		1.0	10	598	500	660	1000	4.6	1000	3.0
18	12.4	0.074	3.9	f/1.3	0.27	30	635		1.0	10	622	500	660	1000	4.1	1000	7.0
M1	0.62	0.11	4.4	f/5	0.43	15	r	0.078		1	35	64	66	98	0.58	300	3.0
2	0.75	0.089	4.1	f/5	0.42	15	r	0.075		10	40	64	(790)	790	0.057	3000	0.13
3	0.76	0.088	4.1	f/5	0.41	15	r	0.076		30	40	64	(2400)	2400	0.020	3000	0.03
4	1.63	0.19	5.9	f/2	0.19	280	104		8.0	10	124	3000	660	3100	0.18	3000	0.14
5	3.8	0.33	10.0	f/1.3	0.37	100	191		4.0	16	498	1650	1060	2100	0.18	1200	0.08
6	6.8	0.14	4.9	f/1.3	0.37	30	r		0.6	100	429	500	(6000)	6000	1.6	6000	1.2
7	10.8	0.085	4.0	f/1.3	0.35	30	r		1.0	10	557	500	660	1000	3.2	1200	1.8
8	12.3	0.074	3.9	f/1.3	0.27	30	r		1.0	10	617	500	660	1000	4.1	1200	0.67
9	0.88	0.076	3.9	f/5	0.41	15	r	0.11		1	44	64	66	100	0.85	300	3.0

There is an optimum exposure time for each band, but the electronics and data handling would be too complex if we had twenty-two separate sampling rates. For this reason we have used but six rates, Column 11, and even this may ultimately be reduced.

The next three columns list the EIFOV that results if the only limit were optics, element size, or image motion. In three cases the image motion EIFOV is enclosed in parentheses to show that we are Nyquist limited. This shows that the Nyquist limited resolution is larger than the resolution defined by 50% MTF as discussed in Section 5.2.

Columns 15 and 16 contain the predicted performance of LEST, and the last two columns show the worst case required performance for comparison. The predicted EIFOV is derived from the root-sum-square of Columns 12, 13, 14. The "required" EIFOV was specified as one number for the Met bands, and as a range of numbers for the ERS bands.

Thus Table 5.3-1 is a summary of the most important data concerning the predicted performance of LEST. We will discuss some aspects of the predictions in the following section.

5.4 DISCUSSION

We have presented a summary of some key parameter values and the resulting performance prediction in Table 5.3-1. We see that LEST is able to achieve all but one of its resolution goals, in some cases by large margins. We also find that LEST exceeds all but one of the NER goals for the visual bands, again by large margins. In the case of Band E1 we do not quite reach the goal of 0.9μw/cm^2 sr required for Application 2. However, the Application - Band matrix in Table 5.4-1 shows that LEST does meet three of the four E1 specifications.

At longer wavelengths we find that LEST meets two of the four worst case Earth resources NER requirements, but misses E13 and E17 by substantial amounts. Referring to Table 5.4-1 again, we see that LEST satisfies only one of the four applications requiring E13, and four of the seven applications requiring E17.

Thus we find that LEST does an excellent job in meeting or bettering most of its performance goals. It does not meet them all, however, and in the following section we will explore techniques by which LEST might come even closer to satisfying all the goals set for it by NASA's scientists. We will see, however, that the technologies or complexities of the techniques generally militate against their use in the LEST concept being discussed in this report.

5.4.1 Near IR: Bands E13, M4, and M5

The Phase 1 trade studies indicated that the 2.2μm (E13) and 1.63μm (M4) bands should be at an intermediate focal ratio such as f/2. At the time Band M5 was also included at the f/2 focus, but in Phase 2 it got moved to the f/1.3. If we could also move Bands E13 and M4 to the f/1.3 focus then we could drop the most difficult relay from further consideration. We have compared f/2 and f/1.3 performance for these two bands, with the following results:

E13	f/2	ℓ = 15μm	t = 3ms	∴EIFOV = 280m	NER = 3.0μm/cm^{2}sr
	f/1.3	15	1	280	2.2
M4	f/2	280	10	3100	0.18
	f/1.3	180	10	3100	0.12

Table 5.4-1 — Noise Equivalent Radiance ($\mu W/cm^2 \cdot sr$) for Essential Spectral Bands

Application	Band												
	E1	E3	E4	E5	E6	E7	E8	E9	E11	E13	E16	E17	E18
1			5.6	6.0	3.3	5.0	4.0						
2	0.9		1.4	1.6	1.0	1.2					5	3	7
3							2.1						
4						89.					19	12	14
5					3.3	5.3	3.8						
6	1.2		4.9		3.0	3.8					5	3	7
7			5.6	9.0	4.7	8.0	5.0				10	7	8
8						6.8							
9						3.4							
10						5.2		4.4					
11							30.						
12		7.2	3.8	4.4		4.0							
13				30.	20.				13.	6.8	16		12
14	3.8	9.6	5.8		3.0	5.0					5	3	7
15											2,050	1,040	2,060
16			8.3			6.4			6.2	1.8			
17	4.3	4.8								1.8			
18				68.		2.6		3.7	22.	0.8	16	10	12
19													
20						2.7		4.6					

Thus we bring M4 within the $0.14\mu w/cm^2$ sr NER specification, and come closer to the E13 Application 16 and 17 goals (NER = $1.8\mu w/cm^2$ sr). We would easily achieve both sets of NER goals if the PbS detector arrays were put on the cold plate already provided for the thermal IR bands, since the D* would probably double. Only the E13 Application 18 specification would still not be met.

While this is obviously a very attractive goal, it is unachievable with the existing f/1.3 relay design, which uses germanium lenses. Unfortunately, germanium does not transmit below 1.8μm, so it is opaque to the M4 wavelengths. The solution would be to use an all-reflecting f/1.3 relay, but, as we discussed in Section 3.2, this does not look promising.

Band M5 has been a consistant problem throughout this study, and it remains the one band where we have failed to reach its spatial resolution goal. As with all bands, it is possible to trade between EIFOV and NER, improving one at the expense of the other. We can use equation 2-10 and 2-11 in the Phase 1 Final Report to demonstrate the relationship (note correction of error in 2-11, and addition of 45% chopping factor):

$$\text{optimum } \ell^3 = 6.81 \times 10^{20}\, \dot{\theta} DF^5 / [XD^*_1(NER)]^2$$

$$\text{optimum EIFOV}^2 = (18a\lambda/D)^2 + 3\left|6.47 \times 10^{24}\, \dot{\theta}[F/DXD^*_1(NER)]^2\right|^{2/3}$$

These are plotted for Band M5 in Fig. 5.4-1, where we see that our baseline design offers a compromise on EIFOV and NER. With a 180μm detector we could have achieved the $0.08\mu m/cm^2$sr NER goal, but the EIFOV would be 3600m. Alternatively, we could have reached the 1200m EIFOV goal by using a 55μm detector, but now the NER would be $0.47\mu m/cm^2$sr. The best design point should be chosen by NASA's scientists.

5.4.2 Thermal IR Bands: E16, E17, E18, M6, M7, M8

There appears to be little we can do at this time to improve the NER performance of LEST in the thermal IR. We cannot increase the exposure time significantly, because we would rapidly exceed the spatial resolution goals. We cannot realistically assume still faster optics, even with immersed detector elements. Perhaps our best hope is that current HgCdTe development will result in a factor of two improvement in D*; this would allow the NER requirements for all but M8 to be met. Because single element HgCdTe performance is already more than twice our assumed values, we believe there is every likelihood of obtaining suitable arrays in a few years.

Even without an improvement in detectivity we could better the M6 NER goal by assigning it its own HgCdTe detector array rather than sharing an array with E17. We have two solutions: use larger detector elements, or tailor the material "mix" for shorter wavelength response. Either approach becomes very attractive if the E18 and M8 spectral pass bands turn out to be identical. Since this is already true of E16 and M7, then addition of a special detector array for M6 would do away with the need for a filter changer, and reliability would be enhanced.

We conclude from this discussion of the visible, near IR and thermal IR performance that the current LEST design will meet most of the goals set for it by the Earth resources scientists. While the meteorological performance is less satisfactory at this time, we believe that current progress in HgCdTe technology will allow LEST to meet most of these more difficult objectives in a few years.

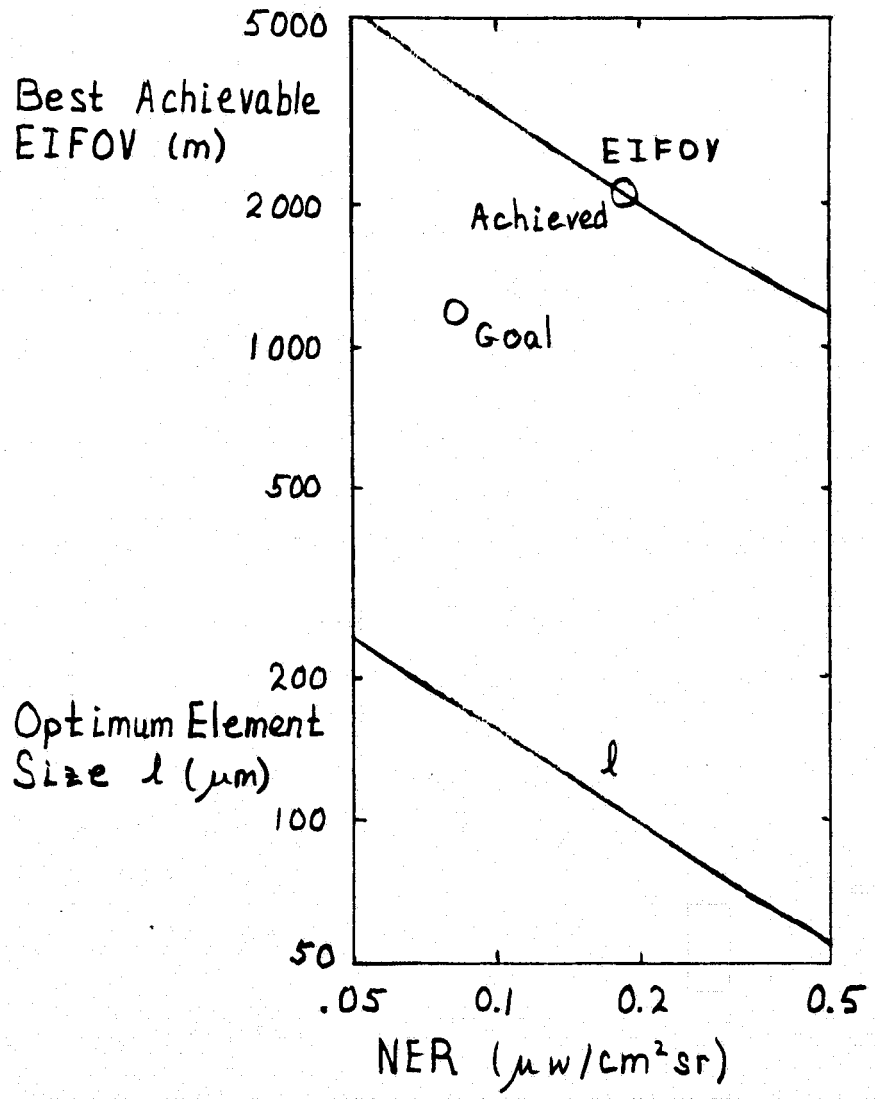

Fig. 5.4-1 EIFOV/NER Tradeoff, Band M5

6. DEGRADATION CONSIDERATIONS

SEOS is conceived of as having a five year life. During that time there will inevitably be a gradual degradation of performance due to dust accumulation on the cryogenic radiator and optics, radiation effects on various electronic components, and changing characteristics of thermal paints. Eventually the performance will be degraded to an unacceptable level, or there will be a catastrophic failure of some critical component. What happens then will depend on the availability and compatibility of a space Tug. Without the Tug, SEOS will have to be turned off and discarded. With the Tug, either replacement of failed or degraded parts can be attempted in space, or SEOS can be brought back to earth for refurbishment. Earth return would be more attractive because it allows restoration of major components such as the primary mirror, cryogenic radiator, and solar paddles.

In earlier sections we have discussed such diurnal performance degrading factors as stray light and thermo-optical misalignments. Now we will address some of the long-term effects which can cause a monotonic degradation of LEST performance. It turns out that most of these effects impact NER directly; they affect EIFOV only if the exposure time is increased in order to maintain an acceptable NER. Our discussions are qualitative because the mathematical analyses required to model radiation effects or reliability are far beyond the scope of this feasibility study.

6.1 RELIABILITY

The basic reliability requirement for LEST is that it operate for five years without refurbishment or resupply. This has not been converted to a probability of success, but we can reasonably expect a goal of perhaps 80% will be desired.

The most complete reliability analysis of a large long life space optical system was performed for the 3m LST. While LST has a fifteen year life expectation, it will be allowed periodic visits for maintenance (and to change scientific experiments); LST may even be brought back to earth for maintenance, if needed. There is a requirement that LST not require a re-visit for the first 2.5 years of operation. We therefore find that LST poses a less severe reliability problem than LEST.

The reliability analysis of the telescope and scientific sections of LST produced the following estimates for 2.5 year reliability:

OTA (telescope)	62%
SI (sci. instruments)	92-98% each
SI support equipment	97%

The lower OTA reliability is due primarily to three subsystems: thermal control, image motion compensation, and alignment and focus controls. Analysis showed that enough redundancy could be added in these areas to raise the OTA reliability to 80 to 85%, but not to the 95% which had been set as a LST goal.

The LEST optical system will have a similar thermal control concept, and redundancy is easily accomplished. There is no image motion compensation in LEST (but of course the body scanning must operate reliably). LEST will have alignment controls which can be operated open-loop on the basis of performance evaluation. It will also have a focus control which will perhaps have to be operated closed loop, but with a very low duty cycle. It therefore seems reasonable to set 90% as a reliability goal for the LEST telescope to operate at least 2.5 years. Of course this does not necessarily imply an 81% probability for a 5 year mission because burn-in will not continue but wear-out will accelerate.

Most of the LST scientific instruments have mechanisms for changing filters, as does LEST. They have internal optics, a few have movable gratings, and at least one has a cooled detector. The principal difference between the scientific portions of LST and LEST is that LST has very few detector elements (some are image tubes) while LEST numbers its detectors in the thousands. Such large numbers give an increased chance of an element failing, but the result is a blemish that can usually be tolerated. With suitable redundancy it seems unlikely that a catastrophic failure of an entire CCD array, for instance, will occur. The same can be said for the solid state circuitry that will process the commands and data output associated with the detectors.

We conclude from this discussion that we can probably achieve 80% probability of five year life for LEST. (This does not include degradations due to energetic radiation or contamination.) It is clear that redundancy will be required in most critical areas, and this increases both weight and cost. A more detailed reliability analysis should therefore be scheduled as early in the LEST Phase B effort as possible.

6.2 ENERGETIC RADIATION

SEOS will orbit above the Van Allen belts, and thus avoid their radiation except during launch. However, even at synchronous altitude there is enough trapped radiation to outweigh such direct sources as cosmic rays and solar flares. There are several estimates of what the annual trapped proton fluence will be, but we will use the values of Table 6.2-1. Since we expect the LEST structure to provide at least 0.1 inch of aluminum, we will probably have no more than 10^{10} protons per cm^2 per year, with energy near 20 Mev. This thickness will effectively remove the electron fluence, which externally will be on the order of $10^{16}/cm^2$ year with energies above 10 kev.

During 5 years in orbit the proton fluence inside LEST will be on the order of 5×10^{10} proton/cm^2. Figure 6.2-1 shows that we can probably design LEST to be unaffected by this flux; the electronics will evidently be more difficult than the detectors, but such spacecraft as COMSAT show that the job can be done.

TABLE 6.2-1

Proton Fluence and Shielding

Energy	Fluence	Stopping Distance, Aluminum
4 Mev	$3 \times 10^{12}/cm^2 yr$	0.005 inch
15	7×10^{10}	0.05
50	3×10^{9}	0.4

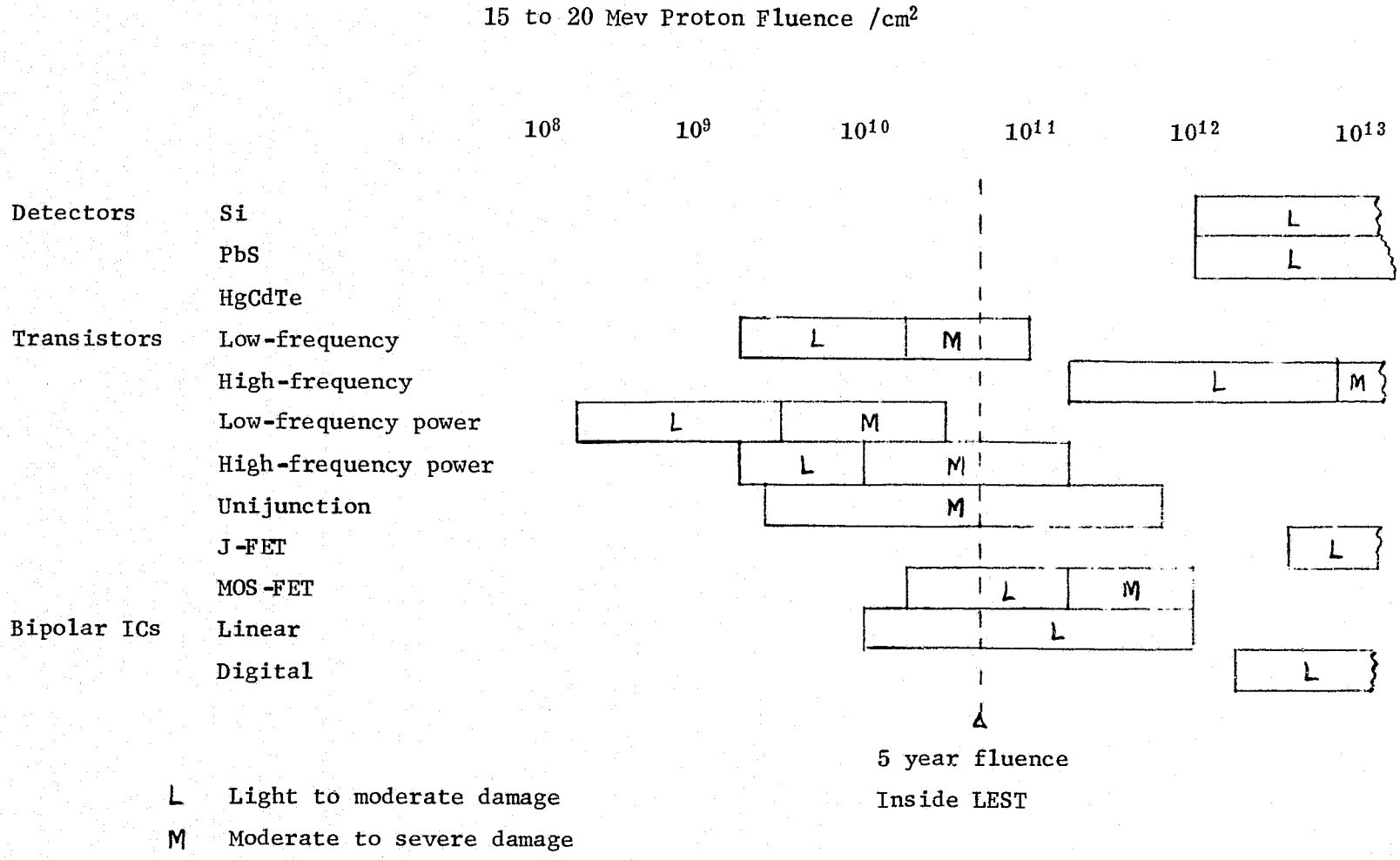

Fig. 6.2-1 Effect of Proton Radiation on Various Electronic Components

REFS: IEEE NS-19, 156, 72; Interim Prog. Rept, Itek Subcontract 8237-A-0003, 11/6/74, Vol. III

The remaining point to consider concerns the primary mirror. While it is shielded from most directions, it can still get direct radiation through the end of the tube. The tube length-to-diameter ratio reduces the hemispheric fluence by about 50x. A study for LST indicated a flat plate 10 Kev proton fluence of about $4 \times 10^{15}/cm^2$ yr. Thus the total fluence on the LEST primary mirror in five years will be $4 \times 10^{14}/cm^2$. Fig. 6.2-2 shows that this is too small to affect the reflectivity of the mirror.

We conclude, then, that with proper design there should be no problems with space radiation for a 5 year LEST mission. This conclusion is borne-out by several existing space programs in synchronous orbit.

6.3 CONTAMINATION

The final source of long-term degradation we will consider is contamination, which can accumulate on the optics and the cryogenic radiator. The LEST optics should suffer less from contamination than LST for several reasons. LEST orbits with the aperture always perpendicular to the line of flight, and it therefore never acts as a scoop for contaminating atoms and molecules. LEST also does not have to contend with Shuttle visits (Shuttle is expected to be a source of contamination). Like LST, on the other hand, the primary mirror of LEST will be substantially warmer than its surroundings, and this should act to minimize the accumulation of contaminants.

A problem LEST faces which LST does not is the periodic illumination of the primary mirror by the sun. Experiments have shown that sunlight in space can cause polymerization of contaminating molecules which results in loss of optical performance. This is a problem which must be investigated further as the LEST studies progress because it can severely influence our ability to observe near local midnight.

Cooler performance can be degraded by contaminates (such as water, oil, etc.) being deposited on the low emissivity finishes (gold and silver) and/or the low solar absorptivity (α) finish second surface mirrors. Detector performance can be degraded by deposition of contaminates on surfaces in the optical path such as lenses, filters, beam splitters, and reflectors. Condensation of contaminates can only occur if the vapor pressure of the contaminate at the condensing surface temperature is less than the local partial pressure of the contaminating gas.

Flight data for the RCA VHRR cooler shows that degradation of the cooler surfaces is relatively insignificant in terms of cooler performance if all cooler surfaces are held at spacecraft temperatures (approximately 300°K) for 10 days before allowing them to cool down to operating temperatures. Although NASA allows 10 days before cooldown, it is felt that a shorter period of time (3 to 5 days) would be sufficient.

Some degradation in detector performance has been encountered in the VHRR due to contamination on the IR filter which operates at about 150°K but no degradation has been observed due to contamination of lenses operated at 105°K since these lenses are protected by a contamination trap. Therefore, all optical elements which operate below the spacecraft temperatures should be protected by contamination traps.

The contamination trap consists of overlapping tubes (gold plated to minimize thermal coupling) which are closed off at one end by the detector assembly,

lenses, filters, or other optical elements. The inner tube is heat sunk to the colder of the two mounting surfaces. For example, the inner tube could be mounted to the cold plate and the outer tube could be mounted to the spacecraft or the cooler first or second stage.

Besides the contamination trap we can minimize contaminant accretion by:

1) Following design guidelines such as those promulgated by NASA which restrict the use of high outgassing materials. These are contained in NASA TN D-7362 "Compilation of Outgassing Data for Spacecraft Materials".

2) Baking out spacecraft components such as solar panels which use large quantities of adhesives and thermal blankets which are trappers of large volume of water vapor.

3) Heating normally cold cooler surfaces for as long after launch as the mission will allow - normally 10-14 days.

4) Periodically reheat or deice the cooler if contaminant accretion reduces the cooler margin to an unacceptable degree.

With such techniques we believe that contamination can be held in check, ensuring the long term success of LEST.

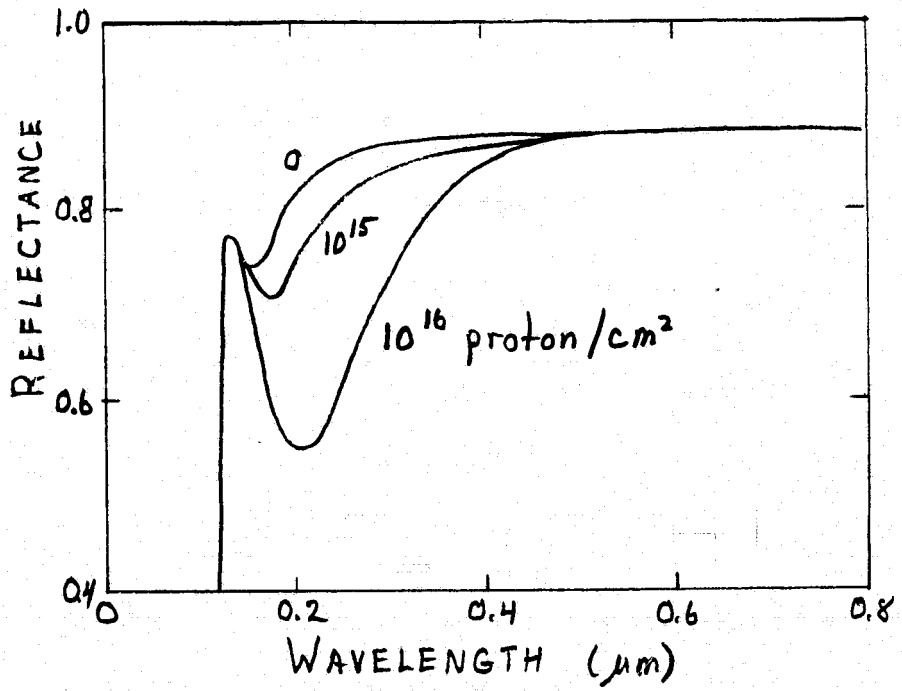

Fig. 6.2-2 Effect of 10 Kev Protons on MgF_2/Aℓ-Coated Cervit[12]

7. STATE OF THE ART AND TECHNICAL RISKS

No major technical breakthroughs are required for realization of the LEST conceptual design outlined in this report. Simple extrapolations of existing technology, particularly with guidance system components and multi-element infrared detector arrays are assumed, however. Also it should be noted that in this period of rapidly expanding technology, it is entirely possible that useful new components, not presently envisioned, will appear and offer even better performance than now predicted.

7.1 OPTICS

Final design and production of the LEST optical components is within the proven capability of Itek Optical Systems Division. High quality mirrors much larger than the 1.4 meter primary have been made and tested. The f/1.5 speed of the primary, however, does mean that better than routine fabrication, handling and test methods must be employed.

Lightweighting of the primary mirror is an area where the risk would be related to the degree of lightweighting and method employed. The 170 kg for the primary mirror in the weight budget is based on ULE egg crate construction with 0.5" front and back plates, and eighty percent lightweighting in the grid sections. The more expensive and longer lead-time cored CERVIT construction would possibly reduce weight by 44 kg. Ultra-thin slab mirrors requiring active figure sensing and control is another approach to lightweighting. The complexity of such a system, however, would not be warranted for the moderate size LEST primary.

Fabrication and test of the refractive IR relay lenses is not considered as an area of technical risk, but will call for development of specialized test methods, and will require homogeneous blanks of the IR transmitting materials called out in the design - section 3.2.

7.2 DETECTORS

CCD detector arrays meeting LEST requirements are essentially available for wavelength bands from 0.4 to 1.0 μm, but will not be available for bands above 1 μm for 2-3 years.

Fairchild has made 1728 element monolithic silicon arrays using a buried channel structure and a distributed floating gate amplifier that are capable of NES values below 100 electrons.

Monolithic CCD arrays for the infrared bands at wavelengths longer than 1 μm are not available at present for the configurations required for LEST. This is because monolithic structures fabricated in narrow bandgap semiconductor material are not well developed.

However, there is considerable work on hybrid arrays where discrete HgCdTe and PbSnTe elements are "hardwired" to a silicon CCD. Hughes-Santa Barbara has achieved near BLIP performance on a developmental 8-element array cooled to 77°K. Honeywell recently received a contract from GSFC to develop 9-element hybrid arrays using both photoconductive and photovoltaic HgCdTe detectors coupled to buried channel CCD registers.

A tentative specification defining detector requirements was submitted to Honeywell to determine if hybrid IR-CCD detectors meeting LEST requirements would be available in 2-3 years. Their conclusion based on current work at Honeywell and Hughes-Santa Barbara is that detectors better than these requirements would be available for the LEST timeframe.

7.3 COOLER

A total of at least 12 passive coolers have flown on spacecraft such as ITOS, NIMBUS, DMSP, VISSR, and ATS 6 since 1972. In orbit, all coolers reached the required detector operating temperature. All coolers also experienced degradation of both cooler margin and thermal channel sensitivity. The six ITOS-VHRR coolers that have flown degraded an average of about 25% in cooler margin and 30-35% in signal sensitivity. The 25% cooler margin loss was asymptotic with the coolers still having virtually unlimited life remaining. The sensitivity loss on all coolers has been almost certainly traced to exposed cold optical elements. The cold trap schemes discussed in section 3.7 are expected to completely solve this problem.

7.4 ATTITUDE CONTROL

The pointing accuracy pushes the state-of-the-art as reflected in gyro and star sensor performance. The Draper Space Gyro is currently being modified to provide a PM torque generator which provides improved linearity and precise operation over a greater range. The present DSG gyro which will be flight tested this year differs from the highly developed third generation gyro only in that it has a lower momentum (wheel speed) and a substitution of hydrogen for helium in the gas bearing (both changes to save power).

Consultation with the star mapper vendor indicates that the brute force approach to increased accuracy - wide optics and greater weight - is not productive. Instead, emphasis is placed on small detailed improvements and better calibration. The budget allows 2 arc sec, 3σ for Kalman filter attitude determination and this is where star sensor errors are manifested.

The technical risks are associated with meeting the pointing accuracy and no one error source can be singled out as predominant. Alignment and calibration need study. Earth landmarks would help greatly in this area.

Procedures for calibrating the ACS by star scan need further investigation.

CMG's with the desired characteristics would be the Sperry Model 30, modified by removing one gimbal, increasing the freedom of the remaining gimbal, and replacing the induction motor with a synchronous motor. Inertia wheels of brushless design are proposed for roll and yaw. The RCA DMSP reaction wheel which has a capacity of 5 ft-lb-sec requires sight circuit changes to obtain roll turn around torque.

The computer would be similar to the DMSP version, with more memory.

The SEOS program is very similar to the RCA DMSP project in that both are precise earth pointing stellar-inertial systems. There is background to successfully apply all the hardware and software experience gained on this program to SEOS.

8. PROGRAM PLAN AND SCHEDULE

A summary SEOS program schedule developed by Itek and based on recently received information on expected program authorization and procurement milestones is shown in Fig. 8.0-1. This schedule includes a 12 to 15 month system Phase B Preliminary Design Phase and a period of critical technology development prior to the Phase C/D LEST date-of-contract shown in August 1979. The planned activities, milestones and hardware flow in the 5-1/2 year period from Phase C/D DOC to first launch in 1985 are discussed in Section 8.4, but first we should look at the remaining study and technology development activities which will lead up to the start of the hardware design phase.

8.1 ADDITIONAL CONCEPTUAL STUDIES

The design concept described in the foregoing sections of this report provides, in its basic parameters and features, a system that will perform the SEOS/LEST mission. However, in the time prior to the start of Phase B, additional studies would be advantageous in order to establish further design confidence, and to explore simplifications for improving reliability.

Some examples of possible additional studies are:

- Thermal-optical sensitivity analysis
- Explore possibility of adding detector arrays in order to simplify filter changer mechanization
- More detailed analysis of geometric and radiometric errors and calibration techniques

It is expected that NASA/LEST-Contractor discussions will highlight areas of greatest benefit for these extended conceptual studies.

8.2 SEOS SYSTEM PHASE B, PRELIMINARY DESIGN

The principal requirements and outputs of the preliminary design phase for LEST will be:

Item Specifications

LEST/CEI Specification (Part I)

Thermal Design Criteria
Structural Design Criteria
Performance Criteria
Reliability Criteria

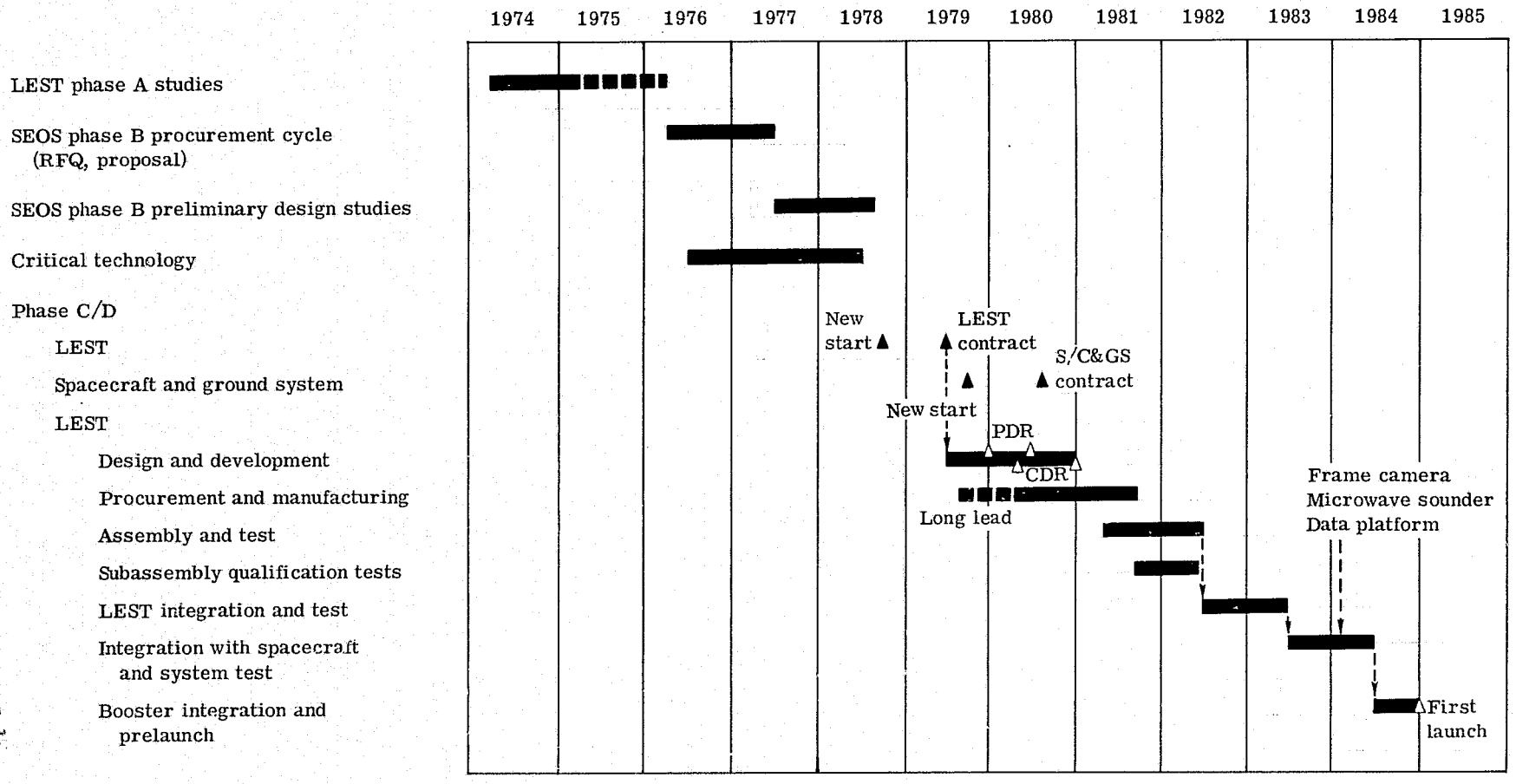

Fig. 8.0-1 SEOS/LEST Summary Program Schedule

LEST/SEOS Interface Documentation

Thermal
Structural, Mass Properties
Power
Command and Telemetry
Mechanical
Sensor Signal Processing, Etc.

Preliminary Design of LEST

Preliminary design of LEST and its internal subsystems will be accomplished such that a family of subsystem interfaces are defined and specifications are prepared. Also, preliminary specifications for major purchased or subcontract items will be prepared.

Identification of Long Lead Items

Ground Support and Test Facilities

Define all major items of ground support, special test equipment and facilities required for use on the program.

Programmatic Data

Prepare a program plan and schedule for Phase C/D
Prepare work breakdown structure and cost estimate for Phase C/D

A twelve month time period is considered minimum for the LEST portion of the SEOS system Phase B program.

8.3 CRITICAL TECHNOLOGY DEVELOPMENT

The conceptual design presented in this report does not require major technical breakthroughs in order to become feasible. However, early initiation of development in some LEST areas will minimize the risk of schedule and cost overruns. Possible examples are:

- Fabrication and test of a refractive relay for the IR bands
- Development of compact multielement multiline detector arrays for operation in the IR bands
- Definition of system electro-optical performance test arrangements for throughput test from moving target-scene to reconstructed image.

We have shown a two year period of critical technology development in the summary schedule, Fig. 8.0-1, ending near the end of Phase B.

8.4 PHASE C/D

In Phase C/D, starting from the preliminary design of Phase B, and incorporating developments from the critical technology studies, we do the detailed design leading to hardware procurement and manufacturing. Preliminary Design Review (PDR) and Critical Design Review (CDR) are planned to be conducted incrementally as subassembly designs are completed. Release for procurement of some long lead items such as the primary mirror and some of the relay lens materials must be made prior to PDR. However, in general, procurement release will be made following CDR.

In conceiving a development test program we have considered both the needs for design verification and launch confidence, and the necessity of minimizing costs. Therefore, the protoflight program envisioned here does not include an engineering model LEST or a complete qualification unit. It is planned that the design of all electrical and electro-mechanical subassemblies, and detector assemblies, will be proven with breadboards and by test of qualification units. Structures, telescope mirrors, and relay lens assemblies will be made for the flight unit only. Environmental test at Itek would be at the subassembly level; not the fully assembled telescope.

Performance testing of the telescope and focal plane assembly will be accomplished using a simulated ground scene and test target inputs in a test arrangement utilizing a large aperture collimator. Testing in this mode will provide the capability of total electro-optical system verification when on-board data processing (if employed), data link, and ground reconstruction are included in the test system.

Earlier testing of the focal plane subassembly separated from the telescope is also possible using a telescope image simulator.

Environmental test of the LEST, including thermal-vacuum, and acoustics must be accomplished at some level of system build-up. The selection of the point in the SEOS system hardware flow should consider, among other factors, the utilization of existing test facilities for minimizing program costs. However it will be important to include the collimator and scene simulator in the thermal vacuum test facility.

Fig. 8.4-1 depicts the hardware assembly and test flow described above.

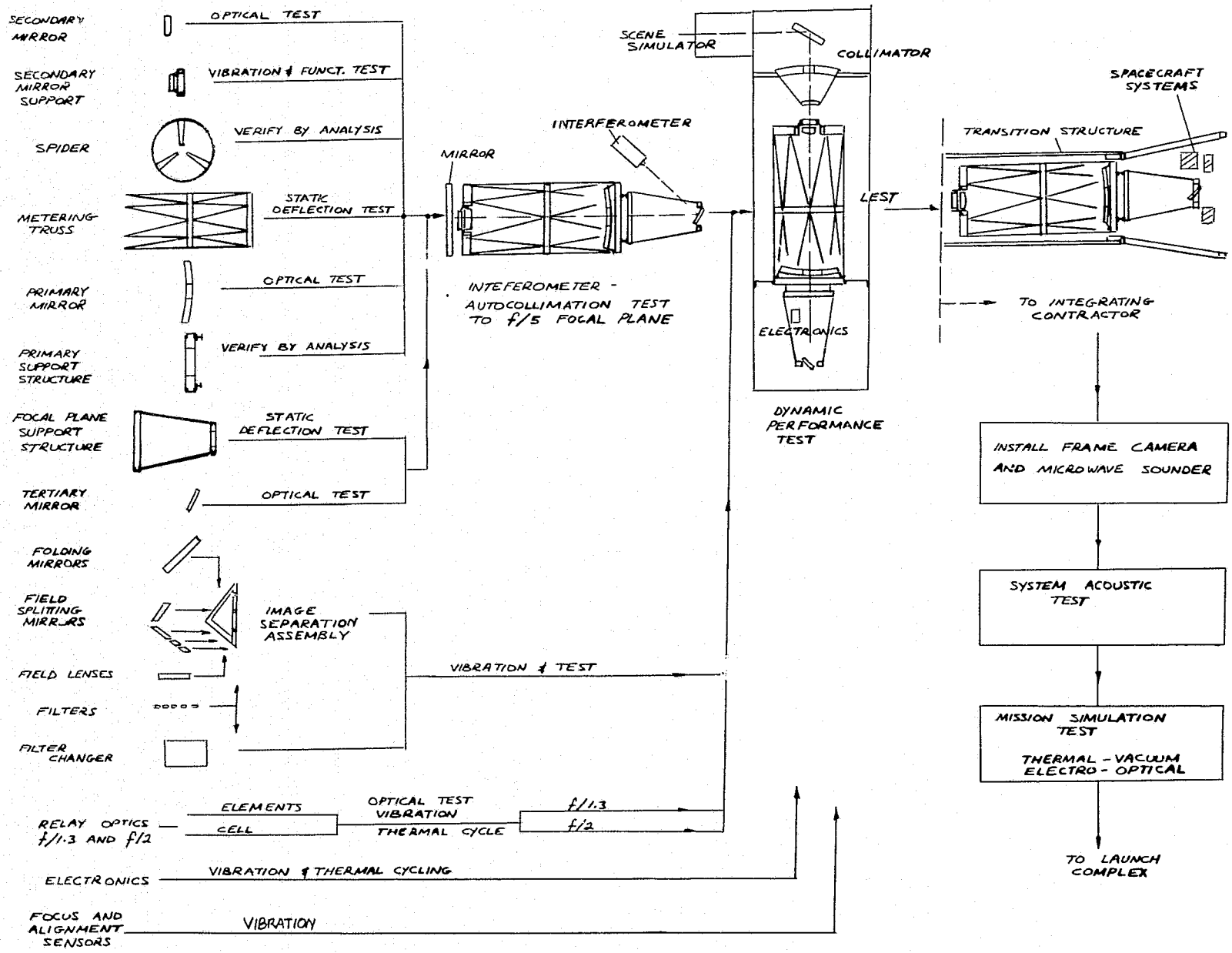

FIGURE 8.4-1
LEST HARDWARE AND TEST FLOW

9. ROUGH ORDER OF MAGNITUDE COST ESTIMATE

In this section, we discuss the major elements which make up the LEST contractor costs for the SEOS program from the end of the present Phase A study until launch of the first SEOS. The rough order of magnitude costs estimated for the program necessarily are based in most cases on extrapolation from similar tasks on other programs, and on engineering judgement. The estimates presented are for the fullup version of LEST. In section 9.3 cost differential for the strip down and minimum system are discussed. As the design matures in subsequent phases, and more specific test plans and schedules are developed, the cost estimate should be updated and reviewed in much greater detail.

Some ground rules employed in this estimate are tabulated below:

- Based on 1975 dollars, fee included
- Cost for IR sounder(s) and special test equipment for the sounder are not included (assumed GFE).
- Cost of spacecraft not included
- Cost for spacecraft attitude determination and control system not included
- LEST/spacecraft detector signal interface taken as serial-analog bit streams from the ten arrays.
- Cost of ground data handling not included.

We include cost for development, production, test, and integration of the LEST Telescope including optics, optical structure, focal plane devices and detector electronics. Also included are the costs for ground support and test equipment and SEOS system integration and launch support.

9.1 COSTS PRIOR TO START OF PHASE C/D

As was discussed in Section 8, there will be a period of about a year from the end of the current LEST Phase A study to the end of the GFSC SEOS Phase A program. The usefulness of additional LEST conceptual design activity has been noted. For tabulation purposes we identify such a Phase A extension as Phase A^1 and estimate its cost at $150K per contractor.

Critical Technology Tasks

Early start-up on some development tasks is important in order to avoid later schedule impact if unforeseen difficulties are found. As noted earlier, IR relay lens fabrication, development of IR detector arrays, and definition of test configurations are possibilities; other areas may also be found fruitful.

A budgetary estimate is:

Critical technology	$500K	This assumes that detector technology development continues under separate NASA Sponsorship.

Phase B:

The requirements of the preliminary design Phase B were outlined in Section 8.2.

The Itek cost for a one year Phase B program is estimated as:

Phase B	$1.5 million

Therefore, the total remaining LEST effort prior to start of Phase C/D is estimated as:

Phase A[1]	$ 150K
Critical Tech.	500K
Phase B	1,500K
	$2,150K per contractor

9.2 PHASE C/D THROUGH FIRST LAUNCH

Fig. 9.2-1 is the Work Breakdown Structure, WBS, prepared to depict the principal tasks for the LEST Phase C/D program. The estimated costs presented herein are aligned to the WBS. In the following sections, a brief definition of each level one WBS task is given, along with any qualifiers or limitations affecting the ROM estimate. Table 9.2-1 summarizes the cost estimates for Phase C/D through the first launch.

TABLE 9.2-1

SUMMARY OF ROM COST, PHASE C/D FOR FULL-UP LEST

	Millions
System Engineering and INtegration	4.5
Design and Development	7.5
Subsystem and System Test Hardware	3.6
Subsystem and System Development Testing	1.5
Ground Support and Special Test Equipment	9.0
Flight Article Procurement, Fabrication and Assembly	11.0
Flight Article Test and Checkout	3.9
Launch Operations	.8
Product Assurance	3.2
Facilities	.3
Program Management	5.7
	$51.0 million

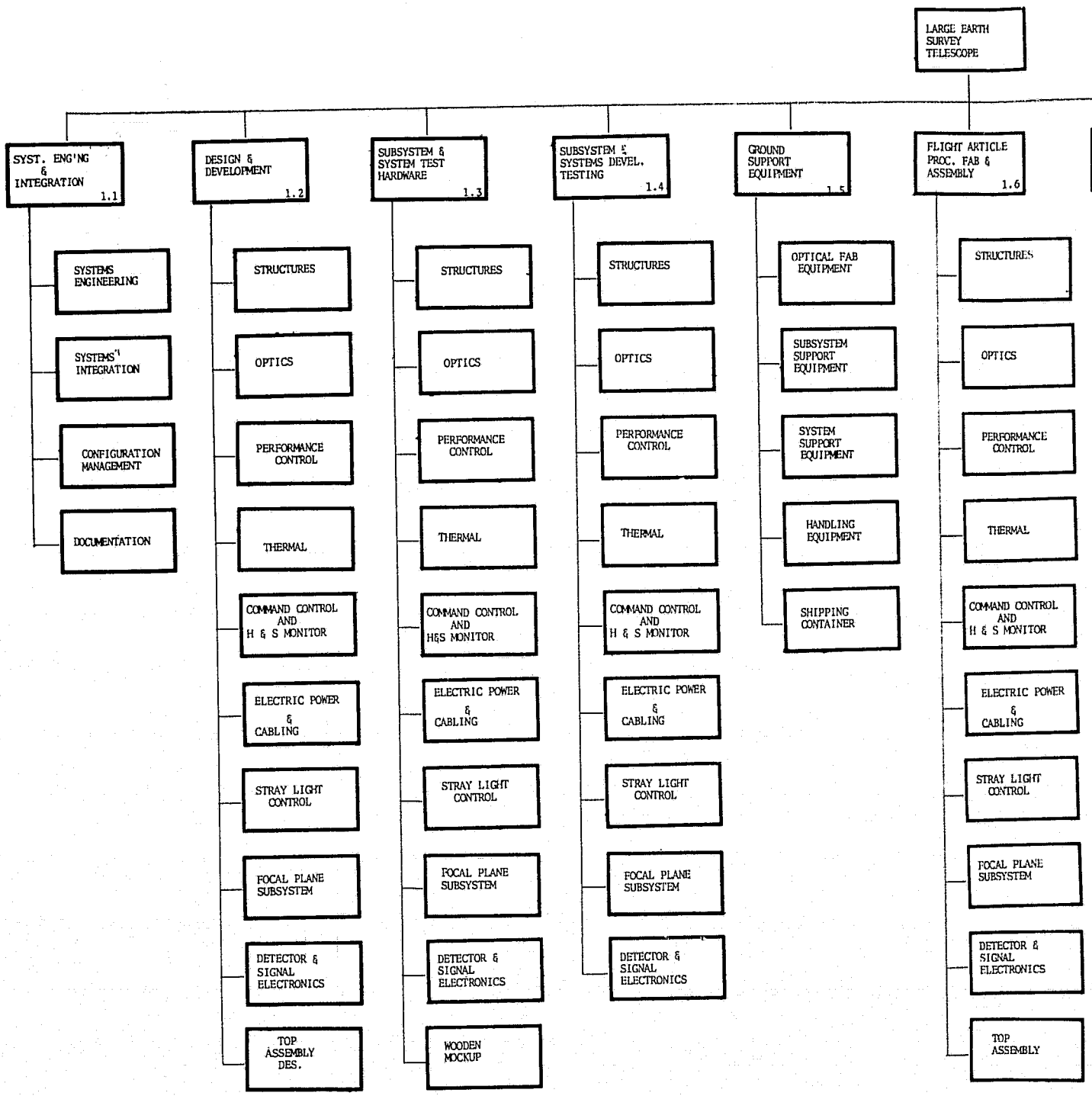

Fig. 9.2-1 — LEST work breakdow

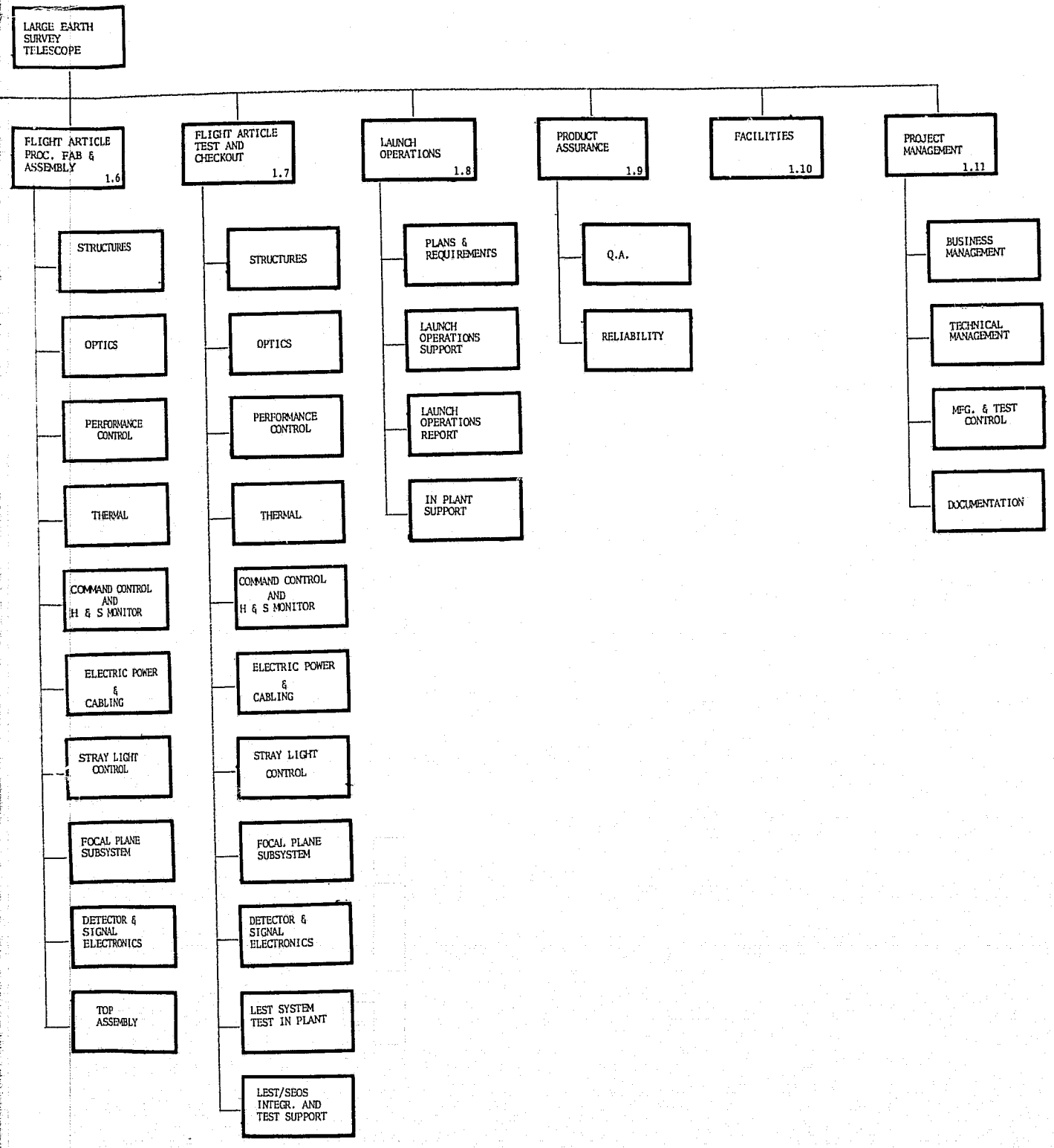

LEST work breakdown structure

FOLDOUT FRAME 2

Task 1.1 System Engineering and Integration

System Engineering

System engineering encompasses the functions of system engineering, documentation, design integration, and test evaluation. System engineering documentation includes the preparation and maintenance of the system specification, design criteria, technical plans, subsystem specification, interface control documentation, GSE/STE specifications, and manuals and training.

Design integration includes the generation of standards and criteria, and design overview for electromagnetic compatibility, mass properties, safety, and material and processes. Also included is the organization, conduct and follow-up for design reviews.

The test evaluation subtask includes data reduction, software, test reports, and test analysis.

System Integration

This subtask includes the in-plant efforts associated with integration and test activities involving LEST at the spacecraft/system-integration contractors facility and NASA test facilities. Included would be inputs to system level test plans and procedures and test evaluation.

Configuration Management

This subtask includes the implementation of a change control system for specifications, design documentation, and test procedures to ensure that the as built and test status records are accurate.

Documentation

The technical editing, typing, and printing cost for CDRL items is covered in this subtask.

Task 1.2 Design and Development

Task 1.2 includes all costs involved in the design and development of the LEST, exclusive of development test hardware and development testing. The subtasks under Task 1.2, aligned to the main assemblies and subassemblies of LEST, are tabulated below, with explanatory comments.

Structure

Structures include all LEST structural components, i.e., metering truss, primary support structure, focal plane support structure, primary mirror mount, secondary spider, etec. Not included in this ROM cost estimate is the outer (spacecraft) structure which surrounds LEST.

Optics

Optics includes all of the mirrors, refractive lens assemblies, and spectral filters, in the LEST system. Design and specification of coatings is also part of the optics design and development task.

Performance Control

Design and development of thesensors and control systems which measure and adjust LEST to the best optical performance while on orbit are covered by this subtask. The anticipated subsystems are focus detection and control, and primary/secondary alignment measurement and control.

Thermal

The thermal subtask includes two major requirements. Thermal/optical design and detector cooling design. The former includes thermal insulation and active heating of the primary and secondary mirror. Estimated costs for the passive cooler for the detector have been included here as attributable to LEST but provided as part of the spacecraft.

Command and Control and H&S Monitor

This subtask covers design of the system which translates commands from the spacecraft into appropriate internal switching, mode control, filter selections, etc. Also included in this subtask is the design of the system which includes transducers and associated signal conditioning for measuring and indicating health and status of LEST.

Electrical Power and Cabling

This subtask covers design of the power distribution and regulation system, plus all power and signal system cabling.

Stray Light Control

This subtask covers design of the stray light control system i.e., baffles, safety shutter, etc.

Focal Plane Subsystem

Included in the focal plane subsystems are the design and development costs for detector arrays, calibration systems, radiometric chopping, and filter changer mechanisms.

Detector and Signal Electronics

This subtask includes design and development of the electronics which power, cycle, and read-out the detector arrays and preamplify and band limit the detector outputs. For purposes of this ROM estimate, the interface with spacecraft systems is taken to be serial analog bit streams from preamps serving each of the ten arrays identified in the conceptual design.

Top Assembly Design

This task covers the top level LEST assembly drawings and LEST/SEOS interface drawings and design. It should be noted that costs have not been included for the scanning system. Attitude determination and control is a necessary part of the spacecraft regardless of the scanning system employed. Since the design discussed in this report uses attitude control for scanning the ground scene, no additional costs are included for this function. It is also planned that the spacecraft (or ground based) computer will program the attitude control system to the profile required to cover a selected area.

Task 1.3 Subsystem and Systems Test Hardware

This task covers the cost of procuring, fabricating, and assembling breadboards and qualifcation subassemblies of selected LEST subassemblies. The subtasks under 1.3 have essentially the same designators as in Task 1.2. Test hardware estimates were based on the previously mentioned plan, i.e., breadboards and qualification models for all electrical and electromechanical subassemblies. In addition, there will be breadboard model filters, detector assemblies, and optical coatings. Qualification model relay lens assemblies are also included.

C-3

Also included in test hardware is a full scale wooden mockup LEST.

Task 1.4 Subsystem Development and Qualification Tests

This task covers the efforts required for testing utilizing the breadboards and qualification hardware which were identified and priced in Task 1.3.

Task 1.5 Ground Support and Special Test Equipment

This task includes all of the design, procurement, assembly and test efforts for the special equipment necessary for fabricating, assembling, lifting, testing and transporting the LEST. The principal classes of items are as follows:

Optical Element Fabrication, Test and Handling Equipment
Relay Lens Assembly and Test Fixtures
Electronic and Electro-Mechanical Subassembly Test Sets
Spectral Band Synthesizers
Telescope Optical Simulator
System Test and Checkout Console
Vibration Test Fixtures
Assembly and Test Dollies
Subassembly Transport Containers
LEST Electrical Simulator
Test Cables and Socket Savers
Test chamber Cables and Adapters
Dynamic Resolution Tester*

*Assumed one set to be used both at Itek and at integrated test level. Also assumed that collimator will include GFE mirror.

Cooling System for Detectors for System Tests run at ambient temperature

Recorder Tape, Paper, Expendable Parts
System Shipping Container

Task 1.6 Flight Article

This task covers the cost of procurement, fabrication and assembly of the flight model LEST. The major subsystems are as defined and listed under Task 1.2; tabulated below we show the estimates for each subtask within this large cost center.

	$ Millions
Structures	1.5
Optics (including spare primary mirror)	2.5
Performance Control	.7
Thermal	.3*
Command Control and Monitor	.3
Elec. Power and Cabling	.25
Stray Light Control	.3

Focal Plane Subsystems	2.75**
Detector and Signal Electronics	.6
Top Assembly Inc. Engr. Support	1.8
	$11.0 million

*Includes cost for cooler, which is on spacecraft but costs are assignable to LEST.

**The cost of this portion of this system is highly dependent on cost of special detector arrays for which little data are available.

Task 1.7 Flight Article Test and Checkout

This task covers the cost of performing acceptance tests on LEST flight hardware subassemblies, subsystems and total system. In addition, it covers Itek participation in SEOS/LEST integration and test operations at the system integration facility and NASA test facilities.

Task 1.8 Launch Operations

This task covers the cost of the LEST contractor's activities in build-up and checkout to launch configuration, preparation of launch readiness checkout plans and launch operations support. The activities priced in this cost account do not include on-orbit mission support except for a brief period for operational verification.

Task 1.9 Product Assurance

We have grouped reliability and product assurance functions under the Product Assurance Task.

Reliability Subtask

Select approved parts for use on the program and oversee part utilization within designs for reliability.

Establish reliability criteria and establish MTBF and subsystem reliability allocations.

Review on-going design for inclusion of fail safe, redundancy and back-up mode features and basic design simplicity for reliability.

Test non-standard components for validation as approved parts.

Do failure analysis on failures occurring in test program

Participate in design reviews, and system sell-off meetings.

Quality Assurance Subtask

Establish and maintain quality control plan

Impose and monitor quality requirement on vendors and subcontractors.

Monitor cleanliness status of assembly and test areas.

Witness subassembly and system testing.

Monitor quality and workmanship throughout the fabrication, assembly and test cycle.

Task 1.10 Facilities

This task covers the cost of special facility modifications that would be required for accommodating and handling LEST and ensuring that cleanliness requirements are met.

Task 1.11 Program Management

The program management task includes all activities needed for technical and business management of the program. The subtasks are identified as:

Business Management: Program management administration, planning, communications, travel.

Technical Management: Chief engineer, customer interface.

Manufacturing and Test Control: Operations manager, model control, testing manager.

The cost of the follow-on units would depend on the amount of overlap, if any, between production of the first unit and follow-on units. The ROM cost presented below is based on no such overlap; therefore, functions such as management and sustaining engineering are included to support the program on its own. Also, we have based the estimate on the follow-on unit being identical to the first unit. See Table 9.2-2 for the estimated cost of follow-on units broken down to the applicable tasks defined previously.

TABLE 9.2-2

ROM COST FOR FOLLOW-ON FULL UP LEST

	$ Millions
System Engineering and Integration	1.5
Ground Support and Special Test Equipment	.5
Flight Article	10.0
Flight Article Test and Checkout	3.0
Launch Operations	.5
Product Assurance	1.8
Program Management	3.2
	$20.5 million

9.3 COST FOR STRIP DOWN AND MINIMUM DESIGN SYSTEMS

9.3.1 Strip-Down System

In earlier discussions, the strip-down LEST was described as having the same basic configuration as the full-up. While the field of the detectors would be limited to the central 0.2°, the telescope and relay designs would have to be shown to be usable to 0.6°. Therefore, there would be little or no saving in the design and fabrication of the optics.

Development costs for the detector and focal plane would not be reduced for the strip-down LEST, but the costs for the flight article detectors would be reduced to about one third.

With fewer detectors in the strip-down LEST, area coverage rates would be reduced, and therefore, data rate for the signal electronics would be reduced. This likely would translate into a somewhat lower cost signal electronics system.

9.3.2 Minimum System

The minimum system configuration, as described in section 4.2 would also be a 1.4 meter Cassegrain system, but would have only a 0.2° field of view. Detailed design of the correcting optics would be somewhat less expensive, and fabrication and assembly costs would also be less. Detector and associated electronics costs would be the same as for the strip-down (one-third of full-up). These savings would be partially offset by the additional costs of the focal plane selector mechanism necessary to bring different detector arrays into use for multiple scans of the same target area.

10.0 RECOMMENDATIONS FOR FURTHER STUDY

The study summarized in this report has made major advances toward the objectives of defining and later implementing a real time monitor survey, and assessment capability for earth resources and meteorological applications.

- Observational requirements have been translated into telescope-related parameters.
- Preliminary performance specifications have been prepared.
- Feasibility of achieving the required resolution and sensitivities has been established.
- Telescope parametric trades have been made, leading to establishment of a favored design concept.
- The design concept has been "fleshed out" to the degree that a preliminary optical design has been made, and conceptual designs for focal plane, thermal, structural, and scanning subsystems have been prepared.
- Performance of LEST based on the defined conceptual design has been calculated. With few exceptions performance requirements for all defined applications have been bettered.

The conceptual design described in this report depends in some areas on reasonable extrapolations of todays technology; however, major technical breakthroughs are not required. Much detailed design of course remains. In the following sections we discuss some of the key areas warranting further study and development.

10.1 OPTICAL DESIGN

The present optical system study has shown that a viable optical system can be designed to meet the performance goals developed in the phase one study. There are a number of details requiring further study or definition before the configuration can be considered as final. The areas requiring further analysis include detector configurations, filter specifications, and a complete lens design and alignment tolerancing study.

The detector array study needed to aid in finalizing the optical configuration involves finding answers to the following questions: 1) Can multiple lines of detectors be laid down on a single chip? 2) If so, how many lines may be laid down and how widely must they be spaced? 3) Must the detectors be on a flat surface, or may the surface be curved to compensate for curvature

of field? 4) Must the line arrays be straight, or may they be curved to offset optical distortion in the lens system? 5) If distortion cannot be corrected in this manner, how much distortion can be tolerated without a breakdown in the scanning and data reduction procedures?

The number of detector arrays and their required spacing is tied to the manner in which the intermediate image is divided and directed to the various sensors, the number of relays involved, and the presence or absence of filter changer mechanisms. To eliminate filter changers from the f/5.0 channel, for example, would require 13 line-arrays of detectors on the same chip. More critically, the f/1.3 channel requires 4 to 6 closely spaced arrays, depending on whether or not a filter changer is required. Moreover, one of these is a different kind of detector from the others.

The questions which must be addressed concerning the narrow bandwidth filters include: 1) What are the detailed definitions of the spectral bandpass channels; e.g., square or Gaussian cross section? 2) What are specifications concerning bandpass tolerances? Stability over long periods of operation? Degree of blocking over spectrum outside bandpass? 3) Can such filters be constructed in the geometry required at intermediate focus?

The answers to the above questions could impact the details of the optical configuration. Beyond this, it is still necessary to complete the detailed lens design, optimizing the various relay designs for both resolution and transmission, and establishing manufacturing tolerances. A complete and detailed tolerance analysis of the entire optical system will also be required.

10.2 ATTITUDE DETERMINATION AND CONTROL

The following topics, while not critical from a feasibility or conceptual viewpoint, should be explored in future phases of the SEOS/LEST study:

a) Effect of gyro transient scale factor changes and input axis misalignment on stellar attitude update frequency.

b) Dynamic settling of telescope optics, including effect of solar panel modes.

c) Optimum actuator configuration (weight - power - reliability) of CMG's and inertia wheels.

d) Attitude determination simulation (Kalman filter).

e) Telescope boresight calibration on orbit.

f) Solar array drive choice.

10.3 DETECTOR ARRAY DEVELOPMENT

As was mentioned in Section 10.1, special detector arrays would result in higher reliability through simplification or elimination of filter changers, and would simplify optical relay design. Continued development progress on multi-element silicon array devices will provide the detector technology required in the SEOS/LEST design phase.

There are a number of organizations presently working toward developing multi-element thermal IR arrays with integral readout circuitry. The principal

approaches are: hybrids such as HgCdTe coupled to silicon CCD's, monolithic HgCdTe devices, and specially doped silicon devices. Of these, the hybrid approach is the most advanced. Continuing development of these devices should be supported.

10.4 GROUND DATA HANDLING

While the ground data handling segment of the SEOS system was not part of the LEST study, it is clear that the usefulness of SEOS and the great advantage over lower Earth orbiting systems lies in the timeliness of the information. Continuing phases of the program should include development of information extraction techniques, automatic scene classification, geometric and radiometric calibration systems, and graphic data display systems.

CCD	Charge Coupled device
CMG	Control Moment Gyro
CSA	Celestial Sensor Assembly
CPU	Central Processing Unit
DMSP	Defense Meteorological Satellite Program
DSG	Draper Space Gyro
EIFOV	Effective instantaneous field of view
ERIM	Environmental Research Institute of Michigan
ER,ERS	Earth Resources
ESA	Earth Sensor Assembly
GG	Gravity Gradient
GIFOV	Geometric instantaneous field of view
HgCdTe	Mercury Cadmium Telluride
InSb	Indium Antimonide
IRU	Inertial reference unit
LEST	Large Earth Survey Telescope
LWIR	Long wave infrared
MET	Meteorological
MTF	Modulation transfer function
MU	Magnetic unloading
NER	Noise equivalent radiance
NES	Noise equivalent signal
NIR	Near IR
PbS	Lead Sulfide
PU	Propulsion unloading
RC	Reaction Control
RSS	Root sum squared
RWA	Reaction Wheel Assembly
SEOS	Synchronous Earth Observatory Satellite
SNR	Signal-to-noise ratio
SS	Sun Sensor
WFE	Wavefront error

μm	Micrometers
μr/ℓρ	Microradians per line pair
μr/s	Microradians per second
a	Empirical constant relating E_o to optical cutoff
D	Aperture diameter
D_1^*	Effective detectivity of detector including amplifier
e	Linear obscuration
E or ϵ	Infrared emissivity
E	Short for EIFOV
E_e	EIFOV if limited only by size of detector
E_1	EIFOV if limited only by integration time
E_o	EIFOV if only optics limited
Δf	Bandwidth
F	Focal ratio
H	Irradiance
ℓ	Detector element size (linear dimension)
N	Radiance
N_s	Number of scans
NEΔT	Noise equivalent change in temperature
NE$\Delta\rho$	Noise equivalent change in reflectivity
t	Minimum exposure time required to achieve specified NER
t_{ex}	Exposure time
t_{sm}	Smear time
w	Detector width
X	Optical transmission
α	Solar absorptivity
β	Sun/SEOS orbital plane angle
θ	Pitch angle
$\dot{\theta}$	Scan rate
λ	Wavelength
δ	Structural damping coefficient
ν	Wave number
ρ	Reflectance
ϕ	Roll angle
ω	Angular spatial frequency

LIST OF REFERENCES

1. Requirements and Concept Design for Large Earth Survey Telescope for SEOS, Itek 75-9510-2A, December 1974.

2. Earth Resources Applications of the Synchronous Earth Observatory Satellite, Environmental Research Institute of Michigan, 103500-1-F (Dec 1973).

3. A Study to Define Meteorological Uses and Performance Requirements for the Synchronous Earth Observatory Satellite, University of Wisconsin, NAS5-21798 (July 1973).

4. Influence of Precision Inertial Systems on Astronomical Observations, by G.A. Ouellette and J.P. Gilmore, AIAA Paper 74-876.

5. Gyroscopes as Prime Attitude References for the Large Space Telescope, by G.A. Ouellette and J.P. Gilmore, AIAA Paper 73-870.

6. Tracking Analysis of Synchronous Satellites by J.J. Goldman, AIAA Paper 70-1068.

7. In-Orbit Performance of the OAO Inertial Reference Unit by R.A. Harris, The Charles Stark Draper Laboratory, P-086, June 1974.

8. Candidate Configuration Trade Study, Stellar-Inertial Measurement System (SIMS) for an Earth Observation Satellite (EOS).

   Interim Reports 1, 2, 3, and Final Report. Charles Stark Draper Laboratory Reports.

   E-2616 November 1971
   E-2630 January 1972
   E-2651 June 1972
   R-741 January 1973

9. Application of High Moment-Producing Techniques for Control of a Manned Space Vehicle Bendix Research Labs. March 1964 FDL-TDR-64-32.

10. A Fine Pointing System for Large Orbiting Telescopes. W.O. Schiehlen, AIAA Paper 73-882.

11. Test Results on Homogeneity of Expansion for a 1.8 m ULE Lightweight Mirror by G. Friedman and G. Gasses, Applied Optics, Vol. II, No. 12, December 1972.

12. NASA CR-1532, February 1970

APPENDIX A

PRELIMINARY PERFORMANCE SPECIFICATION

FOR

FULL-UP SYSTEM

LARGE EARTH SURVEY TELESCOPE

LARGE EARTH SURVEY TELESCOPE
FOR
SYNCHRONOUS EARTH OBSERVATORY SATELLITE

Preliminary Performance Specification
(Full-up System)

1.0 SCOPE

This specification establishes the performance requirements for the Large Earth Survey Telescope (LEST) for the full-up mission Synchronous Earth Observatory Satellite (SEOS).

2.0 APPLICABLE DOCUMENTS

TBD.

3.0 REQUIREMENTS

3.1 ITEM DEFINITION

The Large Earth Survey Telescope is the major electro-optical subsystem of the Synchronous Earth Observatory Satellite for application in earth resources and meteorological sensing tasks from geostationary orbit. The LEST subsystem to which this performance specification is applicable includes the telescope optics and supporting structure, focal plane and detectors, detector cooling devices, and scanning mechanisms (if required). The principal interface of LEST is with the SEOS spacecraft. Operating as part of the SEOS system in conjunction with the microwave sounder and data collection systems, LEST shall provide real time monitor and surveillance capability for selected areas of the earth within the operating range as defined herein.

3.2 CHARACTERISTICS

3.2.1 Performance

3.2.1.1 Operating Modes

SEOS will be utilized for both earth resources and meterological applications. LEST shall be capable of providing, on command, the grouping of spectral bands and coverage rates unique to each mode, as detailed in later sections of this specification. The operating modes to be provided are:

Earth Resources

Meteorological Search, Including 13-Band IR Sounder

Meteorological Monitor

IR Sounder (23 Band)

3.2.1.2 Operating Range

SEOS shall be stationed 35.9×10^3 km over the equator at 105 degrees west longitude. Most applications are limited to those areas where the spacecraft is at least 30 degrees above the horizon. The primary area of interest is the continental United States, but ground resolution in this specification is given at nadir.

3.2.1.3 Area Coverage Rate

The LEST telescope shall meet the resolution and sensitivity requirements of this specification while scanning at areal coverage rates up to those tabulated below (referred to areas centered at 105 degrees west, 40 degrees north). The minimum swath width at nadir shall be 375 km.

Operating Mode	Average Coverage Rate
Earth Resources	20×10^3 km^2/sec
MET Search	4500×9000 km^2/5 minutes

MET Monitor	3 areas 1500 x 1500 km^2/5 minutes within the above 4500 x 9000 km^2 area
IR Sounder (Model 1)	TBD
IR Sounder (Model 2)	750 x 750 km^2/30 minutes

3.2.1.4 Spectral Bands

LEST shall include the optics, filters, detectors, etc. to provide imagery or radiant energy mapping in the spectral bands tabulated below:

For Earth Resources applications LEST shall provide simultaneously, on command, a selection of at least four of the nine visible bands, plus all of the infrared bands listed below:

Earth Resources Bands

	Band Number	Pass band (micrometers)	λ μm	$\Delta\lambda$ μm
Visible	E1	0.42 - 0.46	0.44	0.04
	E3	0.47 - 0.52	0.495	0.05
	E4	0.53 - 0.57	0.55	0.04
	E5	0.56 - 0.60	0.58	0.04
	E6	0.60 - 0.65	0.625	0.05
	E7	0.65 - 0.69	0.67	0.04
	E8	0.70 - 0.73	0.715	0.03
	E9	0.78 - 0.82	0.80	0.04
	E11	0.89 - 0.95	0.92	0.06
NIR	E13	2.05 - 2.35	2.20	0.30
TIR	E16	10.3 - 11.3	10.8	1.0
	E17	11.3 - 12.0	11.6	0.70
	E18	12.0 - 12.9	12.4	0.90

For meteorological applications LEST shall provide simultaneously all of the following spectral bands:

Meteorological Bands

	Band Number	Passband (micrometers)	λ μm	Δλ μm
Visible	M1	0.55 - 0.70	0.025	0.15
	M2	0.744 - 0.759	0.751	0.015
	M3	0.7617 - 0.7663	0.764	0.0046
	M9	0.75 - 1.0	0.875	0.25
NIR	M4	1.58 - 1.68	1.63	0.10
	M5	3.5 - 4.1	3.8	0.6
TIR	M6	6.5 - 7.0	6.75	0.5
	M7	10.3 - 11.3	10.8	1.0
	M8	11.8 - 12.8	12.3	1.0

IR Sounder Mode 1

Band	Wave Number (ν), cm^{-1}	Δν cm^{-1}	λ μm	Δλ μm
1	668.5	5	15.0	0.11
2	680	10	14.7	0.22
3	690	16	14.5	0.34
4	703	16	14.2	0.33
5	716	20	14.0	0.40
6	733	20	13.6	0.38
7	749	20	13.4	0.36
8	900	140	11.1	1.8
9	1,225	60	8.16	0.40
10	1,490	140	6.71	0.64
11	2,360	50	4.24	0.091

12	2,700	440	3.70	0.61
13	0.55 - 1.1μm	S/N = 8.7 at ρ = 5%		

Mode 2 IR sounder operation shall provide the following bands:

	IR Sounder Mode 2			
Band	Wave Number (ν), cm^{-1}	$\Delta\nu$ cm^{-1}	λ μm	$\Delta\lambda$ μm
1	669	5	15.0	0.11
2	680	10	14.7	0.22
3	690	10	14.5	0.21
4	700	10	14.3	0.21
5	705	10	14.2	0.20
6	715	10	14.0	0.20
7	740	10	13.5	0.19
8	750	10	13.3	0.18
9	2,360	40	4.24	0.073
10	2,310	40	4.33	0.76
11	2,290	40	4.37	0.077
12	2,250	20	4.44	0.040
13	2,230	20	4.48	0.041
14	2,210	20	4.52	0.042
15	2,185	20	4.58	0.042
16	900	32	11.1	0.40
17	1,030	50	9.70	0.48
18	2,700	200	3.70	0.27
19	1,490	60	6.71	0.27
20	430	40	23.3	2.2
21	507	80	19.7	3.2

22	1,225	60	8.16	0.40
23	16,000	4,000	0.625	0.16

While operating in IR sounder mode 2, no other spectral bands are required.

3.2.1.5 Radiant Resolution, NER

The LEST will be operated for a wide range of viewing conditions and applications. Tabulated below, for each spectral band are the radiance range capabilities, and sensitivities required in each band. These requirements apply at area coverage rates up to those given in Section 3.2.1.3 for low spatial frequency targets.

Earth Resources Applications

Spectral Band	Radiance Range $\mu w/cm^2$-ster	Percent $(\Delta N/N)$ min	NER $\mu w/cm^2$-ster
E1	55 - 416	1.3	1
E3	107 - 1481	1.8	3
E4	44 - 795	1.2	2
E5	47 - 1631	3.0	2
E6	9 - 823	6.5	1
E7	20 - 1596	2.0	2
E8	8 - 883	3.4	1
E9	158 - 701	1.1	3
E11	218 - 776	2.3	5
E13	19 - 270	1.8	1
E16	656 - 21,700	0.76	5
E17	436 - 11,010	0.69	3
E18	509 - 21,750	1.4	7

Meteorological Applications
(Calculated for 20° Solar Elevation)

Spectral Band	N mw/cm²sr	dN/dT μw/cm²sr°K	T °K	Search NEΔρ %	Search NEΔT °K	Search NER μw/cm²sr	Monitor NEΔρ %	Monitor NEΔT °K	Monitor NER μw/cm²sr
M1	1.71		5800	0.51		9.0	0.17		3.0
M2	0.125		5800	0.30		0.39	0.10		0.13
M3	0.040		5800	0.20		0.081	0.067		0.027
M4	0.141		5800	0.30		0.42	0.10		0.14
M5		0.076	230		3.0	0.23		1.0	0.076
M6		1.15	200		3.0	3.6		1.0	1.2
M7		3.6	200		1.5	5.4		0.5	1.8
M8		13.6	300		0.15	2.0		.05	0.68
M9	1.70		5800	0.51		9.0	0.17		3.0

Mode I IR Sounder

Sensitivity requirements are TBD.

Mode II IR Sounder

Sensitivity requirements are TBD.

3.2.1.6 Radiometric Fidelity

The ability of LEST to detect changes in irradiance from different parts of a scene was specified as NER. Section 3.2.15. The absolute radiometric accuracy is defined as follows:

$$\frac{N_{true} - N_{observed}}{N_{true}}$$

The required accuracy shall be:

visual bands	TBD %
NIR bands	TBD
TIR bands	TBD

3.2.1.7 Spatial Resolution, EIFOV

When operated at the coverage rates of paragraph 3.2.1.3, the Effective Instantaneous Field of View shall be less than or equal to the levels tabulated below. EIFOV is defined as the nadir ground distance corresponding to one half cycle of the spatial frequency at which the system MTF is 50 percent (exclusive of scene modulation).

Earth Resources Applications (EIFOV)

Visible bands	100 meters
Near IR Band	300 meters
Thermal IR Bands	1000 meters

Meteorological Applications (EIFOV)

Band	Search (meters)	Monitor (meters)
M1	600	300
M2	6000	3000
M3	6000	3000
M9	600	300
M4	6000	3000
M5	2400	1200
M6	12,000	6000
M7	2400	1200
M8	2400	1200

Mode I IR Sounder EIFOV

6 x 6 km^2

Mode II IR Sounder EIFOV

36 x 36 km^2

3.2.2 Physical and Environmental Requirements

3.2.2.1 Environments

Ground Handling and Transport - TBD.

Launch - As part of the SEOS spacecraft, LEST shall perform to the requirements of this specification after launch into geostationary orbit with either the Titan IIIE booster or the Shuttle/Tug combination.

The launch environments for these boosters are as detailed in TBD and TBD respectively.

3.2.2.2 Weight and Size Limits

The weight of LEST shall not exceed 1450 kilograms (mass). This weight allocation is to include all telescope optics, structure, shields, baffles, focal plane components and detector cooling.

The physical dimensions of LEST shall be such that the SEOS spacecraft will be within the dynamic envelope defined for the two possible launch vehicles. These areas are denoted in TBD and TBD.

3.2.2.3 Power

Unregulated dc power required for LEST operation shall not exceed

TBD watts for telescope operation,

TBD watts for active thermal control of LEST optics.

APPENDIX B

PRELIMINARY PERFORMANCE SPECIFICATION

FOR

STRIP-DOWN SYSTEM

LARGE EARTH SURVEY TELESCOPE

Large Earth Survey Telescope

for

Synchronous Earth Observatory Satellite

Performance Specification

(Strip-down System)

1.0 SCOPE

This specification establishes the performance requirements for the Large Earth Survey Telescope (LEST) for the strip-down mission Synchronous Earth Observatory Satellite (SEOS).

2.0 APPLICABLE DOCUMENTS

TBD

3.0 REQUIREMENTS

3.1 ITEM DEFINITION

Same as Full-up LEST.

3.2 CHARACTERISTICS

3.2.1 Performance

3.2.1.1 Operating Modes

SEOS will be utilized for both earth resources and meteorological applications. LEST shall be capable of providing, on command, the grouping of spectral bands and coverage rates unique to each mode, as detailed in later sections of this specification. The operating modes to be provided are:

Earth Resources

Meteorological Monitor, including 13-band IR Sounder

IR Sounder (23-band)

3.2.1.2 Operating Range

Same as Full-Up LEST

3.2.1.3 Area Coverage Rate

The LEST telescope shall meet the resolution and sensitivity requirements of this specification while scanning at areal coverage rates up to those tabulated below (referred to areas centered at 105 degrees west, 40 degrees north). The minimum swath width at nadir shall be 125 km. The optical field of the telescope shall correspond to a nadir swath of 375 km minimum.

Operating Mode	Average Coverage Rate
Earth Resources	2×10^3 km^2/sec
MET Monitor IR Sounder (Mode 1) } at same time	375 x 375 km^2 in .25 minute or 750 x 750 km^2 in 1.25 minute or 1500 x 1500 km^2 in 5.00 minute
IR Sounder (Mode 2)	TBD

3.2.1.4 Spectral Bands

Same as Full-up LEST.

3.2.1.5 Radiant Resolution, NER

Same as Full-up LEST, except that MET search mode requirements are not applicable.

3.2.1.6 Radiometric Fidelity

Same as Full-up LEST:

3.2.1.7 Spatial Resolution, EIFOV

Same as Full-up LEST except that MET search mode EIFOV requirements are not applicable.

3.2.2 Physical and Environmental Requirements

3.2.2.1 Environments

Same as Full-up LEST.

3.2.2.2 Weight and Size Limits

Same as Full-up LEST.

3.2.2.3 Power

TBD.